

Iron Complexes with Triazole-Based Ligand: Extend the SCO Molecule to High Dimensional Materials

Dissertation

A Dissertation Submitted to the Department of Chemistry,
Pharmacy and Earth Sciences
on the Requirements for the Degree of
Doctor of Science in
Chemistry

© Johannes Gutenberg University Mainz,
by

Ai-Min Li (厉爱民)

Born in Shan-Dong, China

Mainz, 2018

Dedicated to My Parents.
For Their Enlightenment and Endless Love.

Acknowledgements

Declaration

Erklärung

Die vorliegende Arbeit wurde in der Zeit von April 2015 bis March 2018 unter Anleitung von [REDACTED] im Institut für Anorganische und Analytische Chemie der Johannes Gutenberg-Universität Mainz angefertigt.

Ich erkläre hiermit, dass ich die vorliegende Arbeit selbstständig und ohne fremde Hilfe verfasst habe. Alle verwendeten Quellen und Hilfsmittel sind vollständig angegeben.

Mainz, 21 / 03 / 2018

Dekan: [REDACTED]

Erster Berichterstatter: [REDACTED]

Zweiter Berichterstatter: [REDACTED]

Abstract

The major focus of this thesis involves preparation of new Fe(II) complexes with potential to exhibit SCO transition. In order to acquire and tune SCO properties, a series of novel triazole-based ligands (L1 to L17), as well as their Fe(II) complexes were synthesized and characterized. Special attention was given to construct high dimensional Fe(II) complex with possible spin switching properties.

Ligands can mainly be divided into two different groups based on their flexibility. The first group of ligands shares an urea group between the triazole ring and the functional groups (L1 to L8), which can be treated as flexible ligands; the second group of ligands is built up from triazole Schiff base, with a Schiff base bond as linkage (L10 to L16), which can be assigned to half-rigid ligands. Besides these two groups, a reported ligand 4-(*p*-carboxyphenyl)-1,2,4-triazole (L9) and a newly synthesized ligand 3,3',5,5'-tetra[(2-pyridylmethyl)amino-methyl]-4,4'-azo-1,2,4-triazole (L17) are also prepared for the present study. A number of novel complexes have been synthesized and characterized with these ligands, some of which exhibit interesting magnetic behaviours ranging from SCO transitions to antiferromagnetic coupling to ferromagnetic coupling.

A series of three dinuclear and two trinuclear *N1,N2*-triazole bridged Fe(II) complexes are summarized in Chapter 2 and Chapter 3, which covered the discussion of SCO transitions and antiferromagnetic coupling among these five discrete molecular complexes. Chapter 4 contained three polynuclear Fe complexes with the coordination mediated by a second carboxyl-based ligand (oxalate, citrate). The three structures differed from a Fe(III) dimer to a Fe(II) one dimensional chain to a Fe(II) three dimensional framework. Detailed magnetic properties of these three complexes are explored. The high dimensional networks built up from the [FeN₆] core are summarized in Chapter 5, which covers two examples of 2D Fe(II) layered networks with quite different magnetic behavior: one complex shows ferromagnetic coupling between the linked Fe(II) centers, while the second one exhibits weak antiferromagnetic coupling through the supramolecular interactions.

Beyond the successful synthesis and characterization of these desired complexes, Chapter 6 summarizes several crystal structures that formed as unexpected results during the present study. These structures mainly came out as a result of the competition between the crystallization of the targeted complex and the isolated by-product, either Fe complex or pure ligand form. Detailed discussion has been made in regard to explore the relationship between the supramolecular interactions and the unexpected crystals formation.

Table of Contents

Acknowledgements	III
Abstract	V
Table of Contents.....	VII
Chapter 1 Introduction	1
1.1 Ligand Field Theory	1
1.2 Occurrence of Spin Crossover	2
1.3 Thermal-Triggered Spin Transition.....	4
1.4 Light-Induced Excited Spin-State Trapping (LIESST).....	7
1.5 Other Influence on Spin Transition	9
1.5.1 External Pressure	9
1.5.2 Solvents Effects	10
1.5.3 Nature of Ligand and Counteranion.....	11
1.6 Development of 1,2,4-triazole System	13
1.7 Characterization Techniques of SCO Complexes	17
1.7.1 General Overview.....	17
1.7.2 Single Crystal X-Ray Diffraction.....	18
1.7.3 Magnetic Measurements.....	19
1.7.4 Mössbauer-Spectroscopy.....	19
1.7.5 The Hirshfeld Surface Technique.....	21
1.8 Objective and Scope of the Thesis	23
1.9 References	26
Chapter 2 SCO Investigation of Three Triple <i>N1,N2</i>-Triazole Bridged Fe^{II} Complexes based on Toltrz.....	31
2.1 Abstract.....	31
2.2 Introduction	31
2.3 Experimental Section.....	33

Table of Contents

2.4 Result and discussion	36
2.4.1 Structural Description.....	36
2.4.2 FT–IR spectroscopy	43
2.4.3 Magnetic susceptibility and Mössbauer Spectroscopy.....	44
2.5 Conclusion.....	49
2.6 Acknowledgement.....	50
2.7 Reference.....	50
2.8 Supplementary Information.....	52
Chapter 3 SCO Investigation of Two Triple <i>N1,N2</i>-Triazole Bridged Fe^{II} Complexes based on Prytrz.....	55
3.1 Abstract.....	55
3.2 Introduction	55
3.2 Experimental Section.....	56
3.4.1 Structural Description.....	60
3.4.2 FT–IR spectroscopy	66
3.4.3 Magnetic susceptibility and Mössbauer Spectroscopy.....	67
3.5 Conclusion.....	71
3.6 Acknowledgement.....	71
3.7 Reference.....	72
3.8 Supplementary Information.....	74
Chapter 4 Three Iron Polynuclear Complexes: Magnetic Properties from a Dimer to 1D chain to 3D frame work.....	76
4.1 Abstract.....	76
4.2 Introduction	76
4.3 Experimental Section.....	78
4.4 Result and discussion	81
4.4.1 Structural Description.....	81
4.4.2 FT–IR spectroscopy	87
4.4.3 Magnetic susceptibility.....	89

4.5 Conclusion.....	92
4.6 Acknowledgement.....	92
4.7 Reference.....	92
4.8 Supplementary Information.....	95
Chapter 5 Two 2D Fe^{II} Networks Built Up from Imztrz: Antiferromagnetic v.s. Ferromagnetic Interaction.....	96
5.1 Abstract.....	96
5.2 Introduction.....	96
5.3 Experimental Section.....	98
5.4 Result and discussion.....	101
5.4.1 Structural Description.....	101
5.4.2 FT-IR spectroscopy.....	108
5.4.3 Magnetic properties and Mössbauer Spectroscopy.....	109
5.5 Conclusion.....	115
5.6 Acknowledgement.....	115
5.7 Reference.....	116
Chapter 6 Crystal Structure of “Fleeting Fe complexes” and Ligands: Crystallization Consideration.....	119
6.1 Mononuclear $[Fe^{II}(2-imztrz)_2(CH_3OH)_2(SCN)_2]$ (C11).....	119
6.2 Dinuclear $[Fe^{II}_2(L4)_6(C_2O_4)(H_2O)_2](SeCN)_2(L4)_2(H_2O)_4$ (C3).....	121
6.3 Three Polynuclear Fe ^{II} Complex from Hcpt (L9).....	123
6.3.1 1D Chain Structure of $[Fe^{II}(cpt)(OH)(H_2O)_2]_n$ (C13).....	123
6.3.2 Hexanuclear structure of $[Fe^{II}_6(\mu_3-O)_2(OH)_2(cpt)_6(H_2O)_2]_n$ (C14).....	124
6.3.3 3D structure of $[Fe^{II}_3(\mu_3-O)(OH)(cpt)_3(H_2O)_2]_n$ (C15).....	126
6.4 Layered Structure of Half-Rigid Ligand.....	127
6.5 Layered Structure of Flexible Ligand.....	130
6.6 Rationalization of the Crystallization.....	132
6.7 Reference.....	136

Table of Contents

Chapter 7 General Discussion and Perspective	137
Chapter 8 Methodology and Technique	141
8.1 Materials and Characterization	141
8.1.1 Materials	141
8.1.2 NMR-Spectroscopy	141
8.1.2 Single X-ray Crystallography	141
8.1.3 SQUID Measurements	142
8.1.5 Mössbauer Measurements	142
8.1.6 Infrared Spectroscopy	142
8.1.7 Elemental Analysis	142
8.2 Synthetic Method	143
8.2.1 Preparation of Ligands	143
8.2.2 Preparation of Fe Complex	154
8.3 References	161
Chapter 9 Appendix	162
9.1 Crystallographic Parameters and Tables	162
9.2 NMR Spectra	171
9.3 Infrared Spectra	180
9.4 References	189
List of Abbreviations	191
List of Compounds	193
Curriculum Vitae.....	195

Chapter 1 Introduction

1.1 Ligand Field Theory

As an extended theory of crystal field theory (CFT), ligand field theory (LFT) focuses on the donor atoms' effect on the energy of d orbitals in metal complex. In a free transition atom, all d orbitals are degenerated: d_{z^2} , d_{xy} , d_{yz} , d_{xz} and $d_{x^2-y^2}$. They all have the same energy. According to ligand field theory, ^[1] when the transition metal ion is surrounded by donor ligands, forming a complex, an electrostatic repulsion between the ligands and the electrons of the transition metal ions in the d orbitals is found. Depending on the difference of the coordination number and the geometry that is formed in the complex, the atomic d orbitals interact with the donor orbitals (typically) of the ligands differently. In the case of an octahedral coordination geometry (O_h) with six donor atoms, the d orbitals split into two degenerated subsets: the lower energy t_{2g} and the higher energy e_g orbitals. ^[2] The ligand field splitting (LFS) parameter (Δ_o , $\Delta_o = 10Dq$) defines the energy difference between the two sets of orbitals. For example, when the ligands point directly towards an orbital, the energy level of that orbital increases by $0.6 \Delta_o$. This is the case for the e_g orbitals, that is, $d_{x^2-y^2}$ and d_{z^2} orbitals, with anti-bonding character. Correspondingly, the energy of the remaining t_{2g} orbitals (d_{xy} , d_{yz} , d_{xz} orbitals) decreases by the same amount in total, $0.4 \Delta_o$ for each orbital, with non-bonding character ^[3] The octahedral transition metal complexes with a d orbital occupancy of d^n ($4 \leq n \leq 7$) are able to propose at least two electronic configurations, the most typical ones being either low spin (LS) or high spin (HS). The relative magnitudes of the ligand field splitting (LFS) parameter (Δ_o) and the spin pairing energy (P) (the repulsion between two electrons sharing one orbital) determine the stabilisation of one configuration over another. ^[3] For example, if LFS (Δ_o) is larger than P , the LS state would be energetically favourable. As it takes less energy for electrons to share orbitals, rather than occupy higher energy orbitals. On the other hand, if Δ_o is small whereas the P is relatively large, the electrons will tend to occupy the higher energy orbitals resulting the complex staying in HS state.

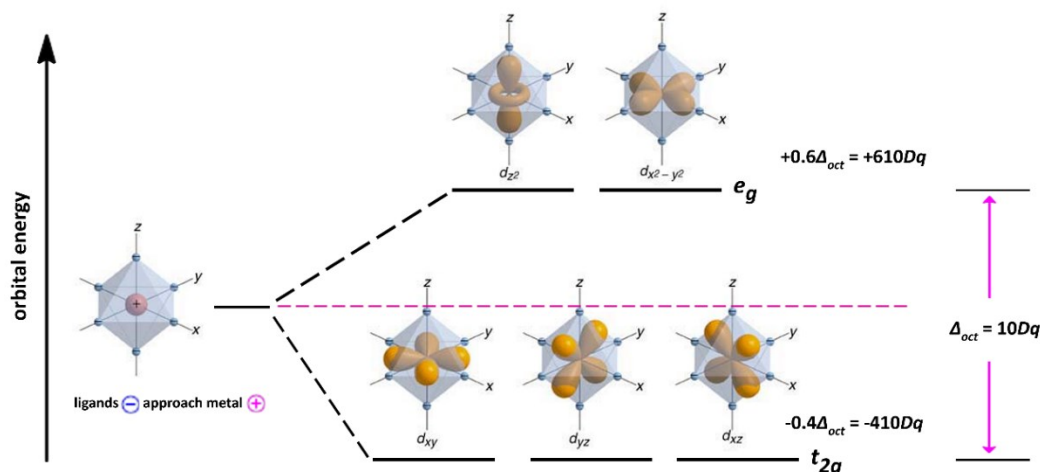


Figure 1.1.: Schematic representation of the d-orbital splitting in an octahedral ligand field and shape of d orbitals during the splitting. The diagram also illustrates the directionality of the metal d orbitals with respect to ligand σ orbitals. It should be noted that the orbitals with e_g symmetry point directly at ligand σ orbitals, whereas the orbitals with t_{2g} symmetry do not. Figure adapted from reference [2b]

Take an example, as the diagram of the energy configurations shown in figure 1.1, for an Fe(II) d^6 system in a weak ligand field ($P > \Delta_o$) will end up with an electronic configuration HS state (maximum number of unpaired electrons). So the final complex will be shown as paramagnetic HS complex ($t_{2g}^4 e_g^2$, ${}^5T_{2g}$, $S = 2$). Conversely, assuming in the same system we have a strong ligand field ($P < \Delta_o$), then the electrons will be completely filled into the t_{2g} orbital and result in a diamagnetic LS complex ($t_{2g}^6 e_g^0$, ${}^1A_{1g}$, $S = 0$). The stable form of the electron occupation can be identified by making a comparison between the LFS (Δ_o) and the spin pairing energy P , such the state of the system can be ensured. As the value of P in transition metal system is nearly constant, the LFS is the only variable factor that determines whether the HS or LS state is preferred. [3,4]

1.2 Occurrence of Spin Crossover

In general, according to Hund's rule, [5] the metal d electrons will fill up the orbitals starting from atomic orbitals with the lowest energy, with one electron per orbital, and all spins parallel to each other. While for transition metal ions with d^4 – d^7 electron configuration, things can change to a quite different situation. As mentioned in the last section, if the metal ion is put in the octahedral symmetry environment, we have two parameters to determine the favorable electron stable states: ligand field splitting parameter (Δ_o) and the spin pairing energy P . Under some specific conditions, when the ligand field is of an intermediate strength ($P \approx \Delta_o$), the competition between LFS (Δ_o) and the pairing energy of the different electrons will lead to complexes of a different spin state for the same geometry. This allows

reversible spin transition between electronic configurations to occur upon the perturbation of the environmental factors, such as temperature, pressure, or light irradiation. This phenomenon is called Spin Crossover (SCO). (Figure 1.2, illustrates the case of a $3d^6$ Fe^{II} ion)

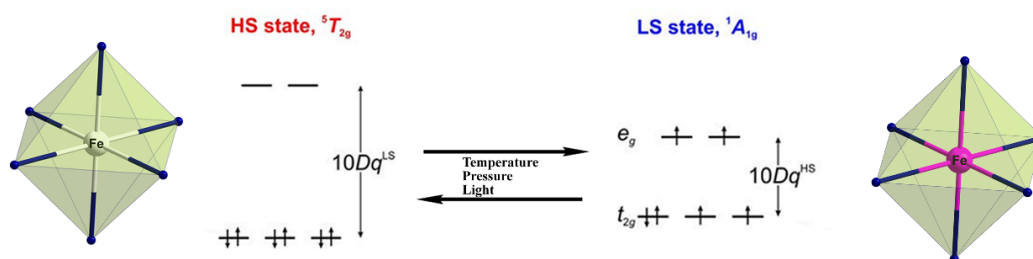


Figure 1.2.: HS and LS states transition for a molecular species formed by Fe^{II} ion surrounded by six ligands situated at the corners of an octahedron.

In principle, this phenomenon can happen in any transition ions with d^4-d^7 electron configuration, while we can find that some metal system has much larger tendency to have SCO behavior than the others. Among the SCO field, majority of complexes have been found in iron(II) and iron(III) system, with a few numbers in cobalt(II) and cobalt(III), while very rare SCO cases were found in chromium(II), manganese(II) or manganese(III). The reason of the scarce SCO examples found in the $4d$ or $5d$ transition rows is accordance with the the increased ligand field splitting energy trends. According to Racah, ^[6] for the complex of metal ions in the same group, with same oxidation state and identical ligand sphere, the ligand field strength increases by around 50 % from $3d$ to $4d$, also from $4d$ to $5d$ elements, whereas the spin-pairing energy does not change so much in this order. For that reason, the LS state is commonly adopted among $4d$ and $5d$ complexes. For Fe(II), on one hand, the low-spin d^6 configuration has maximum ligand field stabilisation energy; on the other hand, the relatively large Fe(II) ion sphere induces a rather weaker ligand field in most ligands. In contrary, for example, Co(III) ion has a relative smaller sphere, even though it also has d^6 configuration, the LS state configuration is almost always adopted. In addition, SCO transition has been found more often in an octahedral sphere than tetrahedral symmetrical environment. The reason being that the low ligand field splitting favors high spin tetrahedral complexes. ^[7,8,9] So from here, our discussion will mainly focus on iron complexes that show SCO behavior, especially attention is given on the octahedral iron(II) systems.

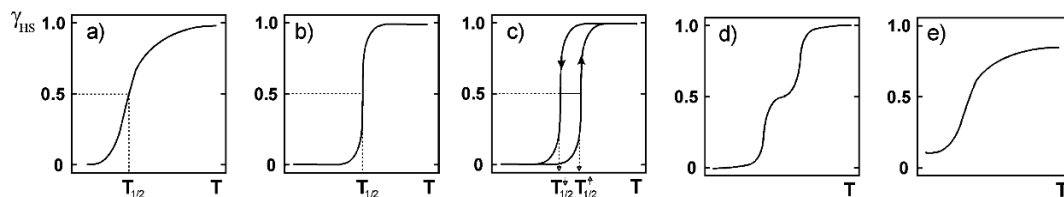


Figure 1.3.: Schematic representation of the main types of SCO event. Displaying as the high-spin fraction (HS) vs. the temperature (T): gradual ST (a), abrupt ST (b), ST with hysteresis (c), two-step ST (d) and incomplete ST (e). Figure adapted from reference [10b]

SCO behaviour can adopt quite different forms with the individual system, there are many factors that can influence the final spin transition behavior. In general, there are five typical categories in which most of the transitions can be divided into: that is, gradual, abrupt, hysteretic, multi-step and incomplete transition. ^[10] (Figure 1.3) When there is minimal or no communication between individual SCO centres, a gradual spin transition is observed, as shown in Figure 1.3a. This phenomenon is mostly found for complexes in the solution, or dispersed in a polymer media. In these systems, there are no effectively interactions between SCO active sites. A system with high degree of communication between the adjacent metal centres will show some degree of cooperativity and give an abrupt transition (Figure 1.3 b and c), when the communication is strong enough, that is, with a strong cooperativity between the SCO centers, a thermal hysteresis would occur. This indicates the memory effect of the bistable compounds, which further makes it possible for electronic device application. ^[11] The SCO systems may also undergo a multi-step transition due to the existence of, or conversion to multiple SCO environments (Figure 1.3 d), or exhibit an incomplete transition process (Figure 1.3e), which mainly arises due to paramagnetic centres that do not have the right ligand environment for SCO.

1.3 Thermal-Triggered Spin Transition

As discussed before, the electronic states of d orbital configuration for a specific electron number can be varied under the influence of an octahedral ligand sphere involving the interplay of electron-electron repulsion and orbital momentum. This can be calculated as functions of the so-called *Racah parameters*. ^[6] The corresponding results can be plotted in a Tanabe-Sugano diagram ^[12], which shows how the electronic states of a free ion split under the influence of an octahedral ligand field. As illustrated in Figure 1.4, the LFS (Δo) is given on the x axis with a value of 10 Dq and at a value of 0 Dq the ground state of a free d^6 ion is shown as 5D state. As Δo increases, the ground state 5D splits into two substates: 5E and 5T_2 state, with the latter being the ground state for the moment. An increasing ligand field

results in the stabilization of the LS 1A_1 ground state, which has its origin in the 1I ground state of the free ion. This suggests that the LS state is stabilized beyond a critical LFS Δ_{crit} where the spin pairing energy P is equal to the LFS (Δo). While Δo strongly depends on the metal-ligand distance r (equation 1.1, μ represent the dipole moment of the ligand) and an increasing distance r results in a decreasing Δo , which further favors the stabilization of the HS state. Theory has been developed regarding to estimate potentials for the HS and LS state dependence of the metal-ligand distance r . [13-15]

$$10 Dq \sim \mu/r^6 \text{ (equation 1.1)}$$

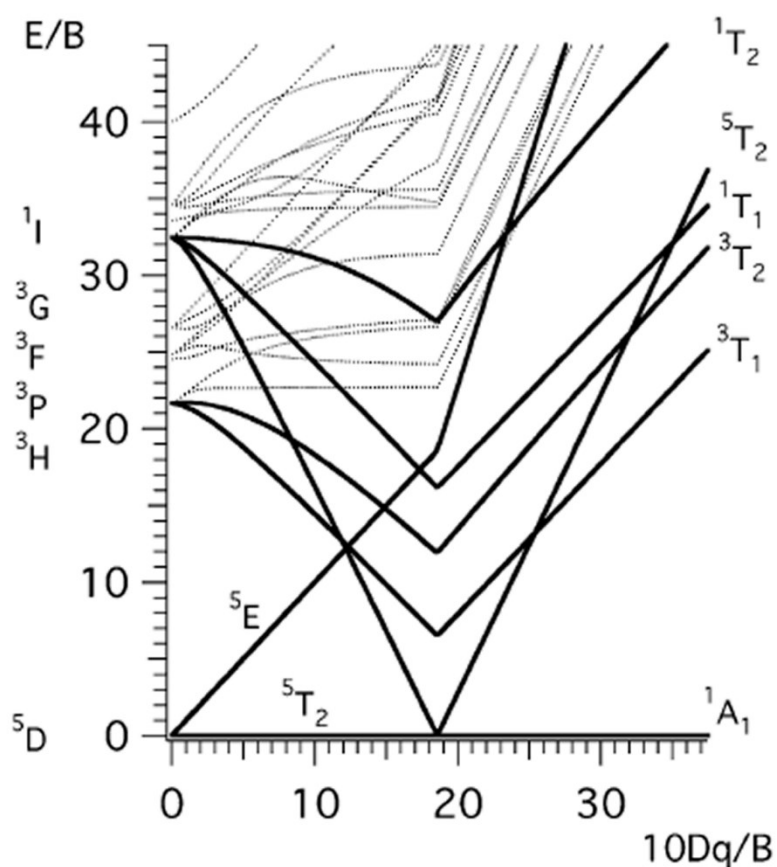


Figure 1.4 Tanabe-Sugano diagram for octahedral d^6 complexes assuming a Racah parameter of $B \approx 1050 \text{ cm}^{-1}$ for iron(II), showing the energy of the excited ligand-field states in units of the Racah parameter of electroelectronic repulsion B relative to the respective ground state, versus the ligand-field strength $10Dq$ also in units of B . [10b]

The representation of the structural change in the electron configuration diagram is the so-called potential energy diagram, where the potential energy (E_p) of the SCO system is plotted as a function of bond difference (Δr) between the HS and the LS metal-ligand bond strength. As shown in Figure 1.5, there are two potential wells stand for the HS and LS state of a spin crossover complex along the nuclear coordinate r_{Fe-L} , where the minima of the potential wells are displaced vertically and horizontally to each other. The population of

anti-bonding e_g orbitals in the high spin state leads to a stronger repulsion between the metal center and the donor atoms, which shows in the diagram as the ${}^5T_{2g}$ (HS) potential well is shifted toward a larger (Fe-L) distance. While in the case of 1A_g , all the electrons are in the non-bonding t_{2g} orbitals, resulting a rather shorter metal-ligand distance.

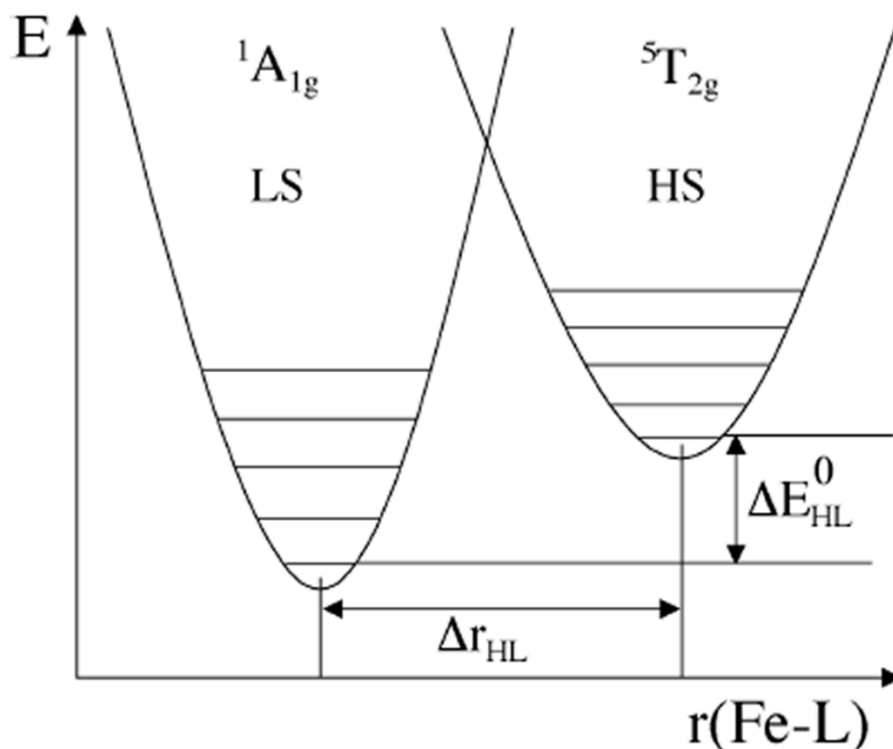


Figure 1.5: Representative scheme of the potential wells for the low-spin and high-spin state of an iron(II) spin-crossover complex.[10b]

The scheme of the potential wells (figure 1.5) also displays the zero-point energy difference of the LS and HS state ΔE_{HL}^0 , which represent for the most important factor for the occurrence of a thermal SCO. When suitable ligands are chosen, where the ΔE_{HL}^0 ($\Delta E_{HL}^0 = E_{HS}^0 - E_{LS}^0$) is in the order of magnitude of the thermal energy $k_B T$ ($k_B T \approx \Delta E_{HL}^0 \approx 200 \text{ cm}^{-1}$ at $T = 293 \text{ K}$), a thermally induced SCO could be achieved. The spin transition in the thermally induced SCO system is entropy-driven and includes two different contribution: a vibrational contribution and an electronic contribution. The spin degeneracy of the HS state and the higher density of its vibrational states leads to a larger entropy of this spin state compared to LS state. [16] The order of the enthalpy difference ΔH is usually $10\text{-}20 \text{ kJ mol}^{-1}$ and the entropy difference ΔS is between 50 and 80 kJ mol^{-1} during the spin transition. The relation between *Gibbs* free energy and the entropy ΔS is given in the *Gibbs-Helmholtz-equation*:

$$\Delta G = G_{HS} - G_{LS} = \Delta H - T\Delta S \text{ (equation 1.2)}$$

Where $\Delta H = H_{HS} - H_{LS}$ and $\Delta S = S_{HS} - S_{LS}$. At low temperature case, the LS state is stable (with $\Delta H > 0$ and $\Delta G > 0$). As the temperature increases, the $T\Delta S$ term becomes dominant, with $\Delta G < 0$, the HS state becomes more stable. ^[17] When $\Delta G = 0$, the value of $T_{1/2}$ can be expressed by Eq. (1.3). The transitional temperature $T_{1/2}$ can be defined as the temperature where the compound has an equivalent ratio of LS and HS.

$$T_{1/2} = \Delta H/\Delta S \text{ (equation 1.3)}$$

Based on theoretical and empirical derivations, general trends can be assigned in which energy region of ligand field makes it possible for SCO to occur. ^[13] (Scheme 1)

$10Dq^{HS} < 11000 \text{ cm}^{-1}$	HS complex
$10Dq^{HS} \approx 11500\text{--}12500 \text{ cm}^{-1}$ and	
$10Dq^{LS} \approx 19000\text{--}21000 \text{ cm}^{-1}$	spin crossover complex
$10Dq^{LS} > 21500 \text{ cm}^{-1}$	LS complex

Scheme 1.: The $10Dq$ ranges at which HS, LS or SCO complexes are expected.

1.4 Light-Induced Excited Spin-State Trapping (LIESST)

It was mentioned earlier that it is also possible to excite low spin centres into high spin states by irradiation with an appropriate wavelength of light. This phenomenon is called Light-Induced Excited Spin-State Trapping, also abbreviated as LIESST effect (taken each initial letter in the capital form). The process of photo induced switching was first observed in solution in 1982. ^[18] In 1984, Decurtins et al. ^[19] demonstrated the ability to convert $[\text{Fe}(\text{L})_6] \cdot [\text{BF}_4]_2$ (L = 1-propyltetrazole) from LS state to the metastable HS state with light irradiation at 514 nm at 10 K. The scheme in figure 1.6 shows the potential wells of the LS ground state (1A_1), the HS state (5T_2) with the respective higher excited states and illustrates the mechanism of the LIESST effect and the inverse effect called reverse LIESST.

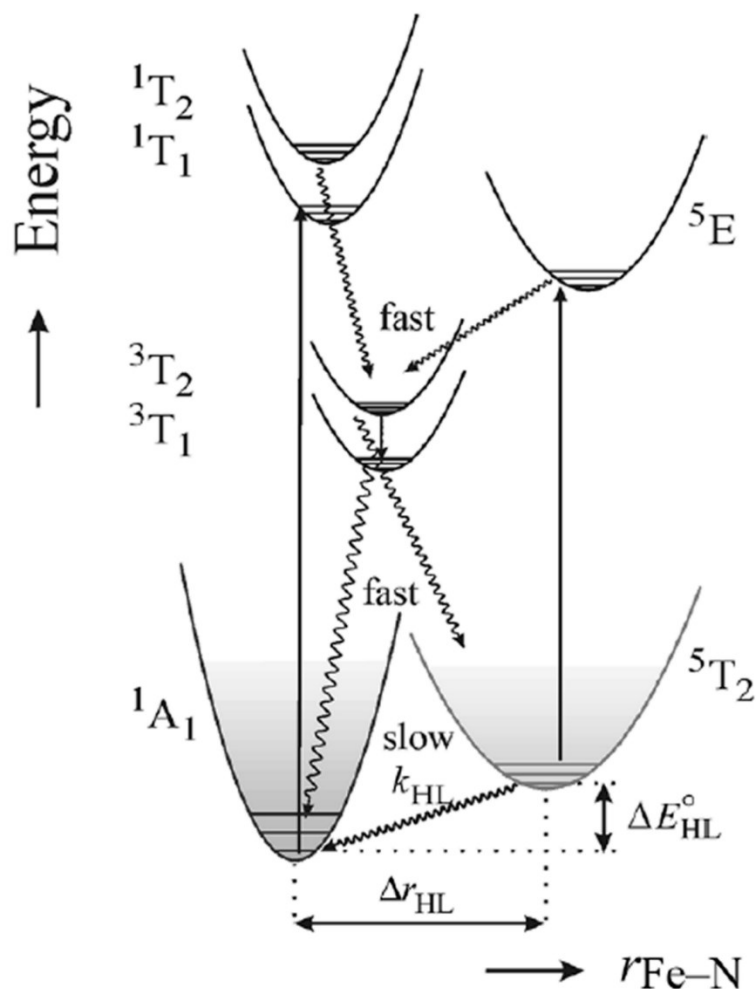


Figure 1.6.: Schematic illustration of LIESST and reverse LIESST of a d^6 complex in the SC range. Spin allowed d–d transitions are denoted by arrows and the radiationless relaxation processes by wavy lines. [14]

Irradiation of a sample in the LS state at low temperature with light of appropriate wavenumbers (commonly green light, 515 nm) leads to the spin-allowed population of the 1T_1 state, followed by an intersystem crossing decay into the triplet states 3T_2 or 3T_1 , and a second intersystem crossing decay further leads the system into the metastable 5T_2 state. As the radiative relaxation into the LS ground state is forbidden and the thermal tunneling into the 1A_1 state goes very slowly at low temperatures, this makes it possible that the metastable 5T_2 state can have a rather long lifetime at low temperatures. Interestingly, when a second irradiation with a different wavelength (such as a red light, 820 nm) is applied to the complex in the metastable 5T_2 state, the relaxation can go back into the 1A_1 ground state. (Figure 1.6) This process is called reverse LIESST. To date, the LIESST effect has been reported in a large number of iron(II) and a few iron(III) complexes. [20] The highest LIESST value at the moment is around 135 K, which is still very far from requirement for practical applications. [21]

1.5 Other Influence on Spin Transition

1.5.1 External Pressure

Apart the two major factors mentioned above (temperature, light irradiation) that can trigger spin transition (ST) among the $3d$ transition metal complexes, there are many other factors that can influence or even trigger the ST process. Another possibility to achieve or modify a spin transition is forcing pressure on the potential compounds. As the volume of the compound (ion and crystal lattice) will become smaller after the applying of external pressure, the metal-ligand distance will also be shorter, which increase the ligand field around the metal center. Intuitively, this will most likely favour the LS, *i.e.*, to increase the transition temperature. This has been confirmed ever since the first discovery of the pressure effect on a spin crossover system. [22] Figure 1.7 demonstrated the imposing of pressure on the SCO sample changes the ST from an abrupt curve to a gradual transition, with the $T_{1/2}$ increased during the process.

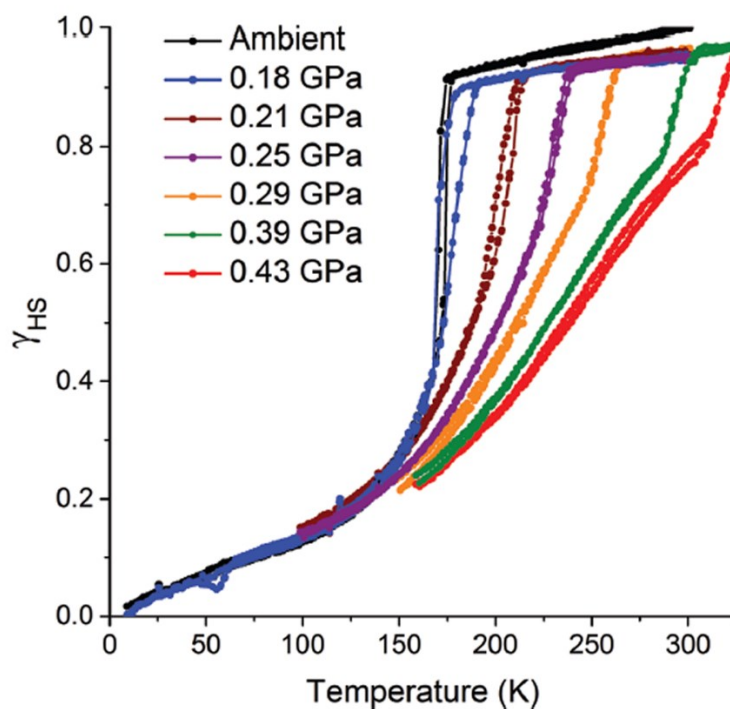


Figure 1.7.: Pressure induced phase transition triggered abrupt vs. gradual components of spin crossover. [22b]

An increase in pressure can effectively increase the separation between the zero point energies of the low spin and high spin states by the work term of $P\Delta V$. Prove has also been

shown that the application of pressure on a complex can in fact induce a transition in a HS system for which a thermal transition does not occur before the pressure addition. [23]

1.5.2 Solvents Effects

The solvents embedded in the crystal lattice could dramatically influence the spin-crossover properties of the complex, like water molecules as mostly discussed, sometimes non-coordinated ligand can also act as solvents. The solvents involved in the crystal lattice brings multiple intra- or intermolecular interactions that can make a fine-tuning of the SCO behavior. Even though this effect is hardly predictable, it is very important to discover and explore the relationship between these supramolecular interactions and the magnetic behavior. On one hand, there are many positive examples reported that the elastic interactions strengthened by the lattice solvents bring a stronger cooperativity between the active magnetic center, such leading to an abrupt transition or even hysteresis effect. [24] While on the other side, it is also known that such guest molecules may have a dilution effect so that it inhibits intermolecular contacts (negative effect). [25] A recent publication by our group also provided one example showing the lattice solvents (DMF) can initiate quite different SCO processes: from a gradual and incomplete ST to a half SCO in a dinuclear complex. [26] Another markable example has been given by the group of Sally Brooker [27]: In a dinuclear iron(II) complex, by putting the sample in different guest gas vapor (H₂O, EtOH, CH₃CN), the complex undergoes reversible single-crystal-to-single-crystal (SCSC) transformation process. The solvents involved here not only changed the magnetic behavior, but also brought clear color difference. This makes the SCO complex suitable for potential solvent sensor development. Interestingly, quite different from the gas adsorption in Metal Organic Frameworks (MOFs) materials, this complex does not own any porous voids inside the structure, indicating the guest recognition process is purely because of weak supramolecular interactions involved.

The adsorption abilities of different solvents in MOFs is well-known and widely studied, especially on the porous MOFs, they show dramatic characters with potential gas storage and application. [28] Guest-dependent SCO on MOFs system has also been reported years ago by Cameron J. Kepert and co-workers: [29] (Figure 1.8) The nanoporous metal organic framework Fe₂(azpy)₄(NCS)₄ (guest) (azpy = trans-4,4'-azopyridine) displays reversible uptake and release of guest molecules, and the electronic switching centers are sensitive to the nature of the sorbed guests. The switching of this material arises from the presence of iron(II) spin crossover centers within the framework lattice, the sorbed phases undergoing

“half-spin” crossovers, and the desorbed phase showing no switching property. The interpenetrated framework in the structure is found responsible for the guest uptake and release, causing substantial changes in the local geometry of the iron(II) centers. In this case, it is somehow very similar to the MOFs absorption of CH₄ or H₂ gas accompanying with SCO transition because of the porous character.

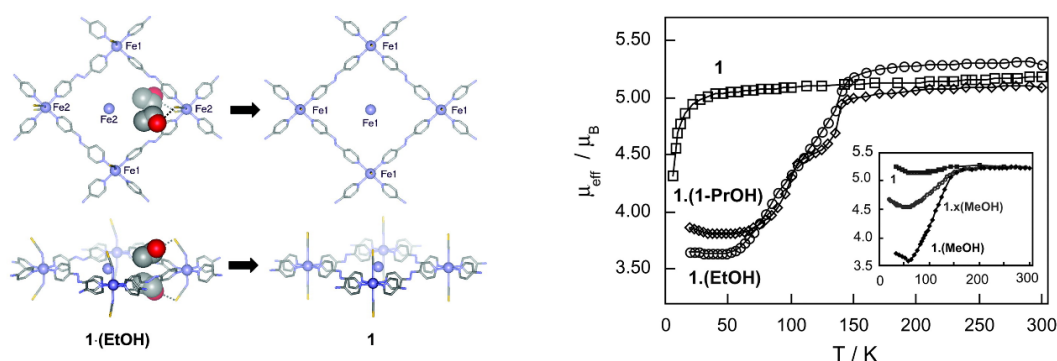


Figure 1.8.: Spin transition triggered by absorption/desorption of guest molecules. [29]

Very recently, the group of Jeffrey R. Long and co-workers have proven that the cooperative binding process is also possible with the SCO complex system. [30] By the selective adsorption of carbon monoxide (CO) in a series of metal organic frameworks with coordinatively unsaturated iron(II) sites. The neighbouring iron(II) sites undergo a SCO transition above a threshold CO pressure, these materials exhibit larger CO separation capacities when the electronic transformation altered the binding properties at neighbouring Fe sites. The demonstration here is that the cooperative adsorption is electronic based (spin based), that the changing of the spin center can also provide more efficient and selective adsorbing abilities of the MOFs.

1.5.3 Nature of Ligand and Counteranion

The replacement of one ligand by another can initiate, or modify the spin-crossover characteristics of a given complex. From an empirical point of view, for mixed complexes [FeA_nB_{6-n}] the rule of “averaged environment” holds [31] which illustrates that the 10Dq values of complexes can be found approximately through linear relationship between 10Dq values for [FeA₆] and [FeB₆]:

$$10Dq ([FeA_nB_{6-n}]) \approx 6/n * 10Dq ([FeA_6]) + 6/(6-n) * 10Dq ([FeB_6]) \quad (\text{equation 1.4})$$

An typical example is given by the system [Fe(py)₄(NCS)₂], which stays in HS state at room temperature and does not show any thermal spin-transition. The substitution of two of the pyridine molecules by relatively strong ligand field 1,10-phenanthroline molecules,

however, gives $[\text{Fe}(\text{phen})(\text{py})_2(\text{NCS})_2]$ which does undergo a thermal transition. ^[32] To modify the SCO properties by substitution of ligand is also possible with the counteranions. As when they coordinate to the metal centers, they directly affect the LFS (Δo) through the donor atoms. There are several reportings regarding this aspect. ^[33] Take the substitution effect of NCX^- ($X = \text{S}, \text{Se}, \text{BH}_3$) for example, a clear relationship has been observed between the replacement of the co-ligands and the the transition temperature $T_{1/2} : T_{1/2}(\text{NCS}^-) < T_{1/2}(\text{NCSe}^-) < T_{1/2}(\text{NCBH}_3^-)$. ^[33a] (Figure 1.9)

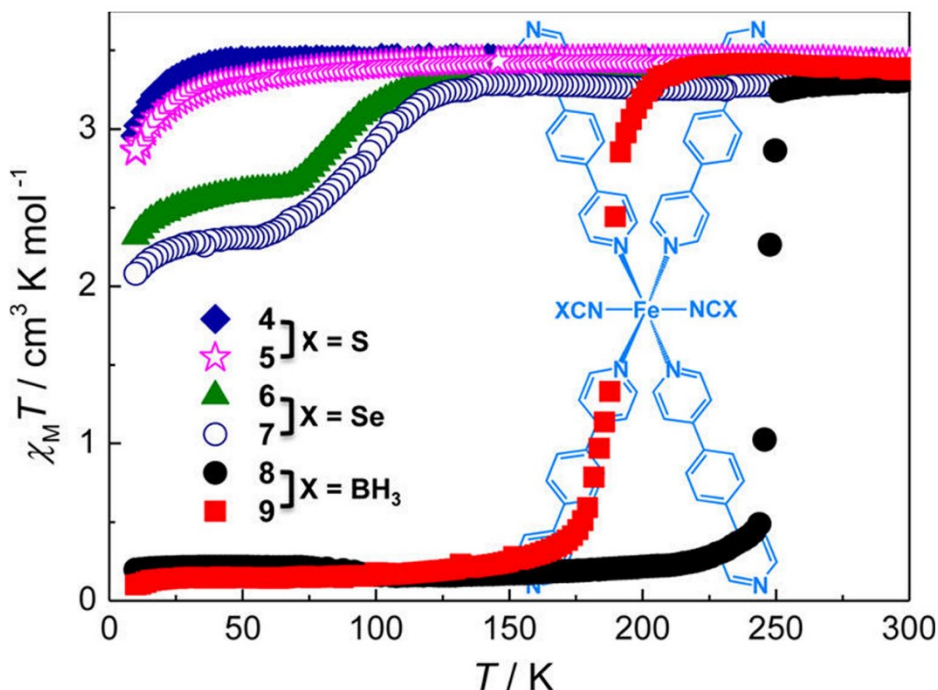


Figure 1.9.: Clear co-ligand effects on the SCO behavior as illustrated in a 3D network. ^[33a]

Another direction to influence the ligand field is the substitution within a ligand that may ultimately alter the spin state of a system. The Halcrow's group has been devoting to explore the relationship between the ligand substitute and counteranion effect with the $[\text{Fe}(\text{bpp})_2]^{2+}$ ($\text{bpp} = 2,6\text{-di}\{\text{pyrazol-1-yl}\}\text{pyridine}$) system for decades. Recently, they generalized a unified relationship between ligand substituents and spin state within this series of complexes. ^[34] As shown in figure 1.10, they summarized that the plots of the SCO transition temperature $T_{1/2}$ in solution vs. the relevant Hammett parameter ^[35] show that the low-spin state of the complex is stabilized either by electron-withdrawing pyridyl ("X") substituents, or by electron-donating pyrazolyl ("Y") substituents. However, the unsharp trends here can be unified by taking subset of complexes with halogeno X or Y substituents into consideration: the two sets of compounds instead show identical trends of a small reduction in $T_{1/2}$ with increasing substituent electronegativity.

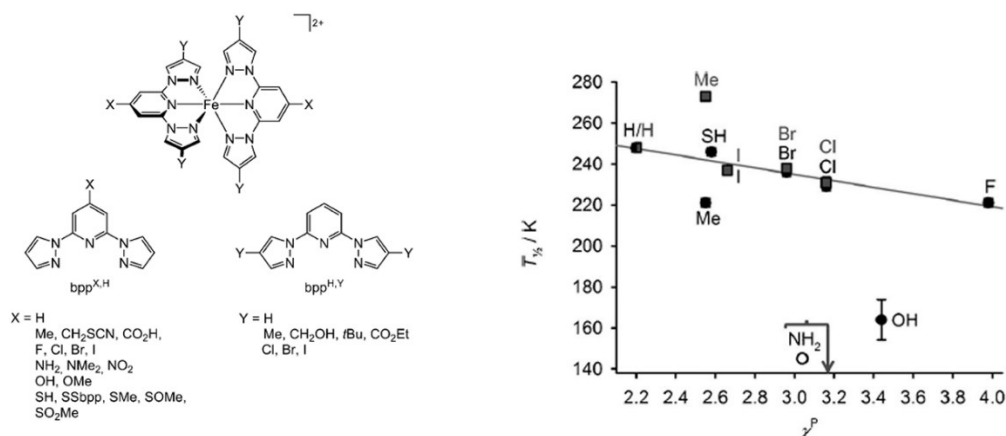


Figure 1.10.: Correlation between $T_{1/2}$ versus the substituent electronegativity χ^P in the $[\text{Fe}(\text{bpp})_2]^{2+}$ system. [34]

Another factor that we need to take into account is the steric hindrance that might give rise to the crystal lattice when replacing one functional group with another. The steric hindrance effect can substantially decrease the ligand field strength and destabilize the singlet ground state of iron(II) ion. [36] This is well demonstrated by a group of three-fold symmetric, four-coordinate iron(II) phosphoraminate complex $\text{PhB}(\text{MesIm})_3\text{Fe}-\text{N}=\text{PRR}'\text{R}''$ ($\text{PRR}'\text{R}'' = \text{PMePh}_2, \text{PMe}_2\text{Ph}, \text{PMe}_3, \text{and P}^n\text{Pr}_3$). [37] A detailed quantitative insight by correlating the $T_{1/2}$ against phosphine steric and electronic parameters suggests that transition temperature $T_{1/2}$ is primarily influenced by the size of the phosphoraminate ligand, with smaller ligands favoring the low-spin state.

1.6 Development of 1,2,4-triazole System

With the initial work of Cambi and Szegő in 1931, [38] the subject of SCO in d block metal complexes spans around nine decades and is one of the most intriguing areas of inorganic research. During the past decades, numerous of SCO complexes have been found and reported from the molecular level (mono-, tri-, tetra-, penta- and hexa-nuclear species) to one-dimensional (1D) chain structures, two-dimensional (2D) network, and three-dimensional (3D) porous SCO Materials. [39] The detailed study of these compounds provides us valuable information about the ligand substitution effect, counteranion effect, and crystal packing effect on SCO behavior. These research and studies partially reveals the relationship between the modified ligand field, supramolecular interactions and the SCO behavior, which guides us to design new SCO materials with wide hysteresis loop and large $T_{1/2}$. Despite the unique and markable SCO potential of all these excellent works, to understand the origin of the cooperativity and design strong cooperative spin-transition

compounds is still a very challenging task. The conception of rational design for SCO materials is still far away from practical application.

While one of the most important information from the last decades' research experience is that the cooperativity between the active spin metal centers is linked via the communication between them. This includes the supramolecular interactions, crystal packing and covalently linking bonds, *et cetera*. The idea of linking the spin crossover centers covalently to enhance the cooperative and abruptness is not new, ^[11] while the number of high dimensional (1D, 2D, 3D) complexes is still pretty rare. Most of the current ligand system on SCO research is confined with the molecular compounds, ^[40] which is limited for the full study of SCO origin. The Fe(II)-triazole system, a rather old system, however, shows as perfect candidate for such design consideration. Different from the above model examples listed in references 40, the Fe(II)-triazole system can not only build up the molecular level dinuclear and trinuclear SCO complex, but also is able to expand the dimension to 1D chains, 2D sheets and 3D networks showing different SCO behavior.

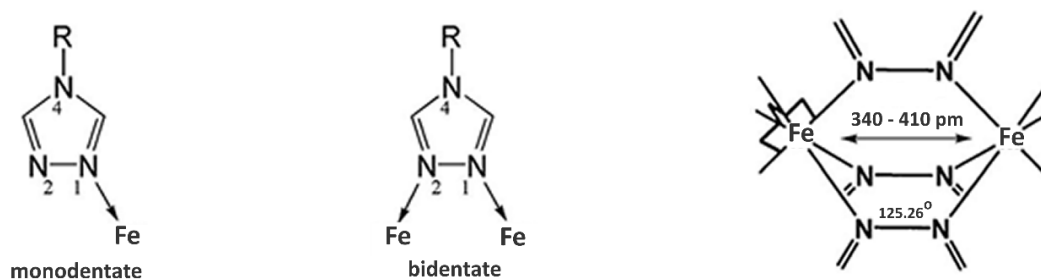


Figure 1.11.: Left, monodentate bridging binding modes of 4-substituted-1,2,4-triazoles; Middle, the bidentate bridging mode; Right, geometry of the stable triple $N1,N2$ -triazole bridge.

After the first reporting of Fe(II) nitrate and chloride complexes with 1,2,4-triazole and 4-amino-1,2,4-triazole in 1986, ^[41] the very good characteristics of these SCO complexes drawn great interest among researchers, especially under some leadership of P. Gütlich (*University of Mainz*), O. Kahn (*University of Bordeaux*), J. G. Haasnoot (*University of Leiden*) and L. G. Lavrenova (*Novosibirsk State University*). The 1,2,4-triazole (Htrz) and its derivatives without substituents at 1- and 2-positions tend to coordinate to metal centers in a bidentate bridging mode (Figure 1.11), forming either oligo- or polynuclear compounds. ^[42] This $N1,N2$ -triazole triple bridging mode is very stable, as the angle formed (125.26°) is quite similar to the angle of the exocyclic free donor electron pair of a regular five-membered ring (126°). The monodentate coordination mode can act as the same function like pyridine, which makes this ligand multi-functional for constructing SCO from

molecular compound to high dimensional structures. The detailed discussion of the reported iron(II)-triazole SCO complexes will be given as following:

Mono-nuclear complex

There are two reported examples with the mono- species, while in both cases, the triazole ligand adapt the monodentate coordination modes with the counteranion thiocyanate [43a] and dicyanamide [43b] facilitate the coordinate such that no SCO process was found. (Figure 1.12) Unlike the tetrazole ligand, where six tetrazole molecules binding to the Fe center leading to a SCO, [44] the ligand field from the counteranion here within the triazole compound must be too weak that it stays in HS state for the whole temperature range.

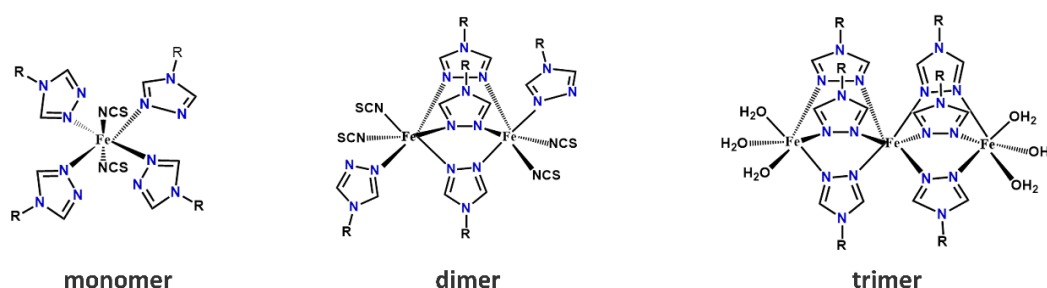


Figure 1.12.: The monomer, dimer and trimer compounds linked by different coordinate modes from triazole N.

bi- / tri-nuclear complex

When people try to construct the 1D chain structure, in many cases, especially for those containing a bulky R substituent at the 4-position of the triazole ring, only bi-, or trinuclear compounds were isolated rather than polynuclear 1D chains. (Figure 1.12) Listed as appendix, table 9.1 and 9.2 summarize the reported bi- and tri-nuclear Fe(II)-triazole compounds in Chapter 9, among them, only a few showing sharp SCO transition. Additionally, two exciting trimer compounds [45, 46] together with one dimer compound [47] have been reported this year, indicating intense interest and severe demanding in this family of SCO complex.

1D chain

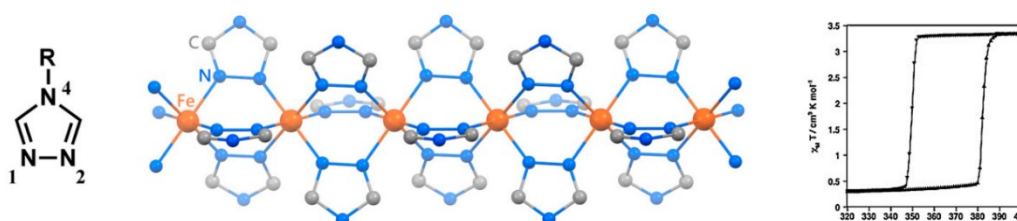


Figure 1.13.: Illustration of the one-dimensional (1D) coordination polymer chains of $[\text{Fe}(\text{R-trz})_3]$ and corresponding the high transition temperature with wide hysteresis loop. Figure adapted from reference. [48]

Among the few examples exhibiting remarkable SCO behavior, the famous 1D polymer with general formula $[\text{Fe}(\text{Rtrz})_3]\text{A}_2 \cdot n\text{Solvent}$ ($\text{A} = \text{mono anion}$) still remains among the most promising materials for future applications in electronic devices since some of them display wide thermal hysteresis loops around room temperature (Figure 1.13).^[11] Up to now, a large number of this polynuclear 1D chain complexes have been synthesized and studied. Due to poor crystallinity, most of these complexes are structurally characterized through a combination of X-ray absorption experiments (EXAFS), powder diffraction (PXRD) and comparison with their linear trinuclear compounds or other analogues. The synthesis and study of the linear polynuclear iron(II) complexes with 1,2,4-triazoles have been discussed in a number of reviews.^[42] Despite the paramount interest of this family, after the first isolation of the structure of $[\text{Fe}(\text{NH}_2\text{trz})_3](\text{NO}_3)_2$ in 2011, there is only one more crystal structure found very recently in this year.^[49] Compare to the large number of reports and huge interest in this family of complex, further systematic study of these complexes and the isolation of more crystal structures is in severe need.

2D & 3D structures

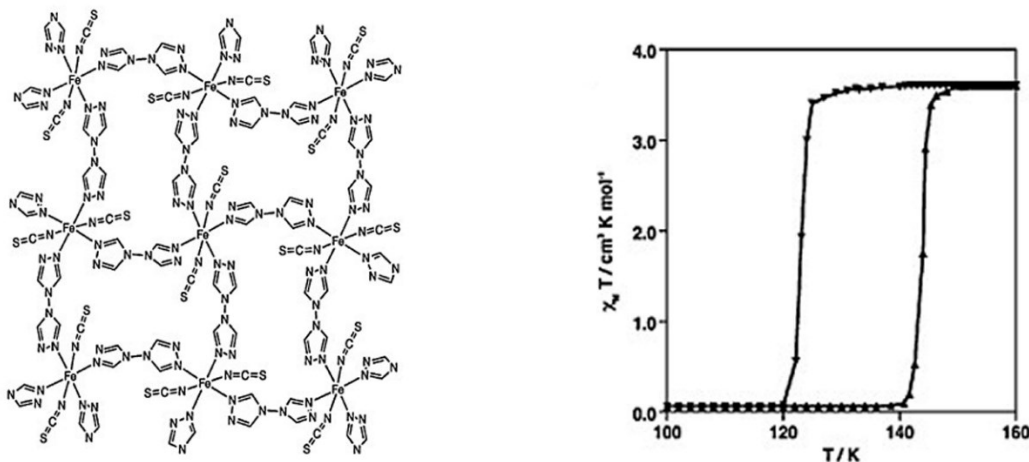


Figure 1.14.: Illustration of the two-dimensional (2D) framework of $[\text{Fe}(\text{btr})_2(\text{NCS})_2]$ and its high cooperativity between the active Fe centers. Figure adapted from reference.^[50]

The well-known iron(II) SCO coordination polymer in a 2D framework, $[\text{Fe}(\text{btr})_2(\text{NCS})_2] \cdot \text{H}_2\text{O}$ ($\text{btr} = 4,4'$ -bis-1,2,4-triazole) is found to exhibit an abrupt spin transition with 25 K hysteresis.^[51] This derivative represents the first example of a 2D spin transition compound and has become a model material in SCO research. In the structure, as shown in figure 1.13, the triazole ligand adapts the monodentate mode on both sides, acting with similar function as 4,4'-bipyridine (bpy) to link the metal centers to a 2D network. The apical positions are filled with the counteranion thiocyanate to finish the coordination

sphere. Later research has been made based on this model, and two other compounds have been reported with the very similar bi-triazole feature ligands linked via different groups ($-CH_2CH_2-$, $-N=N-$) between the two triazole rings. [52] Just like the bpy system, the azide-triazole complex also gave a result of 1D chain, which further showed a single-crystal-to-single-crystal (SCSC) transformation to a 3D network after dehydration of the coordinated water molecules, accompanying with SCO behavior. [53] Additionally, in the case of 4, 4'-bis-1,2,4-triazole, a three dimensional compound was discovered, showing a two-step spin conversion. [54]

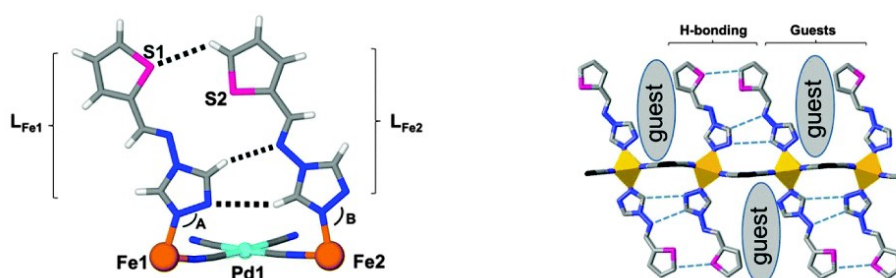


Figure 1.15.: Illustration of the Hoffmann type framework constructed via triazole ligand (monodentate mode). Figure adapted from reference. [55a]

Very recently, the triazole-based ligand has been successfully applied to the Hoffmann clathrates system. As illustrated in figure 1.15, the triazole ligand adapt the mono-dentate coordination mode to finish the axial coordination sphere, linking the structure to a high dimensional network with SCO properties. This work was first started by the group of Cameron J. Kepert and Suzanne M. Neville, [55a] four remarkable papers have been published recently, including one excellent work with four step iron(II) spin state transition. [55] These exciting works suggests a big breakthrough in triazole-based SCO system, which also implies the importance of further effort to be made in order to discover the full potential embedded inside this family of ligands.

1.7 Characterization Techniques of SCO Complexes

1.7.1 General Overview

During the SCO transition in a d metal complex, the electronic rearrangement around the d orbitals can bring lots of changes, from tiny electron configuration, magnetic moment to the properties of the bulk material. For thermally induced SCO, more oftenly, it will be accompanied by a change of color from LS state of purple (or pink–magenta) color to white (or light-reddish) HS state. The color change can even be detected by naked eye, while the

corresponding physical quantifying might need the help of advanced set up or spectrometers. For the magnetic moment, the old and typical methods like the Gouy- and Faraday-balance can not play too much role here as their application is more or less confined with room temperature. The differential scanning calorimetry (DSC) method provide a way to investigate the changes in the heat capacity of a sample and can be used to calculate enthalpy and entropy changes during different state transitions. As was discussed in section 1.3, based on the integration of the heat capacity, the transition temperature $T_{1/2}$ can be calculated. Common modern techniques to detect and quantify SCO processes include: variation-temperature single X-ray diffraction, magnetic measurements and Mössbauer spectroscopy. These techniques will be given a detailed explanation in the following section. In addition, there are also some less frequently used methods during the characterization of SCO behavior, like IR (Infra-red) and Raman spectroscopy, UV/Visible (UV/Vis) spectroscopy and Electron Paramagnetic Resonance (EPR) spectroscopy.

1.7.2 Single Crystal X-Ray Diffraction

Single Crystal X-Ray Diffraction (SC-XRD) is one of the most valuable analysis techniques we can use to detect and analyze a SCO process. As was discussed in section 1.3, because of the difference population of antibonding e_g orbitals, the metal to donor atoms bond lengths for the different spin states can be quite different. In general, for iron(II) complexes, the average distances (Fe-N) are between 1.9 Å and 2.0 Å for LS state and 2.1 Å to 2.2 Å for HS state, this also brings up about 3~4% difference in cell volume. [56] These detailed experimental values can be obtained in SC-XRD. More importantly, it can also provide us lots of other valuable information such as molecular symmetry, distortion in complex geometry and intra-/inter-molecular interactions, *et cetera*. These factors are vital to uncover the mystery of SCO transition deep into the atomic level. In common case, the change of bond lengths during the spin transition directly alters the geometry of the complex leading to a more distorted octahedral sphere in the high-spin-state. The degree of the distortion within the octahedral coordination sphere is given as the octahedral distortion parameter Σ_{ODP} :

$$\Sigma_{ODP} = \sum_{i=1}^{12} (|90 - \alpha_i|) \text{ (equation 1.5)}$$

α_i is the *cis*-bond angles between the donor atoms of the ligand and the metal center

As the the geometry is more ordered in the LS state, commonly the Σ_{ODP} value is below 80° for LS and above 100° for HS state. [57]

1.7.3 Magnetic Measurements

From the magnetic point of view, the most dramatic change during a spin transition is quite obvious. Ideally, for a Fe(II) SCO complex, the changing from HS to LS state leads to a changing of paramagnetic ($S=2$) metal center to a total diamagnetic ($S=0$) metal center. This alteration can be easily detected via magnetic measurements using a SQUID (Superconducting QUantum Interference Device) magnetometer. The SQUID is based on superconducting loops containing Josephson junctions, and it allows the measurement of extremely low magnetic fields such brings high sensitivity towards any tiny change in the magnetic susceptibility. The temperature dependence of the susceptibility of a given sample can be measured and from the collected data, we can plot the $\chi_m T$ vs. T plot. These plots contain information about the magnetic susceptibilities changes during the spin transition.

1.7.4 Mössbauer-Spectroscopy

For ^{57}Fe containing samples, there is the very particular Mössbauer spectroscopy, [58] which is based on the recoil-free resonant absorption and emission of gamma rays in solids. Only specific elements can be analysed using Mössbauer spectroscopy, as two requirements need to be met: low energy gamma rays and long-lived excited state. The most commonly analysed isotope is ^{57}Fe , but ^{119}Sn , ^{151}Eu , ^{121}Sb and ^{161}Dy can also be analysed. [59] This technique probes the hyperfine interactions between the Mössbauer nuclei and its surrounding electrons. Typically, the Mössbauer spectra of iron complexes can consist of three different features: a singlet (isomer shift, δ), a doublet (quadrupole splitting, Δ), or a sextet (magnetic splitting), corresponding to three different interactions involved: the electric monopole interaction, the electric quadrupole interaction and the magnetic dipole interaction. (Figure 1.16) Due to the high energy and extremely narrow line widths of gamma rays, among all different spectroscopies, Mössbauer spectroscopy is the most sensitive techniques with highest resolving power of 6.5×10^{-13} . [60]

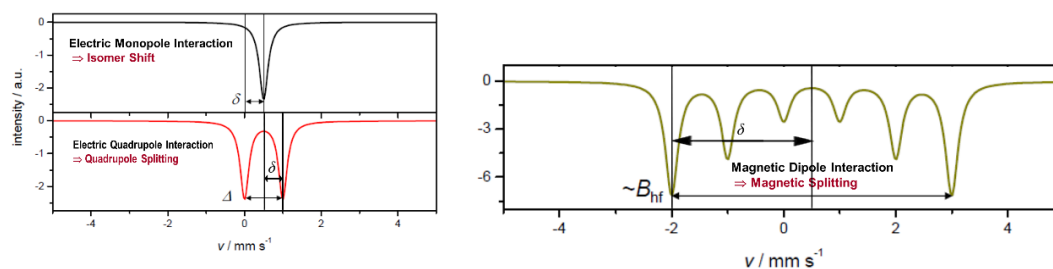


Figure 1.16.: Illustration of typical Mössbauer Spectra.

For the Fe complex in different spin states, the different electronic environments around the Fe center leads to an obvious difference of the quadrupole splitting Δ_{EQ} and the isomer shift δ distinguishing the HS- and the LS-state. A very remarkable example is given as for the mononuclear SCO complex $[\text{Fe}(\text{phen})_2(\text{NCS})_2]$ with transition temperature $T_{1/2} = 180\text{K}$ and its derivative complex $[\text{Fe}(\text{phen})_3]\text{X}_2$, which has no spin transition from 300K to 2K. [61] As shown in figure 1.17, for the SCO $[\text{Fe}(\text{phen})_2(\text{NCS})_2]$, the quadrupole splitting Δ_{EQ} in the Mössbauer spectrum going from a HS doublet at 300 K to a LS doublet at low 77 K is clearly different, where the HS Fe center has a big Δ_{EQ} and the LS metal center has a relatively small quadrupole splitting. The process from 300K to 188K, 186K, 180K, 189K and 77K, perfectly explains the SCO transition process with the area beneath the signal of a HS or LS-species indicating its corresponding abundance in the sample. While for the non-SCO $[\text{Fe}(\text{phen})_3]\text{X}_2$ complex, there is no obvious change observed from 300K to 5K, the quadrupole splitting Δ_{EQ} stayed the same during the temperature range.

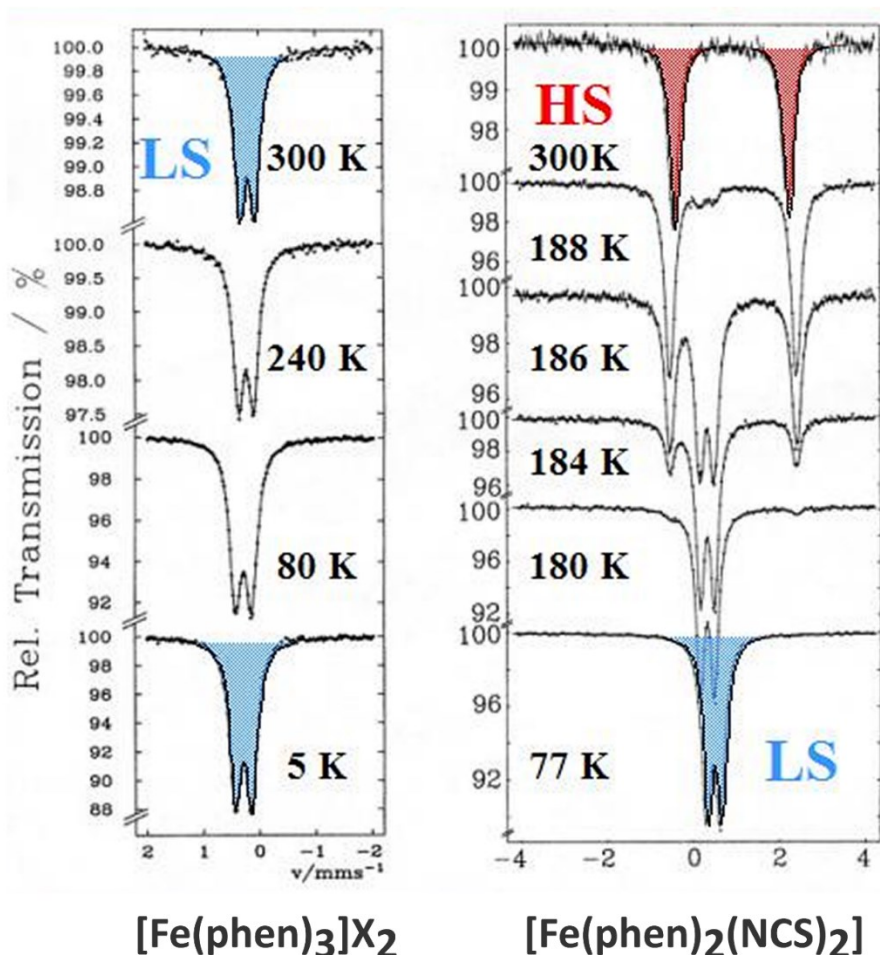


Figure 1.17.: Illustration of Mössbauer Spectra on a group of non-SCO and SCO complex.

1.7.5 The Hirshfeld Surface Technique

As previously discussed in section 1.7.2, the single crystal X-ray diffraction technique offers a great detailed insight into the structural and spatial arrangement of individual molecules within a crystal, which is of vital importance for the analysis of the crystal packing and supramolecular interactions within the solid lattice. However the crystal data itself gives no definitive answer about the molecular contacts and much of the detailed information is therefore based on observation and detailed explanation of those short contacts. A recently developed method, the Hirshfeld Surface Analysis, [62] however, provides visualized information about the crystal packing and the strength of the intermolecular interactions inside the crystal lattice. This makes the analysis of the crystal structure simpler and clearer, especially on the intermolecular interaction analysis.

The Hirshfeld surfaces represents the partition of the total crystalline electron density into molecular fragments. Hirshfeld partitioning is an extension of the Hirshfeld stockholder concept, [63] which divides the electron density of a molecule into continuous atomic fragments. The concept was generalized to extract continuous molecular fragments from electron density distributions by defining a molecular weight function:

$$w(r) = \frac{\sum_{A \in \text{Molecule}} \rho_A(r)}{\sum_{A \in \text{Crystal}} \rho_A(r)} = \frac{\rho_{\text{promolecule}}(r)}{\rho_{\text{procrystal}}(r)} \quad (\text{Equation 1.6, taken from ref [64]})$$

Where $\rho_A(r)$ are spherically averaged atomic electron density functions [64] centered on the position of the atoms. The $\rho_{\text{promolecule}}(r)$ and $\rho_{\text{procrystal}}(r)$ are the appropriate sums of the electron density of the atoms belonging to molecule and crystal, respectively. Such the integration over the weighted electron density can reflect the molecular properties. [65] The defined molecular Hirshfeld surfaces, where $w(r)$ equals to $\frac{1}{2}$, represent partitioned regions over the space where the total electron density of spherical atoms of a molecule (promolecule) dominates the corresponding sum of the crystal (procrystal). [66] The volume inside the Hirshfeld surface satisfies the condition that the weight function ≥ 0.5 , this cut-off value guarantees maximum proximity of neighbouring molecular volumes, *i. e.*, the molecular surfaces will at most touch but never overlap. The surfaces therefore pack very tightly, only leaving small gaps between molecular surfaces where no molecule dominates the electron density. Compared to other molecular analysis methods, like, quantum theory of atoms in molecules (QTAIM), [67] Wigner–Seitz Cell (WS), [68] fused Van der Waal surface [69] and solvent excluded/accessible surfaces, [70] the Hirshfeld surfaces method bears several advantages besides as the function of the molecular geometry. Hirshfeld surfaces are defined within the crystal lattice, hence necessarily reflect the interplay between

different atomic sizes and intermolecular contacts in the crystal: intermolecular interactions. [71]

With the assistance of the *CrystalExplorer Program* released by Spackman and McKinnon, [66b] a large range of properties can be visualized on the Hirshfeld surface, including the distance of external atoms, d_e , and internal atoms, d_i , to the surface. The distance information among the surface can be condensed into a 2D histogram of d_e and d_i , containing the unique close contact information for molecules in a crystal structure, called a fingerprint plot (Figure 1.18). [66a] Besides plotting d_e and d_i onto the Hirshfeld surface, a normalized contact distance, d_{norm} , is also defined:

$$d_{norm} = \frac{d_i - r_i^{vdW}}{r_i^{vdW}} + \frac{d_e - r_e^{vdW}}{r_e^{vdW}} \pi r^2 \quad (\text{Equation 1.7, taken from ref [66a]})$$

Where the r^{vdW} is the van der Waals radius of the appropriate internal or external atom of the surface. This new defined d_{norm} is introduced to explain the drawback that the d_e/d_i surfaces does not take into account the size of atoms. For example, close contacts between smaller atoms (H, C, N and O) are highlighted better using the d_e function than those between larger atoms, e.g. P, S, Cl. The d_{norm} property avoids this problem by plotting a measure of whether the contact between atoms is greater, the same, or less than the sum of the van der Waals radii. The d_{norm} based Hirshfeld surface mapped the surface using a colour scale from blue (contacts longer than vdW separation), through white (around vdW separation) to red (shorter than vdW separation), by means of this, the close contacts are displayed visualized as different colored regions. (Figure 1.18) Additionally, as the d_{norm} here highlights both donors and acceptors equally on the surface, less prominent contacts, such as weak C–H... π interactions, becomes visible.

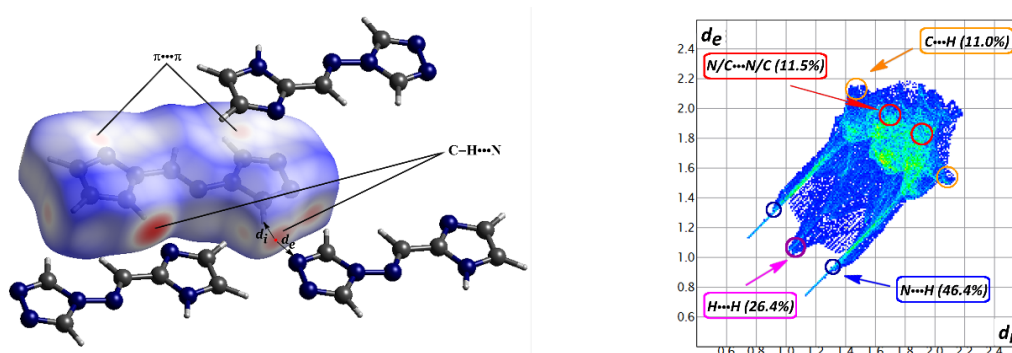


Figure 1.18.: Illustration of the Hirshfeld surface (d_{norm} based) of crystal structure of ligand **3** (2-imztrz), the distances d_i and d_e are illustrated schematically for a single point (red dot) (left), and shown on the right side the corresponding 2D fingerprint highlighted with different short contacts.

An example is given here with the organic crystal structure of ligand **3** of the present work, as shown in figure 1.18, the left side shows the Hirshfeld surface based on d_{norm} , and the right side gives the corresponding two dimensional fingerprint plot. It is very clear from the Hirshfeld surface that the red circles represent the C–H \cdots N hydrogen bonding interactions, while the rather faint red spots on the top of the surface reflect the $\pi\cdots\pi$ stackings between the triazole and imidazole rings. The 2D fingerprint plot shows characteristic shapes and occupation of the different short contacts. The sharp spike-like green regions in the plots correspond to the H–bondings, and the C \cdots H/H \cdots C contacts (defined as the C–H $\cdots\pi$ interactions) appear as “wing” in the upper left and right of the 2-D fingerprint plot. From the occupation of these short contacts, we can tell that for this structure, the H-bonding interactions involving N atoms is the dominant force that leads to the final 3D solid structure packing.

1.8 Objective and Scope of the Thesis

As we discussed in section 1.6, despite the numerous studies that have been devoted to the origin of the cooperativity between the spin transition metal centers and how to design strongly cooperative spin-transition compounds in the past decades, the conception of rational design for SCO materials is still far away from practical application. Considering the scarce example of high dimensional complexes showing SCO and the fact that most of the current research interest is more focused on the lower dimensional molecular clusters, the present study tries to make up the gap. Our objective herein is not confined with the molecular clusters, but we also try to expand the low dimensional molecules to covalently linked high dimensional complexes with the expectation of higher cooperativity between the covalently linked active Fe centers.

The major aim of this work was the synthesis of new spin crossover complexes based on modified triazole ligands. The potential virtue of the modified triazole ligand makes it possible to expand the molecular system to high dimension (high nuclearities). In the meantime, we are also very interested in the typical molecular systems, where the counteranion effect, supramolecular interactions and crystal packing effects play a great role on the final SCO behavior. We want to explore the cooperative interactions between these chemically (supramolecularly) connected spin centers, to study the relationship between dimensionality (supramolecular interactions) and the cooperativity in SCO complex, and to uncover the mystery behind these fascinating SCO effects.

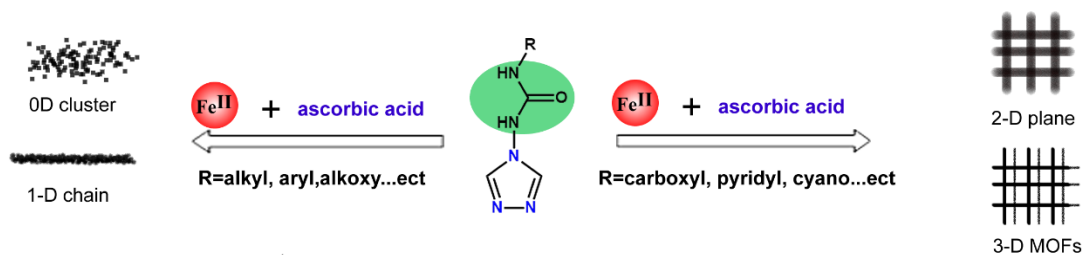
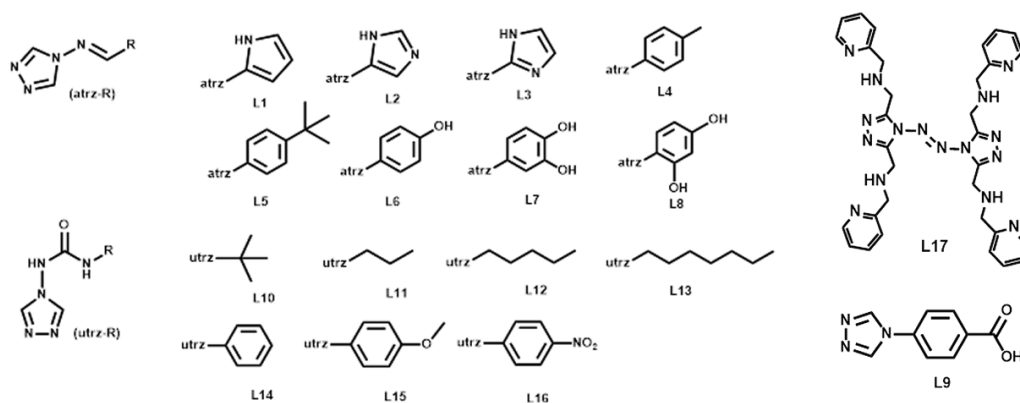


Figure 1.19.: Overview of two approaches to design-synthesize ligand for constructing SCO materials. The spacer shown as green ellipse can be rigid linkages like phenyl, vinyl and ethynyl group or flexible linkages like urea, thiourea and methylene group.

To fulfill such purpose, the ligand design approach is applied, together with the supramolecular method as effective control of crystallization process. As shown in Figure 1.19, starting from urea triazoles, we design two ways to construct SCO materials from molecular cluster to higher dimensional materials. Firstly, by introducing different substituents with variant electron-donating or -withdrawing groups, we plan to focus on mono-, bi-, and tri-nuclear molecules systems. (Figure 1.19, left) For these compounds, the weak intermolecular contacts between separate SCO centers, solvents and anions are of primary importance for the defining of the SCO properties of these materials. To get the higher dimensional complex, we tend to change the substituent to groups with a second coordination site. (Figure 1.19, right) The variation of the ending group like carboxyl, pyridyl or cyano group could link the metal center from the other side, such giving a 2-D or 3-D metal organic framework. Different from the lower dimensional complex, covalent bonds are expected to play a decisive role in the manifestation of the desired complex in these polymeric or 3-D systems, and they could possibly provide strong short-range interactions between the active centers.

Based on these considerations, a series of modified triazole ligands (L1 to L17) (scheme 2) were synthesized and characterized. Attempts has been made to isolate the corresponding iron(II) complexes and to analyze their magnetic properties.



Scheme 2.: Ligand systems that have been developed for this study. Detailed nomenclature of these ligands are listed in the back of the thesis, following the appendix.

Chapter 2 contains three molecular complexes isolated from ligand **1**. These complexes represent rare discrete dimeric/trimeric species, with μ_2 -*N1,N2*-triazole bridges linking the Fe^{II} centers. Magnetic susceptibility measurements reveal a gradual single-step SCO behavior of complex **4** on the central Fe(II) site.

Chapter 3 introduces two more molecular compounds isolated from ligand **2**. Magnetic susceptibility measurements revealed an abrupt single-step SCO behavior of the trinuclear complex **6** with a transition temperature $T_{1/2} = 120\text{K}$. The two molecular clusters own similar structure as the three compounds in chapter 2, but the change of the substitution and counteranion leads to quite different magnetic behavior.

Chapter 4 covers three polynuclear Fe compounds. Complex **7** and **8** are oxalate bridged Fe(II) complex with **7** showing a linear 1D chain and **8** exhibiting a zigzag chain based 3D interpenetrated framework. Both structures showed a rather big void in the 3D architecture ($\sim 15\%$ of the crystal volume). Complex **9** is a binuclear Fe(III) complex, which is bridged by two citrate ligands to form a centrosymmetric structure. Magnetic susceptibility measurements indicate for all three compounds similar magnetic behavior with slightly different degree of antiferromagnetic coupling between the adjacent Fe centers.

Chapter 5 presents two results of high dimensional networks (2D) built up from ligand **2** and ligand **3**. The rather weak ligand field formed by nitrogen donors from the imidazole and imine groups here trapped the Fe centers at HS state for both complexes. Pleasantly, complex **12** was found to behave as a ferromagnetic model, while complex **10** showed weak antiferromagnetic coupling through the supramolecular interactions in the crystal lattice.

Chapter 6 summarizes several *unexpected* crystal structures during the synthesis of SCO Fe complex in the present study. They showed out as the result of the competition between the crystallization of the targeted complex and the isolated structure, either Fe complex or pure ligand form. Relationship has been explored that the multi-supramolecular interactions found in these structures not only stabilize the solid packing in the crystal lattice, but also partially explain the reason why it more likely to crystallize as ligand rather than the desired complex.

Chapter 7 lists a general discussion of obtained results and some perspective on the present study system has been given.

Chapter 8 attaches the appendix for the thesis.

1.9 References

- [1] C. E. Housecroft, A. G. Sharpe, *Inorganic chemistry*, Pearson Prentice Hall, Upper Saddle River, N. J, *4th ed*, **2012**.
- [2] a) H. Bethe, *Ann. Phys.*, **1929**, *395*, 133–208; b) <http://wps.prenhall.com/wps/media/objects/3085/3159106/blb2406.html>.
- [3] B. Neumüller, *Angewandte Chemie.*, **1990**, *102*, 1411–1412.
- [4] C. K. Jørgensen in *Absorption Spectra and Chemical Bonding in Complexes*, Pergamon, **1962**, 107-133.
- [5] N. Shenkuan, *J. Chem. Educ.*, **1992**, *69*, p 800.
- [6] a) G. Racah, *Phys. Rev.*, **1943**, *63*, 367–382. b) G. Racah, *Phys. Rev.*, **1949**, *76*, 1352–1365.
- [7] Y. Jean, *Les orbitales moléculaires dans les complexes: Cours et exercices corrigés*. (Editions Ecole Polytechnique, **2003**).
- [8] R. H. Crabtree, *The Organometallic Chemistry of the Transition Metals*. (John Wiley & Sons, **2009**).
- [9] E. K. Byrne, D. S. Richeson, K. H. Theopold, *J. Chem. Soc. Chem. Commun.*, **1986**, *19*, 1491-1492.
- [10] a) I. Salitros, N. T. Madhu, R. Boca, J. Pavlik, M. Ruben, *Monatsh. Chem.*, **2009**, *140*, pp. 695-733; P. Gülich, H. A. Goodwin. *Spin Crossover in Transition Metal Compounds I, Topics in Current Chemistry 233*, Springer, Berlin Heidelberg, **2004**, 1–47; c) P. Gülich; A. Hauser, H. Spiering, *Angew. Chem. Int. Ed.* **1994**, *33*, 2024.
- [11] O. Kahn, M. C. Jay, *Science*, **1998**, *279*, 44-48.
- [12] a) Y. Tanabe, S. Sugano, *J. Phys. Soc. Jpn.*, **1954**, *9*, 753–766; b) Y. Tanabe, S. Sugano, *J. Phys. Soc. Jpn.*, **1954**, *9*, 766–779; c) S. Sugano, Y. Tanabe, H. Kamimura, *Pure and Applied Physics*, Vol. 33, Academic Press, New York, **1970**, 82.

- [13] A. Hauser in *Spin Crossover in Transition Metal Compounds I, Topics in Current Chemistry* 233, Springer Berlin Heidelberg, **2004**, S. 49–58.
- [14] P. Gütllich, Y. Garcia, H. A. Goodwin, *Chem. Soc. Rev.*, **2000**, 29, 419–427.
- [15] P. Gütllich, A. Hauser, H. Spiering, *Angew. Chem. Int. Ed. Engl.*, **1994**, 33, 2024–2054.
- [16] a) H. Hagiwara, A. Kawano, T. Fujinami, N. Matsumoto, Y. Sunatsuki, M. Kojima, H. Miyamae, *Inorganica Chim. Acta*, **2011**, 367, 141–150; b) N. Hassan, A. B. Koudriavtsev, W. Linert, *Pure Appl. Chem.*, **2008**, 80, 1281–1292; c) O. Kahn, *Curr. Opin. Solid State Mater. Sci.*, **1996**, 1, 547–554.
- [17] J. Linares, E. Codjovi, Y. Garcia, *Sensors*, **2012**, 12, 4479–4492.
- [18] J. J. Mcgarvey, I. Lawthers, *J. Chem. Soc., Chem. Commun.*, **1982**, 906–907.
- [19] H. S. S. Decurtins, P. Gütllich, K. M. Hasselbach, A. Hauser, *Inorg. Chem.*, **1985**, 24, 2174–2178.
- [20] M. Clemente-León, E. Coronado, M. López-Jordà, J. C. Waerenborgh, C. Desplanches, H. Wang, J.-F. Létard, A. Hauser, A. Tissot, *J. Am. Chem. Soc.*, **2013**, 135, 8655–8667; J.-F. Létard, *J. Mater. Chem.*, **2006**, 16, 2550–2559.
- [21] P. Guionneau, F. Le Gac, A. Kaiba, J. S. Costa, D. Chasseau, J.-F. Létard, *Chem. Commun.*, **2007**, 3723–3725.
- [22] a) D. C. Fisher, H. G. Drickamer, *J. Chem. Phys.*, **1971**, 54: 4825–4837; b) R. G. Miller, S. Narayanaswamy, S. M. Clark, P. Dera, G. B. Jameson, J. L. Tallon, S. Brooker, *Dalton Trans.*, **2015**, 44, 20843–20849.
- [23] M. L. Boillot, J. Zarembowitch, J. P. Itié, A. Polian, E. Bourdet, J. G. Haasnoot, **2002**, *New J. Chem.*, 26, 313–322.
- [24] a) T. M. Pfaffeneder, S. Thallmair, W. Bauer, B. Weber, *New J. Chem.*, **2011**, 35, 691; b) B. Weber, E. Kaps, J. Obel, K. Achterhold, F.G. Parak, *Inorg. Chem.*, **2008**, 47, 10779.
- [25] a) H. Spiering, E. Meissner, H. Köppen, E.W. Müller, P. Gütllich, *Chem. Phys.*, **1982**, 68, 65; b) B. Weber, E. Kaps, C. Desplanches, J.-F. Létard, K. Achterhold, F.G. Parak, *Eur. J. Inorg. Chem.*, **2008**, 4891.
- [26] C. Herold, S. Shylin, E. Rentschler, *Inorg. Chem.* **2016**, 55, 6414–6419.
- [27] S. Rodríguez-Jiménez, H. L. Feltham, S. Brooker, *Angew. Chem. Int. Ed.*, **2016**, 55, 15067–15071.
- [28] a) J. L. Rowsell, E. C. Spencer, J. Eckert, J. A. Howard, O. M. Yaghi, *Science*, **2005**, 309, 1350–1354;) D. Britt, H. Furukawa, B. Wang, T. G. Glover, O. M. Yaghi, *Proc. Natl. Acad. Sci. U.S.A.*, **2009**, 106, 20637–20640; c) R. Banerjee, A. Phan, B. Wang, C. Knobler, H. Furukawa, M. O'keeffe, O. M. Yaghi, *Science*, **2008**, 319, 939–943.
- [29] G. J. Halder, C. J. Kepert, B. Moubaraki, K. S. Murray, J. D. Cashion, *Science*, **2002**, 298, 1762–1765.
- [30] D. A. Reed, B. K. Keitz, J. Oktawiec, J. A. Mason, T. Runčevski, D. J. Xiao, L. E. Darago, V. Crocellà, S. Bordiga, J. R. Long, *Nature*, **2017**, 550, 96–100.
- [31] H. L. Schläfer, G. Gliemann, *Einführung in die Liganfeldtheorie*, Akademische Verlagsgesellschaft, Frankfurt/Main, **1967**.

- [32] a) R. Claude, J. A. Real, J. Zarembowitch, O. Kahn, L. Ouahab, D. Grandjean, K. Boukheddaden, F. Varret, A. Dworkin, *Inorg. Chem.*, **1990**, *29*, 4442-4448; b) P. Spacu, M. Teodorescu, G. Filotti, P. Telnic, *Z. Anorg. Allg. Chem.*, **1972**, *392*, 88-92.
- [33] X. R. Wu, H. Y. Shi, R. J. Wei, J. Li, L. S. Zheng, J. Tao, *Inorg. Chem.* **2015**, *54*, 3773-3780; b) R. W. Hogue, R. G. Miller, N. G. White, H. L. Feltham, G. N. Jameson, S. Brooker, *ChemComm.*, **2014**, *50*, 1435-1437.
- [34] L. J. Kershaw Cook, R. Kulmaczewski, R. Mohammed, S. Dudley, S. A. Barrett, M. A. Little, R. J. Deeth, M. A. Halcrow, *Angew. Chem. Int. Ed.*, **2016**, *55*, 4327-4331.
- [35] C. Hansch, A. Leo, R.W. Taft, *Chem. Rev.*, **1991**, *91*, 165 –195.
- [36] H. A. Goodwin, *Top. Curr. Chem.*, **2004**, *233*, 59-90.
- [37] H. J. Lin, D. Siretanu, D. A. Dickie, D. Subedi, J. J. Scepaniak, D. Mitcov, R. Clérac, J. M. Smith, *J. Am. Chem. Soc.*, **2014**, *136*, 13326-13332.
- [38] L. Cambi, L. Szegő, *Über die magnetische Suszeptibilität der komplexen Verbindungen. Ber. Dtsch. Chem. Ges.*, **1931**, *Teil B*, *64*: 2591–2598.
- [39] M. A. Halcrow, *Spin-crossover materials: properties and applications*. **2013**, John Wiley & Sons.
- [40] a) K. S. Murray, *Eur. J. Inorg. Chem.*, **2008**, *20*, 3101-3121; b) B. Weber, *Coord. Chem. Rev.*, **2009**, *253*, 2432-2449; c) M. Nihei, T. Shiga, Y. Maeda, H. Oshio, *Coord. Chem. Rev.*, **2007**, *251*, 2606-2621; d) H. L. Feltham, A. S. Barltrop, S. Brooker, *Coord. Chem. Rev.*, **2017**, *344*, 26-53; e) D. J. Harding, P. Harding, W. Phonsri, *Coord. Chem. Rev.*, **2016**, *313*, 38-61; f) M. A. Halcrow, *Coord. Chem. Rev.*, **2009**, *253*, 2493-2514.
- [41] a) L. G. Lavrenova, V. N. Ikorskii, V. A. Varnek, I. M. Oglezneva, S. V. Larionov, *Koord. Khim.*, **1986**, *12*, 207-215.
- [42] a) J. G. Haasnoot, *Coord. Chem. Rev.*, **2000**, *200*, 131-185; b) G. Aromí, L. A. Barrios, O. Roubeau, P. Gamez, *Coord. Chem. Rev.*, **2011**, *255*, 485-546; d) O. Roubeau, *Chem. Eur. J.*, **2012**, *18*, 15230-15244; e) L. G. Lavrenova, O. G. Shakirova, *Eur. J. Inorg. Chem.*, **2013**, 670-682; f) A. Hauser in *Spin Crossover in Transition Metal Compounds I, Topics in Current Chemistry 233*, Springer Berlin Heidelberg, **2004**, S. 229-257.
- [43] a) X. X. Wu, Y. Y. Wang, P. Yang, Y. Y. Xu, J. Z. Huo, B. Ding, Y. Wang, X. Wang, *Cryst. Growth Des.*, **2013**, *14*, 477-490; b) B. Zhai, Z. Y. Li, X. F. Zhang, X. X. Wu, J. H. Guo, J. Z. Huo, B. Ding, *Z. Anorg. Allg. Chem.*, **2016**, *642*, pp.260-267.
- [44] a) A. Ozarowski, B. R. McGarvey, *Inorg. Chem.*, **1989**, *28*, 2262-2266; b) E. Dova, R. Peschar, M. Sakata, K. Kato, H. Schenk, *Chem. Eur. J.*, **2006**, *12*, 5043-5052; c) A. Urtizberea, O. Roubeau, *ChemComm.*, **2017**, *8*, 2290-2295.
- [45] W. B. Chen, J. D. Leng, Z. Z. Wang, Y. C. Chen, Y. Miao, M. L. Tong, W. Dong, *Chem. Commun.*, **2017**, *53*, 7820-7823.
- [46] N. Pittala, F. Thétiot, C. Charles, S. Triki, K. Boukheddaden, G. Chastanet, M. Marchivie, *Chem. Commun.*, **2017**, *53*, 8356-8359.

- [47] J. L. Wang, Q. Liu, Y. S. Meng, H. Zheng, H. L. Zhu, Q. Shi, T. Liu, *Inorg. Chem.*, **2013**, *56*, 10674-10680.
- [48] A. Sugahara, H. Kamebuchi, A. Okazawa, M. Enomoto, N. Kojima, *Inorganics.*, **2017**, *5*, 50.
- [49] a) A. Grosjean, N. Daro, B. Kauffmann, A. Kaiba, J.F. Létard, P. Guionneau, *Chem. Commun.*, **2011**, 47, 12382-12384; b) N. Pittala, F. Thétiot, S. Triki, K. Boukheddaden, G. Chastanet, M. Marchivie, *Chem. Mater.*, **2016**, *29*, 490-494.
- [50] M. C. Muñoz, J. A. Real, *Coord. Chem. Rev.*, **2011**, *255*, 2068-2093.
- [51] a) J. G. Haasnoot, W. L. Groeneveld, *Z Naturforsch.*, **1979**, *34b*, 1500; b) A. Ozarowski, Y Shunzhong, B. R. McGarvey, A Mislankar, J. E. Drake, *Inorg Chem.*, **1991**, *30*, 3167; c) W. Vreugdenhil, J. H. van Diemen, R. A. G. De Graaff, J. G. Haasnoot, J. Reedijk, A. M. van der Kraan, O. Kahn, J. Zarembowitch, *Polyhedron*, **1990**, *9*, 2971-2979.
- [52] a) Y. C. Chuang, C. T. Liu, C. F. Sheu, W. L. Ho, G. H. Lee, C. C. Wang, Y. Wang, , *Inorg Chem.*, **2012**, *51*, 4663-4671; b) Y. Garcia, G. Bravic, C. Gieck, D. Chasseau, W. Tremel, P. Gülich, *Inorg Chem.*, **2005**, *44*, 9723-9730.
- [53] Y. C. Chuang, W. L. Ho, C. F. Sheu, G. H. Lee, Y. Wang, *ChemComm*, **2012**, *48*, 10769-10771.
- [54] Y. Garcia, O. Kahn, L. Rabardel, B. Chansou, L. Salmon, J. P. Tuchagues, *Inorg Chem.*, **1999**, *38*, 4663-4670.
- [55] a) Y. M. Klein, N. F. Sciortino, F. Ragon, C. E. Housecroft, C. J. Kepert, S. M. Neville, *ChemComm*, **2014**, *50*, 3838-3840; b) E. Milin, V. Patinec, S. Triki, E. E. Bendeif, S. Pillet, M. Marchivie, G. Chastanet, K. Boukheddaden, *Inorg Chem.*, **2016**, *55*, 11652-11661; c) N. F. Sciortino, F. Ragon, K. A. Zenere, P. D. Southon, G. J. Halder, K. W. Chapman, L. Piñeiro-López, J. A. Real, C. J. Kepert, S. M. Neville, *Inorg Chem.*, **2016**, *55*, 10490-10498.; d) N. F. Sciortino, K. A. Zenere, M. E. Corrigan, G. J. Halder, G. Chastanet, J. F. Létard, C. J. Kepert, S. M. Neville, *Chem. Sci.*, **2017**, *8*, 701-707.
- [56] E. König in *Complex Chemistry, Structure and Bonding 76*, Springer Berlin Heidelberg, **1991**, S. 51–152.
- [57] a) M. G. B. Drew, C. J. Harding, V. McKee, G. G. Morgan, J. Nelson, *J. Chem. Soc. Chem. Commun.*, **1995**, 1035–1038; b) M. A. Halcrow, *Coord. Chem. Rev.*, **2009**, *253*, 2493-2514; c) M. Marchivie, P. Guionneau, J. F. Létard, D. Chasseau, *Acta Cryst. B.*, **2005**, *61*, 25-28.
- [58] U. Gonser (Eds.), *Mössbauer Spectroscopy*, Springer, New York, **1975**.
- [59] B. Fultz, "Mössbauer spectrometry" in *Characterization of Materials*. E. N. Kaufmann, 2nd ed. New York: John Wiley, **2011**.
- [60] P. Gülich, *Chem. Unserer Zeit.*, **1970**, *4*, 133.
- [61] P. Gülich, *Z. anorg. allg. Chem.*, **2012**, *638*, 15–43.
- [62] a) M. A. Spackman, *Phys. Scr.* **2013**, *87*, 048103; b) M. A. Spackman, D. Jayatilaka, *CrystEngComm*, **2009**, *11*, 19–32; c) J. J. McKinnon, D. Jayatilaka, M. A. Spackman, *Chem. Commun.*, **2007**, *37*, 3814–3816.
- [63] F. L. Hirshfeld, *Theoretica Chimica Acta*, **1977**, *44*, 129-138.
- [64] E. Clementi, Roetti, C., *Atomic Data and Nuclear Data Tables*, **1974**, *14*, 177-478.
- [65] G. Moss and P. Coppens, *Chem. Phys. Lett.*, **1980**, *75*, 298-302.

Chapter 1 Introduction

[66] a) M. A. Spackman and P. G. Byrom, *Chem. Phys. Lett.*, **1997**, 267, 215-220; b) J. J. McKinnon, M. A. Spackman and A. S. Mitchell, *Acta Cryst. B.*, **2004**, 60, 627-668.

[67] R. F. W. Bader, *Atoms in Molecules – A Quantum Theory*, Oxford University Press, Oxford **1990**.

[68] E. Wigner, F. Seitz, *Phys Rev.*, **1933**, 43, 804.

[69] a) D. C. Whitley, *J. Math. Chem.*, **1998**, 23, 377-397; b) M. Petitjean, *J. Comput. Chem.*, **1994**, 15, 507-523.

[70] a) M. Connolly, *J. Appl. Crystallogr.*, **1983**, 16, 548-558; b) M. L. Connolly, *J. Mol. Graphics Modell.*, **1993**, 11, 139-141.

[71] J. J. McKinnon, A. S. Mitchell, M. A. Spackman, *Chem. Eur. J.*, **1998**, 4, 2136-2141.

Chapter 2 SCO Investigation of Three Triple *N1,N2*-Triazole Bridged Fe^{II} Complexes based on Toltrz

This chapter covers the summary results of three triple *N1,N2*-triazole bridged Fe^{II} complexes based on ligand 4 (toltrz), which is manuscripted to the journal submission of *Eur. J. Inorg. Chem.* Manuscript detailing will be presented in the following:

Fe^{II} Complexes with Triple *N1,N2*-Triazole Bridge Schiff base Ligand: Antiferromagnetic Dimer v.s. Spin Conversion Trimer

Ai-Min Li,^{a,b} Tim Hochdörffer,^c Dr. Juliusz A. Wolny^c, Volker Schünemann^c and Eva Rentschler^{d*}

^a Institute of Inorganic and Analytical Chemistry, Johannes Gutenberg University Mainz, Duesbergweg 10-14, 55128 Mainz, Germany

rentschler@uni-mainz.de

^b Graduate School Materials Science in Mainz, Staudingerweg 9, D-55128 Mainz, Germany

^c Fachbereich Physik, Technische Universität Kaiserslautern, Erwin-Schrödinger-Str. 46, 67663 Kaiserslautern, Germany

KEYWORDS Spin crossover / trinuclear / binuclear / 1,2,4-triazole / Schiff bases

2.1 Abstract

Based on the *p*-tolyl functionalized Schiff base 1,2,4-triazole ligand 4-(*p*-tolylidene-amino)-4H-1,2,4-triazole (toltrz), a series of three triazole-bridged Fe^{II} complexes have been prepared. The compounds represent rare discrete dimeric/trimeric species, with μ_2 -*N1,N2*-triazole bridges linking the Fe^{II} centers. Mössbauer spectroscopy and magnetic susceptibility measurements reveal a gradual single-step spin crossover (SCO) behavior for the trimeric compound **4** on the central Fe^{II} site. Single-crystal X-ray diffraction at 120 K confirms that the central Fe^{II} sites undergoes a HS to LS transition while the peripheral Fe^{II} remain in HS state (HS = high spin; LS = low spin). Compounds **1** and **2** are isostructures with different terminal ligand XCN (X = S, Se), these two compounds stay in high spin state over the whole temperature range but display weak antiferromagnetic exchange coupling.

2.2 Introduction

Spin crossover (SCO), known as the inter-conversion between electronic spin states in metal-organic compounds, has drawn fascination and research attention for both chemist and physicist since the discovery of the first SCO compound in 1931. [1-3] The potential

Chapter 2 SCO Investigation of Three Triple *NI,N2*-Triazole Bridged Fe^{II} Complexes based on Toltrz

applications of such materials for data storage, molecular electronics and thermosensors [4-6] impel the chemists to optimize the SCO compounds with higher T_c and larger hysteresis loop area. Among the few examples exhibiting remarkable SCO behavior, the system based on the 1,2,4-triazole ligand still remains the most promising materials for future applications. Particularly the 1D coordination polymers of general formula $[\text{Fe}(\text{Rtrz})_3](\text{X})_2$ (Rtrz = 4-substituted-1,2,4-triazole, X^- = standard monoanions), display wide thermal hysteresis loops around room temperature. [7] However, the challenge to obtain crystalline compounds of such coordination polymers makes it difficult to investigate the structural data at the molecular and inter-molecular scales. Alternatively, discrete polynuclear complexes, i.e., dinuclear or trinuclear triazole-based complexes, involving similar triple triazole bridges, are currently receiving great interest. [2, 3] The versatile feature of the 1,2,4-triazole-based ligands makes them suitable candidates for building up discrete polynuclear complexes, with variety of coordination modes. [8] As summarized in Prof. Brooker's recent review [8a], selectively functionalizing the ³C, ⁵C, and/or ⁴N positions of the triazole ring gives access to a wide range of discrete Fe^{II} SCO complexes. [9] Similarly to the triple *NI,N2*-1,2,4-triazole bridged analogues, these discrete SCO complexes provide fundamental insights into the influence over the SCO, like counteranion effect, supramolecular interactions and crystal packing effects, to help us understand and design-synthesize the polymeric SCO systems.

The focus of the present study is on solely ⁴N position modified 1,2,4-triazole-based ligands. Despite the early discovery of the first *NI,N2*-1,2,4-triazole bridged trinuclear Fe^{II} species in 1983 by the group of Prof. Jan Reedijk, [10] and a continuous endeavor on this family of compounds, the successful preparation of discrete *NI,N2*-1,2,4-triazole bridged SCO Fe^{II} complexes based on ⁴N functionalized 1,2,4-triazole ligands is still very challenging. For example, Yann Garcia et al. reported the first such structure of a binuclear Fe^{II} complex in two different spin states only in 2011. [11] The three newly published examples in last year, together with a very recent case in 2018, [12] indicate the lasting-hot topic in this field. A detailed list of the reported discrete *NI,N2*-1,2,4-triazole bridged complexes can be found in table 9.1, 9.2, from which we can see the vitality and creativity in this family of compounds. By introducing an electron-withdraw and steric bulky group, *p*-toluyl, the main objective in this study is to explore the different supramolecular interactions effecting on the spin transition behavior. We add herein three additions to this short list of complexes, enlarging the library of switchable *NI,N2*-1,2,4-triazole bridged complexes for the elaboration of polynuclear architectures. We report the synthesis, structure, and magnetic

properties of a series of three polynuclear triazole-bridged Fe^{II} complexes based on a Schiff base modified triazole ligand, *i.e.*, 4-(*p*-tolylidene-amino)-4H-1,2,4-triazole (toltrz) : [Fe^{II}₂(toltrz)₅(SCN)₄] · 3H₂O (**C1**), [Fe^{II}₂(toltrz)₅(SeCN)₄] · 3H₂O (**C2**) and [Fe^{II}₃(toltrz)₆(H₂O)₆] · 6(BF₄) · 2H₂O · 2CH₃CH₂CO₂CH₃ (**C4**). Single X-ray diffraction and magnetic measurements reveal that compounds **1** and **2** are isomorphous binuclear Fe^{II} complexes showing weak antiferromagnetic exchange interactions, while compound **4** is a trinuclear Fe^{II} complex exhibiting a gradual spin transition behavior.

2.3 Experimental Section

General Methods and Materials

All commercially purchased chemicals and solvents were used without further purification. Magnetic susceptibility data were collected with a Quantum Design SQUID magnetometer MPMS XL-7 in a temperature range of 2-300 K with an applied field of 1 kOe. Samples were prepared in gelatin capsules and held in plastic straws for insertion into the magnetometer. Magnetic susceptibility values were corrected for the diamagnetic susceptibility according to Pascal's constants. ^[13a] ⁵⁷Fe Mössbauer spectra were recorded in transmission geometry using a constant acceleration spectrometer operated in conjunction with a 512-channel analyzer in the time-scale mode (WissEl GmbH). The source contained ⁵⁷Co diffused in Rh with an activity of 1.4 GBq. The spectrometer was calibrated against α -iron at room temperature (RT). Variable temperature measurements were performed with a continuous flow cryostat (Optistat^{DN}, Oxford Instruments). Spectral data were transferred from the multi-channel analyzer to a PC for further analysis employing the public domain program Vinda running on an Excel 2003® platform. ^[13b] The spectra were analyzed by least-squares fits using Lorentzian line shapes, *I*. Elemental analysis (C, H, and N) was measured at the microanalytical laboratories of the Johannes Gutenberg University Mainz. Infrared spectra (FT-IR) were recorded as potassium bromide pellets in the range from 4000 to 400 cm⁻¹ with a JASCO FT/IR-4200 at the Johannes Gutenberg-University Mainz.

Single Crystal X-ray Diffraction

Single-crystal X-ray diffraction data (**C1** and **C2** at 173 K) were collected on a Bruker Smart APEX II CCD diffractometer, operating at 45 kV and 35 mA using Mo K α radiation (λ = 0.71073 Å). The diffractometer was equipped with a nitrogen cold stream operating at 173(2) K. The crystal of **C4** (at 120 K and 173 K) was measured on a Stoe IPDS II diffractometer operating with a Mo-K α (λ = 0.71073 Å) X-ray tube with a graphite

Chapter 2 SCO Investigation of Three Triple *N1,N2*-Triazole Bridged Fe^{II} Complexes based on Toltrz

monochromator. Data reduction was performed using the SMART and SAINT software [14] and an empirical absorption correction was applied using the SADABS program. [15] All structures were solved by direct methods and refined by full-matrix least squares on F^2 using the SHELXTL program package, [16] and the Olex2 program. [17] The ordered non-hydrogen atoms in each structure were refined with anisotropic displacement parameters, while the hydrogen atoms were placed in idealized positions and allowed to ride on their parent atoms. In compound **1** and **2**, the N18 and C35 atoms are respectively disordered over two positions with a ratio of 1:1. In compound **4**, there is a disordering over one *p*-tolyl fragment (C3 to C10) with a ratio of 1:1 at both temperatures. While the refinement of the reflection data yielded poorly resolved structural results: there is one more N4 (connected with the disordered *p*-tolyl ring) disordering, plus the ethyl ethylate solvent molecule was also disordered at the carbonyl group C33=O1 over three positions with a ratio of 0.5:0.25:0.25. Even though, the structure of **C4** at 120 K got a poor reflection data with the final $R_1 (I > 2\sigma(I))$ value of 0.1473, the major part of the structure is still reliable and gives us valuable data for the structure and property investigation (see in the main text). In all the structures, the lattice water molecules were refined with anisotropic displacement parameters, while the hydrogen atoms were not defined. Thus, in the discussion in the main text, all the lattice water molecules or the disordered parts were not included. The crystallographic data and refinement parameters of **C1**, **C2**, **C4** (173 K) and **C4** (120 K) are listed in Table 1. CCDC numbers 1587514–1587517 contain the supplementary crystal data of the compounds: 1587514 (**C1**), 1587515 (**C2**), 1587516 (**C4** at 173 K) and 1587517 (**C4** at 120 K), which can be obtained free of charge from The Cambridge Crystallographic Data Centre via www.ccdc.cam.ac.uk/data_request/cif. All structure figures are generated with DIAMOND-3. [18]

Syntheses

Synthesis of the ligand

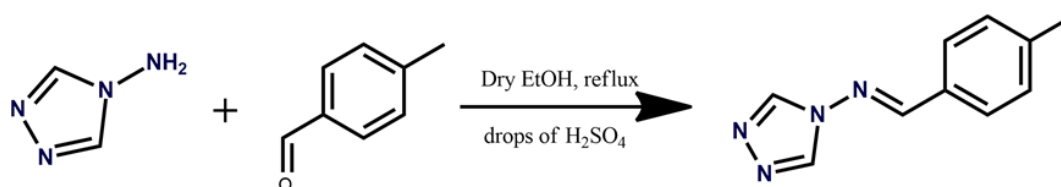


Figure 2.1.: Synthetic scheme to prepare the toltrz ligand.

Chapter 2 SCO Investigation of Three Triple *N1,N2*-Triazole Bridged Fe^{II} Complexes based on Toltrz

The ligand 4-(*p*-tolylidene-amino)-4*H*-1,2,4-triazole (toltrz) (Figure 2.1) was prepared via a modified procedure from the reported article. ^[19a] To avoid the possible by-product, we choose ethanol as the reaction solvent. 4-Amino-1,2,4-triazole (1.68 g, 0.02 mol, 1.0 eq.) and 4-methylbenzaldehyde (2.65 g, 0.022 mol, 1.1 eq.) were dissolved in ethanol with the addition of few drops of H₂SO₄, acting as acidic catalyst. The reaction mixture was slowly heated up to 80 °C until it started to boil, then refluxed at this temperature for 10 h. When cooled down to r.t., the excess of the solvent was removed by rotary evaporator at 35 °C. The product such obtained was washed with small amounts of cold ethanol and diethyl ether, and then dried in the desiccator with phosphorus pentoxide as dry agent. A white powder with intense smelling was obtained. Yield: 3.53 g (94.85%), m.p.137–163 °C; IR (KBr) 1608 cm⁻¹ (H–C=N), 3101 cm⁻¹ (Ar, CH-strech.); 817 cm⁻¹, 2918 cm⁻¹ (Ar-CH₃). ¹H-NMR (Figure 9.4) (CD₃OD) 7.35–7.82 (dd, 4H, Ar–H), 8.94 (s, 1H, H–C=N), 9.05(s, 2H, triazole), 2.43(s, 3H, *p*-CH₃).

Synthesis of the Complex

Synthesis of [Fe^{II}₂(toltrz)₅(SCN)₄] 3H₂O (C1)

To a stirring solution of toltorz (150 mg, 0.8 mmol) in methanol (5 mL) was added an aqueous solution of FeSO₄ 7H₂O (90 mg, ~ 0.3 mmol) and NH₄SCN (50 mg, ~ 0.6 mmol). The solution turned from colorless to light yellow immediately. One spatula-amount (~35 mg) of ascorbic acid was added to prevent possible oxidation process. The reaction mixture was then stirred for 3~4 hours before filtrated with rapid filter paper. The obtained clear light reddish solution was kept in a small vial and left stand still to evaporate the solvent slowly. After one week, light yellow plate-like crystals of C1 were deposited at the bottom of the vial. After removing the mother liquid, the single crystals were quickly dried in an argon stream, and stored under argon. Yield: 62.3 mg (47.15% based on Fe). Anal. Calcd (Found) for C₅₄H₅₆N₂₄O₃S₄Fe₂: C, 49.06 (49.17); H, 3.74 (4.03); N, 25.43 (25.38). IR (KBr) n/cm⁻¹: 3104 (w), 2976 (m), 2920 (w), 2072 (s), 1607 (vs), 1121 (vs), 1062 (m), 817 (m), 620 (vs), 505 (m), 396 (w).

Synthesis of [Fe^{II}₂(toltrz)₅(SeCN)₄] 3H₂O (C2)

The preparation of compound 2 is almost the same as the procedure for compound 1, except for changing of NH₄SCN (50 mg, ~ 0.6 mmol) to KSeCN (47 mg, ~ 0.6 mmol). As the selenium compound is slightly light sensitive, all the procedures here (reaction, evaporation ...) were performed in a rather dark environment. Yield: 63.4 mg (41.97% based on Fe). Anal. Calcd (Found) for C₅₄H₅₆N₂₄O₃Se₄Fe₂: C, 42.93 (42.48); H, 3.34 (3.48); N, 22.25 (21.46). IR (KBr) n/cm⁻¹: 3217 (w), 3108 (m), 2975 (w), 2854 (m), 2070 (s), 1607

Chapter 2 SCO Investigation of Three Triple *N1,N2*-Triazole Bridged Fe^{II} Complexes based on Toltrz

(vs), 1524 (s), 1369 (m), 1179 (m), 1115 (vs), 1063 (m), 881 (m), 817 (m), 755 (m), 622 (vs), 509 (m), 443 (w).

Synthesis of $[Fe^{II}_3(\text{toltrz})_6(H_2O)_6](BF_4)_6 \cdot 2H_2O \cdot 2CH_3CH_2CO_2CH_3$ (**C4**)

To the dissolved Fe(BF₄)₂ · 6H₂O (135 mg, 0.4 mmol) in 10 mL ethyl acetate, one spatula amount (~35 mg) of ascorbic acid added to prevent possible oxidation process. After the completeness of dissolving the iron salt, a solution of toltrz (150 mg, 0.8 mmol) dissolved in ethyl acetate (5~10 mL) was slowly added to the above solution. This reaction solution was then stirred for around 3-4 hours before filtrated with rapid filter paper. The obtained almost colorless solution was kept in a small vial and left stand still to evaporate the solvent slowly. After five days, light-green block crystals of **C4** were deposited at the bottom of the vial. After removing the mother liquid, the single crystals were quickly dried in an argon stream, and stored under argon. After the drying process, the crystalline sample was found to change color from light green to pale-green. The same sample powder such obtained was used for SQUID and Mössbauer measurements without further modification. Yield: 61.26 mg (58.18% based on Fe). Anal. Calcd (Found) for solvent-free C₃₀H₄₄N₁₂O₇B₃F₁₂Fe_{1.5}: C, 35.02 (34.74); H, 4.31 (4.03); N, 16.34 (16.43). IR (KBr) ν/cm^{-1} : 3132 (m), 3032 (m), 2975 (w), 2921 (w), 2859 (m), 1606 (vs), 1567 (s), 1532 (s), 1307 (m), 1181 (m), 1084 (vs), 1073 (vs), 1037 (vs), 993 (m), 889 (w), 817 (m), 726 (m), 627 (s), 533 (m), 522 (m), 397 (w).

2.4 Result and discussion

2.4.1 Structural Description

Crystallographic data for the compounds **1**, **2** and **4** are summarized in Table 2.1 and the selected bond lengths and angles are given in Table 2.2, S2.1.

**Chapter 2 SCO Investigation of Three Triple *N1,N2*-Triazole Bridged
Fe^{II} Complexes based on Toltrz**

Table 2.1. Crystallographic Data and Refinement Parameters for Compounds 1, 2 and 4.

Compound	C1	C2	C4 (120 K)	C4 (173 K)
Empirical formula	C ₅₄ H ₄₉ Fe ₂ N ₂₄ O ₃ S ₄	C ₅₄ H ₅₀ Fe ₂ N ₂₄ O ₃ Se ₄	C ₃₄ H ₂₈ B ₃ F ₁₂ Fe _{1.5} N ₁₂ O ₆	C ₃₄ H ₃₆ B ₃ F ₁₂ Fe _{1.5} N ₁₂ O ₆
Formula weight	1322.11	1510.72	1044.89	1052.95
Crystal size	0.2×0.14×0.03	0.35×0.15×0.13	0.44×0.28×0.04	0.57×0.35×0.15
Crystal system	Triclinic	Triclinic	Triclinic	Triclinic
Space group	<i>P</i> -1 (<i>No.</i> 2)	<i>P</i> -1 (<i>No.</i> 2)	<i>P</i> -1 (<i>No.</i> 2)	<i>P</i> -1 (<i>No.</i> 2)
<i>a</i> (Å)	11.7271(14)	11.7281(11)	12.713(3)	12.7127(7)
<i>b</i> (Å)	14.1648(17)	14.2238(12)	13.406(3)	13.4058(7)
<i>c</i> (Å)	21.415(2)	21.7330(19)	16.821(3)	16.8209(9)
α (°)	74.800(3)	74.846(2)	67.48(3)	67.484(2)
β (°)	75.809(3)	75.784(2)	84.64(3)	84.639(2)
γ (°)	80.439(3)	79.688(2)	78.43(3)	78.432(2)
<i>V</i> (Å ³)	3308.4(7)	3366.6(5)	2593.9(11)	2593.9(2)
<i>Z</i>	2	2	2	2
<i>D</i> _{calc} (g/cm ³)	1.327	1.490	1.388	1.348
μ (Mo-K α) (mm ⁻¹)	0.624	2.652	0.517	0.518
<i>F</i> (000)	1362	1508	1052	1068
Reflections collected	22926	10413	24183	33228
Independent reflections	11322 (0.1115)	10247 (0.0112)	12389 (0.0764)	12332 (0.0804)
Parameters	834	825	742	716
Goodness-of-fit	0.920	1.025	1.451	1.050
<i>R</i> ₁ [<i>I</i> > 2 σ (<i>I</i>)] ^a	0.0703	0.0848	0.1473	0.0920
<i>wR</i> ₂ (all data) ^b	0.2274	0.2755	0.4542	0.3159

^a $R_1 = \frac{\sum ||F_o| - |F_c||}{\sum |F_o|}$. ^b $wR_2 = \frac{\{\sum [w(F_o^2 - F_c^2)^2]\}}{\sum [w(F_o^2)^2]}^{1/2}$

Chapter 2 SCO Investigation of Three Triple *N1,N2*-Triazole Bridged Fe^{II} Complexes based on Toltrz

Crystal structure of $[Fe^{II}_2(toltrz)_5(SCN)_4] \cdot 3H_2O$ (**C1**) and $[Fe^{II}_2(toltrz)_5(SeCN)_4] \cdot 3H_2O$ (**C2**)

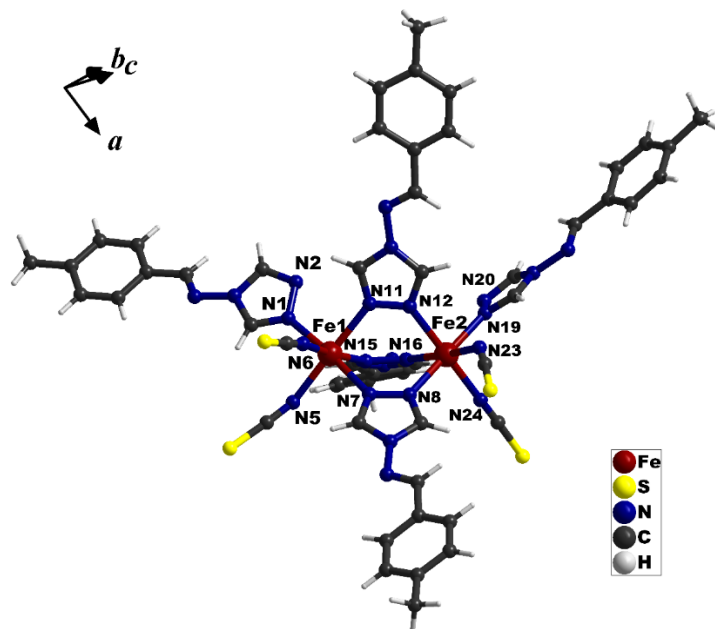


Figure 2.2.: View of the dinuclear molecular structure of **C1** at 173 K. Only selected atoms are labelled for clarity.

Compounds **1** and **2** are isostructural, and the molecular structures were determined at 173(2) K. Both compounds crystallize in triclinic space group *P*-1. The asymmetric unit contains one full neutral dinuclear complex plus partial six (**C1**) and four (**C2**) lattice aqua molecules, although some of these aqua molecular positions are partially occupied resulting in a total of 3 aqua molecules in both structures. As shown in Figure 2.2, for each compound, the two Fe^{II} centers are linked through three μ_2 -*N1,N2*-triazole bridges with a distance of 4.005 (7) Å (**C1**), 3.981 (9) Å (**C2**), respectively. Each Fe^{II} coordination sphere is completed by three N atoms from one terminal triazole ligand and two thiocyanate (**C1**) or selenocyanate (**C2**) anions. The terminal average Fe–N bond lengths 2.139(1) Å (**C1**), and 2.144(1) Å (**C2**) are shorter than the central average Fe–N bond lengths 2.197(1) Å (**C1**) and 2.191(1) Å (**C2**). (Table S2.1) In both cases, the bond range makes the Fe centers sitting well in the range expected for high spin state value at 173 K, [20] which is further confirmed by magnetic measurement. (See below) The NCS anions in **C1** are non-linear with the N–C–S fragment showing an angle around 175°; the angle at N–atom coordinating to the iron atoms, Fe...N–C, is split into two groups with the angle being around 140° and 175°. (See Table S2.1) In both compounds, there is one of the bridging ligands being disordered over the C=N bond part with a relative occupancy of 0.5/0.5 (C18, N15).

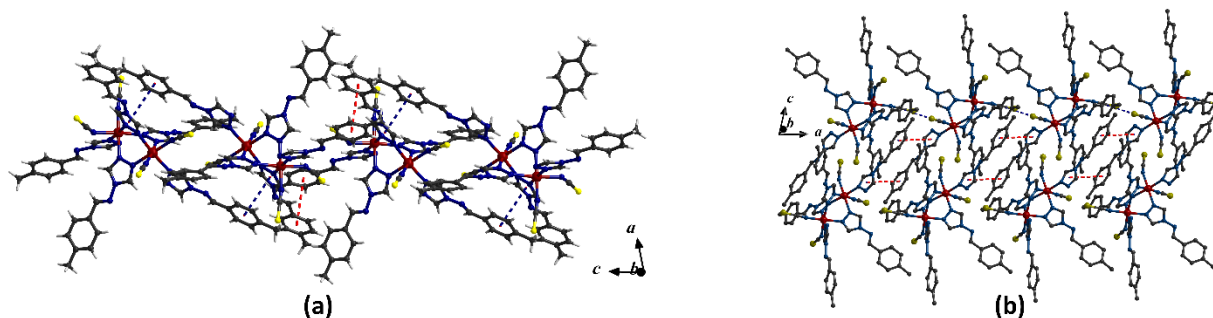


Figure 2.3. The 1D chain connected via $\pi\cdots\pi$ stacking in **C1** (left) and **C2** (right). The dashed lines represent different $\pi\cdots\pi$ stacking.

In compound **1**, the adjacent neutral dinuclear units are interconnected through π (phenyl) $\cdots\pi$ (phenyl) (centroid \cdots centroid = 3.9796(4) Å) and π (phenyl) $\cdots\pi$ (triazole) (centroid \cdots centroid = 3.8134(3) Å) stacking interactions forming a 1D chain along *c* axis. (Figure 2.3, Table S2.2) This chain is further connected through another two groups of intermolecular $\pi\cdots\pi$ stacking (Table S4) together with one set of non-classical $\text{S}\cdots\pi$ stacking [21] ($\text{S}\cdots$ centroid = 3.7232(5), $c = x + 1, y, z$) to form a 3D structure. While similarly, in compound **2**, a group of double $\pi\cdots\pi$ stacking interactions through phenyl and triazole ring, as well as a $\text{Se}\cdots\pi$ [21] ($\text{Se1}\cdots$ centroid = 3.6503(3) Å) contact was found to facilitate the 1D structure along the *a* axis. This 1D structure is stabilized and further extended via $\pi\cdots\pi$ stacking from different directions to form a 3D supramolecular architecture. (Figure 2.3, Table S2.2)

Crystal structure of $[\text{Fe}^{\text{II}}_3(\text{toltrz})_6(\text{H}_2\text{O})_6](\text{BF}_4)_6 \cdot 2\text{H}_2\text{O} \cdot 2\text{CH}_3\text{CH}_2\text{CO}_2\text{CH}_3$ (**C4**)

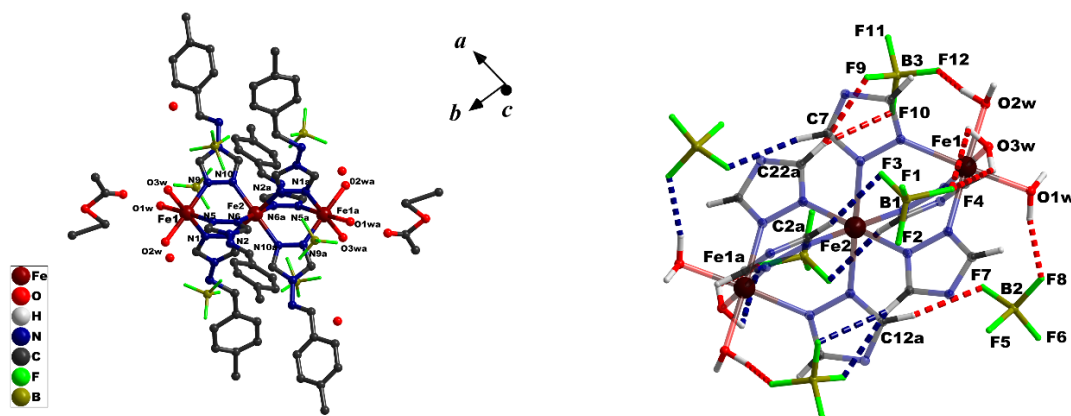


Figure 2.4.: (left) View of the centrosymmetric trinuclear complex in **C4** at 173 K. Only the metal, oxygen and nitrogen atoms involved in coordination bonds are labelled for clarity. ($a = -x + 1, -y + 1, -z + 1$); (right) The intense intramolecular H-bonding involved with the BF_4^- anion, the symmetrical part is labelled as blue for comparison.

Chapter 2 SCO Investigation of Three Triple *N1,N2*-Triazole Bridged Fe^{II} Complexes based on Toltrz

$[Fe^{II}_3(toltrz)_6(H_2O)_6] (BF_4)_6 \cdot 2H_2O \cdot 2CH_3CH_2CO_2CH_3$ crystallizes in the triclinic space group *P-1*. The structures at 173 and 120 K are mutually isomorphous. The structure was found to be comparable to other reported trinuclear 1,2,4-triazole analogues.^[13,18] It consists of a linear trinuclear unit, where the central Fe2 is bridged to the exterior iron(II) atoms by three toltrz ligands via a μ_2 -*N1,N2*-donating (N2, N6, N10) mode. (Figure 2.4a, this drawing corresponds to the structure obtained at 173 K) The terminal coordination sites are occupied by three H₂O molecules. The central Fe^{II} ion sits on an inversion center such that there are only two unique metal centers per trinuclear unit, Fe1 and Fe2. The central Fe2 is in an octahedral [FeN₆] coordination environment, while the outer Fe^{II} ions, Fe1 and Fe1a (a = -x + 1, -y + 1, -z + 1), are in a [FeN₃O₃] coordination environment due to the coordination of the terminated aqua molecules. Each trinuclear unit is cationic with a 3+ charge which is balanced by three BF₄⁻ counteranions.

As shown in figure 2.4b, the BF₄⁻ anions are involved in intensive intramolecular H-bonding with the terminated aqua molecules and the bridging ligands (Table S2.3), which lead to a strong binding between the counter anions and the positively charged trimer unit. This further explains why we can isolate the crystals in the not very polar solvent (ethyl ethylate) other than the polar solvent like methanol. The structure also shows at both temperatures one tolyl fragment being disordered with a relative occupancy of 0.5/0.5 (C3 to C10 at 173K, N4, C3 to C10 at 120K).

Table 2.2. Selected bond distances (Å) and angles (°) of compound **4** at 173K and 120K.

Compound 4 at 120 K					
Fe(1)-O(3W)	2.125(7)	Fe(1)-N(1)	2.154(7)	Fe(2)-N(2)	2.150(7)
Fe(1)-O(2W)	2.131(6)	Fe(1)-N(5)	2.177(6)	Fe(2)-N(2)#1	2.150(7)
Fe(1)-O(1W)	2.152(6)	Fe(2)-N(6)	2.161(6)	Fe(2)-N(10)	2.193(6)
Fe(1)-N(9)	2.167(7)	Fe(2)-N(6)#1	2.161(6)	Fe(2)-N(10)#1	2.193(6)
O(3W)-Fe(1)-O(2W)	89.9(3)	O(1W)-Fe(1)-N(1)	89.9(3)	N(2)#1-Fe(2)-N(6)#1	90.4(2)
O(3W)-Fe(1)-O(1W)	89.9(3)	O(1W)-Fe(1)-N(5)	177.7(3)	N(2)-Fe(2)-N(6)#1	89.6(2)
O(3W)-Fe(1)-N(9)	89.8(3)	N(9)-Fe(1)-N(5)	91.0(2)	N(2)#1-Fe(2)-N(6)	89.6(2)
O(3W)-Fe(1)-N(1)	179.2(3)	N(1)-Fe(1)-N(9)	90.9(3)	N(2)-Fe(2)-N(6)	90.4(2)
O(3W)-Fe(1)-N(5)	90.5(3)	N(1)-Fe(1)-N(5)	89.7(2)	N(2)-Fe(2)-N(2)#1	180.0
O(2W)-Fe(1)-O(1W)	87.2(3)	N(6)#1-Fe(2)-N(6)	180.0	N(2)-Fe(2)-N(10)#1	88.6(2)
O(2W)-Fe(1)-N(9)	178.4(2)	N(6)#1-Fe(2)-N(10)#1	91.3(2)	N(2)#1-Fe(2)-N(10)#1	91.4(2)
O(2W)-Fe(1)-N(1)	89.3(3)	N(6)-Fe(2)-N(10)#1	88.7(2)	N(2)-Fe(2)-N(10)	91.4(2)
O(2W)-Fe(1)-N(5)	90.5(2)	N(6)#1-Fe(2)-N(10)	88.7(2)	N(2)#1-Fe(2)-N(10)	88.6(2)
O(1W)-Fe(1)-N(9)	91.3(3)	N(6)-Fe(2)-N(10)	91.3(2)	N(10)-Fe(2)-N(10)#1	180.0
Compound 4 at 173 K					
Fe(1)-O(1W)	2.122(4)	Fe(1)-N(5)	2.161(4)	Fe(2)-N(6)#1	2.173(3)
Fe(1)-O(2W)	2.116(4)	Fe(1)-N(9)	2.150(4)	Fe(2)-N(6)	2.173(3)
Fe(1)-O(3W)	2.132(4)	Fe(2)-N(2)#1	2.157(4)	Fe(2)-N(10)#1	2.192(3)
Fe(1)-N(1)	2.156(4)	Fe(2)-N(2)	2.157(4)	Fe(2)-N(10)	2.193(3)
O(1W)-Fe(1)-O(3W)	89.86(2)	O(3W)-Fe(1)-N(5)	89.85(16)	N(2)#1-Fe(2)-N(10)#1	91.18(1)
O(1W)-Fe(1)-N(1)	89.04(2)	O(3W)-Fe(1)-N(9)	89.99(16)	N(2)-Fe(2)-N(10)	91.18(2)
O(1W)-Fe(1)-N(5)	177.56(2)	N(1)-Fe(1)-N(5)	91.24(14)	N(2)#1-Fe(2)-N(10)	88.82(2)
O(1W)-Fe(1)-N(9)	89.84(2)	N(9)-Fe(1)-N(1)	90.13(14)	N(2)-Fe(2)-N(10)#1	88.82(2)
O(2W)-Fe(1)-O(1W)	88.50(2)	N(9)-Fe(1)-N(5)	92.59(15)	N(6)#1-Fe(2)-N(6)	180.0
O(2W)-Fe(1)-O(3W)	89.01(2)	N(2)#1-Fe(2)-N(2)	180.0	N(6)-Fe(2)-N(10)#1	88.48(2)
O(2W)-Fe(1)-N(1)	90.84(2)	N(2)-Fe(2)-N(6)	90.67(14)	N(6)#1-Fe(2)-N(10)	88.48(1)
O(2W)-Fe(1)-N(5)	89.07(2)	N(2)-Fe(2)-N(6)#1	89.33(13)	N(6)#1-Fe(2)-N(10)#1	91.52(1)

**Chapter 2 SCO Investigation of Three Triple *N1,N2*-Triazole Bridged
Fe^{II} Complexes based on Toltrz**

O(2W)-Fe(1)-N(9)	178.06(2)	N(2)#1-Fe(2)-N(6)#1	90.67(13)	N(6)-Fe(2)-N(10)	91.52(2)
O(3W)-Fe(1)-N(1)	178.90(2)	N(2)#1-Fe(2)-N(6)	89.33(13)	N(10)#1-Fe(2)-N(10)	180.0

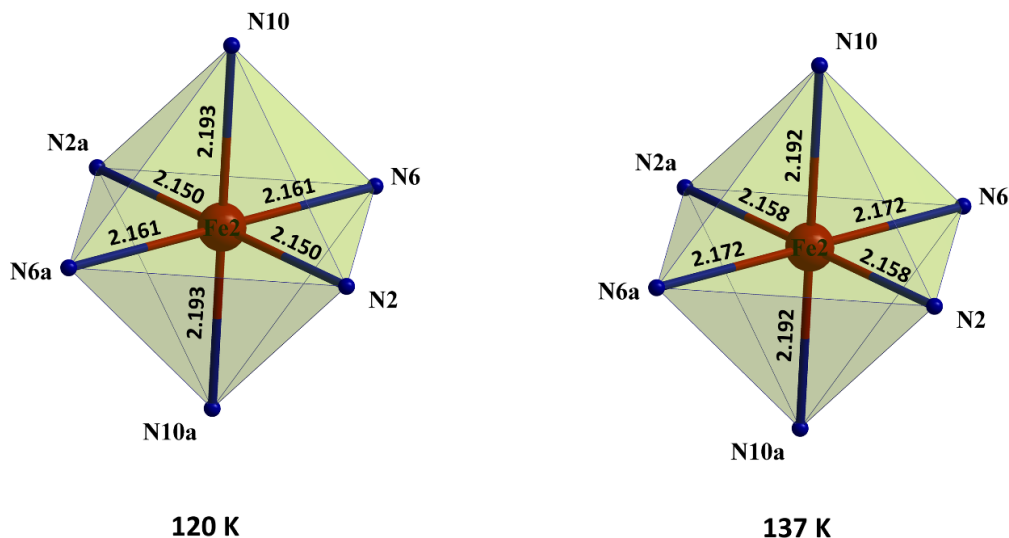


Figure 2.5.: Comparison of the coordination environment of the central Fe^{II} ion of C4 at 120 and 173 K. Colour code: Red (Fe), Blue (N).

Of the two crystallographically unique iron(II) ions, only the central one (Fe2) is in the expected coordination environment for SCO to occur. From magnetic susceptibility measurements, a partial spin transition is shown to occur between 200K–50K gradually. (See below) The crystal structure determination was conducted at 173 K and 120 K, right in the beginning and middle of the SCO transition range. Although the structures at 175 and 120 K are similar, small, but significant differences are observed in a number of bond distances and angles. The comparison of the coordination environment of the central ion in C4, at 120 and 173 K (Figure 2.5, Table 2.2), displays the typical structural changing during a spin transition. At 120 K, the bond distances between the six nitrogen atoms and the central iron ion are of 2.150(7), 2.161(6) and 2.193(6) Å for Fe2–N2, Fe2–N6 and Fe2–N10, respectively. These values are obviously shorter than the bond distances measured at 173 K, which are 2.157(4), 2.173(3) and 2.192(3) Å, respectively. (Figure 2.5) The decrease is slightly shorter than the average values observed in Fe^{II} HS → LS transitions for which the coordination distances are shortened by approximately 0.15–0.20 Å. However, the gradual transition in our compound happens from 50 K to 200K, as such the small changes in the coordination distances confirm that we have a transition process from HS to LS. Moreover, the even though small while clear bond distance difference here can not be ascribed to purely thermal expansion, as the relative rate of thermal expansion, ^[22] α , usually lies within the range $0 \times 10^{-6} \text{ K}^{-1} < \alpha < 20 \times 10^{-6} \text{ K}^{-1}$. And in our case, the relative rate of thermal expansion α at the measured two temperatures (120 K and 173 K) is around $2.0 \times 10^{-4} \text{ K}^{-1}$.

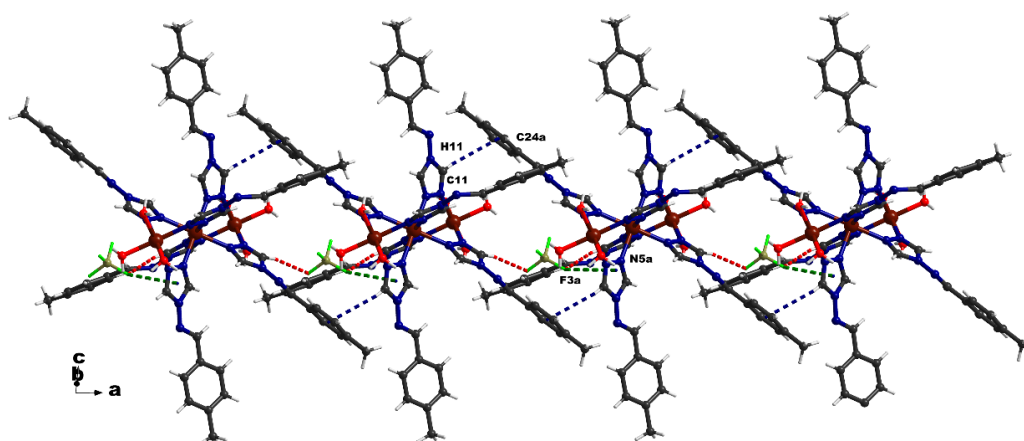


Figure 2.6.: The 1D chain formed in compound C4 along *a* axis.

Supramolecular interactions play an important role in the stabilization of the structures. Apart from the intensive intramolecular H-bonding involved with the counteranion BF_4^- between the terminated aqueous molecules and the bridging ligands as mentioned above, other groups of intermolecular H-bonding involving BF_4^- anion and adjacent C–H from triazole rings are found, together with a group of C–H $\cdots\pi$ stacking (C11–H11 \cdots C24a ring centroid = 3.1060(1) Å, $a = -x + 2, -y + 1, -z + 1$) and F $\cdots\pi$ stacking (F3 \cdots N5 ring centroid = 3.3033(2) Å) to link the independent trinuclear units into a 1D chain along *a* axis (Figure 2.6). This chain is further interconnected by a group of C–H $\cdots \pi$ stacking interaction (C14 ring centroid \cdots C14a ring centroid = 3.8326(2) Å, $a = -x + 1, -y + 1, -z$) in *bc* plane, which is stabilized and extended into a 3D supramolecular architecture via different groups of H-bonding interactions (Table S2.3).

2.4.2 FT–IR spectroscopy

The FT-IR spectra of the three compounds are very similar and dominated by the spectral characteristics of the Schiff base ligand. However, some significant changes could be found due to the coordination of the compound. The bands between 2800 cm^{-1} and $1630\text{--}1280\text{ cm}^{-1}$ (1609, 1531 and 1412 cm^{-1}) are attributable to the $\text{C}_{\text{ar}}\text{--C}_{\text{ar}}$, and $\text{C}_{\text{ar}}\text{=N}$ stretching vibration frequencies of the aromatic groups. The characteristic band for the triazole ring at 1502 cm^{-1} with a strong intensity can be assigned to the ω -ring vibration. [23] This band moves to a medium peak at 1531 cm^{-1} for all complexes, indicating the coordination of the N-donor atoms from triazole ring. The medium-intensity doublet peaks around 1305 cm^{-1} can be assigned to vibrations of the ν -triazole nucleus, it stays almost the same for all the compounds. [23] In addition, the peaks at 1235 (m) , 1180 (m) , 1065 (m) , and $816\text{ (s)}\text{ cm}^{-1}$

Chapter 2 SCO Investigation of Three Triple *N1,N2*-Triazole Bridged Fe^{II} Complexes based on Toltrz

can be assigned to the C–H in-plane or out-of-plane bend ring breathing, and ring deformation absorptions of the organic ligands. These bands can be noticed for all the compounds. They are shifted as compared to the ligand spectrum (Figure 2.7), which could be related with the change in the geometry of the *p*-tolyl fragment upon complex formation. The characteristic azomethine (HC=N) stretching ^[24] at 1636 cm⁻¹ in the ligand remains unchanged in all the compounds showing the non-coordinating character of the C=N groups. ^[25] The spectrum for **C1** and **C2** is very similar with the strong C=N stretching at 2070 cm⁻¹ suggesting the presence of XCN (X = S, Se) in the compounds. The 20 cm⁻¹ hypsochromic shift as compared to the spectrum of KNCS/KNCSe (2050 cm⁻¹) indicates the fact that XCN is coordinated with Fe^{II} via the nitrogen atoms. ^[26] In addition, the spectrum of **C4** shows bands for the tetrafluoroborate counterions at 1083 cm⁻¹.

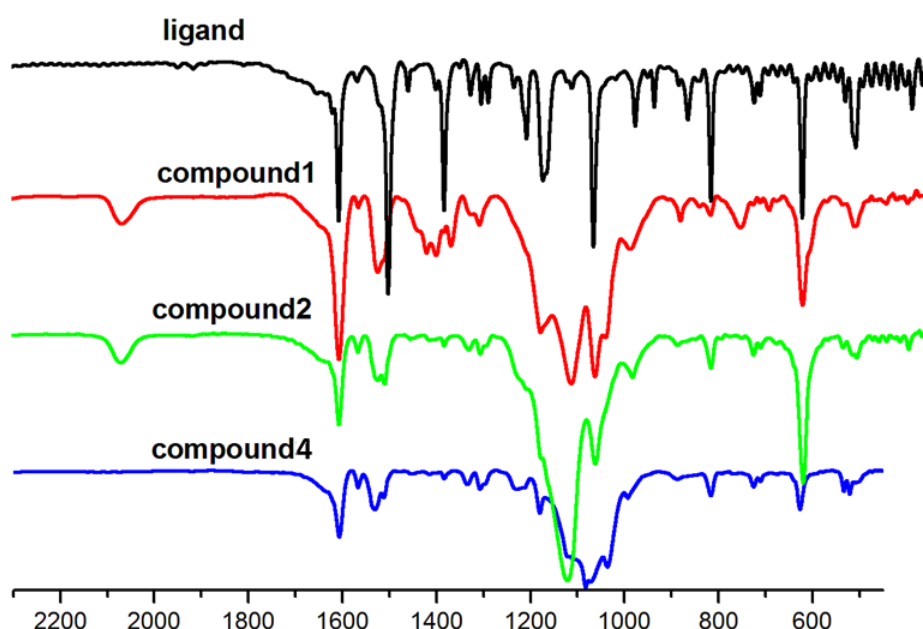


Figure 2.7.: The FT-IR spectra of ligand toltrz and compounds **1**, **2** and **4**.

2.4.3 Magnetic susceptibility and Mössbauer Spectroscopy

The variable-temperature magnetic susceptibility data of compound **1** and **2** have been recorded in the 300–2 K range (Figure 2.8). At the temperature of 300 K, the χ_{MT} value of 7.13 cm³·K·mol⁻¹ (**C1**) and 7.86 cm³·K·mol⁻¹ (**C2**) can be ascribed to the corresponding two high-spin Fe(II) ions. This value remains almost constant at 7.10 – 7.14 cm³·K·mol⁻¹ for compound **1** from 300 K down to 60 K; below this temperature, the χ_{MT} value starts to decrease more and more abruptly to reach a value of 1.93 cm³·K·mol⁻¹ at 2 K. For **C2**, χ_{MT} drops to 6.71 cm³·K·mol⁻¹ from 300 K down to 100 K, with a slight slope showing small

Chapter 2 SCO Investigation of Three Triple *N1,N2*-Triazole Bridged Fe^{II} Complexes based on Toltrz

TIP effect for the measurement. Below 100 K, the $\chi_M T$ value decreases more drastically all the way down to $1.53 \text{ cm}^3 \cdot \text{K} \cdot \text{mol}^{-1}$ at 2 K. Such temperature dependence reveals typical rather weak antiferromagnetic exchange interaction between two Fe^{II} ions in the high-spin state. The magnetic properties of these two compounds are thus in accordance with an $S = 2$ HS ground state for the Fe^{II} ions throughout the whole temperature range.

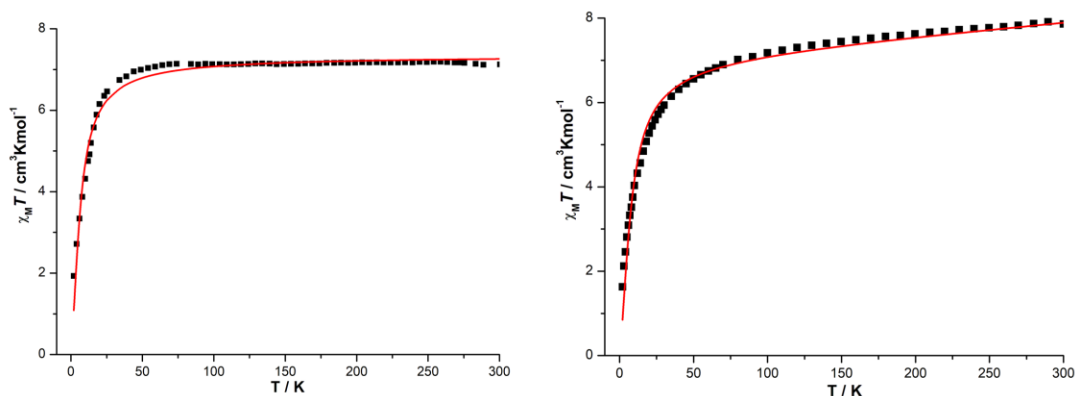


Figure 2.8.: The temperature-dependent magnetic susceptibility for **C1** and **C2** (the solid line represents the best fit curve).

To evaluate the antiferromagnetic interaction through the triple *N1,N2*-triazole bridge, the magnetic data of the entire temperature range was simulated using the PHI [27] program with values $g = 2.22$ (**C1**) and 2.18 (**C2**), coupling constants $J = -0.62(2) \text{ cm}^{-1}$ (**C1**) and $-0.78(2) \text{ cm}^{-1}$ (**C2**), respectively. A TIP contribution of $0.003 \text{ cm}^3 \text{ mol}^{-1}$ was applied for the data simulation of compound **2**. (Figure 2.8) The values for the exchange coupling are small and in accordance with data for similar binuclear Fe(II) analogues. [5,11,12]

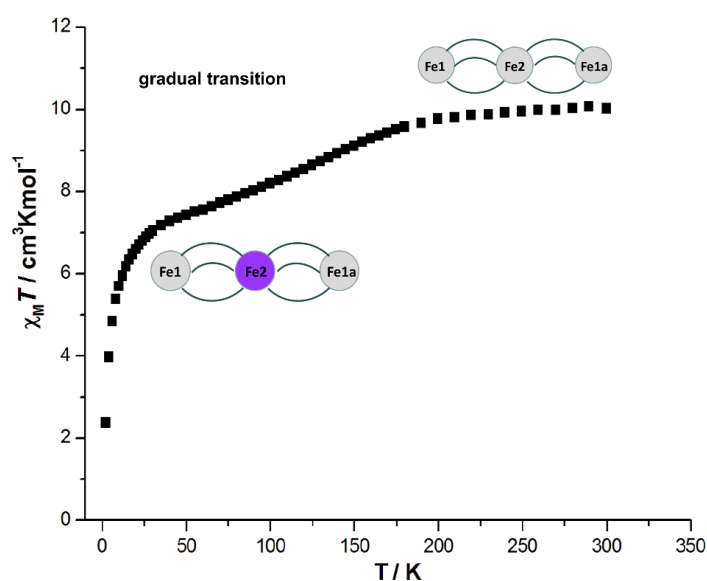


Figure 2.9.: The temperature-dependent magnetic susceptibility ($\chi_M T$ v.s. T) for compound **3**.

Chapter 2 SCO Investigation of Three Triple *N1,N2*-Triazole Bridged Fe^{II} Complexes based on Toltrz

Temperature dependent magnetic susceptibility measurements on a bulk crystalline sample of compound **4** were also made from 300 K to 2 K range. The data revealed a gradual one-step SCO (Figure 2.9). At 300 K, the χ_{MT} values of 10.08 cm K mol⁻¹ is in agreement with all Fe(II) sites of the trinuclear unit being in the HS state. The slightly higher value compared to the expected spin only ones for three Fe(II) ions here suggests possible spin orbital contribution being involved. The values remain approximately constant until 200 K where there is a gradual decrease in χ_{MT} values to 7.43 cm K mol⁻¹ by 50 K. The χ_{MT} value at 50 K indicates a SCO of one-third of the Fe(II) sites to the LS state with a transition temperature of \sim 130 K. Again the χ_{MT} values of 7.43 cm K mol⁻¹ here is a bit too large for two spin only HS Fe(II) ions, assuming the central iron ion has a full spin transition at this temperature. No thermal hysteresis was observed. This information was further explored by Mössbauer spectroscopy (see below).

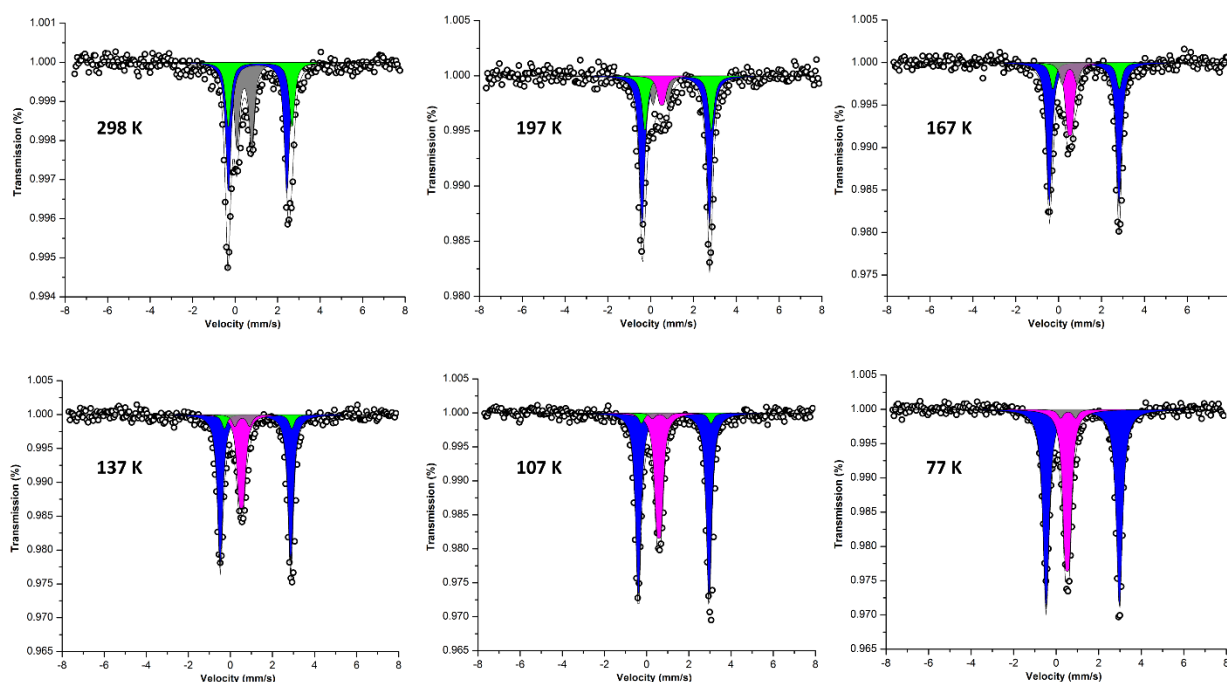


Figure 2.10.: Mössbauer spectra of compound **4** at 77 K, 107 K, 137 K, 167 K, 197 K and 298 K. The open circles are the experimental data, the black solid line shows a superposition of the following components: subspectrum 1 (purple) represents the [LS] fraction of central iron (Fe2), subspectrum 2 (blue) is due to the [HS] fraction of terminal iron (Fe1 and Fe1a), and 3 (green) is the [HS] fraction of central iron (Fe2). In addition, a minor high-spin ferric impurity species is represented by subspectrum 4 (grey). Parameters see Table 3.

In order to understand the details of SCO process of compound **4**, temperature dependent Mössbauer spectroscopy was performed on a bulk crystalline sample (Figure 2.10). The spectra have been analyzed with in total 4 different subspectra. The parameters (δ : isomer

Chapter 2 SCO Investigation of Three Triple *N1,N2*-Triazole Bridged Fe^{II} Complexes based on Toltrz

shift, ΔE_Q : quadrupole splitting, Γ : line width at half maximum, A : relative spectral area) are listed in table 2.3.

Table 2.3. ⁵⁷Fe Mössbauer parameters of compound 4 as obtained from the analysis shown in Figure 2.10.

T=77K					
Subspectra	HS Fe1	LS Fe2	HS Fe1a	HS Fe2	Fe(III)-oxides
δ [mm/s]	1,25 ± 0,03	0,52 ± 0,04	-	-	0,56 ± 0,15
ΔE_Q [mm/s]	3,45 ± 0,50	0,20 ± 0,05	-	-	0,70 ± 0,17
Γ [mm/s]	0,35 ± 0,02	0,30 ± 0,05	-	-	0,30 ± 0,10
Rel. Area [%]	65,00 ± 1,10	32,50 ± 1,30	0	0	2,40 ± 1,20
T=107K					
δ [mm/s]	1,22 ± 0,02	0,52 ± 0,03	1,19 ± 0,02	1,34 ± 0,03	0,56 ± 0,16
ΔE_Q [mm/s]	3,45 ± 0,04	0,10 ± 0,02	3,60 ± 0,03	3,30 ± 0,04	0,70 ± 0,05
Γ [mm/s]	0,40 ± 0,02	0,28 ± 0,03	0,30 ± 0,02	0,30 ± 0,05	0,30 ± 0,03
Rel. Area [%]	49,10 ± 1,60	23,50 ± 1,5	17,10 ± 0,80	8,50 ± 2,10	1,70 ± 1,90
T=137K					
δ [mm/s]	1,20 ± 0,05	0,52 ± 0,04	1,17 ± 0,04	1,32 ± 0,03	0,56 ± 0,04
ΔE_Q [mm/s]	3,32 ± 0,04	0,10 ± 0,02	3,60 ± 0,03	3,20 ± 0,04	0,70 ± 0,05
Γ [mm/s]	0,40 ± 0,04	0,28 ± 0,03	0,30 ± 0,04	0,30 ± 0,04	0,30 ± 0,05
Rel. Area [%]	39,7 ± 1,40	19,9 ± 0,90	24,8 ± 1,20	12,4 ± 1,60	3,17 ± 1,70
T=167K					
δ [mm/s]	1,20 ± 0,03	0,52 ± 0,04	1,13 ± 0,03	1,28 ± 0,05	0,52 ± 0,04
ΔE_Q [mm/s]	3,25 ± 0,05	0,10 ± 0,03	3,30 ± 0,04	3,10 ± 0,04	0,70 ± 0,05
Γ [mm/s]	0,40 ± 0,03	0,28 ± 0,04	0,30 ± 0,03	0,30 ± 0,04	0,30 ± 0,08
Rel. Area [%]	34,50 ± 0,90	17,3 ± 1,10	27,6 ± 1,40	13,8 ± 1,20	6,90 ± 1,80
T=197K					
δ [mm/s]	1,15 ± 0,03	0,52 ± 0,04	1,13 ± 0,04	1,28 ± 0,05	0,46 ± 0,03
ΔE_Q [mm/s]	3,10 ± 0,05	0,10 ± 0,03	3,30 ± 0,04	3,10 ± 0,05	0,70 ± 0,05
Γ [mm/s]	0,40 ± 0,03	0,28 ± 0,04	0,30 ± 0,03	0,30 ± 0,03	0,30 ± 0,04
Rel. Area [%]	17,20 ± 1,00	7,30 ± 1,90	43,1 ± 0,50	21,6 ± 0,90	10,77 ± 1,60
T=227K					
δ [mm/s]	1,15 ± 0,04	0,52 ± 0,04	1,11 ± 0,02	1,28 ± 0,03	0,46 ± 0,02
ΔE_Q [mm/s]	3,10 ± 0,05	0,10 ± 0,02	3,15 ± 0,04	3,10 ± 0,03	0,70 ± 0,04
Γ [mm/s]	0,40 ± 0,03	0,28 ± 0,05	0,30 ± 0,03	0,30 ± 0,04	0,30 ± 0,02
Rel. Area [%]	12,70 ± 0,80	6,40 ± 1,80	44,40 ± 1,20	22,60 ± 0,90	14,00 ± 1,10
T=257K					
δ [mm/s]	1,13 ± 0,03	0,52 ± 0,04	1,10 ± 0,03	1,24 ± 0,05	0,43 ± 0,03
ΔE_Q [mm/s]	3,10 ± 0,04	0,10 ± 0,03	2,90 ± 0,05	2,90 ± 0,05	0,70 ± 0,04
Γ [mm/s]	0,40 ± 0,02	0,28 ± 0,04	0,30 ± 0,03	0,30 ± 0,04	0,30 ± 0,05
Rel. Area [%]	8,54 ± 1,20	4,30 ± 1,90	42,7 ± 0,80	21,30 ± 1,20	23,10 ± 0,70
T=298K					
δ [mm/s]	-	-	1,08 ± 0,02	1,18 ± 0,03	0,43 ± 0,03
ΔE_Q [mm/s]	-	-	2,85 ± 0,03	2,90 ± 0,04	0,70 ± 0,04
Γ [mm/s]	-	-	0,30 ± 0,04	0,30 ± 0,02	0,30 ± 0,03
Rel. Area [%]	0	0	47,00 ± 1,50	23,50 ± 1,60	29,40 ± 1,20

As illustrated in Figure 2.10 and Table 2.3, the spectrum at 77 K shows two distinctly different doublets. Doublet 1 (purple) has $\delta = 0.52 \text{ mm}\cdot\text{s}^{-1}$ and $\Delta E_Q = 0.20 \text{ mm}\cdot\text{s}^{-1}$. Such a low quadrupole splitting is characteristic for a LS iron(II) with a half filled 3d shell embedded in an octahedral ligand field. Doublet 2 (blue) has $\delta = 1.25 \text{ mm}\cdot\text{s}^{-1}$ and $\Delta E_Q =$

Chapter 2 SCO Investigation of Three Triple *N1,N2*-Triazole Bridged Fe^{II} Complexes based on Toltrz

3.45 mm·s⁻¹, values which are typical fingerprints of a high-spin iron(II) species in an octahedral N/O ligand environment [28]. The relative intensity ratio of 1:2 between these two doublets indicates that the central iron(II) is in its low spin state, *i.e.*, for complex **4** a HS-LS-HS state is stabilized at 77 K, which is in accordance with the magnetic susceptibility results discussed above. With increasing temperature, the intensity of doublet 1 representing the central LS iron(II) decreases while a new doublet 3 (green) emerges which has $\delta > 1$ mm·s⁻¹, an isomer shift typical for Fe(II) HS. Nevertheless, the parameters of doublet 3 are clearly distinct from those of 2. Thus, doublet 3 can, without any doubts, be assigned to originate from the central Fe site. The SCO of this central Fe is reflected in the Mössbauer spectra displayed in Figure 2.10 by an intensity increase of the green doublet 3 which is on the expense of the decreasing intensity of the purple doublet 1 representing the central iron in its LS state. At 298 K, doublet 1 vanishes, and the approximate 2:1 relative area ratio of the HS doublet 2 and the HS doublet 3 reflects the SCO transition of complex **4** from a HS-LS-HS state to a HS-HS-HS state. At 167 K, the relative HS and LS ratio reaches 1:2, which gives us the hint of the transition temperature around 170K. The gradual character of this spin transition made it difficult to spot the exact transition temperature, while a derivative plot of the $\chi_M T$ *v.s.* T curve (figure S1) helps us to identify the $T_{1/2}$ at 180 K. This is in good agreement with the Mössbauer data discussed above.

Subspectrum 4 has an isomer shift of $\delta \sim 0.56$ mm·s⁻¹ and a quadruple splitting of $\Delta E_Q \sim 0.7$ mm·s⁻¹ which are characteristic parameters for Fe(III)-oxide/hydroxides. [28] (Figure 2.10, Table 2.3). Since this component accounts only for 2 to 3% of the total spectral area at 77 K, it represents clearly a small impurity fraction. The increasing of the relative area of this component (30 % at 298 K) is caused by the large Lamb-Mössbauer factor of Fe(III)-oxide/hydroxide nanoparticles compared to that of Fe(II) in a relatively soft complex environment. A further confirmation for only a very small impurity of the sample is provided by the magnetization measurements.

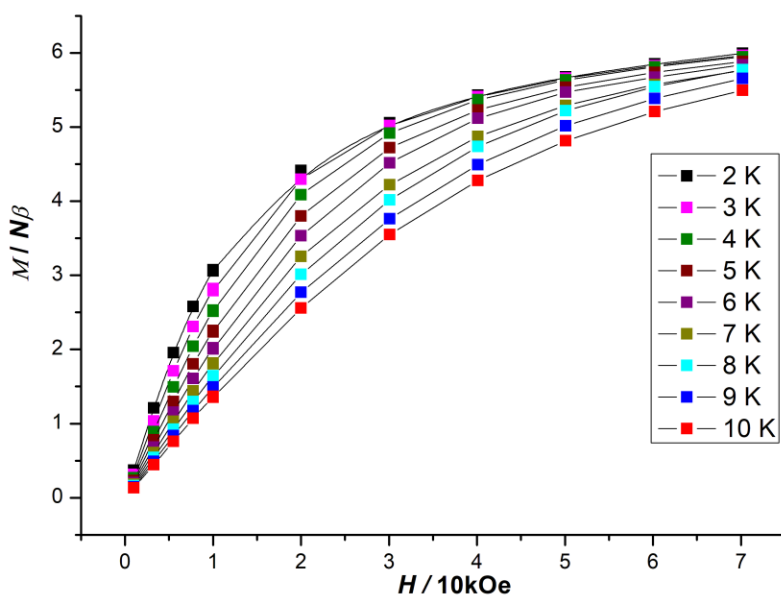


Figure 2.11.: Plot of reduced magnetization ($M/N\beta$) v.s. H for compound **4** in the 2–10 K range. The solid lines are just for the guidance of the eye, does not represent any simulated results.

As shown in figure 2.11, the variable field isotherms measurements were performed in the range 2–10 K under external magnetic fields up to 70 kOe. The maximum value of 5.99 $N\beta$ at 70 kOe (2K) matches perfectly with the theoretical saturation magnetization value of $Fe(II)$ ion (8.00 $N\beta$), suggesting good homogenous character of the sample. In addition, the reduced magnetization plots (M vs. H/T) exhibit significant separations between the isofield curves, confirming the existence of zero field splitting, which possibly explains the dropping of χ_{MT} values below 30 K (figure S1, S2).

In conclusion the temperature dependent Mössbauer spectra displayed in Figure 2.10 clearly show that the central iron(II) in complex **4** is able to undergo SCO starting at around 100K and completing at room temperature in accordance with the magnetic susceptibility data shown in Figure 2.9.

2.5 Conclusion

The work described herein represents three new examples of discrete polynuclear Fe^{II} complexes from the 4-substituted 1,2,4-triazole. Based on the ligand 4-(p-tolylidene-amino)-4*H*-1,2,4-triazole (toltrz), a series of crystalline coordination Fe^{II} complexes, that is, two binuclear [$Fe^{II}_2(\text{toltrz})_5(\text{SCN})_4$] $3H_2O$ (**C1**), [$Fe^{II}_2(\text{toltrz})_5(\text{SeCN})_4$] $3H_2O$ (**C2**) and one trinuclear [$Fe^{II}_3(\text{toltrz})_6(\text{H}_2O)_6$] $6(\text{BF}_4)$ $2H_2O$ $2\text{CH}_3\text{CH}_2\text{CO}_2\text{CH}_3$ (**C4**) has been synthesized and structurally as well as magnetically characterized. A gradual spin transition was found in compound **3**, while isostructural **C1** and **C2** showed a similar and weak antiferromagnetic exchange coupling between the linked Fe^{II} centers. As there are still only a few examples for these binuclear Fe^{II} crystalline complexes, the successful preparation and analysis of

Chapter 2 SCO Investigation of Three Triple *N1,N2*-Triazole Bridged Fe^{II} Complexes based on Toltrz

these compounds is still a challenge and interesting work. More related crystalline coordination materials with 4-substituted-1,2,4-triazole derivatives also need to be synthesized and characterized in order to deeply understand the structural–magneto correlation of these coordination compounds and provide some fundamental trends for the SCO field.

2.6 Acknowledgement

We kindly thank *SPIN + X* Program for the support of Mössbauer measurement at *Technische Universität Kaiserslautern*. Dr. Dieter Schollmeyer and Regine Jung-Pothmann (*Johannes Gutenberg University, Mainz*) are kindly acknowledged for collecting the crystal structural data. A.M.L. acknowledges the financial support from graduate school MAINZ and is a recipient of a DFG fellowship through the Excellence Initiative by the Graduate School Materials Science in Mainz (DFG/GSC 266).

2.7 Reference

- [1] a) L. Cambi, L. Szegö, *Ber. Deutsch. Chem. Ges.*, **1931**, *64*, 2591–2598; b) L. Cambi, L. Szegö, *Ber. Deutsch. Chem. Ges.*, **1933**, *66*, 656–661; c) L. Cambi, L. Malatesta, *Ber. Deutsch. Chem. Ges.*, **1937**, *70*, 2067–2078.
- [2] a) H. A. Goodwin, *Coord. Chem. Rev.*, **1976**, *18*, 293–325; b) E. König, R. Gerhard, S. K. Kulshreshtha, *Chem. Rev.*, **1985**, *85*, 219–234.
- [3] a) P. Gülich, G. Yann, A. G. Harold, *Chem. Soc. Rev.*, **2000**, *29*, 419–427; b) M. A. Halcrow, *Chem. Soc. Rev.*, **2011**, *40*, 4119–4142. c) E. Coronado, M. E. Guillermo, *Chem. Soc. Rev.*, **2013**, *42*, 1525–1539.
- [4] a) O. Kahn, J. Kröber, C. Jay, *Adv. Mater.*, **1992**, *4*, 718–728; b) P. Gülich, Y. Garcia, H. A. Goodwin, *Chem. Soc. Rev.*, **2000**, *29*, 419–427.
- [5] a) R. N. Muller, V. Elst, S. Laurent, *J. Am. Chem. Soc.*, **2003**, *125*, 8405–8407; b) J. F. Letard, O. Nguyen, N. Daro, Patent, **2007**, FR2894581.
- [6] a) M. Matsuda, H. Isozaki, H. Tajima, *Chem. Lett.*, **2008**, *37*, 374–375; b) S. Kanegawa, S. Kang, O. Sato, *Eur. J. Inorg. Chem.*, **2013**, *2013*, 725–729.
- [7] a) O. Kahn, M. C. Jay, *Science*, **1998**, *279*, 44–48; b) J. G. Haasnoot, *Coord. Chem. Rev.*, **2000**, *131*, 200–201; c) O. Roubeau, *Chem. Eur. J.*, **2012**, *18*, 15230–15244.
- [8] a) H. L. C. Feltham, A. S. Barltrop, S. Brooker, *Coord. Chem. Rev.*, **2017**, *344*, 26–53; b) M. H. Klingele, S. Brooker, *Coord. Chem. Rev.*, **2003**, *241*, 119–132; c) J. A. Kitchen, S. Brooker, *Coord. Chem. Rev.*, **2008**, *252*, 2072–2092.
- [9] a) H. L. Feltham, K. Dankhoff, C. J. Meledandri, S. Brooker, *ChemPlusChem.*, **2018**, *83*, 1–9; b) H. L. Feltham, M. G. Cowan, J. A. Kitchen, G. N. Jameson, S. Brooker, *Supramol Chem.*, **2018**, *30*, 296–304; c) S. Rodríguez-Jiménez, A. S. Barltrop, N. G. White, H. L. Feltham, S. Brooker, *Inorg. Chem.*, **2018**, *57*, 6266–6282; d) S. Rodríguez-Jiménez, S. Brooker, *Inorg. Chem.*, **2017**, *56*, 13697–13708.
- [10] G. Vos, R. A. Le Febre, R. A. De Graaff, J. G. Haasnoot, J. Reedijk, *J. Am. Chem. Soc.*, **1983**, *105*, 1682–1683.

Chapter 2 SCO Investigation of Three Triple *N1,N2*-Triazole Bridged Fe^{II} Complexes based on Toltrz

- [11] Y. Garcia, F. Robert, A. D. Naik, G. Y. Zhou, B. Tinant, K. Robeyns, S. Michotte, L. Piraux, *J. Am. Chem. Soc.*, **2011**, *133*, 15850–15853.
- [12] a) J. L. Wang, Q. Liu, Y. S. Meng, H. Zheng, H. L. Zhu, Q. Shi, T. Liu, *Inorg. Chem.*, **2017**, *56*, 10674–10680; b) W. B. Chen, J. D. Leng, Z. Z. Wang, Y. C. Chen, Y. Miao, M. L. Tong, W. Dong, *Chem. Commun.*, **2017**, *53*, 7820–7823; c) N. Pittala, F. Thétiot, C. Charles, S. Triki, K. Boukheddaden, G. Chastanet, M. Marchivie, *Chem. Commun.*, **2017**, *53*, 8356–8359; d) W. B. Chen, Y. C. Chen, M. Yang, M. L. Tong, W. Dong, *Dalton Trans.*, **2018**, *47*, 4307–4314.
- [13] a) G. A. Bain, J. F. Berry, *J. Chem. Edu.*, **2008**, *85*, 532; b) H. P. Gunnlaugsson, *Hyperfine Interact.*, **2016**, *237*, 79.
- [14] *SMART 5.0 and SAINT 4.0 for Windows NT, Area Detector Control and Integration Software*, Bruker Analytical X-Ray Systems Inc., Madison, WI, 1998.
- [15] G. M. Sheldrick, *SADABS: Program for Empirical Absorption Correction of Area Detector Data*, University of Göttingen, Göttingen, Germany, 1996.
- [16] a) G. M. Sheldrick, *Acta Crystallogr.*, **2015**, *C71*, 3–8; b) G. M. Sheldrick, *SHELXTL 5.1 for Windows NT: Structure Determination Software Programs*, Bruker Analytical X-ray Systems, Inc., Madison, WI, 1997.
- [17] O. V. Dolomanov, L. J. Bourhis, R. J. Gildea, J. A. K. Howard, H. J. Puschmann, *Appl. Crystallogr.*, **2009**, *42*, 339–341.
- [18] *Diamond - Crystal and Molecular Structure Visualization Crystal Impact* - Dr. H. Putz & Dr. K. Brandenburg GbR, Kreuzherrenstr. 102, 53227 Bonn, Germany.
- [19] a) T. Khan, R. Yadav, *Heterocycl. Lett.*, **2016**, *6*, 757–766; b) A. Kwiecień, M. Barys, Z. Ciunik, *Molecules*, **2014**, *19*, 11160–11177.
- [20] P. Chakraborty, A. Tissot, L. Peterhans, L. Guenee, C. Besnard, P. Pattison, A. Hauser, *Phys. Rev., B* **2013**, *87*, 2143.
- [21] a) A. Bauzá, T. J. Mooibroek, A. Frontera, *CrystEngComm*, **2016**, *18*, 10–23; b) G. A. Senchyk, A. B. Lysenko, D. Y. Naumov, V. P. Fedin, H. Krautscheid, K. V. Domasevitch, *Inorg. Chem. Commun.*, **2010**, *13*, 1576–1579.
- [22] a) Krishnan, R. S., Srinivasan, R. & Devanarayanan, S. *Thermal Expansion of Crystals*, Pergamon, **1979**; b) Barron, T. H. K. & White, G. K. *Heat Capacity and Thermal Expansion at Low Temperatures*, Kluwer Academic, **1999**; c) K. Takenaka, *Sci Technol Adv Mater.*, **2012**, *13*, 013001; d) B. R. Mullaney, L. Goux-Capes, D. J. Price, G. Chastanet, J. F. Létard, C. J. Kepert, *Nat. Commun.*, **2017**, *8*, 1053.
- [23] E. Borello, A. Zecchina, *Spectrochimica Acta*, **1963**, *19*, 1703–1715.
- [24] Y. Prashanthi, S. Raj, *Journal of Scientific Research*, **2010**, *2*, 114–126.
- [25] S. H. Sumrra, Z. H. Chohan, *Spectrochimica Acta A: Molecular and Biomolecular Spectroscopy*, **2012**, *98*, 53–61.
- [26] a) A. A. Salaudeen, C. A. Kilner, M. A. Halcrow, *Polyhedron*, **2008**, *12*, 2569–2576; b) K. Nakamoto, *Infrared and Raman Spectra of Inorganic and Coordination Compounds Part B (5th ed.)* Wiley Interscience, New York, **1997**, 116.
- [27] N. F. Chilton, R. P. Anderson, L. D. Turner, A. Soncini, K. S. Murray, *J. Comput. Chem.*, **2013**, *34*, 1164.
- [28] V. Schünemann, H. Winkler, *Rep. Prog. Phys.*, **2000**, *63*, 263–353.

2.8 Supplementary Information

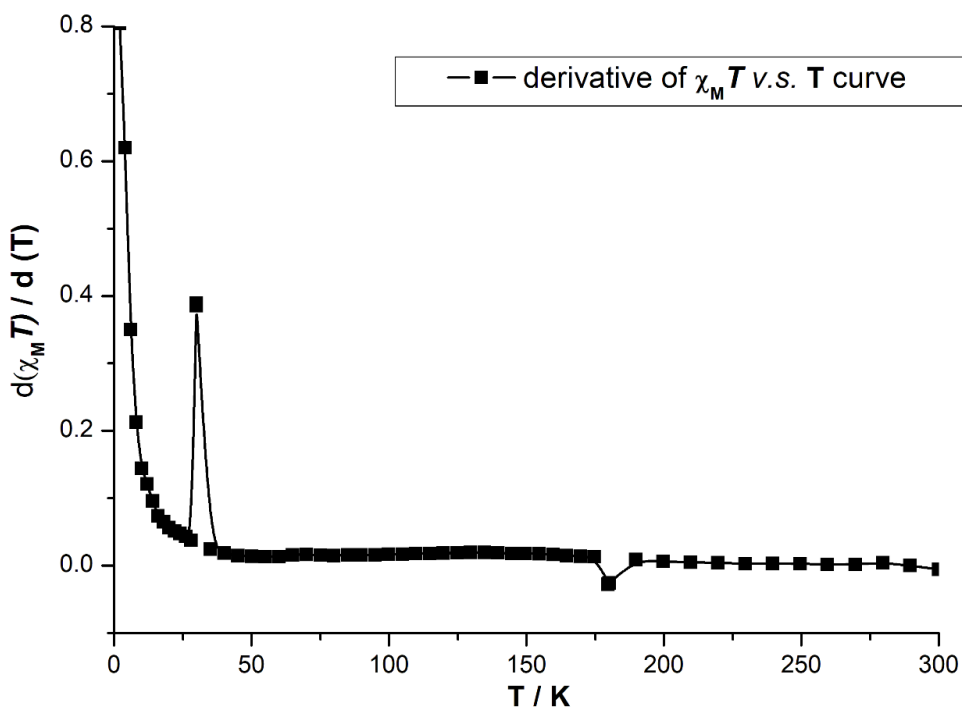


Figure S1. A derivative plot of the $\chi_M T$ v.s. T curve for complex 4.

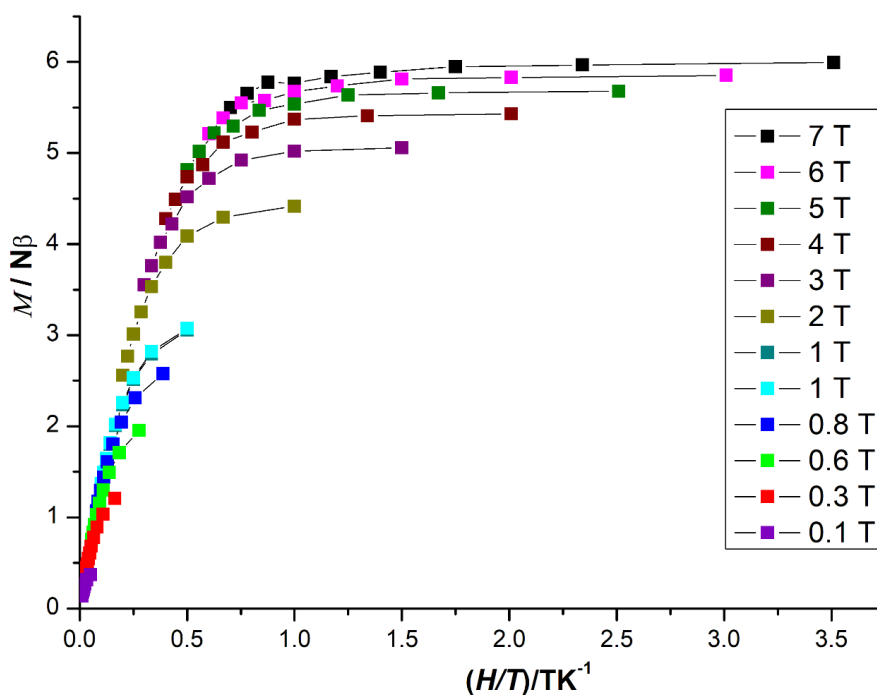


Figure S2. Reduced magnetization data for 4. The solid lines are just for the guidance of the eye, does not represent any simulated results.

**Chapter 2 SCO Investigation of Three Triple *N1,N2*-Triazole Bridged
Fe^{II} Complexes based on Toltrz**

Table S2.1 Selected bond lengths [Å] and angles [°] for compounds **1** and **2**.

Compound 1					
Fe(1)-N(1)	2.155(8)	Fe(1)-N(5)	2.147(7)	Fe(1)-N(6)	2.109(7)
Fe(1)-N(7)	2.174(8)	Fe(1)-N(11)	2.223(6)	Fe(1)-N(15)	2.205(7)
Fe(2)-N(8)	2.179(7)	Fe(2)-N(12)	2.198(7)	Fe(2)-N(16)	2.200(7)
Fe(2)-N(19)	2.177(7)	Fe(2)-N(23)	2.165(8)	Fe(2)-N(24)	2.079(8)
N(1)-Fe(1)-N(7)	174.5(3)	N(1)-Fe(1)-N(11)	93.0(3)	N(1)-Fe(1)-N(15)	91.9(3)
N(5)-Fe(1)-N(1)	86.3(3)	N(5)-Fe(1)-N(7)	88.3(3)	N(5)-Fe(1)-N(11)	177.1(3)
N(5)-Fe(1)-N(15)	94.0(3)	N(6)-Fe(1)-N(1)	92.5(3)	N(6)-Fe(1)-N(5)	92.6(3)
N(6)-Fe(1)-N(7)	89.0(3)	N(6)-Fe(1)-N(11)	90.2(2)	N(6)-Fe(1)-N(15)	172.4(3)
N(7)-Fe(1)-N(11)	92.3(3)	N(7)-Fe(1)-N(15)	87.3(3)	N(15)-Fe(1)-N(11)	83.2(2)
N(8)-Fe(2)-N(12)	88.6(2)	N(8)-Fe(2)-N(16)	88.4(3)	N(12)-Fe(2)-N(16)	86.9(2)
N(19)-Fe(2)-N(8)	176.1(3)	N(19)-Fe(2)-N(12)	90.4(3)	N(19)-Fe(2)-N(16)	95.3(3)
N(23)-Fe(2)-N(8)	87.0(3)	N(23)-Fe(2)-N(12)	86.6(3)	N(23)-Fe(2)-N(16)	172.1(3)
N(23)-Fe(2)-N(19)	89.2(3)	N(24)-Fe(2)-N(8)	91.6(3)	N(24)-Fe(2)-N(12)	179.2(3)
N(24)-Fe(2)-N(16)	92.3(3)	N(24)-Fe(2)-N(19)	89.4(3)	N(24)-Fe(2)-N(23)	94.2(3)
C(11)-N(5)-Fe(1)	148.8(7)	C(54)-N(24)-Fe(2)	168.6(9)	N(23)-C(53)-S(3)	175.8(8)
C(12)-N(6)-Fe(1)	171.6(7)	N(5)-C(11)-S(2)	177.8(10)	N(24)-C(54)-S(4)	177.5(10)
C(53)-N(23)-Fe(2)	138.8(7)	N(6)-C(12)-S(1)	179.0(9)		
Compound 2					
Fe(2)-N(8)	2.178(9)	Fe(2)-N(23)	2.091(11)	Fe(1)-N(11)	2.233(9)
Fe(2)-N(16)	2.181(9)	Fe(2)-N(24)	2.193(10)	Fe(1)-N(1)	2.165(13)
Fe(2)-N(12)	2.206(9)	Fe(1)-N(7)	2.178(11)	Fe(1)-N(5)	2.142(12)
Fe(2)-N(19)	2.181(9)	Fe(1)-N(15)	2.181(10)	Fe(1)-N(6)	2.116(11)
N(8)-Fe(2)-N(16)	88.6(4)	N(23)-Fe(2)-N(16)	91.0(4)	N(1)-Fe(1)-N(11)	92.4(4)
N(8)-Fe(2)-N(12)	90.0(4)	N(23)-Fe(2)-N(12)	177.5(3)	N(5)-Fe(1)-N(7)	87.4(4)
N(8)-Fe(2)-N(19)	176.0(4)	N(23)-Fe(2)-N(19)	89.1(3)	N(5)-Fe(1)-N(15)	94.6(4)
N(8)-Fe(2)-N(24)	86.3(4)	N(23)-Fe(2)-N(24)	95.1(4)	N(5)-Fe(1)-N(11)	179.3(4)
N(16)-Fe(2)-N(12)	86.9(3)	N(24)-Fe(2)-N(12)	87.1(3)	N(5)-Fe(1)-N(1)	87.6(5)
N(16)-Fe(2)-N(19)	95.4(4)	N(7)-Fe(1)-N(15)	87.8(4)	N(6)-Fe(1)-N(7)	89.4(4)
N(16)-Fe(2)-N(24)	172.1(4)	N(7)-Fe(1)-N(11)	92.6(3)	N(6)-Fe(1)-N(15)	173.3(4)
N(19)-Fe(2)-N(12)	89.6(3)	N(15)-Fe(1)-N(11)	84.7(3)	N(6)-Fe(1)-N(11)	89.4(4)
N(19)-Fe(2)-N(24)	89.7(4)	N(1)-Fe(1)-N(7)	175.1(4)	N(6)-Fe(1)-N(1)	91.2(5)
N(23)-Fe(2)-N(8)	91.4(4)	N(1)-Fe(1)-N(15)	92.1(4)	N(6)-Fe(1)-N(5)	91.3(4)
C(11)-N(5)-Fe(1)	149.2(10)	C(54)-N(24)-Fe(2)	139.2(9)	N(5)-C(11)-Se(2)	178.4(12)
C(12)-N(6)-Fe(1)	174.7(11)	N(23)-C(53)-Se(4)	177.0(12)	N(6)-C(12)-Se(1)	178.8(13)
C(53)-N(23)-Fe(2)	166.3(11)	N(24)-C(54)-Se(3)	177.5(10)		

Chapter 2 SCO Investigation of Three Triple *N1,N2*-Triazole Bridged Fe^{II} Complexes based on Toltrz

Table S2.2. Geometry of the π (phenyl/triazole) / X (X = S, Se) ... π (phenyl/triazole) in compounds **1** and **2**.

centroid1 / X (X = S, Se)	centroid2	distance of centroid1/X ... centroid2 (Å)	Symmetry codes of centroid2
Compound 1			
C16 ring	C49 ring	4.0357(5)	$-x + 1, -y + 1, -z + 2$
N7 ring	C6 ring	3.8134(3)	$-x + 1, -y + 1, -z + 1$
C51 ring	C16 ring	3.9796(4)	$-x + 1, -y + 1, -z + 2$
C4 ring	C13 ring	4.0083(3)	$-x + 1, -y + 1, -z + 1$
S1	C16 ring	3.7232(5)	$x + 1, y, z$
Compound 2			
N11 ring	C29 ring	4.2776(5)	$-x, -y + 1, -z + 2$
Se1	C16 ring	3.6503(3)	$x - 1, y, z$
C16 ring	C49 ring	4.002(3)	$-x + 1, -y + 1, -z + 2$
N2 ring	C7 ring	4.2609(3)	$-x, -y + 1, -z + 1$
N7 ring	C7 ring	3.8363(3)	$-x + 1, -y + 1, -z + 1$

^a Angle of the centroid 1 ... π axis to the plane of the centroid 2 cycle contacted.

Table S2.3. Hydrogen-bonding interactions in compound **4**.

D-H	A	H...A (Å)	D...A (Å)	\angle D-H...A (°)	Symmetry codes of A
O2w-H2wb	F12	1.852	2.628(3)	146.32	x, y, z
O2w-H2wa	F11	2.113	2.813(2)	137.21	$-x + 1, -y, -z + 1$
O3w-H3wa	F4	2.056	2.674(2)	127.19	x, y, z
O1w-H1wb	F8	1.849	2.688(4)	165.36	x, y, z
C12-H12a	F7	2.322	3.217(3)	156.78	$-x + 1, -y + 1, -z + 1$
C2-H2a	F3	2.303	3.237(2)	167.52	$-x + 1, -y + 1, -z + 1$
C18-H18a	F6	2.537	3.365(2)	146.67	$-x + 1, -y + 1, -z$
C22-H22a	F9	2.391	3.280(3)	155.61	$-x + 1, -y + 1, -z + 1$
C22-H22a	F10	2.486	3.347(2)	150.67	$-x + 1, -y + 1, -z + 1$
C31-H31b	F10	2.542	3.1137(2)	117.35	$-x + 2, -y, -z + 1$
C33-H33b	F11	2.513	3.195(2)	126.58	$-x + 1, -y + 2, -z + 1$
C21-H21a	F1	2.518	3.421(3)	163.83	$-x + 2, -y + 1, -z + 1$

Chapter 3 SCO Investigation of Two Triple *N1,N2*-Triazole Bridged Fe^{II} Complexes based on Prytrz

This chapter covers the summary results of two triple *N1,N2*-triazole bridged Fe^{II} complexes based on ligand 1 (pyrtrz), which is manuscripted to a journal submission of *Z. Anorg. Allg. Chem.* Manuscript detailing will be presented in the following:

Triple *N1,N2*-Triazole Bridged Dinuclear and Trinuclear Fe^{II} complexes: Antiferromagnetic coupling *v.s.* Spin Conversion

Ai-Min Li^{a,b} and Eva Rentschler^{a*}

^a Institute of Inorganic and Analytical Chemistry, Johannes Gutenberg University Mainz, Duesbergweg 10-14, 55128 Mainz, Germany

rentschler@uni-mainz.de

^b Graduate School Materials Science in Mainz, Staudingerweg 9, D-55128 Mainz, Germany

KEYWORDS Spin crossover / trinuclear / binuclear / 1,2,4-triazole / Schiff bases

3.1 Abstract

Based on the *pyrrolyl* functionalized Schiff base 1,2,4-triazole ligand 4-((1H-pyrrol-2-yl)methylene-amino)-4H-1,2,4-triazole (pyrtrz), a group of two multi-nuclear triazole-bridged Fe^{II} compounds has been prepared. These two compounds represent rare discrete multi-nuclear species, with μ_2 -*N1,N2*-triazole bridges linking the Fe^{II} centers. Magnetic susceptibility measurements revealed an abrupt single-step spin crossover (SCO) behavior of compound **6** on the central Fe^{II} sites and single-crystal X-ray diffraction (173 K) showed that this compound crystallizes in the monoclinic space group (*P21/c*), and multiple intramolecular interactions were found responsible for the abrupt transition. Compound **5** is a dinuclear complex with thiocyanate as terminal ligands, this compound stayed in high spin state over all temperature range and display weak antiferromagnetic exchange coupling.

3.2 Introduction

During the development of spin crossover (SCO) complex preparation and characterization, the molecular complexes are most commonly reported, like the mononuclear [Fe(bpp)₂]²⁺ (bpp = 2,6-di{pyrazol-1-yl}pyridine) system, ^[1] the triazole-based dinuclear [Fe₂(PMAT)₂]⁴⁺ system, ^[2] and the very recently reported thiadiazole and oxadiazole dinuclear system by our group. ^[3] Comparable to these well-explored systems, the discrete

polynuclear complexes based on triazole ligand, *i.e.*, dinuclear and trinuclear complexes triple-bridged by *N1,N2*-1,2,4-triazole ligands, are currently receiving great interest. [4] This family of compounds stands for the attempting and endeavor made to explore and isolate the famous 1D coordination polymers of general formula [Fe((Rtrz)₃)(X)₂] (Rtrz = 4-substituted-1,2,4-triazole, X = standard monoanions), some of which displayed wide thermal hysteresis loops around room temperature. [5] Compared to the typical molecular system mentioned above, the triazole-based compounds bear benefits of expanding the discrete nuclearities to multinuclear or 1D polymeric complex, which is of vital importance in the exploration of cooperativity between the covalently linked iron (II) centers. After the first structural report on the 1D polymeric structure [Fe(NH₂trz)₃](NO₃)₂ in 2011, there is only one more crystal structure found very recently in the last year. [6] However, a series of the discrete di-, and tri-nuclear complexes were synthesized and studied, with the intention of better understanding of the 1D polymer at the molecular and inter-molecular scales, such to understand and fine tune its SCO properties (Table 9.1, 9.2). [7-12] Interestingly, among the limited examples of the discrete polynuclear complexes that displayed SCO, the five trinuclear complexes with *p*-tolylsulfonate (Tos⁻) as counteranion [13, 14] all showed gradual transition with different transition temperatures. (Table 9.1, 9.2). In the present work, we report the first example of a trimer complex showing an abrupt spin transition with tolylsulfonate (Tos) as counteranion. Herein, we report the synthesis, structure, and magnetic properties of two poly-nuclear triazole-bridged Fe^{II} complexes based on a Schiff base modified triazole ligand, *i.e.*, 4-((1H-pyrrol-2-yl)methylene-amino)-4H-1,2,4-triazole (pyrtrz): [Fe^{II}₂(pyrtrz)₅(SCN)₄]-4H₂O (**5**) and [Fe^{II}₃(pyrtrz)₆(TsO)₆].7H₂O.2CH₃OH (**6**). Single X-ray diffraction and magnetic measurement reveal that both compounds are bridged by μ_2 -*N1,N2*-1,2,4-triazole ligands, complex **5** is a binuclear Fe^{II} complex showing weak antiferromagnetic interactions, while complex **6** is a trinuclear Fe^{II} complex exhibiting an abrupt spin transition behavior. Multiple intramolecular interactions were found being responsible for the sharp transition.

3.2 Experimental Section

General Methods and Materials.

All commercially purchased chemicals (Alfa Aesar, Sigma-Aldrich and Acros Organics) and solvents were used without further purification. Magnetic susceptibility data were collected with SQUID magnetometer MPMS XL-7 in a temperature range of 2~300 K with an applied field of 1000 Oe. Samples for SQUID measurement were prepared in gelatin

Chapter 3 SCO Investigation of Two Triple N1,N2-Triazole Bridged Fe^{II} Complexes based on Prytrz

capsules and held in plastic straws for insertion into the magnetometer. The obtained magnetic susceptibility values were corrected for diamagnetic susceptibility according to the Pascal's constants. ^[15] Elemental analysis (C, H, and N) was measured in the microanalytical laboratories at Johannes Gutenberg University Mainz. Infrared spectra (FT-IR) were recorded as potassium bromide pellets in the range from 4000 to 400 cm⁻¹ with a JASCO FT/IR-4200 at the Johannes Gutenberg-University Mainz.

Single Crystal X-ray Diffraction

Single-crystal X-ray diffraction data (**C5** and **C6**) were collected on a Bruker Smart APEX II CCD diffractometer. The diffractometer was operated at 45 kV and 35 mA with Mo K α radiation ($\lambda = 0.71073 \text{ \AA}$), and a nitrogen cold stream was applied to contain the collection temperature at 173(2) K. Each data reduction was performed using the SAINT and SMART softwares ^[16] and an empirical absorption correction was applied with the SADABS program. ^[17] Both structures (**C5** and **C6**) were solved by direct methods, refined by full-matrix least-squares on F^2 with the SHELXTL program package, ^[18] and the Olex2 program. ^[19] The ordered non-hydrogen atoms in each structure were refined with anisotropic displacement parameters, while the hydrogen atoms were placed in idealized positions and allowed to ride on their parent atoms. In compound **5**, the C39 and S4 atoms are respectively disordered over two positions with a ratio of 2:1. In compound **6**, the refinement of the reflection data yielded acceptable resolved structural results with highly disordering fragments: there are four disordering positions over the *pyrrolyl* fragments (C31 to C35, N36; N54, C56, N57, C58 to C60; N42, C43 to C47, N48; C67 to C71, N72), all with a ratio of 1:1, and four more disordering positions were found over the counter anion *p*-toluenesulfonate parts (C94 to C100, S4, O16 to O18; C87 to C93; C208 to C214, S6, O22 to O24; C101 to C107, S5, O19 to O20), all with a ratio of 1:1. Even though, with all these disordering positions, we managed to get a final refinement with the final R_1 ($I > 2\sigma(I)$) value of 0.0852 (completeness of 0.996), the major part of the structure is still reliable and gives us valuable data for the structure and property investigation (see in the main text). In all the structures, the lattice water molecules were refined with anisotropic displacement parameters, while the hydrogen atoms were not defined. Thus, in the discussion of the main text, unless specified, all the lattice water molecules or the disordered parts were not included. The crystallographic data and refinement parameters of **C5** and **C6** are listed in Table 3.1. CCDC numbers 1815489-1815490 contain the supplementary crystal data of the compounds: 1815489 (**C5**) and 1815490 (**C6**), which can be obtained free of charge from

Chapter 3 SCO Investigation of Two Triple *N1,N2*-Triazole Bridged Fe^{II} Complexes based on Prytrz

The Cambridge Crystallographic Data Centre via www.ccdc.cam.ac.uk/data_request/cif.

All structure figures are generated with DIAMOND-3. [20]

Syntheses

Synthesis of the ligand

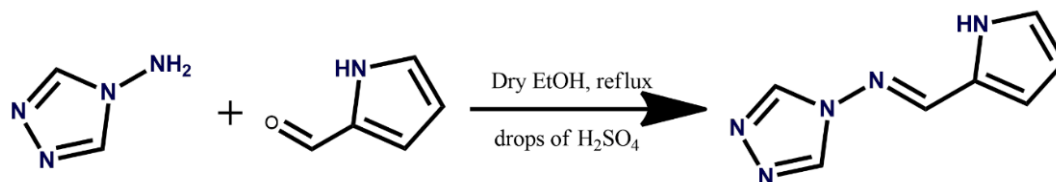


Figure 3.1.: Synthetic scheme to prepare the pytrtz ligand.

The ligand 4-((1H-pyrrol-2-yl)methylene-amino)-4H-1,2,4-triazole (pytrtz) (Figure 3.1) was prepared by the condensation reaction: [21] 4-Amino-1,2,4-triazole (1.68 g, 0.02 mol, 1.0 eq.) and pyrrole-2-carboxaldehyde (2.09 g, 0.022 mol, 1.1 eq.) were dissolved in ethanol with the addition of few drops of H₂SO₄, acting as acidic catalyst. The reaction mixture was slowly heated up to 80 °C until it started to boil, then kept refluxing for 10 h. When it cooled down to r.t., the excess of the solvent was removed by rotary evaporator at 35 °C. The products such obtained was washed with small amount of cold ethanol, diethyl ether and then dried in the desiccator with phosphorus pentoxide as dry agent. Dark purple powder was obtained. Yield: 3.14 g (97.52%), m.p., 207.5–210.7 °C; IR (KBr): 1635 cm⁻¹ (vw), 3127(w), 1169 (s), 1062 (vs), 860(s), 762 and 621 cm⁻¹ (Ar, CH-strech); 817 cm⁻¹, 2918 cm⁻¹ (Ar-CH₃). ¹HNMR (Figure 9.1) (CD₃OD) 7.91 (s, 1H, Ar-H), 7.99 (s, 1H, Ar-H), 8.92 (s, 1H, H-C=N), 9.07 (s, 2H, triazole).

Synthesis of the Complex

Synthesis of [Fe^{II}₂(pytrtz)₅(SCN)₄].6H₂O (C5)

To a stirring solution of pytrtz (129 mg, 0.8 mmol) in methanol (5 mL) was added an aqueous solution of FeSO₄·7H₂O (90 mg, ~ 0.3 mmol) and NH₄SCN (50 mg, ~ 0.6 mmol). The solution turned from light yellow to dark red immediately. To prevent possible oxidation process, one spatula amount (~35 mg) of ascorbic acid was added into the reaction solution. The reaction mixture was then stirred for around 3~4 hours before filtrated with rapid filter paper. The clear light reddish solution such obtained was kept in a small vial and left stand still to allow the solvent evaporate slowly. After one week, light brown block-like crystals of C5 were deposited at the bottom of the vial. After removing the mother liquid, the single

Chapter 3 SCO Investigation of Two Triple *N1,N2*-Triazole Bridged Fe^{II} Complexes based on Prytrz

crystals were quickly dried in an argon stream, and stored under argon. Yield: 127.1 mg (34.90% based on Fe). Anal. Calcd (Found) for C₃₉H₃₅Fe₂N₂O₄S₄: C, 38.59 (36.38); H, 2.91 (3.63); N, 33.46 (32.62). IR (KBr) cm^{-1} : 3125 (w), 2927 (m), 2856 (w), 2078 (s), 1609 (vs), 1523 (m), 1422 (w), 1385 (vs), 1311 (m), 1246(vs), 1127 (s), 1063 (m), 1037 (m), 985 (m), 881(w), 759(m), 621 (s), 593 (m), 506 (w).

Synthesis of [Fe^{II}₃(pyrtrz)₆(TsO)₆].7H₂O.2CH₃OH (C6)

Freshly prepared Fe(TsO)₂ (120 mg, ~0.3 mmol) in 3 mL H₂O was added into a stirring solution of pyrtrz (97 mg, 0.6 mmol) dissolved in MeOH (2~3 mL). After stirring for half hour, one spatula amount (~35 mg) of ascorbic acid was added. This solution was then stirred for 3~4 hours before filtrated. The obtained clear light yellow solution was then kept in a small vial and left stand still to evaporate the solvent slowly. After two weeks, light pink needle-like crystals of C6 were deposited at the bottom of the vial. After removing the mother liquid, the single crystals were quickly dried in an argon stream, and stored under argon. Yield: 257.3 mg (35.83% based on Fe). Anal. Calcd (Found) for C₈₅H₈₈Fe₃N₃O_{31.5}S₆: C, 42.65 (42.26); H, 3.71 (4.22); N, 17.55 (17.62). IR (KBr) cm^{-1} : 3097 (w), 2988(w), 2922(w), 2857 (w), 1605 (vs), 1530 (s), 1446(m), 1423(m), 1368 (s), 1189(vs), 1125 (s), 1072 (s), 1035 (vs), 1010(s), 883 (m), 844(m), 815 (m), 752 (m), 682(s), 624 (m), 606(w), 566 (s), 513 (w).

3.4 Result and discussion

3.4.1 Structural Description

Crystallographic data for the compounds **5** and **6** are summarized in Table 3.1 and the selected bond lengths and angles are presented in Table S3.1.

Table 3.1. Crystallographic Data and Refinement Parameters for compounds **5** and **6**.

Compound	C5	C6
Empirical formula	C ₃₉ H ₃₅ Fe ₂ N ₂₉ O ₄ S ₄	C ₈₅ H ₈₈ Fe ₃ N ₃₀ O _{31.5} S ₆
Formula weight	1213.90	2393.76
Crystal size	0.14×0.13×0.07	0.51×0.11×0.03
Crystal system	Triclinic	Triclinic
Space group	<i>P</i> -1 (<i>No.</i> 2)	<i>P</i> 121/ <i>c</i> 1 (<i>No.</i> 14)
<i>a</i> (Å)	11.9168(13)	19.3399(19)
<i>b</i> (Å)	13.8948(15)	15.6171(15)
<i>c</i> (Å)	18.830(2)	37.287(4)
α (°)	90.543(3)	90
β (°)	101.891(3)	96.902(2)
γ (°)	102.381(3)	90
<i>V</i> (Å ³)	2975.4(6)	11180.2(19)
<i>Z</i>	2	4
<i>D</i> _{calc} (g/cm ³)	1.355	1.422
μ (Mo-K α) (mm ⁻¹)	0.691	0.583
<i>F</i> (000)	1240	4936
Reflections collected	28747	64247
Independent reflections	10485 (0.1442)	26617 (0.1035)
Parameters	668	1858
Goodness-of-fit	0.919	0.996
<i>R</i> ₁ [<i>I</i> > 2 σ (<i>I</i>)] ^a	0.1123	0.0852
<i>wR</i> ₂ (all data) ^b	0.3641	0.2743

$${}^a R_1 = \frac{\sum ||F_o| - |F_c||}{\sum |F_o|}, {}^b wR_2 = \left\{ \frac{\sum [w(F_o^2 - F_c^2)^2]}{\sum [w(F_o^2)^2]} \right\}^{1/2}$$

Crystal structure of [Fe^{II}₂(pyrtrz)₅(SCN)₄]-4H₂O (C5)

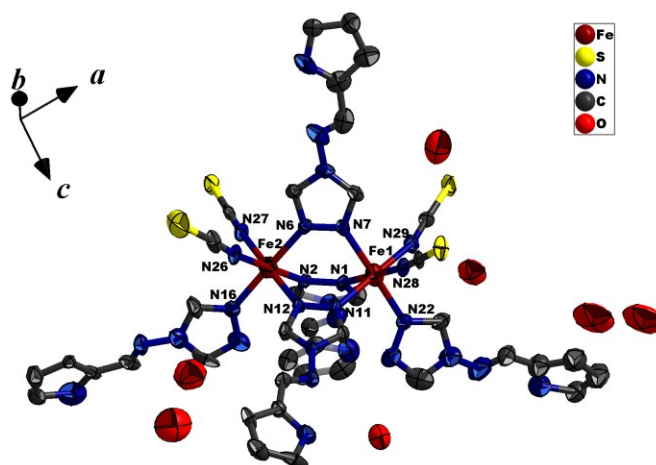


Figure 3.2.: Thermal ellipsoid view of the binuclear molecular structure of C5 at 173 K, shown with 40% probability ellipsoids. All H atoms are omitted, and only selected atoms are labelled for clarity.

Compound **5** crystallizes in the triclinic space group *P*-1. The asymmetric unit contains one full neutral dinuclear complex plus 6 lattice aqua molecules, although some of these aqua molecules are partially occupied resulting in a total of 4 aqua molecules in the structure. As shown in Fig. 3.2, for each compound, the two Fe^{II} centers are linked through three μ_2 -*N1,N2*-triazole bridges with the distance of 3.988 (7) Å. Each Fe^{II} coordination sphere is further completed by three N atoms from one terminal triazole ligand and two *cis*-thiocyanate anions. The terminal average Fe–N bond length of 2.113(3) Å is shorter than the central average Fe–N bond length of 2.159(3) Å. (Table S3.1) While in both cases, the bond range makes the Fe centers sitting well in the range of high-spin state value at 173 K,^[22] which is further confirmed by magnetic measurement. (See below) The NCS⁻ anions are almost linear with the N–C–S angle around 178°; the angle of coordination to iron Fe...N–C is split into two groups with the angle being around 160° and 175°. (See Table S3.1) Within the structure, there is one of the terminal thiocyanates being disordered over the C39–S4 bond part with a relative occupancy of 2:1.

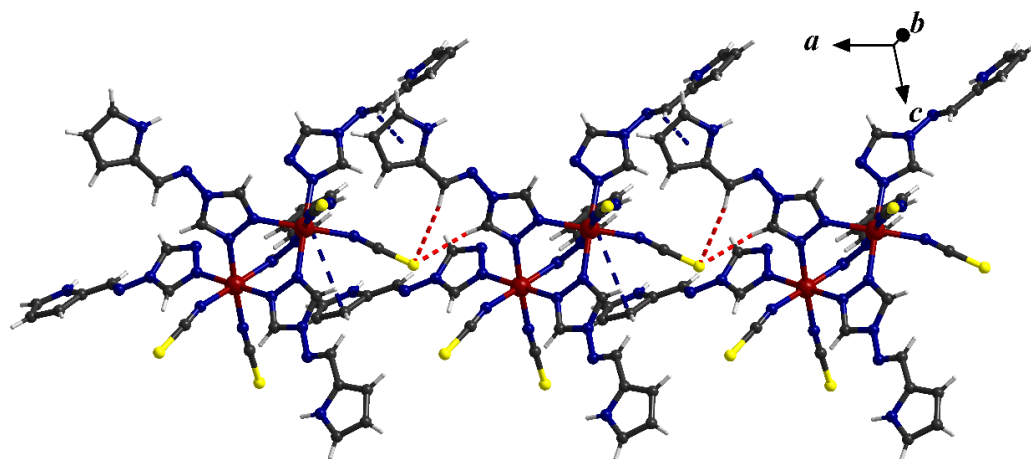


Figure 3.3.: The 1D chain connected via different intermolecular interactions along *a* axis. The red dashed lines represent H-bonding, while the blue dashed lines represent $\pi\cdots\pi$ stacking.

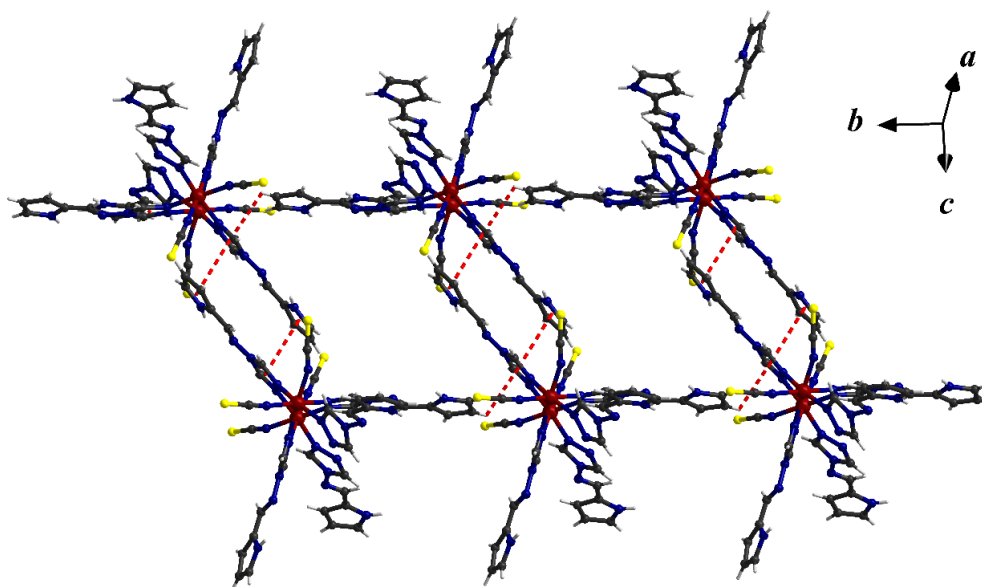


Figure 3.4.: The $\pi\cdots\pi$ stacking in *bc* plane.

In compound **5**, the adjacent neutral dinuclear units are interconnected through $\text{C31-H31}\cdots\pi_{\text{N15-ring}}$ stacking ($\text{C31-H31}\cdots\text{centroid} = 2.6070(2) \text{ \AA}$) and a group of one-to-two H-bonding ($\text{S4} \cdots \text{H17} = 2.9763(3) \text{ \AA}$, $\text{S4}\cdots\text{H16} = 2.6145(2) \text{ \AA}$) interactions to form a 1D chain along *a* axis. (Figure 3.3) This chain is further connected in *bc* plane through another two groups of parallel intermolecular $\pi\cdots\pi$ stacking ($\text{centroid}\cdots\text{centroid} = 3.5625(2) \text{ \AA}$) together with one set of $\text{C6-H6}\cdots\pi_{\text{N5 ring}}$ stacking ($\text{C6-H6}\cdots\text{centroid} = 3.7232(5) \text{ \AA}$) to form a 3D supramolecular architecture. (Figure 3.4)

Crystal structure of [Fe^{II}₃(pytrtz)₆(TsO)₆].6.5H₂O.CH₃OH (C6)

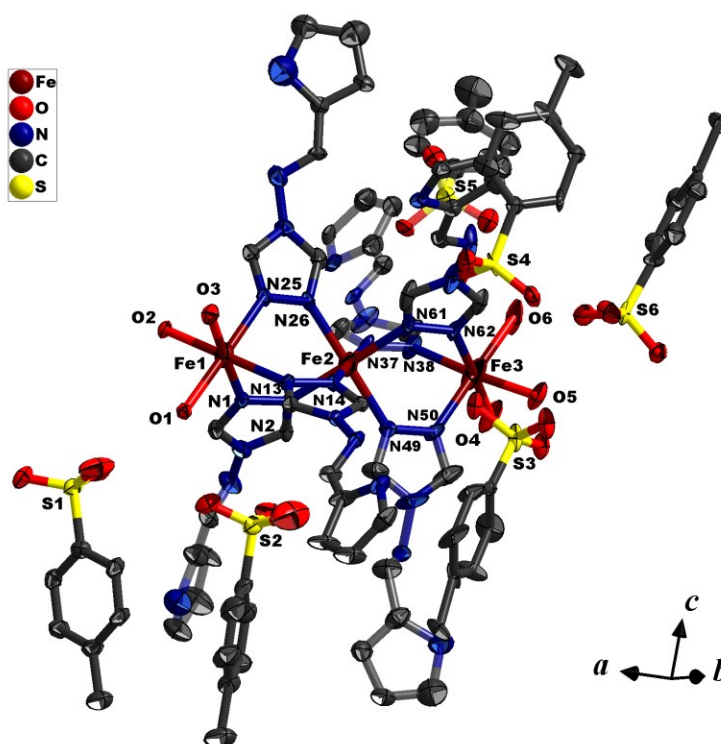


Figure 3.5.: Thermal ellipsoid view of the linear trinuclear complex C6 at 173 K, shown with 40% probability ellipsoids. All water, methanol solvent molecules and H atoms are omitted for clarity, and only selected atoms are labelled.

Compound **6** was found crystallized in monoclinic space group *P21/c*. Within the linear trinuclear basic units, the Fe^{II} ions are linked by three μ_2 -*N1,N2*-donating triazole ligands, the terminal coordination sites are occupied by three H₂O molecules to complete its [N₃O₃] hexa-coordination. (Figure 3.5) Quite surprisingly, this structure consists of three complete Fe centers within the asymmetrical units, where there are only two other examples among the 17 reported linear trimer analogues. [10b, 11a] The central Fe2 is in an octahedral [FeN₆] coordination environment, while the outer Fe^{II} ion, Fe1 and Fe3, are in a [FeN₃O₃] coordination environment due to the coordination of the terminated aqua molecules. Each trinuclear unit is cationic with a 6⁺ charge, which is balanced by six free *p*-toluenesulfonate counteranions. Interestingly, due to different groups of H-bonding and π stacking, (Figure 3.6, table S3.2, S3.3, only predominant ones are discussed regards to the disordering fragments) the *p*-toluenesulfonate ions are embedded unequally around the three linear Fe units. This unique feature makes the central Fe centers crystallographically independent without symmetrical center, such the structure ended up with monoclinic space group with

Chapter 3 SCO Investigation of Two Triple *N1,N2*-Triazole Bridged Fe^{II} Complexes based on Prytrz

three independent Fe centers within the asymmetrical unit. The X-ray analysis also reveals two methanol and seven water molecules linked to the trinuclear units via different H-bonding interactions, as some atoms are only partially occupied, resulting only in a total of one methanol and 6.5 water molecules identified. The hydrogen from the water molecules are not defined here, such potential supramolecular interactions are not discussed here. Though one significant point need to be pointed out that six of the seven water molecules scattered exclusively along one side of the trimer with another one (O29) embedded in the middle of the trimer units (Figure 3.5). The balance of the unevenly distributed water molecules is achieved by the same unequally embedded *p*-toluenesulfonate anions, which further explains the uniqueness of the structure.

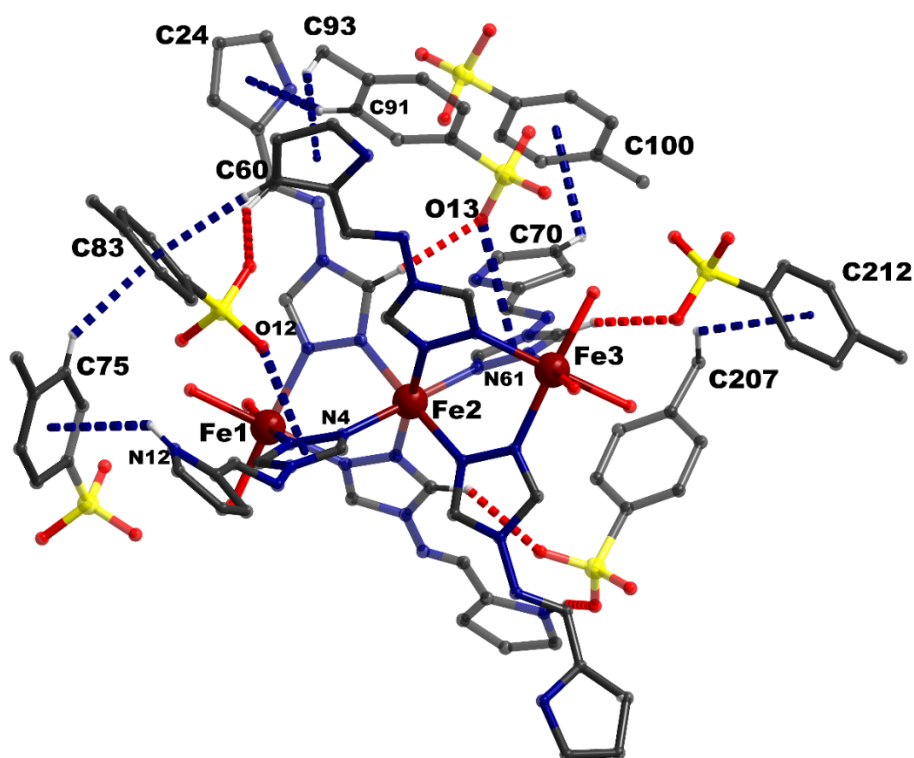


Figure 3.6.: The different intramolecular interaction found in the trimer units. The red dashed lines represent H-bonding, while the blue dashed lines represent $\pi\cdots\pi$ stacking.

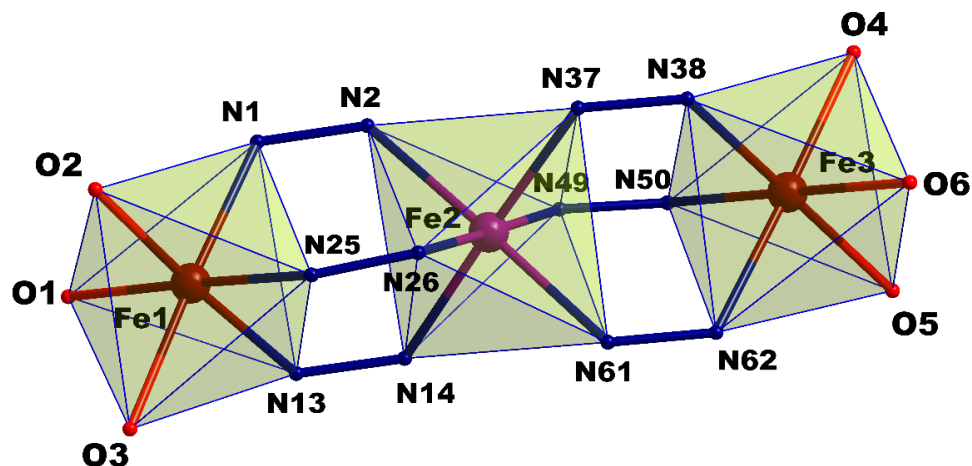


Figure 3.7.: Labeled core of the linear trinuclear complex. Iron(II) sites (spheres) are coloured differently to distinguish the spin state. (high spin (HS): red, low spin (LS): purple)

According to the ligand-field theory, the total ligand-field strength is larger for the central metal centre (coordinated by six triazole N atoms) than for the peripheral ions (surrounded by three triazole N and three O atoms from water). Considering the coordination environment among the three crystallographically unique iron(II) ions, only the central one (Fe2) is in the expected coordination environment for SCO to occur. According to the magnetic susceptibility measurement, the spin transition between the central Fe^{II} sites happens between 150 K ~ 95 K with $T_{1/2}$ around 120 K (details in the magnetic part). The crystal structure determination was conducted at 173 K, right in the beginning of the spin transition. While still, significant differences were observed between the central Fe and the peripheral ones. The examination of the Fe2–N distances reveal bond lengths of approximately 2.08 Å (Table S3.1) which are consistent with this site being in the middle of LS and HS state at this temperature (Figure 3.7). The Fe2–N and Fe3–N bond distances of approximately 2.16 Å are consistent with a HS state as expected for this coordination environment. (Table S3.1, Figure 3.7) In addition, numerous of intra- and inter-molecular interactions involving the sulfonate oxygen atoms of the free *p*-tolylsulfonate anions lead to the final crystal packing. These supramolecular interactions explains the unusual sharp transition found in the rather bulky π -rich ligand system. ^[7b] A comprehensive list of all the interactions is shown in Table S3.3.

3.4.2 FT-IR spectroscopy

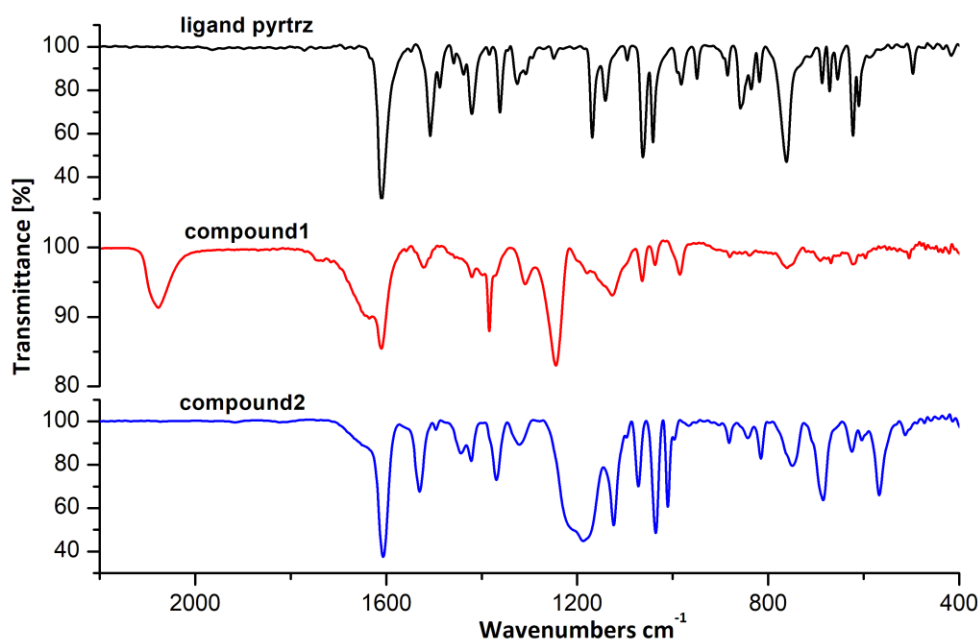


Figure 3.8.: The FT-IR spectra of ligand pytrz and compounds **5**, **6**.

The FT-IR spectra of compounds **5** and **6** indicate that the ligand pytrz almost exhibit the similar vibration to that in the neat form pytrz. As shown in Figure 3.8, the spectra of the two compounds are very similar and dominated by the spectral characteristics of the Schiff base ligand. However, a careful inspection can allow the assignment of significant changes due to the coordination of the complex. The vibration frequencies of the aromatic groups ($C_{ar}-C_{ar}$ and $C_{ar}=N$) can be found between 1310 cm^{-1} and 1610 cm^{-1} in both compounds and the free ligand. The peak at 1508 (s, pytrz), 1522 (m, **C5**) and 1529 (s, **C6**) cm^{-1} can be assigned to the characteristic ω -triazole ring vibration. The $\sim 15\text{ cm}^{-1}$ hypsochromic shifts between the compounds and the free ligand indicates the coordination of nitrogen atoms to the metal centers. ^[23] Additionally, the peaks at 1169 (s), 1062 (vs), and 762 (vs) cm^{-1} can be assigned to the C-H in-plane or out-of-plane bend ring breathing, and ring deformation absorptions. The characteristic azomethine (HC=N) stretching ^[24] around 1635 cm^{-1} in the ligand somehow showed as very faint peak. ^[25] The spectrum of **C6** showed strong C=N stretching at 2078 cm^{-1} suggesting the presence of the thiocyanate in the compounds. The 28 cm^{-1} hypsochromic shift compared to the spectrum of KNCS (2050 cm^{-1}) indicates the fact that SCN is coordinated with Fe^{II} via the nitrogen atoms. ^[26] In addition, the spectrum of **C5** showed signature bands for the *p*-toluenesulfonate counterions: The band at 1446 cm^{-1} could be ascribed to the $-CH_3$ vibrations of the anion, and the bands at 1035 , 1010 cm^{-1} may be assigned to the internal vibrations of the $CH_3C_6H_4$ parts. ^[27] While the broad

band at 1189 cm⁻¹ and sharp one at 1125 cm⁻¹ are assigned to vas(-SO₃⁻) and vas(-SO₃⁻) vibrations, respectively.

3.4.3 Magnetic susceptibility and Mössbauer Spectroscopy

As shown in figure 3.9, the magnetic susceptibility data of compound **5** has been recorded in the temperature range 300–2 K. The $\chi_M T$ value of 6.55 cm³·K·mol⁻¹ (**C5**) at 300 K can be ascribed to the corresponding two high spin Fe(II) ions. This value remains almost constant at 6.55 ~ 6.27 cm³·K·mol⁻¹ for compound **5** from 300 K down to 140 K; below this temperature, it starts to decrease more and more abruptly to reach a final value of 0.88 cm³·K·mol⁻¹ (2 K). This temperature dependent behavior indicates typical antiferromagnetic magnetic coupling between two Fe(II) ions in the high spin state.

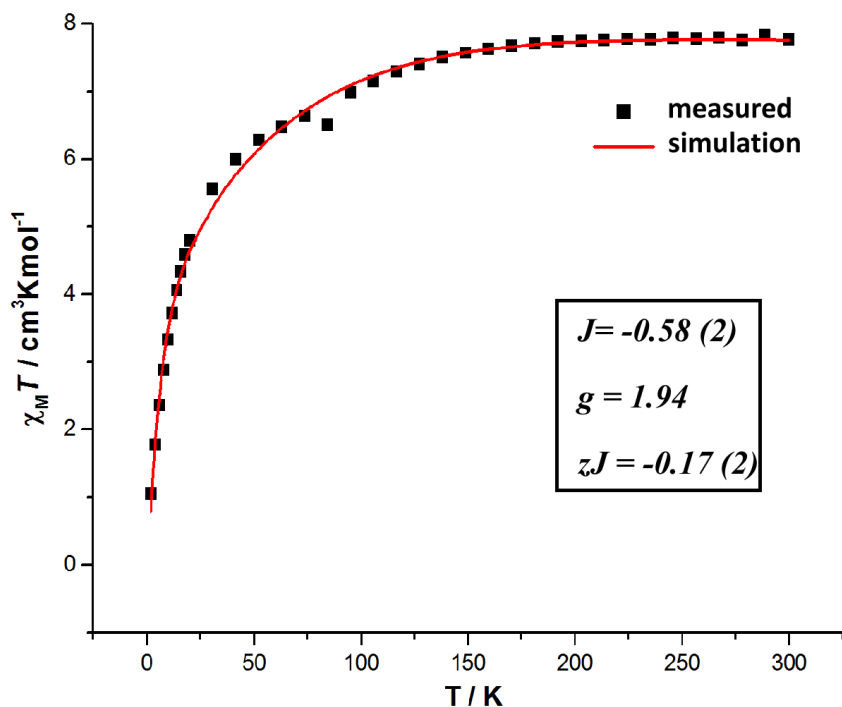


Figure 3.9.: The temperature-dependent magnetic susceptibility for compound **5** (the solid line represents the best fit curve).

To evaluate the antiferromagnetic coupling through the triple *N1,N2*-triazole bridge in the dinuclear complex, the magnetic data are simulated with PHI [28] program over the entire temperature range. Considering the multiple supramolecular interactions found between the adjacent dimer molecules. The intermolecular interaction parameter zJ was implemented with the fitting progress. The best fitting result gives us the value $g = 1.94$, $zJ = -0.17(2)$ cm⁻¹ and coupling constants $J = -0.58(2)$ cm⁻¹. (Figure 3.9) The result suggests that the antiferromagnetic coupling between the two adjacent Fe^{II} centers is weak, and the

supramolecular interactions found in the crystal lattice was found assisting for the antiferromagnetic coupling.

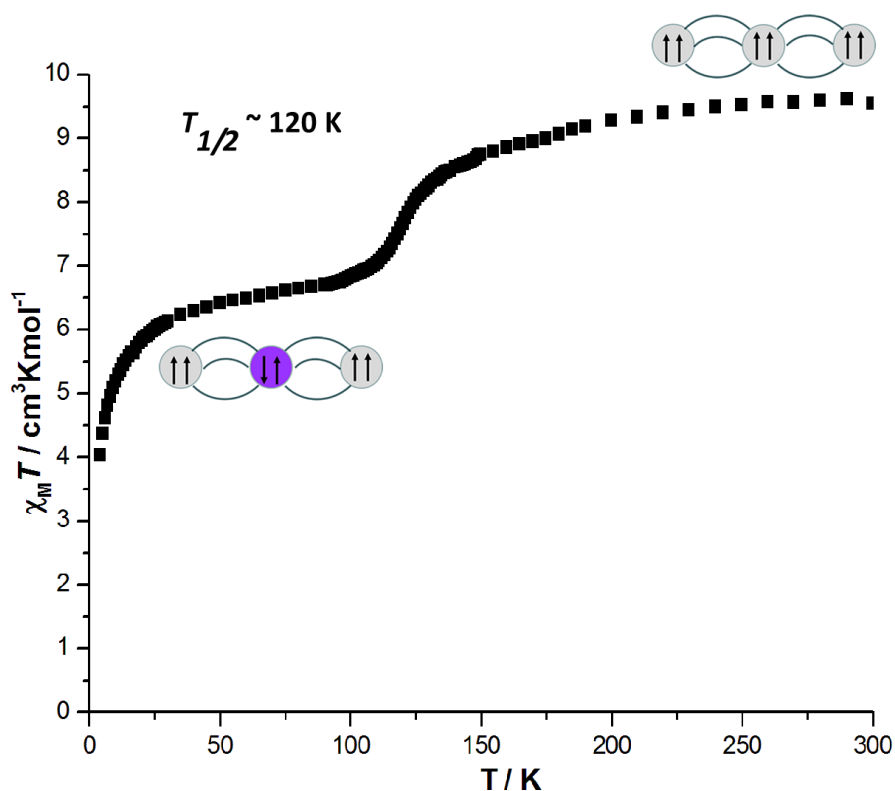


Figure 3.10. The temperature-dependent magnetic susceptibility (χ_{MT} v.s. T) for compound **6**.

Temperature dependent magnetic susceptibility measurements on a bulk crystalline sample of compound **6** was also made from 300 K to 4 K range. The data revealed an abrupt one-step SCO (Figure 3.10). At 300 K, the χ_{MT} values of 9.63 cm K mol⁻¹ are in agreement with all Fe(II) sites being in the HS state per trinuclear unit. This value remains approximately constant until 150 K where the decrease in χ_{MT} values became abruptly all the way down to 6.75 cm·K mol⁻¹ by 95 K. The process indicates of a sharp SCO transition of one-third of the Fe(II) sites to the LS state with a $T_{1/2}$ around 120K. No thermal hysteresis was observed with heating process.

In order to understand the details of SCO process of compound **6**, temperature dependent Mössbauer spectroscopy was performed on a bulk crystalline sample (Figure 3.11). Spectra were recorded at 77 K, 107 K, 137 K, 167 K and 197 K. The spectra have been analyzed with in total 3 different subspectra. The full parameters (δ : isomer shift, Δ_{EQ} : quadrupole splitting, Γ : line width at half maximum, A: relative spectral area) are listed in Table 3.2.

Chapter 3 SCO Investigation of Two Triple N1,N2-Triazole Bridged Fe^{II} Complexes based on Prytrz

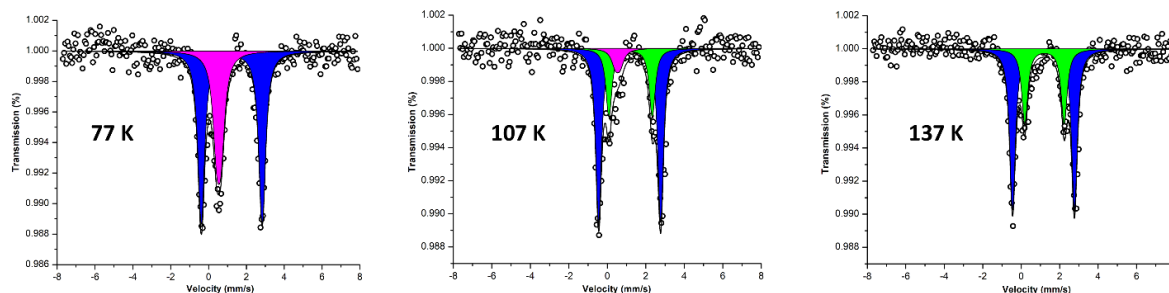


Figure 3.11. Mössbauer spectra of compound 6 at 77 K, 107 K and 137 K. The open circles are the experimental data, the black solid line shows a superposition of the following components: subspectrum 1 (purple) represents the [LS] fraction of central iron (Fe2), subspectrum 2 (blue) is due to the [HS] fraction of terminal iron (Fe1 and Fe3), and subspectrum 3 (green) is the [HS] fraction of central iron (Fe2). Parameters see Table 3.2.

Table 3.2. ⁵⁷Fe Mössbauer parameters of compound 6 at different temperatures.

T = 77 K			
Subspectra	HS Fe1 and Fe3	LS Fe2	HS Fe2 and Fe3
δ [mm/s]	1.22 ± 0.02	0.54 ± 0.04	-
ΔE_0 [mm/s]	3.22 ± 0.02	0.24 ± 0.03	-
Γ [mm/s]	0.41 ± 0.03	0.47 ± 0.03	-
Rel. Area [%]	66.00 ± 1.00	34.00 ± 1.00	0
T = 107 K			
δ [mm/s]	1.16 ± 0.03	0.54 ± 0.05	1.21 ± 0.04
ΔE_0 [mm/s]	3.22 ± 0.04	0.24 ± 0.10	2.25 ± 0.02
Γ [mm/s]	0.34 ± 0.02	0.47 ± 0.07	0.36 ± 0.04
Rel. Area [%]	65.00 ± 1.00	8.00 ± 2.00	27.00 ± 1.00
T = 137 K			
δ [mm/s]	1.16 ± 0.03	-	1.21 ± 0.03
ΔE_0 [mm/s]	3.22 ± 0.04	-	2.05 ± 0.04
Γ [mm/s]	0.34 ± 0.02	-	0.44 ± 0.03
Rel. Area [%]	65.00 ± 2.00	-	35.00 ± 1.00
T = 167 K			
δ [mm/s]	1.15 ± 0.02	-	1.21 ± 0.04
ΔE_0 [mm/s]	3.16 ± 0.02	-	1.93 ± 0.03
Γ [mm/s]	0.34 ± 0.01	-	0.36 ± 0.05
Rel. Area [%]	64.00 ± 2.00	-	36.00 ± 2.00
T = 197 K			
δ [mm/s]	1.15 ± 0.04	-	1.21 ± 0.03
ΔE_0 [mm/s]	3.16 ± 0.04	-	1.87 ± 0.04
Γ [mm/s]	0.34 ± 0.02	-	0.36 ± 0.01
Rel. Area [%]	67.00 ± 1.00	-	33.00 ± 1.00

As clearly shown in Figure 3.11 and Table 3.2, the Mössbauer spectrum at 77 K shows two distinctly different doublets. Doublet 1 (purple) has $\delta = 0.54 \text{ mm}\cdot\text{s}^{-1}$ and $\Delta E_Q = 0.24 \text{ mm}\cdot\text{s}^{-1}$. Such a low quadrupole splitting is characteristic for a LS iron(II) embedded in an octahedral ligand field. Doublet 2 (blue) has $\delta = 1.22 \text{ mm}\cdot\text{s}^{-1}$ and $\Delta E_Q = 3.22 \text{ mm}\cdot\text{s}^{-1}$, values which are

typical fingerprints of a high-spin iron(II) species in an octahedral N/O ligand environment. [29] The relative intensity ratio of 1:2 between these two doublets indicates that the central iron(II) is in its low spin state, i.e., for complex 6, a HS-LS-HS state is stabilized at 77 K, which is in accordance with the magnetic susceptibility results discussed above. With increasing temperature, at 107 K, the intensity of doublet 1 representing the central LS iron(II) decreases while a new doublet 3 (green) emerges which has $\delta > 1 \text{ mm}\cdot\text{s}^{-1}$, an isomer shift typical for Fe(II) HS. The SCO of the central Fe is perfectly reflected in the Mössbauer spectra displayed at this temperature (at 107 K), that is, the intensity increasing of the green doublet 3 (central iron HS) is at the expense of the decreasing intensity of the purple doublet 1 (central iron LS). It is worth noticing that the intensity of LS and HS species here does not reflect the actual concentrations of the different iron sites because of the different Lamb-Mössbauer factors for the LS and HS state. [14a,30] Nevertheless, the total intensity sum of green doublet 3 and purple doublet 1 still keeps a 1:2 ratio to the blue doublet 2 (external iron HS), confirming the SCO process undergoing on the central iron center only. At 137 K, doublet 1 vanishes, and the approximate 2:1 relative area ratio of the HS doublet 2 and the HS doublet 3 reflects the SCO transition of complex 6 from a HS-LS-HS state to a HS-HS-HS state. Further measurements of higher temperature (167 K and 197 K) reveal good agreement with the steady HS and LS ratio of 1:2, which confirms the stability of HS-HS-HS state after the spin transition. Additionally, the relative intensity ratio of 3:1 between the green doublet 3 and purple doublet 1 at 107 K gives us the hint of the transition temperature being around 120 K. As the spin transition in compound 6 is abrupt, with the help of the derivative plot of the χ_{MT} vs. T curve (Figure S1), a spin transition temperature of 120 K is also easily spotted. In conclusion, the temperature dependent Mössbauer spectra displayed in Figure 11 clearly shows that the central iron(II) in complex 6 is able to undergo SCO with $T_{1/2}$ around 120 K, which is in good accordance with the magnetic susceptibility data shown in Figure 3.10.

The abrupt SCO behavior of this compound suggests medium strong cooperativity between molecules in the lattice, which is in accordance with the structural analysis. The multiple intra- and inter-molecular H-bonding interactions found in the crystal lattice explain the strong cooperativity between the active Fe(II) centers. Interestingly, even though studies have shown that ligands with bulky aromatic substituents and aromatic anions might have a “dilute or separation effect” on the overall cooperativity of the SCO compounds. [13a,14b] The abrupt transition observed here stands for an example with the supramolecular interactions overcome the “aromatic dilute effect”. A further study can be followed by synthesis of

similar compounds with different degree of aromatic substitutions, either from the triazole ligands or from the counter anions. Furthermore, the relatively low transition temperature (120 K) for this compound is consistent with other similar discrete molecular species containing bulky aromatic 1,2,4-triazole ligands. [13,14]

3.5 Conclusion

The work presented here shows two new examples of discrete triazole-based multi-nuclear Fe^{II} complexes. Based on the ligand 4-((1*H*-pyrrol-2-yl)methylene-amino)-4*H*-1,2,4-triazole (pyrtrz), a group of two crystalline coordination Fe^{II} complexes, i.e., one binuclear $[Fe^{II}_2(pyrtrz)_5(SCN)_4] \cdot 7H_2O$ (C5) and one trinuclear $[Fe^{II}_3(pyrtrz)_6(TsO)_6] \cdot 10H_2O \cdot 2CH_3OH$ (C6), has been synthesized and magnetically characterized. An abrupt spin transition ($T_{1/2} = 120$ K) was found in compound **2**, which was confirmed and explored by the magnetic susceptibility, Mössbauer spectra and structural measurements. The binuclear complex **5** did not show the spin transition, while a weak antiferromagnetic exchange coupling inside the dimer molecules was detected, assisted by the supramolecular interactions in the crystal lattice. The trimer complex described here represents the first example of an abrupt transition found with the accompanying of tolylsulfonate anion. This work suggests that apart from the inefficient communication the bulky aromatic groups might bring into the SCO system, the multiple supramolecular interaction formed can sometimes also lead to a good cooperativity between the active metal centers. The future work might need to focus on the isolation of more similar compounds with different degree of potential supramolecular interactions to examine their effect more quantitatively.

3.6 Acknowledgement

We kindly thank Dr. Dieter Schollmeyer and Regine Jung-Pothmann (*Johannes Gutenberg University, Mainz*) for collecting the crystal structural data. A.M.L. acknowledges the financial support from graduate school MAINZ and is a recipient of a DFG fellowship through the Excellence Initiative by the Graduate School Materials Science in Mainz (DFG/GSC 266).

3.7 Reference

- [1] M. A. Halcrow, *Coord. Chem. Rev.*, **2009**, 253, 2493-2514.
- [2] H. L. Feltham, A. S. Barltrop, S. Brooker, *Coord. Chem. Rev.*, **2017**, 344, 26-53.
- [3] a) C. F. Herold, L. M. Carrella, E. Rentschler, *Eur. J. Inorg. Chem.*, **2015**, 22, 3632-3636; b) C. Köhler, E. Rentschler, *Eur. J. Inorg. Chem.*, **2016**, 13-14, 1955-1960.
- [4] a) J. L. Wang, Q. Liu, Y. S. Meng, H. Zheng, H. L. Zhu, Q. Shi, T. Liu, *Inorg. Chem.*, **2013**, 56, 10674-10680; b) W. B. Chen, J. D. Leng, Z. Z. Wang, Y. C. Chen, Y. Miao, M. L. Tong, W. Dong, *Chem. Commun.*, **2017**, 53, 7820-7823; c) N. Pittala, F. Thétiot, C. Charles, S. Triki, K. Boukheddaden, G. Chastanet, M. Marchivie, *Chem. Commun.*, **2017**, 53, 8356-8359.
- [5] a) O. Kahn, M. C. Jay, *Science* **1998**, 279, 44-48; b) J.G. Haasnoot, *Coord. Chem. Rev.*, **2000**, 131, 200-201; c) O. Roubeau, *Chem. Eur. J.* **2012**, 18, 15230-15244.
- [6] a) A. Grosjean, N. Daro, B. Kauffmann, A. Kaiba, J.F. Létard, P. Guionneau, *Chem. Commun.*, **2011**, 47, 12382-12384; b) N. Pittala, F. Thétiot, S. Triki, K. Boukheddaden, G. Chastanet, M. Marchivie, *Chem. Mater.*, **2016**, 29, 490-494.
- [7] a) X. X. Wu, Y. Y. Wang, P. Yang, Y. Y. Xu, J. Z. Huo, B. Ding, Y. Wang, X. Wang, *Cryst. Growth Des.*, **2013**, 14, 477-490; b) Y. Garcia, F. Robert, A. D. Naik, G. Y. Zhou, B. Tinant, K. Robeyns, S. Michotte, L. Piraux, *J. Am. Chem. Soc.*, **2011**, 133, 15850-15853; c) H. Z. Scott, T. M. Ross, B. Moubaraki, K. S. Murray, S. M. Neville, *Eur. J. Inorg. Chem.*, **2013**, 803-812.
- [8] a) X. Cheng, Q. Yang, C. Gao, B. W. Wang, T. Shiga, H. Oshio, Z. M. Wang, S. Gao, *Dalton Trans.*, **2015**, 44, 11282-11285; b) A. Kolnaar, J. Jeroen, M. I. de Heer, H. Kooijman, A. L. Spek, G. Schmitt, V. Ksenofontov, P. Gülich, J. G. Haasnoot and J. Reedijk, *Eur. J. Inorg. Chem.*, **1999**, 881-886.
- [9] a) O. Roubeau, P. Gamez, S. J. Teat, *Eur. J. Inorg. Chem.*, **2013**, 934-942; b) B. Ding, Y. Y. Liu, Y. Wang, J. G. Ma, Z. Niu, W. Shi, P. Cheng, *Inorg. Chem. Commun.*, **2013**, 31, 44-48; c) G. Vos, R. A. De Graaff, J. G. Haasnoot, A. M. Van der Kraan, P. De Vaal, J. Reedijk, *Inorg. Chem.*, **1984**, 23, 2905-2910.
- [10] a) M. B. Bushuev, L. G. Lavrenova, Yu. G. Shvedenkov, A. V. Virovets, L. A. Sheludyakova and S. V. Larionov, *Russ. J. Inorg. Chem.*, **2007**, 52, 46-51; b) O. G. Shakirova, L. G. Lavrenova, Y. G. Shvedenkov, G. A. Berezovskii, D. Y. Naumanov, L. A. Sheludyakova, G. V. Dolgushin and S. V. Larionov, *Russ. J. Coord. Chem.*, **2004**, 30, 473-479.
- [11] a) Y. Garcia, P. Guionneau, G. Bravic, D. Chasseau, J. A. K. Howard, O. Kahn, V. Ksenofontov, S. Reiman and P. Gülich, *Eur. J. Inorg. Chem.*, **2000**, 1531-1538; b) G. Vos, R. A. Le Febre, R. A. G. de Graaff, J. G. Haasnoot and J. Reedijk, *J. Am. Chem. Soc.*, **1983**, 105, 1682-1683.
- [12] a) V. Gómez, J. Benet-Buchholz, E. Martin and J. R. Galan-Mascarós, *Chem. Eur. J.*, **2014**, 20, 5369-5379; b) V. Gómez, C. S. de Pipaón, P. Maldonado-Illescas, J. C. Waerenborgh, E. Martin, J. Benet-Buchholz and J. R. Galan-Mascarós, *J. Am. Chem. Soc.*, **2015**, 137, 11924-11927.
- [13] a) Y. M. Klein, N. F. Sciortino, C. E. Housecroft, C. J. Kepert, and S. M. Neville, *Magnetochemistry*, **2016**, 2-8; b) M. Thomann, O. Kahn, J. Guilhem and F. Varret, *Inorg. Chem.*, **1994**, 33, 6029-6037.
- [14] a) J. J. A. Kolnaar, G. van Dijk, H. Kooijman, A. L. Spek, V. Ksenofontov, P. Gülich, J. G. Haasnoot and J. Reedijk, *Inorg. Chem.*, **1997**, 36, 2433-2440; b) D. Savard, C. Cook, G. D. Enright, I. Korobkov, T. J. Burchell and M. Murugesu, *CrystEngComm*, **2011**, 13, 5190-5197.

Chapter 3 SCO Investigation of Two Triple N1,N2-Triazole Bridged Fe^{II} Complexes based on Prytrz

- [15] G.A. Bain, J.F. Berry, *J. Chem. Edu.* **2008**, *85*, p. 532.
- [16] *SMART 5.0 and SAINT 4.0 for Windows NT, Area Detector Control and Integration Software*, Bruker Analytical X-Ray Systems Inc., Madison, WI, 1998.
- [17] G. M. Sheldrick, *SADABS: Program for Empirical Absorption Correction of Area Detector Data*, University of Göttingen, Göttingen, Germany, 1996.
- [18] a) G. M. Sheldrick, *Acta Crystallogr.* **2015**, *C71*, 3–8; b) G. M. Sheldrick, *SHELXTL 5.1 for Windows NT: Structure Determination Software Programs*, Bruker Analytical X-ray Systems, Inc., Madison, WI, 1997.
- [19] O. V. Dolomanov, L. J. Bourhis, R. J. Gildea, J. A. K. Howard, H. J. Puschmann, *Appl. Crystallogr.* **2009**, *42*, 339–341.
- [20] *Diamond - Crystal and Molecular Structure Visualization Crystal Impact* - Dr. H. Putz & Dr. K. Brandenburg GbR, Kreuzherrenstr. 102, 53227 Bonn, Germany.
- [21] a) T. Khan, R. Yadav, *Heterocycl. lett.* **2016**, *6*, 757–766; b) A. Kwiecień, M. Barys, Z. Ciunik, *Molecules* **2014**, *19*, 11160–11177.
- [22] P. Chakraborty, A. Tissot, L. Peterhans, L. Guenee, C. Besnard, P. Pattison, A. Hauser, *Phys. Rev. B* **2013**, *87*, 2143.
- [23] E. Borello, A. Zecchina, *Spectrochimica Acta*, **1963**, *19*, 1703–1715.
- [24] Y. Prashanthi, S. Raj, *Journal of Scientific Research*, **2010**, *2*, 114–126.
- [25] S. H. Sumra, Z. H. Chohan, *Spectrochimica Acta A: Molecular and Biomolecular Spectroscopy*, **2012**, *98*, 53–61.
- [26] A. A. Salaudeen, C. A. Kilner, M. A. Halcrow, *Polyhedron*, **2008**, *12*, 2569–2576; K. Nakamoto, *Infrared and Raman Spectra of Inorganic and Coordination Compounds Part B (5th ed.)* Wiley Interscience, New York, **1997**, 116.
- [27] A. L. Arduini, M. Garnett, R. C. Thompson, T. C. T. Wong, *Can. J. Chem.* **1975**, *53*, 3812–3819.
- [28] N. F. Chilton, R. P. Anderson, L. D. Turner, A. Soncini, K. S. Murray, *J. Comput. Chem.* **2013**, *34*, 1164.
- [29] V. Schünemann, H. Winkler, *Rep. Prog. Phys.* **2000**, *63*, 263–353.
- [30] a) J. Jung, H. Spiering, Z. Yu, P. Gülich, *Hyperfine Interact.* **1995**, *95*, 107–128; b) A. Kolnaar, J. Jeroen, M. I. de Heer, H. Kooijman, A. L. Spek, G. Schmitt, V. Ksenofontov, P. Gülich, J. G. Haasnoot, J. Reedijk, *Eur. J. Inorg. Chem.* **1999**, *5*, 881–886.

3.8 Supplementary Information

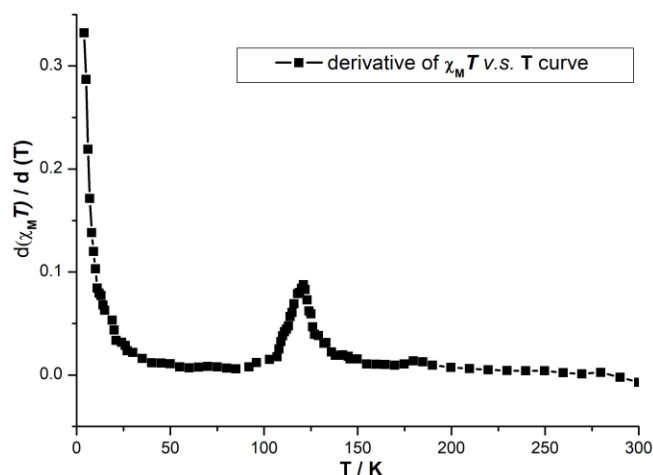


Figure S1. A derivative plot of the $\chi_M T$ v.s. T curve for compound **6**.

Table S3.1 Selected bond lengths [\AA] and angles [$^\circ$] for **C5** and **C6**.

Compound 5					
Fe(1)-N(1)	2.142(5)	Fe(1)-N(28)	2.095(11)	Fe(2)-N(12)	2.201(9)
Fe(1)-N(7)	2.142(5)	Fe(1)-N(29)	2.128(11)	Fe(2)-N(16)	2.108(6)
Fe(1)-N(11)	2.172(9)	Fe(2)-N(2)	2.161(5)	Fe(2)-N(26)	2.090(10)
Fe(1)-N(22)	2.163(6)	Fe(2)-N(6)	2.134(5)	Fe(2)-N(27)	2.094(11)
N(1)-Fe(1)-N(7)	87.2(3)	N(28)-Fe(1)-N(29)	92.6(4)	N(16)-Fe(2)-N(12)	88.5(3)
N(1)-Fe(1)-N(11)	86.7(3)	N(29)-Fe(1)-N(1)	90.0(3)	N(26)-Fe(2)-N(2)	176.9(4)
N(1)-Fe(1)-N(22)	86.9(3)	N(29)-Fe(1)-N(7)	90.3(3)	N(26)-Fe(2)-N(6)	89.9(4)
N(7)-Fe(1)-N(11)	90.9(3)	N(29)-Fe(1)-N(11)	176.4(4)	N(26)-Fe(2)-N(12)	90.8(4)
N(7)-Fe(1)-N(22)	173.8(3)	N(29)-Fe(1)-N(22)	87.8(4)	N(26)-Fe(2)-N(16)	86.7(4)
N(22)-Fe(1)-N(11)	90.6(3)	N(2)-Fe(2)-N(12)	86.4(3)	N(26)-Fe(2)-N(27)	92.5(4)
N(28)-Fe(1)-N(1)	177.0(3)	N(6)-Fe(2)-N(2)	88.6(3)	N(27)-Fe(2)-N(2)	90.3(4)
N(28)-Fe(1)-N(7)	91.2(3)	N(6)-Fe(2)-N(12)	87.9(3)	N(27)-Fe(2)-N(6)	92.4(3)
N(28)-Fe(1)-N(11)	90.8(4)	N(16)-Fe(2)-N(2)	94.6(3)	N(27)-Fe(2)-N(12)	176.7(4)
N(28)-Fe(1)-N(22)	94.8(3)	N(16)-Fe(2)-N(6)	175.0(3)	N(27)-Fe(2)-N(16)	91.4(4)
C(36)-N(26)-Fe(2)	161.0(14)	C(38)-N(28)-Fe(1)	174.1(10)	N(27)-C(37)-S(2)	178.7(13)
C(37)-N(27)-Fe(2)	172.9(11)	N(26)-C(36)-S(1)	174.7(17)	N(28)-C(38)-S(3)	179.0(12)
Compound 6					
Fe(1)-O(1)	2.149(3)	Fe(2)-N(2)	2.093(4)	Fe(3)-O(4)	2.118(5)
Fe(1)-O(2)	2.069(4)	Fe(2)-N(14)	2.075(5)	Fe(3)-O(5)	2.124(5)
Fe(1)-O(3)	2.133(4)	Fe(2)-N(26)	2.094(5)	Fe(3)-O(6)	2.159(5)
Fe(1)-N(1)	2.173(5)	Fe(2)-N(37)	2.081(5)	Fe(3)-N(38)	2.134(5)
Fe(1)-N(13)	2.157(5)	Fe(2)-N(49)	2.130(5)	Fe(3)-N(50)	2.156(5)
Fe(1)-N(25)	2.160(4)	Fe(2)-N(61)	2.108(6)	Fe(3)-N(62)	2.173(6)
O(4)-Fe(3)-O(5)	91.3(2)	O(5)-Fe(3)-O(6)	88.0(2)	N(38)-Fe(3)-O(6)	88.4(2)
O(4)-Fe(3)-O(6)	87.7(3)	O(5)-Fe(3)-N(38)	175.7(2)	N(38)-Fe(3)-N(50)	92.3(2)
O(4)-Fe(3)-N(38)	91.0(2)	O(5)-Fe(3)-N(50)	91.23(19)	N(38)-Fe(3)-N(62)	87.1(2)
O(4)-Fe(3)-N(50)	91.9(2)	O(5)-Fe(3)-N(62)	90.6(2)	N(50)-Fe(3)-O(6)	179.2(2)
O(4)-Fe(3)-N(62)	178.1(2)	O(6)-Fe(3)-N(62)	92.5(2)	N(50)-Fe(3)-N(62)	87.87(19)

**Chapter 3 SCO Investigation of Two Triple N1,N2-Triazole
Bridged Fe^{II} Complexes based on Prytrz**

Table S3.2. Geometry of intra-molecular C–H/O ... π (pyrrole/triazole) in compound **6**.

Atom (X)	centroid	X...centroid distance/Å	ϕ /deg ^a
C70b–H70b	C94 ring	2.9070(2)	70.509(5)
O13	N61 ring	3.462(5)	79.035(3)
O12 ring	N1 ring	2.992(6)	78.413(3)
C75–H75	C80 ring	2.748(2)	85.609(4)
C60–H60	C80 ring	2.630(2)	86.995(3)
C93–H93a	C60 ring	2.813(2)	89.298(5)

^a Angle of the X... π axis to the plane of the centroid cycle contacted.

Table S3.3. Intra- and inter-molecular Hydrogen-bonding interactions in compound **6**.

D–H	A	H...A (Å)	D...A (Å)	\angle D–H...A (°)	Symmetry codes of A
C27–H27	O19b	2.412	3.231(6)	144(2)	x, y, z
N36–H36	O21b	1.913	2.726(7)	153(1)	x, y, z
C19–H19	O11	2.442	3.169(9)	133(3)	x, y, z
C15–H15	O13	2.267	3.199(7)	166(2)	x, y, z
C63–H63	O23	2.523	3.342(5)	144(3)	x, y, z
N48–H48	O29	1.938	2.799(8)	167(2)	x, y, z
N72–H72	O32	1.914	2.769(6)	166(2)	x, y, z
C27–H27	O20	2.101	3.051(2)	173(2)	x, y, z
C33b–H33a	O21	1.983	2.847(3)	150(3)	x, y, z
C53–H53	O12	2.292	3.161(5)	151(5)	x, y, z
N21–H21	O26	1.932	2.807(9)	173(2)	$-x + 1, y + 0.5, -z + 0.5$
N57–H57	O29b	2.233	2.962(7)	140(5)	$-x, y + 0.5, -z + 0.5$
N72b–H72b	O7	1.755	2.591(3)	157(2)	$-x + 1, y + 0.5, -z + 0.5$
C3–H3	O22	2.193	3.083(2)	156(5)	$-x, y - 0.5, -z + 0.5$
C9–H9	O28a	1.975	2.905(6)	166(2)	$-x + 1, y - 0.5, -z + 0.5$
C17–H17	O17	2.156	2.994(7)	147(3)	$-x + 1, y - 0.5, -z + 0.5$
C39–H39	O14	2.241	3.082(9)	147(5)	$-x, y - 0.5, -z + 0.5$
C41–H41	O18b	2.071	2.991(8)	162(2)	$x, y - 1, z$

Chapter 4 Three Iron Polynuclear Complexes: Magnetic Properties from a Dimer to 1D chain to 3D framework

This chapter covers the summary results of three iron polynuclear complexes based on ligand 4 (toltrz) and ligand 3 (5-imztrz), which is manuscripted to the journal submission of *CrystEngComm*. Manuscript detailing will be presented in the following:

1,2,4-triazole Schiff base directed synthesis of Iron Polynuclear Complexes: investigating the magnetic properties from a dimer to 1D chain to 3D framework

Ai-Min Li^{a,b} and Eva Rentschler^{a*}

^a Institute of Inorganic and Analytical Chemistry, Johannes Gutenberg University Mainz, Duesbergweg 10-14, 55128 Mainz, Germany

rentschler@uni-mainz.de

^b Graduate School Materials Science in Mainz, Staudingerweg 9, D-55128 Mainz, Germany

KEYWORDS Polynuclear / Iron / 1,2,4-triazole / Schiff bases

4.1 Abstract

Based on two functionalized Schiff base ligands 4-(1*H*-imidazol-5-ylmethylene-amino)-4*H*-1,2,4-triazole (imztrz) and 4-(*p*-tolylidene-amino)-4*H*-1,2,4-triazole (toltrz), a series of three polynuclear triazole based Fe compounds has been prepared. Compounds **7** and **8** are oxalate bridged Fe^{II} complex with **C7** showing a linear 1D chain and **C8** exhibiting a zigzag chain based 3D interpenetrated framework. Both structures show rather big void in the 3D architecture (~ 15% of the crystal volume). Compound **9** is a binuclear Fe^{III} complex, which is bridged by two citrate ligands to form a face-shared centrosymmetric structure. Magnetic susceptibility measurements indicate that all three compounds show weak antiferromagnetic exchange interaction between the adjacent Fe centers.

4.2 Introduction

In recent years, interest has grown among chemists and physics to design and build up extended 3*d* metal networks based on small chelating anionic ligands such as oxalate and citrate. Particularly, in the field of magnetic materials, ^[1] oxalato-bridged complexes have been intensively studied because of their versatile abilities to mediate magnetic coupling between the paramagnetic metal centers with a rather large separation (~5 Å). ^[2] Numerous

Chapter 4 Three Iron Polynuclear Complexes: Magnetic Properties from a Dimer to 1D chain to 3D framework

of polynuclear chains and networks have been reported with regard to this aspect. [3-7] The binuclear iron system was first studied long ago by the pioneers Earnshaw, Lewis and Murray, [8] while there are only few examples with dimeric Fe^{III} citrate complexes reported until now. [9] Success in characterization of polynuclear compounds has been achieved, by the combination of oxalate with 4, 4'-bipyridine (bpy) [7a] and its derivatives like 2, 2'-bipyrimidine (bpym) [6b] as chelating bridging ligands, which resulted in chain or layered compounds. Compared to oxalate bridged metal complexes of Cu/Cr/Ni, the number of reports on characteristics for oxalate-bridged Fe^{II} complexes is still limited. Similar to bpym/bpy derivatives, 1,2,4-triazole based ligand has been a useful building block for the construction of metal-organic co-ordination frameworks since years, especially on the synthesis of spin crossover molecules. A number of polymeric compounds bridged by the μ_2 -N1,N2-triazoles has been isolated and reported with interesting magnetic properties. [10] It is well known that the 1,2,4-triazole ligand can also adopt the monodentate mode when coordinating to the metal center, [11] while only very recently, the feature of this type of ligand has been well-developed to construct higher dimensional magnetic based materials. [10c, 12] However, such coordination mode blended with oxalate / citrate for constructing metal coordination compounds have been rarely explored. [13] Incidentally, in the preparation of triazole based polynuclear complexes, for the first time, we isolated two Fe^{II} compounds with the interest of co-ordination between oxalate and monodentate triazole ligands and one citrate Fe^{III} compound with the triazole ligand acting as a charge balance. Herein, we report the synthesis, structure, and magnetic properties of a series of three polynuclear Fe complexes based on oxalate/citrate and Schiff base modified triazole ligands, *i.e.*, 4-(*p*-tolylidene-amino)-4H-1,2,4-triazole (toltrz) and 4-(1*H*-imidazol-5-ylmethylene-amino)-4H-1,2,4-triazole (5-imztrz) : [Fe^{II}(toltrz)₂(C₂O₄)]·5H₂O (**7**), [Fe^{II}(5-imztrz)(C₂O₄)]·2H₂O (**8**) and [Fe^{III}(cit) (H₂O)](5-imztrzH)·3H₂O (**9**). Single X-ray diffraction and magnetic measurements reveal that compounds **7** and **8** are oxalate bridged Fe^{II} complexes with porous character showing different antiferromagnetic interactions. Both structures differ significantly from the bpy/bpym structures, [6b, 7a] while compound **9** is a citrate bridged Fe^{III} face-shared dimer exhibiting a weak antiferromagnetic interactions, which can be compared with the reported similar analogues. [9a-c]

4.3 Experimental Section

General Methods and Materials.

All chemicals and solvents were purchased from the commercial companies (Alfa Aesar, Sigma–Aldrich and Acros Organics) and used without further purification. The magnetic measurement were proceeded with a Quantum Design SQUID magnetometer MPMS XL-7 over the temperature range of 2-300 K with an applied field of 0.1T. Samples for the magnetic measurement were prepared in gelatin capsules and held in plastic straws for insertion into the magnetometer. The obtained magnetic susceptibility values were corrected with diamagnetic susceptibility according to the Pascal's constants. ^[14] Elemental analysis (C, H, N) was measured in the microanalytical laboratories at Johannes Gutenberg University Mainz. Infrared spectra (FT-IR) were recorded as potassium bromide pellets in the range from 4000 to 400 cm⁻¹ with a JASCO FT/IR-4200.

Single Crystal X-ray Diffraction

Single-crystal X-ray diffraction data for all the three compounds were collected on a Bruker Smart APEX II CCD diffractometer. The diffractometer was operated at 45 kV and 35 mA with Mo K α radiation ($\lambda = 0.71073 \text{ \AA}$), and a nitrogen cold stream was applied to aquire the data collection environment of 173(2) K. Each data reduction was performed using the SMART and SAINT software ^[15] and an empirical absorption correction was applied using the SADABS program. ^[16] All the three structures were solved by direct methods and refined by full-matrix least-squares on F^2 using the SHELXTL program package, ^[17] and the Olex2 program. ^[18] The ordered non-hydrogen atoms in each structure were refined with anisotropic displacement parameters, while the hydrogen atoms were placed in idealized positions and allowed to ride on their parent atoms. The lattice water molecules were refined with anisotropic displacement parameters in all three structures, and all positions of the hydrogen atoms of the water molecules in **C8** and **C9** were obtained from Fourier-difference maps, while in compound **7**, the hydrogen atoms were not defined. The crystallographic data and refinement parameters of **C7**, **C8** and **C9** are listed in Table 4.1. CCDC numbers 1815493-1815495 contain the supplementary crystal data of the compounds: 1815493 (**C7**), 185494 (**C8**) and 1815495 (**C9**), which can be obtained free of charge from The Cambridge Crystallographic Data Centre via www.ccdc.cam.ac.uk/data_request/cif. All structure figures are generated with DIAMOND-3. ^[19]

Syntheses

Synthesis of the ligand

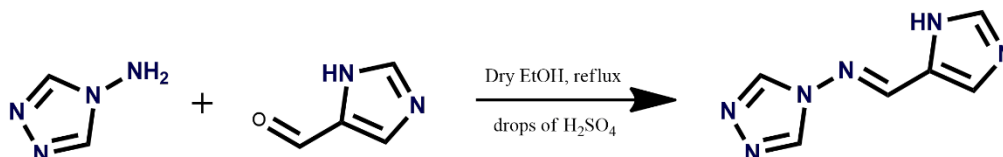


Figure 4.1.: Synthetic scheme to prepare the 5-imztrz ligand.

The ligand 4-(1H-imidazol-5-ylmethylene-amino)-4H-1,2,4-triazole (5-imztrz) (Figure 4.1) was prepared by the by the condensation reaction of a modified literature procedure. [20] First dissolved 4-amino-1,2,4-triazole (1.68 g, 0.02 mol, 1.0 eq.) in ethanol, heated the reaction solution to boiling (80 °C). Then, the second reactant 1H-Imidazole-4-carbaldehyde (2.11 g, 0.022 mol, 1.1 eq.) dissolved in ethanol was added dropwise through a dropping funnel. After the addition, few drops of catalytic H₂SO₄ was added. The reaction mixture was then kept for refluxing for another 10 h. When cooled down to r.t., the excess of the solvent was removed by rotary evaporator at 35 °C. The product such obtained was washed with small amount of cold ethanol, diethyl ether and then dried in the desiccator with phosphorus pentoxide as dry agent. Light-yellow powder was obtained. Yield: 2.98 g (91.89%), m.p.253.5–265.7 °C; IR (KBr) 3116 cm⁻¹ (Ar, CH-strech.); 1625 cm⁻¹ (H–C=N); 1504 cm⁻¹, 1187 cm⁻¹, 1065 cm⁻¹, 857 cm⁻¹, 620 cm⁻¹ (C=N, C=C). ¹HNMR (Figure 9.2) (*d*⁶-DMSO): 9.07 (s,2H, triazole), 8.92 (s, 1H, H–C=N), 7.91 (s, 1H, imidazole ring), 7.79 (s, 1H, imidazole ring).

The ligand 4-(p-tolylidene-amino)-4H-1,2,4-triazole (toltrz) was prepared in the similar manner, except changing of 1H-Imidazole-4-carbaldehyde (2.11 g, 0.022 mol) to 4-methylbenzaldehyde (2.65 g, 0.022 mol). A white powder with intense smelling was obtained. Yield: 3.53 g (94.85%), m.p.137.5–157.8 °C; IR (KBr): 1608 cm⁻¹ (H–C=N), 3101 cm⁻¹ (Ar, CH-strech); 817 cm⁻¹, 2918 cm⁻¹ (Ar-CH₃). ¹HNMR (Figure 9.4) (CD₃OD): 7.35–7.82 (dd, 4H, Ar–H), 8.94 (s, 1H, H–C=N), 9.05(s,2H, triazole), 2.43(s,3H,p-CH₃).

Synthesis of the Complex

Caution! The prepared perchlorate complexes are potentially explosive. Even though explosions never occurred, only small amounts should be prepared and handled with care!

Synthesis of [Fe^{II}(toltrz)₂(C₂O₄)]·5H₂O (C7)

This compound was first obtained as an unexpected product from the following procedure: To a stirring solution of toltrz (150 mg, 0.8 mmol) in methanol (3 mL) was added an 5 mL

Chapter 4 Three Iron Polynuclear Complexes: Magnetic Properties from a Dimer to 1D chain to 3D framework

aqua solution of $\text{Fe}(\text{ClO}_4)_4 \cdot 6\text{H}_2\text{O}$ (80 mg, ~ 0.3 mmol). The solution turned from colorless to a slightly dark reddish color solution. Then two spatula-amount (~ 70 mg) of ascorbic acid were added to prevent possible oxidation process. The reaction mixture was then stirred at 60°C for 3 hours before filtrated with rapid filter paper. The obtained clear reddish solution was kept in a small vial and left stand still to evaporate the solvent slowly. After three weeks, light yellow needle-like crystals of **C7** were deposited at the bottom of the vial. After removing the mother liquid, the single crystals were quickly dried in an argon stream, and stored under argon. Yield: 35.7 mg (34.80% based on Fe). The oxalate anion seen from the X-ray diffraction result violates the basic starting materials that we put into the reaction in the first place. The only explanation is that it came from the decomposition of the ascorbic acid when it was working against the oxidation of Fe^{II} ions. There are several reports regarding this way to achieve the oxalate as starting material. [21] We thus tried to prepare the oxalate compound by using $(\text{NH}_4)_2(\text{C}_2\text{O}_4)$ (38 mg, ~ 0.3 mmol, with the ratio of 1:1 compared to Fe) instead of ascorbic acid in a rather mild reaction conditions (stirred at r.t.). Same light-yellow crystals formed after one week with a higher yield of 66.96% (68.7 mg, based on Fe). Anal. Calcd (Found) for $\text{C}_{22}\text{H}_{20}\text{FeN}_8\text{O}_{11}$: C, 42.06 (41.44); H, 3.21 (3.59); N, 17.83 (17.57). IR (KBr) n/cm^{-1} : 3115 (m), 2921 (w), 1643 (vs), 1605 (s), 1523 (m), 1421 (w), 1122 (m), 829 (m), 619 (m), 489 (w).

Synthesis of $[\text{Fe}^{\text{II}}(5\text{-imztrz})(\text{C}_2\text{O}_4)] \cdot 2\text{H}_2\text{O}$ (C8)

This compound was also first obtained as an unexpected product with the same procedure for compound **8**, except for changing of toltrz (150 mg, 0.8 mmol) to imztrz (130 mg, 0.8 mmol). Yield: 38.7 mg (20.54% based on Fe). The preparation with ammonium oxalate give us the same crystalline compound with a yield of 72.98% (137.5 mg, based on Fe) Anal. Calcd (Found) for $\text{C}_8\text{H}_{10}\text{FeN}_6\text{O}_6$: C, 28.09 (27.75); H, 2.95 (3.28); N, 24.57 (23.70). IR (KBr) n/cm^{-1} : 3121 (m), 2923 (w), 1683 (vs), 1634 (vs), 1616 (vs), 1520 (m), 1433 (w), 1353 (m), 1311 (m), 1167 (m), 1113 (vs), 1062 (vs), 1006 (m), 956 (m), 799 (s), 693 (m), 647 (m), 620 (s), 513 (m), 485 (w).

Synthesis of $[\text{Fe}^{\text{III}}(\text{cit})(\text{H}_2\text{O})](5\text{-imztrzH}) \cdot 3\text{H}_2\text{O}$ (C9)

To a stirring 3 mL methonic solution of imztrz (130 mg, 0.8 mmol), $\text{Fe}(\text{ClO}_4)_4 \cdot 6\text{H}_2\text{O}$ (80 mg, ~ 0.3 mmol) in 5 mL H_2O was added. The solution color changed from light yellow to a bit darker. Then citric acid (60 mg, ~ 0.3 mmol) was added as a powder into the reaction solution, the reaction was then kept stirring at 60°C for 5 hours before filtrated with rapid filter paper. The obtained light-yellow solution was kept in a small vial and left stand still to evaporate the solvent slowly. After five days, light-yellow (looks like white too) block crystals of **C9** were deposited at the bottom of the vial. After removing the mother liquid,

**Chapter 4 Three Iron Polynuclear Complexes:
Magnetic Properties from a Dimer to 1D chain to 3D framework**

the single crystals were picked up and blew with an argon stream to dryness before stored in a small vial. Yield: 81.7 mg (56.85% based on Fe). Anal. Calcd (Found) for C₁₂H₁₉FeN₆O₁₁: C, 30.08 (30.78); H, 4.00 (3.75); N, 17.54 (18.37). IR (KBr) ν /cm⁻¹: 3136 (m), 2959 (w), 2853 (w), 2620 (w), 1683 (vs), 1634 (vs), 1617 (vs), 1570 (m), 1523 (m), 1506 (w), 1343 (w), 1384 (w), 1351 (m), 1313 (m), 1257 (w), 1164 (m), 1112 (s), 1063 (s), 1007 (m), 958 (m), 863 (m), 801 (s), 690 (w), 620 (m), 512 (m), 486 (m).

4.4 Result and discussion

4.4.1 Structural Description

Crystallographic data for the compounds 7–9 are summarized in Table 4.1 and the selected bond lengths and angles are presented in Table 4.2.

Table 4.1. Crystallographic Data and Refinement Parameters for Compounds 7–9.

Compound	C7	C8	C9
Empirical formula	C ₂₂ H ₂₀ FeN ₈ O ₁₁	C ₈ H ₁₀ FeN ₆ O ₆	C ₁₂ H ₁₉ FeN ₆ O ₁₁
Formula weight	628.31	342.07	479.18
Crystal size	0.27×0.13×0.09	0.27×0.15×0.13	0.23×0.16×0.10
Crystal system	Monoclinic	Monoclinic	Triclinic
Space group	<i>C2/c</i> (No. 15)	<i>Pc</i> (No. 7)	<i>P-1</i> (No. 2)
<i>a</i> (Å)	24.005(8)	8.7922(9)	9.0449(12)
<i>b</i> (Å)	19.357(5)	8.9323(9)	9.9703(15)
<i>c</i> (Å)	5.4461(12)	8.6926(9)	11.8286(16)
α (°)	90	90	68.265(4)
β (°)	93.213(9)	105.468(2)	75.823(4)
γ (°)	90	90	68.729(4)
<i>V</i> (Å ³)	2526.6(12)	657.94(12)	915.8(2)
<i>Z</i>	4	2	2
<i>D</i> _{calc} (g/cm ³)	1.652	1.727	1.738
μ (Mo-K α) (mm ⁻¹)	0.676	1.186	0.899
<i>F</i> (000)	1288	348	494
Reflections collected	8064	5500	7451
Independent reflections	3042 (0.0904)	2455 (0.0341)	4315 (0.0538)
Parameters	233	194	281
Goodness-of-fit	0.924	1.008	0.979
<i>R</i> ₁ [<i>I</i> > 2 σ (<i>I</i>)] ^a	0.0621	0.0379	0.0609
<i>wR</i> ₂ (all data) ^b	0.1417	0.0852	0.1480

$$^a R_1 = \frac{\sum ||F_o| - |F_c||}{\sum |F_o|}, \quad ^b wR_2 = \left\{ \frac{\sum [w(F_o^2 - F_c^2)]^2}{\sum [w(F_o^2)]^2} \right\}^{1/2}$$

Crystal structure of $[Fe^{II}(\text{toltrz})_2(\text{C}_2\text{O}_4)] \cdot 5\text{H}_2\text{O}$ (C7)

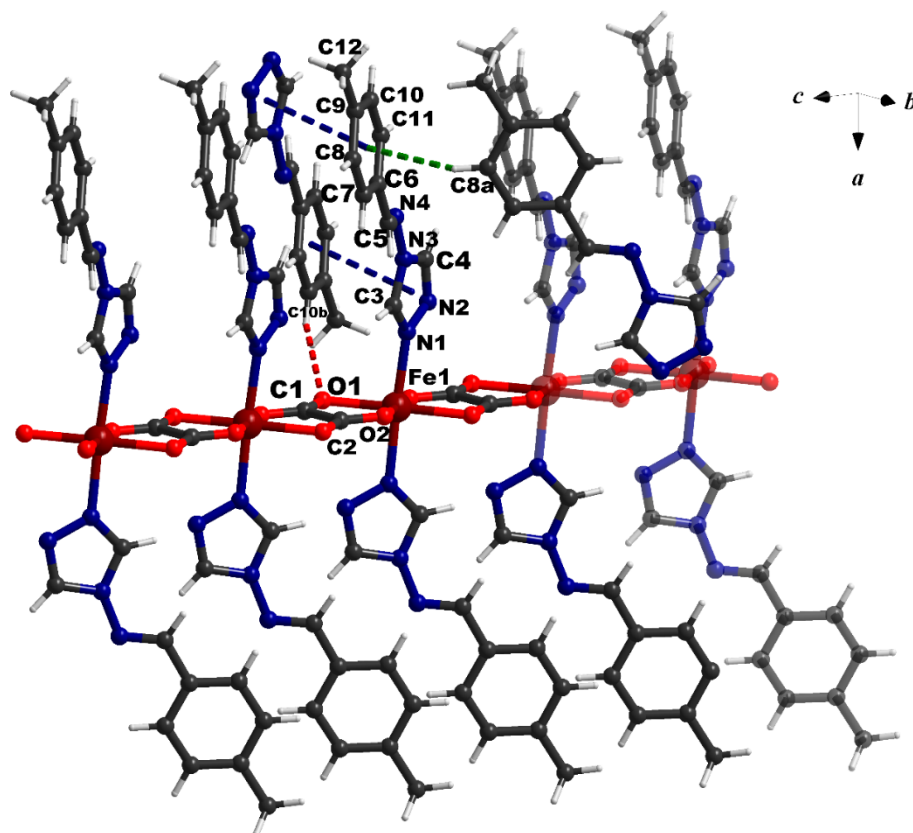


Figure 4.2.: Perspective drawing of the 1D framework of compound 7, and supramolecular interactions involved. . ($a = -x, -y + 1, z - 0.5$; $b = x + 0.5, -y + 0.5, z - 0.5$)

Compound 7 crystallizes in the monoclinic space group $C2/c$. It is built up from 1D $[\text{Fe}(\mu_2\text{-C}_2\text{O}_4)(\text{toltrz})_2]$ linear chains, that are further linked by supramolecular interactions (H-bonding, $\pi \cdots \pi$ stacking) to a 3D supramolecular network. The polymeric linear chains consist of $[\text{Fe}(\text{toltrz})_2]^{2+}$ units bridged sequentially by the oxalate ligands (bis-bidentate mode). The selected bonding parameters for C7 are listed in Table 4.2. As shown in Figure 4.2, in each chain, the crystallographically unique Fe(1) atom in octahedral geometry is surrounded by two N donors from two symmetrical toltrz molecules and four O donors from two symmetrical related oxalate ligands with an adjacent Fe...Fe distances of 5.446 Å. The Fe(1)–O distances are 2.073(3) Å (Fe1–O1) and 2.112(3) Å (Fe1–O2), comparable with those reported similar structures.^[2a, 22] The Fe(1)–N distance, [Fe1–N1, 2.148(3) Å] is within the range observed in most iron(II) complexes.^[22] Two toltrz molecules lie on each side of the chain with a dihedral angle of 46.7°, ensuring a minimum steric hindered effect.

Chapter 4 Three Iron Polynuclear Complexes: Magnetic Properties from a Dimer to 1D chain to 3D framework

Table 4.2. Selected bond distances (Å) and angles (°) of compound 7–9.

Compound 7					
Fe(1)-O(1)	2.073(3)	Fe(1)-O(2)#1	2.112(3)	Fe(1)-N(1)	2.148(3)
Fe(1)-O(1)#1	2.073(3)	Fe(1)-O(2)	2.112(3)	Fe(1)-N(1)#1	2.148(3)
O(1)-Fe(1)-O(1)#1	101.50(15)	O(1)#1-Fe(1)-N(1)	92.15(11)	O(2)#1-Fe(1)-N(1)	89.78(11)
O(1)#1-Fe(1)-O(2)	178.92(11)	O(1)-Fe(1)-N(1)	89.88(11)	O(2)-Fe(1)-N(1)	88.15(11)
O(1)-Fe(1)-O(2)	79.54(10)	O(2)-Fe(1)-O(2)#1	99.42(15)	N(1)-Fe(1)-N(1)#1	176.80(19)
Compound 8					
Fe(1)-O(1)	2.195(6)	Fe(1)-O(3)#3	2.234(5)	Fe(1)-N(1)#4	2.145(7)
Fe(1)-O(2)	2.105(5)	Fe(1)-O(4)#3	2.068(6)	Fe(1)-N(6)	2.139(8)
O(1)-Fe(1)-O(3)#2	84.33(11)	O(4)#1-Fe(1)-O(1)	85.7(2)	N(1)#3-Fe(1)-O(1)	87.3(3)
O(2)-Fe(1)-O(1)	77.71(18)	O(4)#1-Fe(1)-O(2)	157.80(11)	N(1)#3-Fe(1)-O(3)#2	170.8(2)
O(2)-Fe(1)-O(3)#2	86.65(19)	O(4)#2-Fe(1)-O(3)#2	77.05(19)	N(6)-Fe(1)-O(1)	173.3(3)
O(2)-Fe(1)-N(1)#3	95.3(2)	O(4)#2-Fe(1)-N(1)#3	98.6(2)	N(6)-Fe(1)-O(3)#2	89.7(3)
O(2)-Fe(1)-N(6)	98.9(2)	O(4)#2-Fe(1)-N(6)	96.0(2)	N(6)-Fe(1)-N(1)#3	98.87(13)
Compound 9					
Fe(1)-O(1W)	2.029(3)	Fe(1)-O(4)#5	2.033(3)	Fe(1)-O(5)	1.984(3)
Fe(1)-O(2)#5	2.008(3)	Fe(1)-O(5)#5	2.071(3)	Fe(1)-O(7)	2.005(3)
O(1W)-Fe(1)-O(4)#5	82.75(11)	O(4)#1-Fe(1)-O(5)#5	80.38(11)	O(5)-Fe(1)-O(7)	88.14(11)
O(1W)-Fe(1)-O(5)#5	162.92(11)	O(5)-Fe(1)-O(1W)	103.89(12)	O(7)-Fe(1)-O(1W)	89.22(11)
O(2)#1-Fe(1)-O(1W)	94.36(12)	O(5)-Fe(1)-O(2)#5	161.50(11)	O(7)-Fe(1)-O(2)#5	89.12(12)
O(2)#1-Fe(1)-O(4)#5	92.56(12)	O(5)-Fe(1)-O(4)#5	92.72(11)	O(7)-Fe(1)-O(4)#5	171.90(12)
O(2)#1-Fe(1)-O(5)#5	83.78(11)	O(5)-Fe(1)-O(5)#5	79.65(12)	O(7)-Fe(1)-O(5)#5	107.68(11)

Symmetry transformations used to generate equivalent atoms:

#1 = $-x + 1, y, -z + 1/2$; #2 = $x, -y + 2, z - 1/2$; #3 = $x - 1, -y + 1, z + 1/2$; ; #4 = $x, -y + 2, z + 1/2$;

#5 = $-x + 1, -y, -z + 1$.

Apart from the ancillary role of the toltz molecules, it also provides the H donor atoms (C10–H10) to participate in the interchain hydrogen-bonded interactions with the O1 atoms from oxalate ligands in the adjacent chain (C10–H10a...O1 = 2.517 (1) Å, C10a...O1 = 3.4016(8) Å, $a = x + 0.5, -y + 0.5, z - 0.5$), through which the polymeric linear chains are linked in the *ab* plane. (Figure 4.3)

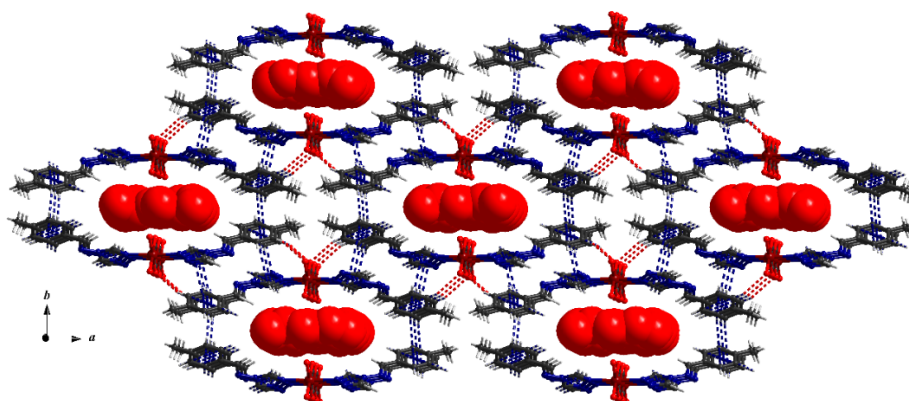


Figure 4.3.: The 3D network formed by supramolecular interactions in C7 with channels filled up with water molecules.

One group of double $\pi \cdots \pi$ stacking involving the triazole ring and the phenyl ring (centroid...centroid = 3.7794 (10) Å) was also found along *c* axis, together with another

Chapter 4 Three Iron Polynuclear Complexes: Magnetic Properties from a Dimer to 1D chain to 3D framework

group of C–H... π interaction ($C8-H8b \cdots \text{centroid}_{C6 \text{ ring}} = 2.9879(8) \text{ \AA}$, $b = x, -y + 1, z - 0.5$), (Figure 4.2, Figure 4.3). These intermolecular interactions further extend the structure into a 3D supramolecular network with porous channels along c axis. (Figure 4.3) Calculations using PLATON, [23] showed that the effective volume for inclusion of these channels is about $2526.6 \text{ \AA}^3 / \text{cell}$ comprising $\sim 16.4\%$ of the crystal volume. The five crystallographically independent water molecules are placed in the channels of the network. While the hydrogen atoms of the water molecules could not be determined, the potential H–bonding interactions involved are not discussed here.

Crystal structure of $[Fe^{II}(\text{imztrz})(C_2O_4)] \cdot 2H_2O$ (**8**)

Compound **8** crystallizes in the monoclinic space group Pc . As shown in Figure 4.4, quite different from the linear chain in compound **7**, this structure consists of zig-zag chains in which the metal centers are bridged by two bis-bidentate centrosymmetric oxalato ligands. The distorted octahedral geometry around the Fe atoms is completed by a chelating imztrz molecule coordinated by two nitrogen atoms: one belonging to the triazole ring and the other one to a symmetrical molecular imidazole substituent. The one-dimensional structure of this compound is shown in Figure 4.4, whereas selected bond lengths and angles of the FeO_4N_2 unit are listed in Table 4.2. The dihedral angles between two consecutive oxalate anions are about 74.7° and the shortest Fe...Fe distance across the oxalate ligands is 5.58 \AA , which is in good accordance with those previously reported oxalato-bridged Fe^{II} complexes. [2a, 22] The imztrz ligand is nearly planar with dihedral angles between the triazole ring and imidazole substituent near to 7° . They are parallel to each other along the chain, forming an angle of 50.35° with the iron-oxalate framework growing direction. (Figure 4.4)

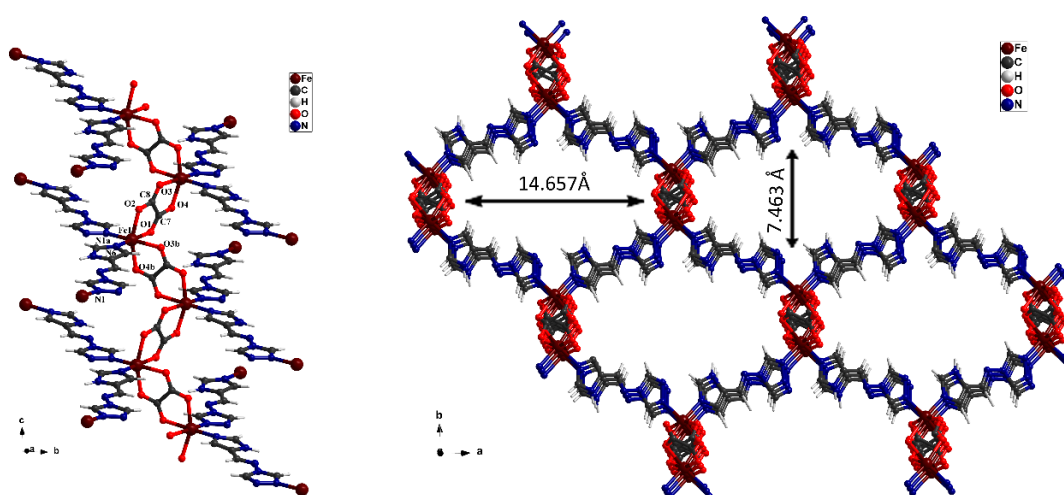


Figure 4.4.: a) View of the 1D chain in compound **8**; b) The porous framework formed via covalent/coordinate bonds in **8**. ($a = x - 1, -y + 1, z$; $b = x, -y + 2, z - 0.5$)

Chapter 4 Three Iron Polynuclear Complexes: Magnetic Properties from a Dimer to 1D chain to 3D framework

The imztrz ligand adopt a μ_2 -bridging mode, which further links the zig-zag chains via coordination bonds to a higher dimensional framework, giving rise to a three-dimensional framework with large rectangular porous channels paralleling to the c axis, by the size of $7.463 \text{ \AA} \times 14.657 \text{ \AA}$. (Fig. 4.4). The Fe...Fe distance across the imztrz ligands here is $12.0890(8) \text{ \AA}$. Apart from the covalent/coordinate bonds linking, multiple groups of H-bonding interactions are found to gather the porous units into a 3D interpenetrate structure with a relatively small void. (Figure 4.5, Table S4.1) Calculations using PLATON, [23] showed that the effective volume for inclusion of these channels is about 657.9 \AA^3 / cell comprising $\sim 18.2\%$ of the crystal volume. The two crystallographically independent water molecules are embedded in the channels of the network via strong H-bonding interactions ($D\cdots A \sim 2.83 \text{ \AA}$, details in table S4.1)

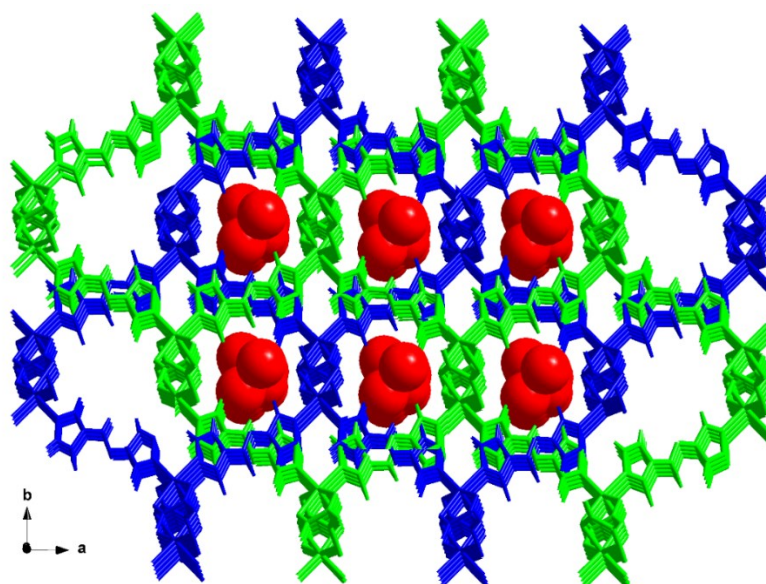


Figure 4.5.: The 3D interpenetrate structure in compound **8** with water molecules embedded in the channels.

Crystal structure of $[\text{Fe}^{\text{III}}(\text{cit})(\text{H}_2\text{O})](5\text{-imztrzH})\cdot 3\text{H}_2\text{O}$ (C9)

Compound **9** crystallizes in the triclinic space group $P-1$. The unit cell of **C9** is made up of two cations $[5\text{-imztrzH}]^+$, one discrete binuclear iron (III) citrate anionic complex $[\text{Fe}^{\text{III}}_2(\text{cit})_2(\text{H}_2\text{O})_2]$ and three lattice water molecules. As shown in Figure 4.6, the anionic complex is an edge-shared bi-octahedral dimer with a centro-symmetric structure, in which the two iron ions are bridged by two μ_2 -alkoxo groups of the two fully deprotonated citrate ligands. All carboxylate groups are coordinated in a monodentate mode to the terminal sites, and two coordinated aqua molecules complete the first coordination sphere of the two octahedral spheres.

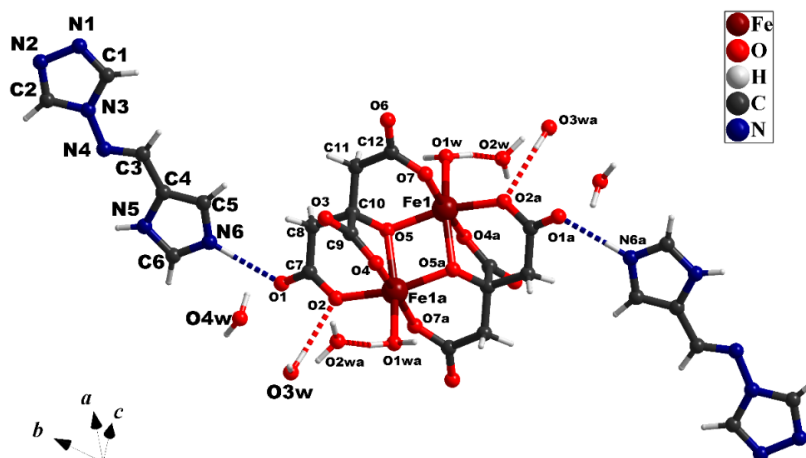


Figure 4.6.: Structure of the $[\text{Fe}^{\text{III}}(\text{cit})(\text{H}_2\text{O})](5\text{-imztrzH})\cdot 3\text{H}_2\text{O}$ complex. Symmetric code: $a = -x + 1, -y, -z + 1$.

The Fe–O bond distances range from 1.984(3) to 2.071(3) Å with the average value of 2.022 Å, and the adjacent non-bonded Fe...Fe distance is around 3.115(2) Å. In the structure, two μ_2 -O atoms and two iron ions form a four-membered $\{\text{Fe}_2\text{O}_2\}$ ring, in which the O–Fe–O angle is 79.65(12)°. (Figure 4.6) These values are in good agreement with those reported in similar structures. ^[9a-c] The selected bond distances and angles are listed in table 4.2, from which we can tell that the octahedron is slightly distorted. In addition, short H–bonding interactions were found between the adjacent dimers via a one-to-two binding mode (O3 to C8–H8A, and O3 to C11–H11A) to link this dimer into a 1D chain along *b* axis, which is further connected through water molecules between the chains to finish with a 2D sheet in *ab* plane. (Figure 4.7, table S4.1).

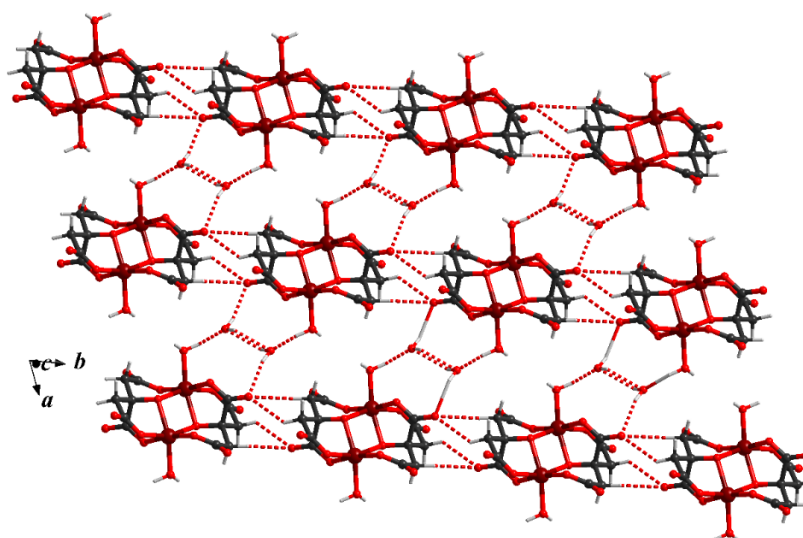


Figure 4.7.: The 2D sheet built from dimer units via H-bonding interaction in compound **9**. The red dashed lines represent different H-bonding involved.

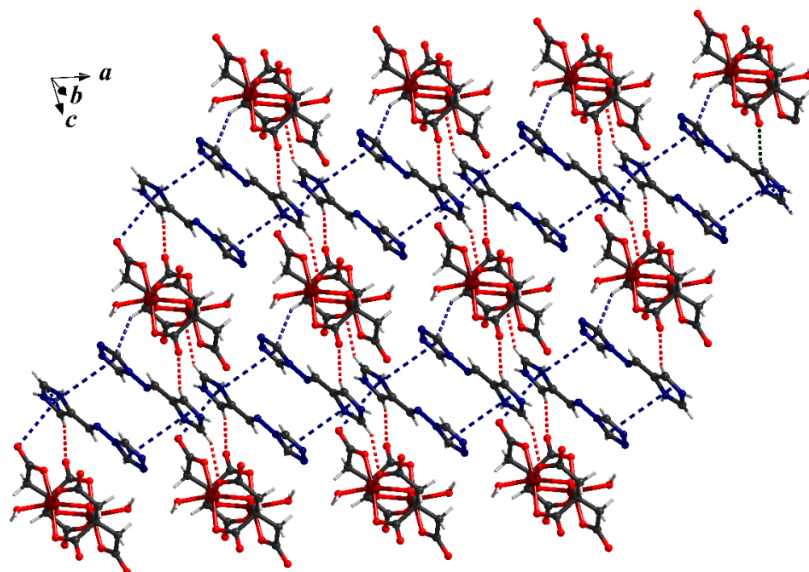


Figure 4.8.: The 3D supramolecular framework connected by different weak interactions in compound **9**. The blue dashed lines represent $\pi\cdots\pi$ stacking and the red dashed lines stand for the H-bonding interactions.

Interesting pairs of π -interactions were found in the structure: anion $\cdots\pi$ ($\text{O6}\cdots\text{centroid}_{\text{imidazole}} = 3.3689(31) \text{ \AA}$), C–H $\cdots\pi$ ($\text{C8–H8B}\cdots\text{centroid}_{\text{triazole}} = 2.8454(3) \text{ \AA}$) and $\pi_{\text{triazole}}\cdots\pi_{\text{imidazole}}$ adopting a head-to-tail mode stacking with a distance of $4.0974(5) \text{ \AA}$. These stackings are arranged along the c axis, which connects the 2D sheet into a 3D supramolecular framework. Other groups of H-bonding interactions were found to stabilize the structure. (Figure 4.8, table S4.1) According to the VBT theory ^[24], the sum of the bond valences around Fe is $2.958(10)$, which is in accordance with the valence of the Fe^{3+} ion. This fact strongly supports the conclusion that although citrate acid is a reductant, the ferric ion is not reduced when it is heated up to $60 \text{ }^\circ\text{C}$ in the reaction solution, *i.e.*, citrate acid can't act as protecting agent as ascorbic acid does from preventing Fe^{II} oxidation process. The valence +3 of the Fe is further confirmed by the magnetic measurement.

4.4.2 FT–IR spectroscopy

The FT-IR spectra of the three compounds indicates that the coordination of the nitrogen atoms with iron(II) salts affect the vibration of ligand (toltrz, 5-imztrz) only to a minor extent. As shown in Figure 4.9, the spectra of compound **7**, compound **8** and **9** are very similar compared to the corresponding ligand toltrz and 5-imztrz. However, a careful examination can detect the significant changes due to the coordination of the compound. The bands between 1675 and 1400 cm^{-1} are attributable to $\text{C}_{\text{ar}}\text{--C}_{\text{ar}}$ and $\text{C}_{\text{ar}}\text{=N}$ stretching vibration frequencies of the aromatic group, with the asymmetric O–C–O vibration overlapping in the same region. For compound **7** and **8**, the ν_{as} (O–C–O) signature for oxalate

Chapter 4 Three Iron Polynuclear Complexes: Magnetic Properties from a Dimer to 1D chain to 3D framework

is found at 1604 cm^{-1} and 1617 cm^{-1} , and those values for citrate appear at 1606 cm^{-1} and 1583 cm^{-1} for **C9**. The $\nu_s(\text{O}-\text{C}-\text{O})$ vibration is found in lower frequency region, 1383 cm^{-1} (**C7**), 1401 cm^{-1} (**C8**), 1379 cm^{-1} (**C9**). Among the three compounds, the difference between the asymmetric and symmetric stretches, $\Delta[\nu_{\text{as}}(\text{COO}^-) - \nu_{\text{s}}(\text{COO}^-)]$, are in the order of 200 cm^{-1} , indicating the different coordination mode of the carboxyl groups, [25] which is consistent with the observed X-ray crystal structures of **C7–C9**. In compounds **8** and **9**, the characteristic band for the triazole ω -ring vibration shifts from a strong signal at 1503 cm^{-1} (free ligand) to a medium peak at 1523 cm^{-1} (**C8**) and 1525 cm^{-1} (**C9**), indicating the coordination of the N-donor atoms from triazole ring in compound **8**, and the protonated N atom in compound **9**. [26] This characteristic band is also identified for compound **7** around 1525 cm^{-1} (1503 cm^{-1} in free toltrz ligand). Additionally, the peaks at 1215 (m) , 1171 (m) , 1063 (m) , and $851\text{ (s)}\text{ cm}^{-1}$ can be assigned to the C–H in-plane or out-of-plane bend ring breathing, and ring deformation absorptions of the organic ligands. These bands can be noticed for all the compounds and they are shifted as compared to the ligand spectrum (Figure 4.9), which can be connected with the change in the geometry of the ligands upon complex formation. The characteristic azomethine ($\text{HC}=\text{N}$) stretching [27] around 1636 cm^{-1} is overlapping with the asymmetric O–C–O vibration and $\text{C}_{\text{ar}}=\text{N}$ stretching in all the compounds, which cannot be assigned any more.

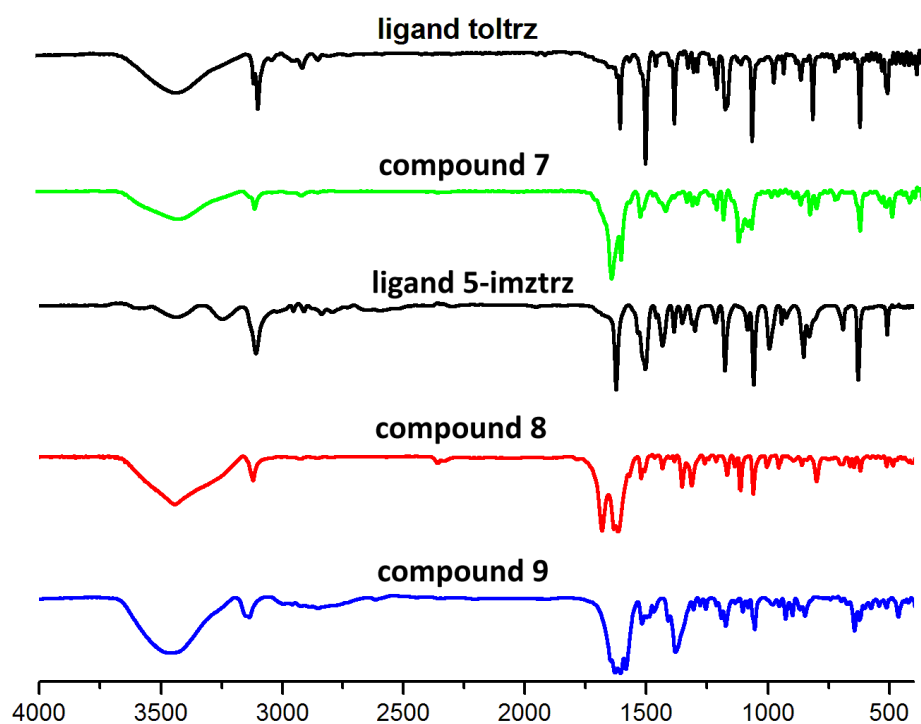


Figure 4.9.: The FT-IR spectra of ligand imztrz, ligand toltrz and compounds 7–9.

4.4.3 Magnetic susceptibility

Although the covalent structure of compound **8** is three-dimensional, we can assume that the long imztrz bridging ligands (Fe...Fe distances of 12.0890 (8) Å) do not couple the Fe(II) ions or at least only in a negligible strength. Thus, from magnetic point of view, the structure can be considered as a pseudo-one-dimensional structure with Fe(II) ions linked by oxalate anion, and quite similar in compound **7**. We analyze the magnetic properties of these two compounds based on the chain models. [28]

The magnetic susceptibility data of compound **7**, **8** and **9** have been recorded in the temperature range 300–2 K. The magnetic properties of compound **7** and **8** in the form χ_{MT} vs T are represented in Figure 4.10. The χ_{MT} value of 7.01 cm³·K·mol⁻¹ (**C7**) and 7.36 cm³·K·mol⁻¹ (**C8**) at 300 K can be ascribed to the corresponding two high-spin Fe(II) ions, which is somehow above the value calculated for a magnetically non-interacting spin quintet through the spin-only formula ($\chi_{MT} = 6.0$ cm³·K·mol⁻¹ with $g = 2.0$). For compound **7**, with the temperature decrease from 300K to 140 K, the χ_{MT} value drops slowly from 7.01 to 6.05 cm³·K·mol⁻¹, below this temperature, χ_{MT} starts to decrease more and more abruptly to reach a value of 0.27 cm³·K·mol⁻¹ at 2 K. For compound **8**, χ_{MT} drops to 6.49 cm³·K·mol⁻¹ from 300K down to 110K, then the value decrease more dramatically all the way down to 0.69 cm³·K·mol⁻¹ at 2 K. The magnetic susceptibility curves (χ_M vs T) exhibit maxima at 30 (**C7**) and 16 K (**C8**), revealing that a significant antiferromagnetic interaction between the high-spin Fe^{II} ions occurs.

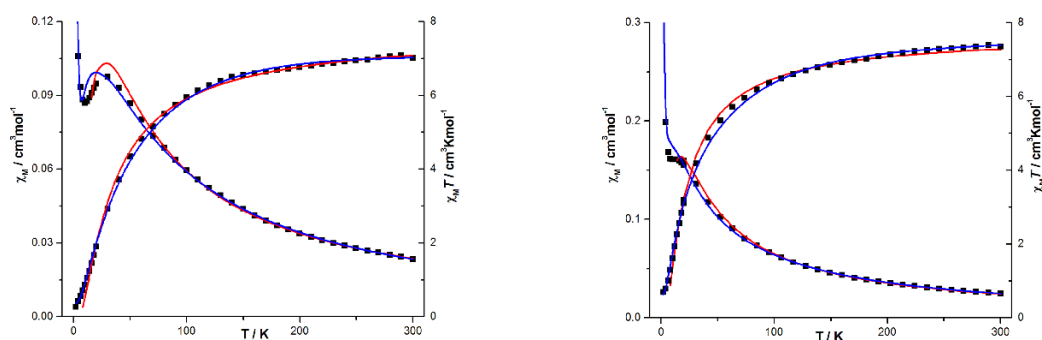


Figure 4.10.: Plots of the experimental and theoretic temperature dependence of χ_{MT} for **C7** (left) and **C8** (right). The solid lines represent the best fit curve: blue line for dimer model fitted with PHI and red line for fitting with the chain model.

An inverse susceptibility plot, $\chi_M^{-1}(T)$, shows linear behavior following Curie–Weiss law above a certain temperature for compound **7** (80 K) and compound **8** (20K), respectively.

Chapter 4 Three Iron Polynuclear Complexes: Magnetic Properties from a Dimer to 1D chain to 3D framework

As shown in figure 4.11, fitting the data with the Curie–Weiss equation ($\chi_M = C/(T - \Theta)$), we obtain Curie constant $C = 7.80(1)$ (C7), $8.08(1)$ (C8) $\text{cm}^3 \cdot \text{K} \cdot \text{mol}^{-1}$ and Weiss constant $\Theta = -30.16(1)$ (C7), $-26.90(1)$ (C8) K, from which we derive a g -value of $1.86(1)$ (C7) and 1.98 (C8). These values confirm the antiferromagnetic coupling between the adjacent active Fe(II) centers.

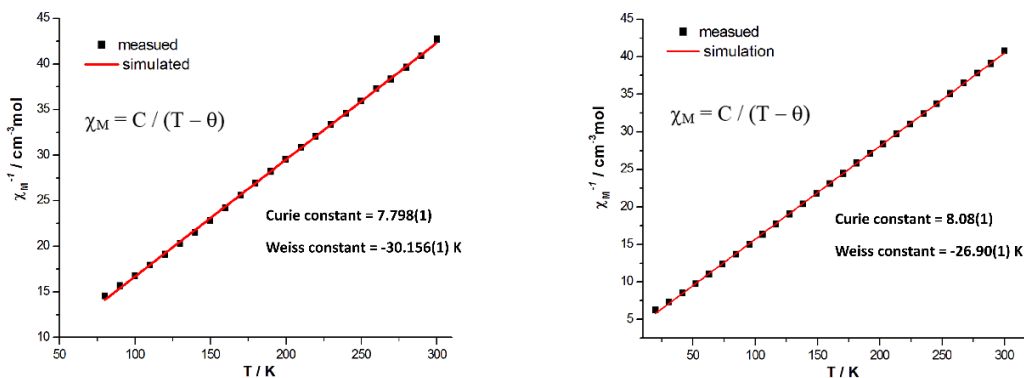


Figure 4.11.: Plots of χ_M^{-1} vs T for compound **7** (left) and compound **8** (right) with fitting to the Curie–Weiss Law.

Based on the crystallographic results, these two compounds have a similar chain structure with almost equal Fe...Fe distances within the structure, therefore, the magnetic behavior can be treated as chain mode as high spin Fe^{II} ions with local spin $S = 2$.^[28] Herein, to evaluate the antiferromagnetic interaction through the oxalate bridge, we analyze the data for an $S = 2$ Ising chain model with the equation from Drillon et al.^[29]:

$$\chi_M = \frac{2Ng^2\mu_B^2}{k_B T} \exp(4J/k_B T) \quad (\text{Equation 4.1})$$

Nonlinear regression of the data resulted in the best fitting result over almost the whole temperature range with $J = -4.70(1) \text{ cm}^{-1}$ and $g = 2.53$ for compound **7**, and $J = -3.01(1) \text{ cm}^{-1}$ and $g = 2.27$ for compound **8**. (Figure 4.10, red solid line) The result of this fitting is illustrated in figure 10, where the smooth curve represents the theoretical calculation. The rather large g values here represent the strong spin–orbit coupling and large orbital contribution involved for the octahedral surrounded Fe(II) ions. In addition, the magnetic data of the entire temperature range are also simulated with a simplified dimer model using PHI^[30] program (Figure 4.10, blue solid line). Interestingly, the fitting results give us quite similar results compared with the chain model with the values $g = 1.95$ (C7) and 1.96 (C8), coupling constants $J = -4.37(2) \text{ cm}^{-1}$ (C7) and $-2.60(2) \text{ cm}^{-1}$ (C8). We have also implemented a paramagnetic impurity ($\rho = 0.074\%$ (C7) and 0.136% (C8)) and a TIP effect ($0.003 \text{ cm}^3 \cdot \text{mol}^{-1}$ (C7) and $0.002 \text{ cm}^3 \cdot \text{mol}^{-1}$ (C8)) for the PHI simulation. This magnetic

analysis result suggests a slightly stronger antiferromagnetic coupling in the rather straight chain compound **7** compared to the zigzag chain based 3D network compound **8**. The J values obtained here are quite close to those found in the similar iron chains with an agreed separation range across the bridging oxalato groups: $[\text{Fe}_2(\text{phen})_2(\text{C}_2\text{O}_4)_2]_n$ ($J = -2.2 \text{ cm}^{-1}$, $\text{Fe} \cdots \text{Fe} = 5.531 \text{ \AA}$, phen = phenanthroline), [3b] and $[\text{Fe}(\text{ox})(\text{abpt})]_n$ ($J = -5.1 \text{ cm}^{-1}$, $\text{Fe} \cdots \text{Fe} = 5.569 \text{ \AA}$, abpt = 4-amino-3,5-bis(2-pyridyl)-1,2,4-triazole). [5]

As shown in figure 4.12, $\chi_M T$ value values for compound **9** at 300K is $8.95 \text{ cm}^3 \cdot \text{K} \cdot \text{mol}^{-1}$, slightly larger than the expected value $8.37 \text{ cm}^3 \cdot \text{K} \cdot \text{mol}^{-1}$ calculated for two isolated Fe^{III} ions with high-spin state ($S = 5/2$), but comparable to those values observed in some compounds with strong anti-ferromagnetic coupling interaction between the two iron centers. [9a-b] Upon cooling, the χ_M exhibits a rounded maximum around 20 K, while the $\chi_M T$ value continuously decreases to $0.27 \text{ cm}^3 \cdot \text{K} \cdot \text{mol}^{-1}$ at 2 K, which indicates of antiferromagnetic coupling between the metal centers.

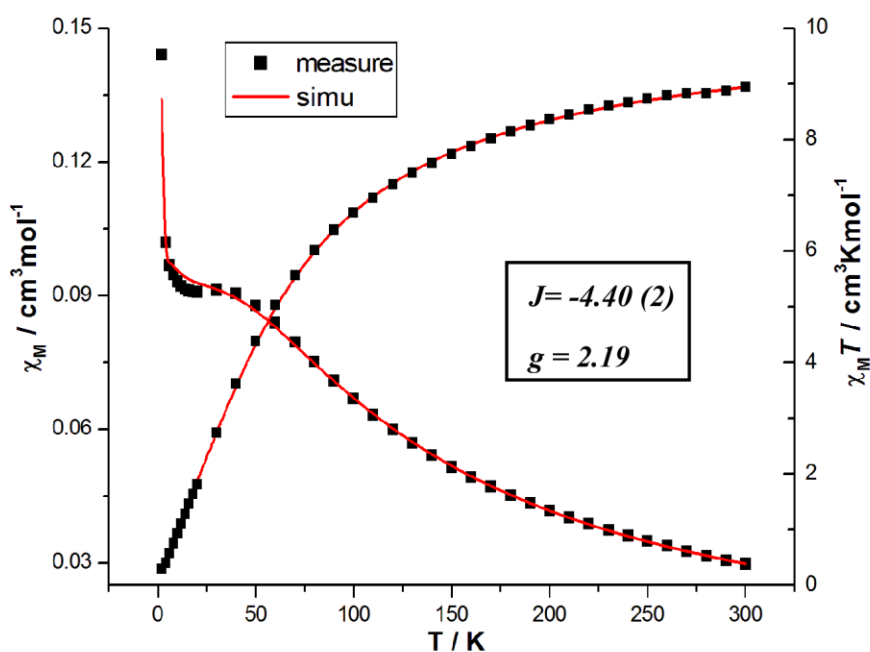


Figure 4.12.: Plots of the experimental and theoretic temperature dependence of χ_M and $\chi_M T$ for compound **9** (the solid line represents the best fit curve).

Assuming isotropic exchange, the experimental magnetic data were simulated for the dimeric $\text{Fe}(\text{III})$ system with PHI program [28], with a simulated g value of 2.20, coupling constants J value of $-4.40(2) \text{ cm}^{-1}$ and impurity ratio p of 0.006%. (Figure 4.12) This value can be compared with other similar $\text{Fe}(\text{III})$ systems reported. [9a-c] The result is in accordance with the reported tendency that ferromagnetic coupling is pretty rare for a face-shared d^5 - d^5

system, ^[9a] even though Zhang and co-workers have stated that the face-shared topological arrangement favors the ferromagnetic coupling between two metal centers. ^[9b]

4.5 Conclusion

The work described herein represents three new examples of polynuclear Fe complexes: a 1D chain, a 3D interpenetrate framework and a dimer compound. For the first time, ligand 4-(1*H*-imidazol-5-ylmethylene-amino)-4*H*-1,2,4-triazole (imztrz) has been successfully synthesized and used as a bridging ligand to construct novel iron–organic supramolecular materials. We have proven that the imidazole ring substitution can function the same as 4,4'-bipyridin for linking chains to layers, layers to 3D framework. Moreover, we have reported here two new examples of Fe^{II} porous compounds, which is rare and may provide useful reference for future porous Fe^{II} based MOFs research, like SCO systems combined with MOFs character. Additionally, the magnetic studies reveal that for all the three compounds, different degree of antiferromagnetic couplings between the adjacent Fe centers occurred, of which are all in good agreement with the available reported data.

4.6 Acknowledgement

Dr. Dieter Schollmeyer and Regine Jung-Pothmann (*Johannes Gutenberg University, Mainz*) were kindly acknowledged for the crystal data collection. A.M.L. acknowledges the financial support from graduate school MAINZ and is a recipient of a DFG fellowship through the Excellence Initiative by the Graduate School Materials Science in Mainz (DFG/GSC 266).

4.7 Reference

[1] a) M. Sadakiyo, T. Yamada, K. Kato, M. Takata, H. Kitagawa, *Chem. Sci.* **2016**, *7*, 1349-1356; b) M. Clemente-León, E. Coronado, M. López-Jordà, C. Desplanches, S. Asthana, H. Wang, J. F. Létard, *Chem. Sci.* **2011**, *2*, 1121-1127; c) E. Cariati, R. Macchi, D. Roberto, R. Ugo, S. Galli, N. Casati, P. Macchi, A. Sironi, L. Bogani, A. Caneschi, D. Gatteschi, *J. Am. Chem. Soc.* **2007**, *129*, 9410-9420; d) T. A. Hudson, K.J. Berry, B. Moubaraki, K. S. Murray, R. Robson, *Inorg. Chem.* **2006**, *45*, 3549-3556.

[2] a) L.L. Li, K. Lin, C.J. Ho, C.P. Sun, H.D. Yang, *Chem. Commun.* **2006**, 1286–1288; b) A. Taku Fujino, B. Yoshimasa Hoshino, A. Satoshi Igarashi, C. Yoshio Masuda, Yasuhiko Yukawa, *Inorg. Chim. Acta* **2004**, *357*, 11–18; c) E. Coronado, J.R. Galan-Mascaros, C. Martí-Gastaldo, *J. Am. Chem. Soc.* **2008**, *130*, 14987–14989; d) A. Rodríguez-Diéguez, J.M. Seco, E. Colacio, *Eur. J. Inorg. Chem.* **2012**, 203–207; e) C.H. Hendon, A. Walsh, N. Akiyama, Y. Konno, T. Kajiwara, T. Ito, H. Kitagawa, K. Sakai, *Nat. Commun.* **2016**, *7*, 11950.

Chapter 4 Three Iron Polynuclear Complexes: Magnetic Properties from a Dimer to 1D chain to 3D framework

- [3] a) L. L. Li, K. J. Lin, C. J. Ho, C. P. Sun, H. D. Yang, *Chem. Commun.* **2006**, *12*, 1286-1288; b) F. X. Ma, F. X. Meng, K. Liu, H. J. Pang, D. M. Shi, Y. G. Chen, *Transit Metal Chem.* **2007**, *32*, 981-984; c) M. Clemente-León, E. Coronado, C. J. Gómez-García, M. López-Jordà, A. Camon, A. Repollés, F. Luis, *Chem. Eur. J.*, **2014**, *20*, 1669-1676.
- [4] a) J. Y. Lu, M. A. Lawandy, J. Li, T. Yuen, C. L. Lin, *Inorg. Chem.*, **1999**, *38*, 2695-2704; b) C. Sánchez-Sánchez, C. Desplanches, J. M. Clemente-Juan, M. Clemente-León, E. Coronado, *Dalton Trans.*, **2017**, *46*, 2680-2689.
- [5] a) U. García-Couceiro, O. Castillo, J. Cepeda, A. Luque, S. Pérez-Yáñez, P. Román, *Inorganica Chim. Acta*, **2009**, *362*, 4212-4218; b) T. F. Mastropietro, N. Marino, G. D. Munno, F. Lloret, M. Julve, E. Pardo, D. Armentano, *Inorg. Chem.*, **2016**, *55*, 11160-11169.
- [6] a) T. D. Keene, I. Zimmermann, A. Neels, O. Sereda, J. Hauser, M. Bonin, M. B. Hursthouse, D. J. Price, S. Decurtins, *Dalton Trans.* **2010**, *9*, 4937-4950; b) D. Armentano, G. de Munno, F. Lloret, M. Julve, J. Curély, A. M. Babb, J. Y. Lu, *New J. Chem.* **2003**, *27*, 161-165; c) N. Marino, D. Armentano, G. De Munno, F. Lloret, J. Cano, M. Julve, *Dalton Trans.*, **2015**, *44*, 11040-11051.
- [7] a) L. M. Zheng, X. Fang, K. H. Lii, H. H. Song, X. Q. Xin, H. K. Fun, K. Chinnakali, I. A. Razak, *J. Chem. Soc., Dalton Trans.* **1999**, *14*, 2311-2316; b) U. Garcia-Couceiro, O. Castillo, A. Luque, J. P. Garcia-Teran, G. Beobide, P. Román, *Cryst. Growth Des.* **2006**, *6*, 1839-1847.
- [8] a) A. Earnshaw, J. Lewis, *J. Chem. Soc.* **1961**, *71*, 396-404; b) K. S. Murray, *Coord. Chem. Rev.* **1974**, *12*, 1-35.
- [9] a) I. Shweky, A. Bino, D. P. Goldberg, S. J. Lippard, *Inorg. Chem.* **1994**, *33*, 5161-5162; b) X. Hao, Y. Wei, S. Zhang, *Transit Metal Chem.* **2001**, *26*, 384-387; c) J. Q. Liu, Y. Y. Wang, L. F. Ma, W. H. Zhang, X. R. Zeng, F. Zhong, Q. Z. Shi, S. M. Peng, *Inorganica Chim. Acta*, **2008**, *361*, 173-182; d) I. Gautier-Luneau, C. Merle, D. Phanon, C. Lebrun, F. Biaso, G. Serratrice, J. L. Pierre, *Chem. Eur. J.* **2005**, *11*, 2207-2219.
- [10] a) O. Kahn, M. C. Jay, *Science* **1998**, *279*, 44-48; b) A. Grosjean, N. Daro, B. Kauffmann, A. Kaiba, J.F. Létard, P. Guionneau, *Chem. Commun.* **2011**, *47*, 12382-12384; c) N. F. Sciortino, K. A. Zenere, M. E. Corrigan, G. J. Halder, G. Chastanet, J. F. Létard, C. J. Kepert, S. M. Neville, *Chem. Sci.* **2017**, *8*, 701-707.
- [11] a) J. G. Haasnoot, *Coord. Chem. Rev.* **2000**, *200*, 131-185; b) O. Roubeau, *Chem. Eur. J.* **2012**, *18*, 15230-15244.
- [12] a) Y. C. Chuang, C. T. Liu, C. F. Sheu, W. L. Ho, G. H. Lee, C. C. Wang, Y. Wang, *Inorg. Chem.* **2012**, *51*, 4663-4671; b) B. Ding, Y. Y. Wang, S. X. Liu, X. X. Wu, Z. Z. Zhu, J. Z. Huo, Y. Y. Liu, *CrystEngComm* **2015**, *17*, 5396-5409; c) N. F. Sciortino, F. Ragon, K. A. Zenere, P. D. Southon, G. J. Halder, K. W. Chapman, L. Piñeiro-López, J. A. Real, C. J. Kepert, S. M. Neville, *Inorg. Chem.* **2016**, *55*, 10490-10498; d) E. Milin, V. Patinec, S. Triki, E. E. Bendeif, S. Pillet, M. Marchivie, G. Chastanet, K. Boukheddaden, *Inorg. Chem.* **2016**, *55*, 11652-11661.
- [13] a) S. B. Miao, B. M. Ji, L. Zhou, *Russ. J. Coord. Chem.* **2015**, *41*, 339-344; b) Y. Y. Liu, Y. Q. Huang, W. Shi, P. Cheng, D. Z. Liao, S. P. Yan, *Cryst. Growth Des.* **2007**, *7*, 1483-1489; c) Y. Q. Huang, P. Cheng, *Inorg. Chem. Commun.* **2008**, *11*, 66-68; d) U. García-Couceiro, O. Castillo, A. Luque, J. P. García-Terán, G. Beobide, P. Román, *Eur. J. Inorg. Chem.* **2005**, *21*, 4280-4290; e) U. García-Couceiro, D. Olea, O. Castillo, A. Luque, P. Román, P. J. de Pablo, J. Gómez-Herrero, F. Zamora, *Inorg. Chem.* **2005**, *44*, 8343-8348.

Chapter 4 Three Iron Polynuclear Complexes: Magnetic Properties from a Dimer to 1D chain to 3D framework

- [14] G.A. Bain, J.F. Berry, *J. Chem. Edu.* **2008**, *85*, p. 532.
- [15] *SMART 5.0 and SAINT 4.0 for Windows NT, Area Detector Control and Integration Software*, Bruker Analytical X-Ray Systems Inc., Madison, WI, 1998.
- [16] G. M. Sheldrick, *SADABS: Program for Empirical Absorption Correction of Area Detector Data*, University of Göttingen, Göttingen, Germany, 1996.
- [17] a) G. M. Sheldrick, *Acta Crystallogr.* **2015**, *C71*, 3–8; b) G. M. Sheldrick, *SHELXTL 5.1 for Windows NT: Structure Determination Software Programs*, Bruker Analytical X-ray Systems, Inc., Madison, WI, 1997.
- [18] O. V. Dolomanov, L. J. Bourhis, R. J. Gildea, J. A. K. Howard, H. J. Puschmann, *Appl. Crystallogr.* **2009**, *42*, 339-341.
- [19] *Diamond - Crystal and Molecular Structure Visualization Crystal Impact* - Dr. H. Putz & Dr. K. Brandenburg GbR, Kreuzherrenstr. 102, 53227 Bonn, Germany.
- [20] a) T. Khan, R. Yadav, *Heterocycl. lett.* **2016**, *6*, 757-766; b) A. Kwiecień, M. Barys, Z. Ciunik, *Molecules* **2014**, *19*, 11160-11177.
- [21] a) G. De Ruiter, J. S. Costa, K. Lappalainen, O. Roubeau, P. Gamez, J. Reedijk, *Inorg. Chem. Commun.* **2008**, *11*, 787-790; b) W. T. Liu, J. Y. Li, Z. P. Ni, X. Bao, Y. C. Ou, J. D. Leng, J. L. Liu, M. L. Tong, *Cryst. Growth Des.* **2012**, *12*, 1482-1488; c) A. S. Dinca, S. Shova, A. E. Ion, C. Maxim, F. Lloret, M. Julve, M. Andruh, *Dalton Trans.* **2015**, *44*, 7148–7151.
- [22] a) J. Y. Lu, T. J. Schroeder, A. M. Babb, M. Olmstead, *Polyhedron* **2001**, *20*, 2445-2449; b) J. H. Yu, J. Q. Xu, L. J. Zhang, J. Lu, X. Zhang, H. Y. Bie, *J. Mol. Struct.* **2005**, *743*, 243-248; c) L. Wang, W. Wang, D. Guo, A. Zhang, Y. Song, Y. Zhang, K. Huang, *CrystEngComm* **2014**, *16*, 5437-5449.
- [23] A. Spek, PLATON, A Multipurpose Crystallographic Tool, Utrecht University, Holland, 1998.
- [24] (a) H.H. Thorp, *Inorg. Chem.* **31** (1992) 1585; (b) I.D. Brown, D. Altermatt, *Acta Crystallogr., Sect. B* **41** (1985) 244.
- [25] (a) C. Djordjevic, M. Lee, E. Sinn, *Inorg. Chem.* **28** (1989) 719; (b) G.B. Deacon, R.J. Philips, *Coord. Chem. Rev.* **33** (1980) 227.
- [26] E. Borello, A. Zecchina, *Spectrochimica Acta*, **1963**, *19*, 1703-1715.
- [27] Y. Prashanthi, S. Raj, *Journal of Scientific Research*, **2010**, *2*, 114–126.
- [28] a) S. C. Manna, E. Zangrando, M. G. Drew, J. Ribas, N. R. Chaudhuri, *Eur. J. Inorg. Chem.* **2006**, 481–490; b) A. K. Ghosh, D. Ghoshal, E. Zangrando, J. Ribas, N. R. Chaudhuri, *Inorg. Chem.* **2005**, *44*, 1786–1793; c) S. Mukhopadhyay, P. B. Chatterjee, D. Mandal, G. Mostafa, A. Caneschi, J. van Slageren, T. J. Weakley, M. Chaudhury, *Inorg. Chem.* **2004**, *43*, 3413–3420.
- [29] a) T. D. Keene, I. Zimmermann, A. Neels, O. Sereda, J. Hauser, M. Bonin, M. B. Hursthouse, D. J. Price, S. Decurtins, *Dalton Trans.*, **2010**, *39*, 4937–4950; b) A. Maignan, V. Hardy, S. Hébert, M. Drillon, M. R. Lees, O. Petrenko, D. McK. Paul and D. Khomskii, *J. Mater. Chem.*, **2004**, *14*, 1231–1234.
- [30] N. F. Chilton, R. P. Anderson, L. D. Turner, A. Soncini, K. S. Murray, *J. Comput. Chem.* **2013**, *34*, 1164.

**Chapter 4 Three Iron Polynuclear Complexes:
Magnetic Properties from a Dimer to 1D chain to 3D framework**

4.8 Supplementary Information

Table S4.1 Hydrogen-bonding interactions in compounds **8** and **9**.

D-H	A	H···A (Å)	D···A (Å)	<D-H···A (°)	Symmetry codes of A
Compound 8					
O1w-H1wa	O2 w	1.762	2.7714(3)	165.32	$x + 1, y, z + 1$
O1w-H1wb	O3	2.14	2.8381(3)	144	x, y, z
O2w-H2wa	O1	2.00	2.8357(3)	166	x, y, z
O2w-H2wb	O1 w	2.465	2.8078(3)	103	$x - 1, -y + 2, z - 0.5$
N5-H5a	O2	2.189	2.9294(3)	141	$x, -y + 1, z - 0.5$
C1-H1	O1	2.514	3.0272(3)	115	$x + 1, -y + 1, z - 0.5$
C1-H1	O2 w	2.544	3.3430(2)	144	$x + 1, y - 1, z$
C2-H2	O4	2.426	3.1069(3)	130	$x + 1, -y + 2, z - 0.5$
C3-H3	O1 w	2.467	3.2011(3)	136	$x, y, z - 1$
C6 -H6	O3	2.56	3.0841(2)	116	$x, -y + 2, z - 0.5$
Compound 9					
O1w-H1wb	O2 w	1.766	2.5877(4)	153	x, y, z
O2w-H2wa	O3	2.051	2.7361(4)	135	$x + 1, y - 1, z$
O2w-H2wb	O4 w	2.212	2.8172(4)	126	$x + 1, y - 1, z$
O2w-H2wb	O2 w	2.204	2.7873(4)	124	$-x + 2, -y - 1, -z + 1$
N5-H5	O6	1.911	2.7775(4)	168	$x, y + 1, z - 1$
O3w-H3wa	O2	2.022	2.8463(4)	158	x, y, z
N6-H6	O1	1.871	2.7224(4)	162	x, y, z
O3w-H3wb	O4 w	2.336	2.8545(4)	118	x, y, z
O4w-H4wa	O6	2.454	2.8739(4)	110	$-x + 1, -y + 1, -z + 1$
C1-H1	O4 w	2.543	3.1975(5)	126	$x + 1, y, z$
C2-H2	O3 w	2.358	3.1755(5)	144	$-x + 1, -y + 2, -z$
C3-H3	O4 w	2.592	3.2410(5)	126	$x + 1, y, z$
C5-H5a	O3	2.250	3.0974(5)	148	$-x + 1, -y + 1, -z + 1$
C6-H6a	O2	2.391	3.2183(5)	145	$-x + 1, -y + 1, -z$
C6-H6a	O7	2.431	3.0134(5)	119	$x, y + 1, z - 1$
C11-H11a	O3	2.624	3.4879(6)	145	$-x + 1, -y + 1, -z + 1$
C8-H8a	O3	2.527	3.2920(5)	134	$-x + 1, -y + 1, -z + 1$

Chapter 5 Two 2D Fe^{II} Networks Built Up from Imztrz: Antiferromagnetic v.s. Ferromagnetic Interaction

This chapter covers the summary results of two 2D Fe^{II} network complexes based on ligand 2 (5-imztrz) and ligand 3 (2-imztrz), which is manuscripted to the journal submission of *Cryst. Growth Des.* Manuscript detailing will be presented in the following:

Self-assembled 2D Fe(II)-imidazole-imine networks: Structural, Mössbauer, and Magnetic Properties of $[Fe^{II}_2(2\text{-imztrz})_4(SCN)_4]_{\infty}$ and $\{[Fe^{II}(5\text{-imztrz})_2](ClO_4)_2\}_{\infty}$

Ai-Min Li,^{a,b} Tim Hochdörffer,^c Dr. Juliusz A. Wolny^c, Volker Schünemann^c and Eva Rentschler^{a*}

^a Institute of Inorganic and Analytical Chemistry, Johannes Gutenberg University Mainz, Duesbergweg 10-14, 55128 Mainz, Germany

rentschler@uni-mainz.de

^b Graduate School Materials Science in Mainz, Staudingerweg 9, D-55128 Mainz, Germany

^c Fachbereich Physik, Technische Universität Kaiserslautern, Erwin-Schrödinger-Str. 46, 67663 Kaiserslautern, Germany

KEYWORDS 2D / iron(II) / 1,2,4-triazole / Schiff bases / Mössbauer

5.1 Abstract

Based on two functionalized Schiff base ligands 4-(1*H*-imidazol-5-ylmethylene-amino)-4*H*-1,2,4-triazole (5-imztrz) and 4-(1*H*-imidazol-2-ylmethylene-amino)-4*H*-1,2,4-triazole (2-imztrz), two 2D Fe(II) networks have been prepared. Compound **10** and **12** share similar layered structures. Surprisingly, the two 2D networks do not show SCO upon cooling to 2K. A reason might be that the ancillary coordinated nitrogen atoms from the imidazole ring leading to a rather small ligand field around the Fe centers. Pleasantly, compound **12** was found to show ferromagnetic exchanging interactions through the imidazole and imine linkage, while compound **10** acted like isolated mononuclear Fe (II) complex showing weak antiferromagnetic exchanging interactions mediated by supramolecular interactions.

5.2 Introduction

The design and preparation of molecule-based coordination polymers with one- or multi-dimensional structures has attracted intense attention during the last few years. Such high dimensional coordination complexes might not only exhibit structural and topological novelty but also provide valuable information to explore fundamental magnetic interactions

and magneto-structural correlations in molecular systems. Applications have been found in the field of molecular magnetism, nonlinear optical and multiferroic materials. ^[1] It is well-known that the various supramolecular interactions ($\pi\cdots\pi$ stacking, H-bonding, and van der Waals) in the solid packing structure play an important role as information transmitters and, therefore, have a large impact on the intermolecular magnetic exchange. On the other hand, to design and synthesize new molecular extended architectures based on non-covalent interactions is very challenging as those supramolecular interactions are often unpredictable and difficult to control. In contrast, first introduced by Olivier Kahn, ^[2] the idea of linking the active metal sites covalently to increase the cooperativity in polymeric compounds is more feasible. The nature of the covalent bridging ligand and metal ions mainly determines the sign and magnitude of the magnetic exchange coupling between the active metal centers. ^[3] There are only a few polyatomic bridging ligands, i.e, cyanide (CN⁻), ^[4] oxalate (C₂O₄²⁻), ^[5] azido (N₃⁻), ^[6] pyrazine (pz), ^[7] and 4,4'-bipyridine (bpy) ^[8] have been shown effectively mediating rather strong magnetic coupling between the transition metal ions that, in some cases, leads to bulk magnetic ordering. Consequently, there is still a great interest in the search for new bridging ligands that can construct new magnetic materials with intriguing structures and magnetic properties.

The imidazole and imidazolyl-containing ligands have been widely used in coordination chemistry due to their versatility in the preparation of polynuclear complexes. ^[9] More recently, imidazole-imine moiety based ligands have been applied to design-synthesize polynuclear metal complexes, especially on spin crossover materials. Particular attention has been focused on the construction of various supramolecular structures such as molecular clusters (monomer, dimer, tetramer), ^[10] cylindrical molecular boxes, ^[11] molecular cages, ^[12] and helical structures. ^[13] Surprisingly, apart from the only example of one dimensional Cu(II) chain structure reported in 1998 with a salicylic phenol group mediated, there is no other high dimensional structure reported within this kind of ligand. The possible reason could be the same as the story of the famous one dimensional chain SCO model [Fe((Rtrz)3)(X)2 (Rtrz = 4-substituted-1,2,4-triazole, X⁻ = standard monoanions) ^[14]: that the isolation of the crystalline complex of the polynuclear chain or network is very challenging as compared to the molecular structures.

As part of our research for novel SCO materials based on triazole ligand system, we decided to combine the imidazole moiety with 4-amino-1,2,4-triazole in order to prepare new high dimensional Fe(II) magnetic materials making use of both triazole and imidazole-imine potential coordination sites. In this manner, the formed layered structures are covalently

Chapter 5 Two 2D Fe^{II} Networks Built Up from Imztrz: Antiferromagnetic v.s. Ferromagnetic Interaction

connected through the bridging ligand, with the Fe centers surrounded by ligands with suitable ligand strength to allow the spin transition. In addition, this approach should maintain the effective magnetic exchange within the layered plane, allowing possible enhancement of the cooperativity between the active Fe(II) centers. As shown in scheme 1, two new ligands 4-(1H-imidazol-5-ylmethylene-amino)-4H-1,2,4-triazole (5-imztrz, ligand 1) and 4-(1H-imidazol-2-ylmethylene-amino)-4H-1,2,4-triazole (2-imztrz, ligand 2) have been synthesized via a simple condensation reaction. Apart from the well-known virtue of a rather weak ligand field provided by imidazole moiety and the potential H-bond interactions from the ‘spare’ N–H groups, these two imidazole-imine ligands share another advantage: the N–C(*sp*²) σ bonds can be rotated, which makes the ligands more flexible to adapt to different coordination environment. As the energies of intramolecular torsion and intermolecular non-bonded interaction lie in the same range (0.5-10 kcal mol⁻¹), [15] they can influence each other and hence the crystal packing in the solid state compounds.

In this paper we present the application of the two new ligands (2-imztrz, 5-imztrz) to synthesize two layered network $[Fe^{II}_2(2\text{-imztrz})_4(SCN)_4]$ (**10**) and $[Fe^{II}(5\text{-imztrz})_2](ClO_4)_2$ (**12**). Despite both of both Fe(II) ions being in the appropriate $[FeN_6]$ coordination environment, these two materials are SCO-inactive, remaining in the HS state on cooling to low temperature. Compound **12** shows ferromagnetic exchanging interactions through the imidazole and imine linkage, while compound **10** acts as isolated Fe (II) ions showing weak antiferromagnetic interactions mediated by supramolecular interactions in the crystal lattice.

5.3 Experimental Section

General Methods and Materials.

All commercially purchased chemicals and solvents from Alfa Aesar, Sigma–Aldrich and Acros Organics were used without further purification. Magnetic susceptibility measurements were carried out with a Quantum Design SQUID magnetometer MPMS XL-7 over the temperature range of 2~300 K with an applied field of 1 kOe. Samples for the magnetic measurement were prepared in gelatin capsules and held in plastic straws for insertion into the magnetometer. The obtained magnetic susceptibility data were corrected for diamagnetic susceptibility according to the Pascal’s constants. [16] ⁵⁷Fe Mössbauer spectra were recorded and analyzed by fitting to Lorentzian lines at Technische Universität Kaiserslautern by Dr. Juliusz A. Wolny. Elemental analysis (C, H, N, and S) was measured at the microanalytical laboratories of the Johannes Gutenberg University Mainz. Infrared

spectra (FT-IR) were recorded as potassium bromide pellets in the range from 4000 to 400 cm⁻¹ with a JASCO FT/IR-4200 at the Johannes Gutenberg-University Mainz.

Single Crystal X-ray Diffraction. Single-crystal X-ray diffraction data for the two compounds (**C10** and **C12**) were collected on a Bruker Smart APEX II CCD diffractometer, with operating condition: 45 kV, 35 mA, 173(2) K and Mo K α radiation ($\lambda = 0.71073 \text{ \AA}$). The the data collection temperature 173(2) K was reached by the application of a nitrogen cold stream around the diffractometer. Each data reduction was performed using the SMART and SAINT software [17] and an empirical absorption correction was applied using the SADABS program. [18] Both of the two structures were solved by direct methods and refined by full-matrix least-squares on F^2 using the SHELXTL program package, [19] and the Olex2 program. [20] The ordered non-hydrogen atoms in each structure were refined with anisotropic displacement parameters, while the hydrogen atoms were placed in idealized positions and allowed to ride on their parent atoms. The crystallographic data and refinement parameters of compound **10** and **12** are listed in Table 5.1. CCDC numbers 1815516-1815517 contain the supplementary crystal data of the compounds: 1815516 (**C10**) and 1815517 (**C12**), which can be obtained free of charge from The Cambridge Crystallographic Data Centre via www.ccdc.cam.ac.uk/data_request/cif. All structure figures are generated with DIAMOND-3. [21]

Syntheses

Synthesis of the ligand

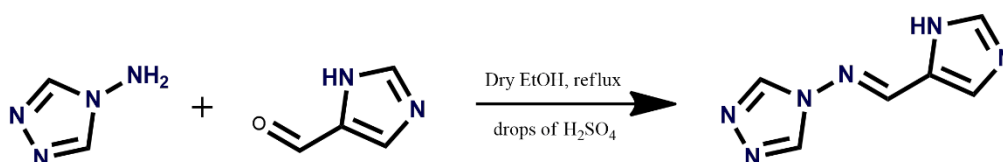


Figure 5.1.: Synthetic scheme to prepare the 5-imztrz ligand.

The ligand 4-(1H-imidazol-5-ylmethylene-amino)-4H-1,2,4-triazole (5-imztrz) (Figure 5.1) was prepared by the condensation reaction of 4-amino-1,2,4-triazole (1.68 g, 0.02 mol, 1.0 eq.) and 1H-imidazole-4-carbaldehyde (2.11 g, 0.022 mol, 1.1 eq.). [22] Ethanol was chosen as the reaction solvent, and few drops of H₂SO₄ was added acting as acidic catalyst. The reaction mixture was refluxed at 80 °C for 18 h before cooled it down to r.t., the excess of the solvent was removed by rotary evaporator at 35 °C. Products such obtained was washed with small amount of cold ethanol, diethyl ether and then dried in the desiccator with phosphorus pentoxide as dry agent. Light-yellow powder was obtained. Yield: 2.98 g (91.89%), m.p.253.5–265.7 °C; IR (KBr) 3109(s), 2838 (w), 1625 (vs), 1504 (vs), 1434 (s),

Chapter 5 Two 2D Fe^{II} Networks Built Up from Imztrz: Antiferromagnetic v.s. Ferromagnetic Interaction

1386 (s), 1299 (s), 1214 (w), 1175 (vs), 1060 (vs), 995 (s), 945 (w), 853 (s), 691 (m), 630 (vs), 510 (m). ¹H-NMR (Figure 9.2) (*d*⁶-DMSO): 9.07 (s, 2H, triazole), 8.92 (s, 1H, H-C=N), 7.91 (s, 1H, imidazole ring), 7.79 (s, 1H, imidazole ring).

The ligand 4-(1*H*-imidazol-2-ylmethylene-amino)-4*H*-1,2,4-triazole (2-imztrz) was prepared in a similar manner, except changing of 1*H*-Imidazole-4-carbaldehyde (2.11 g, 0.022 mol) to 2-imidazolecarboxaldehyde (2.11 g, 0.022 mol). Light-yellow powder obtained. 2.56 g (15.80 mmol, 78.98 %). M.p. 217.6–233.5 °C; IR (KBr): 3115(vs), 3005 (m), 2795 (m), 2711 (m), 1622 (s), 1515 (vs), 1440 (vs), 1348 (s), 1233 (w), 1189 (vs), 1159 (s), 1120 (vs), 1056 (vs), 985 (s), 931 (w), 853 (vs), 781 (vs), 705 (vs), 618 (s), 509 (w). ¹H-NMR (Figure 9.3) (*d*⁶-DMSO): 13.33 (s, H-N_{imidazole}), 9.16 (s, 2H, triazole), 8.96 (s, 1H, H-C=N), 7.45 (s, 1H, imidazole ring), 7.27 (s, 1H, imidazole ring).

Synthesis of the Complex

Synthesis of [Fe^{II}₂(2-imztrz)₄(SCN)₄] (C10)

To a stirring solution of 2-imztrz (129 mg, 0.8 mmol) in methanol (5 mL) was added an aqueous solution of FeSO₄·7H₂O (112 mg, 0.4 mmol), together with NH₄SCN (61 mg, ~ 0.8 mmol). The solution turned from colorless to light reddish immediately after the addition. After stirring for half hour, one spatula-amount (~35 mg) of ascorbic acid was added to the reaction solution. The reaction mixture was then stirred for 3~4 hours at room temperature before filtrated with rapid filter paper. The obtained clear dark reddish solution was kept in a small vial and left stand still to evaporate the solvent slowly. After two weeks, red block crystals of C10 were deposited at the bottom and the wall of the vial. After removing the mother liquid, the single crystals were picked up and blew with an argon stream to dryness before stored in a small vial. Yield: 107.3 mg (54.05% based on Fe). Anal. Calcd (Found) for C₁₄H₁₂FeN₁₄S₂: C, 33.88 (29.38); H, 2.44 (2.37); N, 39.51 (37.99). IR (KBr) cm^{-1} : 3134 (m), 3020 (w), 2925 (m), 2854 (w), 2809 (w), 2718 (w), 2057 (vs), 1626 (s), 1517 (s), 1463 (s), 1447 (s), 1385 (m), 1357 (m), 1297 (w), 1205 (w), 1177 (m), 1155 (s), 1113 (s), 1084 (s), 1057 (s), 996 (m), 945 (m), 858 (m), 778 (s), 708 (m), 633 (m), 616 (s).

Synthesis of [Fe^{II}(5-imztrz)₂](ClO₄)₂ (C12)

A methonolic solution of Fe(ClO₄)₂·7H₂O (112 mg, 0.4 mmol) was added dropwisely into a stirring solution of 5-imztrz (129 mg, 0.8 mmol) in methanol (5 mL). The reaction solution turned from light yellow to light green immediately after the addition. The reaction was kept stiring at room temperature for half hour before added one spatula-amount (~35 mg) of ascorbic acid. The mixture was then stirred for another 3 hours to let the complexation finish. A clear greenish to reddish solution was obtained after filtration, and such solution was kept

**Chapter 5 Two 2D Fe^{II} Networks Built Up from Imztrz:
Antiferromagnetic v.s. Ferromagnetic Interaction**

in a small vial and left stand still to allow the solvent evaporate slowly. Light yellow block crystals of **C12** were deposited at the bottom of the vial after three weeks. After removing the mother liquid, the single crystals were quickly dried in an argon stream, and stored under argon. Yield: 117.46 mg (50.71% based on Fe). Anal. Calcd (Found) for C₃₉H₃₅Fe₂N₂₉O₄S₄: C, 24.89 (24.32); H, 2.09 (2.04); N, 29.03 (28.47). IR (KBr) ν/cm^{-1} : 3296 (s), 3122 (s), 1627 (vs), 1612 (vs), 1516 (s), 1454 (w), 1431 (s), 1384 (s), 1300 (m), 1280 (m), 1217 (m), 1185 (s), 1141 (s), 1121 (vs), 1095 (vs), 961 (s), 927 (m), 869 (s), 799 (w), 715 (s), 624 (vs), 531 (w).

5.4 Result and discussion

5.4.1 Structural Description

Crystallographic data for the compounds **10** and **12** are summarized in Table 5.1 and the selected bond lengths and angles are presented in Table 5.2.

Table 5.1. Crystallographic Data and Refinement Parameters for compounds **10** and **12**.

Compound	C10	C12
Empirical formula	C ₂₈ H ₂₄ Fe ₂ N ₂₈ S ₄	C ₁₂ H ₁₂ Cl ₂ FeN ₁₂ O ₈
Formula weight	992.69	579.09
Crystal size	0.16 x 0.15 x 0.03	0.2 x 0.1 x 0.05
Crystal system	Monoclinic	Monoclinic
Space group	<i>P12/c1 (No. 13)</i>	<i>C12/c1 (No. 15)</i>
<i>a</i> (Å)	11.963(3)	22.438(6)
<i>b</i> (Å)	12.941(3)	14.453(3)
<i>c</i> (Å)	17.899(4)	15.417(7)
α (°)	90	90
β (°)	126.517(12)	123.430(5)
γ (°)	90	90
<i>V</i> (Å ³)	2227.0(10)	4173(2)
<i>Z</i>	2	8
<i>D</i> _{calc} (g/cm ³)	1.480	1.844
μ (Mo-K α) (mm ⁻¹)	0.898	1.052
<i>F</i> (000)	1008	2336
Reflections collected	6305	19208
Independent reflections	5332 (0.2444)	5007 (0.0923)
Parameters	282	316
Goodness-of-fit	1.039	0.898
<i>R</i> ₁ [<i>I</i> > 2 σ (<i>I</i>)] ^a	0.1166	0.0468
<i>wR</i> ₂ (all data) ^b	0.3321	0.1128

^a $R_1 = \Sigma ||F_o| - |F_c|| / \Sigma |F_o|$, ^b $wR_2 = \{ \Sigma [w(F_o^2 - F_c^2)^2] / \Sigma [w(F_o^2)^2] \}^{1/2}$

Crystal structure of [Fe^{II}₂(2-imztrz)₄(SCN)₄] (C10)

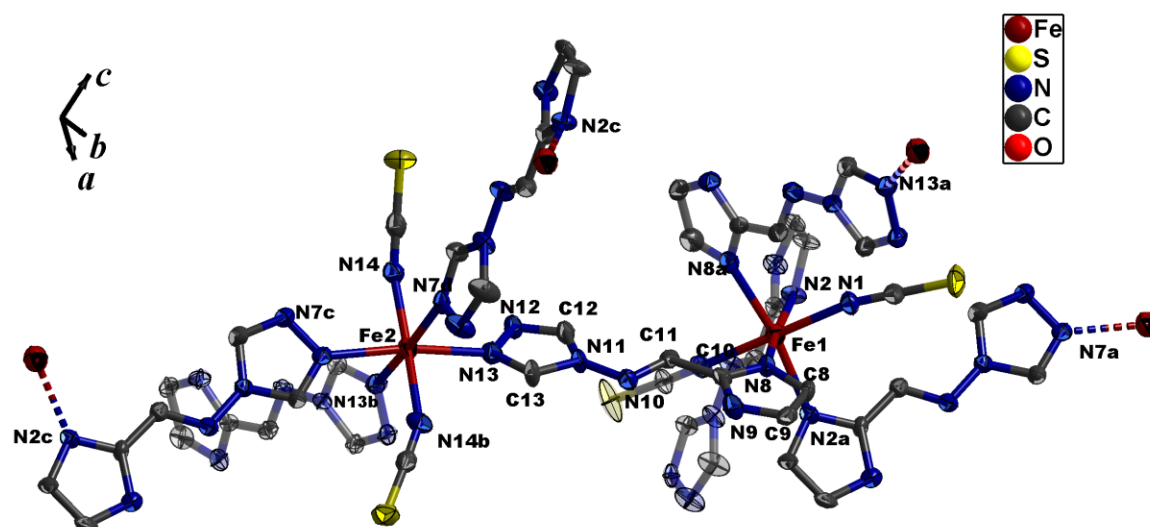


Figure 5.2.: Illustration of the coordination sphere of iron(II), showing the atom numbering. Only selected atoms involved in coordination bonds are labelled for clarity. A = -x, y, -z - 0.5; b = -x -1, y, -z - 1.5; c = -x -1, y -1, -z - 1.5; d = x, y -1, z.

Compound **10** crystallizes in monoclinic space group $P12/c1$. The structure is made up of parallel 2D sheets, each consisting of an infinite square array of iron atoms bridged by bimonodentate 2-imztrz ligands, with monodentate N-binding thiocyanate anions facilitating the pseudo-octahedral configuration around each iron atom (Figures 5.2 and 5.3). Within the asymmetrical unit, there are two independent Fe (II) coordinate sites: Fe1 and Fe2. As illustrated in figure 2, Fe1 is surrounded by four N atoms from the imidazole rings, while four N atoms from the triazole rings gather around Fe2. The 2-imztrz ligand such adopts a bimonodentate coordinate mode, forming the basal plane of the 2D network. The axial positions are occupied by thiocyanate N atoms. Very interestingly, as the N atoms coming from triazole ring and imidazole ring own different coordinate direction, the auxiliary thiocyanate ligands around Fe1 and Fe2 face to each other in a perpendicular arrangement: the ones surrounding Fe1 lies within the plane, while the ones surrounding Fe2 atoms occupies the axial positions. (Figure 5.3) The basic rhombus unit has a Fe...Fe distance of 9.617 (8) Å x 9.778(8) Å, the shortest contacts within the diamond being 4.789 (2) Å (S...S).

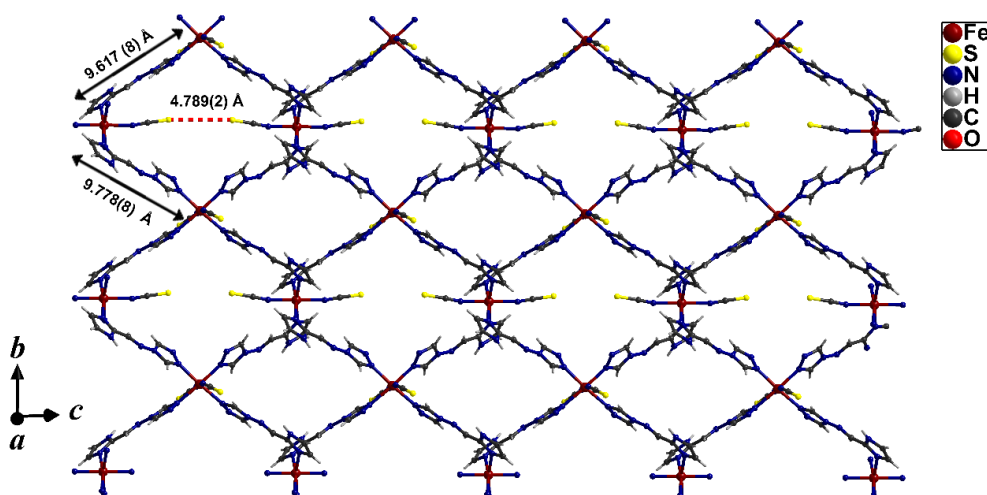


Figure 5.3.: View of the 2D sheet of $[\text{Fe}^{\text{II}}_2(2\text{-imztrz})_4(\text{SCN})_4]_n$, along bc plane.

The average Fe1–N bond length of 2.182 (7) Å is slightly longer than the average of Fe2–N bond length of 2.180(7) Å. (Table 5.2) While in both cases, the bond length range makes the Fe centers sitting well in the range expected for high-spin state at 173 K. [23] The HS-state is further confirmed by magnetic measurement. The NCS⁻ anions are almost linear with the N–C–S having an angle around 178.3(10)° and 177.1(10)°; the Fe–N–C(S) linkages are bent, with the angle of Fe···N–C being around 168.1(8)° and 156.4(8)°. (Table 5.2) These structural data can be compared with the other two compounds (C1, C5) where the terminal NCS group are N-bonded. The dihedral angles between the triazole ring and the imidazole ring within the independent 2-imztrz molecules are 4.45° (N2 containing) and 9.88° (N8 containing), respectively, indicating a slight distortion between the imine linkage.

Table 5.2 Selected bond lengths [Å] and angles [°] for C10 and C12.

Compound 10					
Fe(1)-N(1)	2.126(7)	Fe(1)-N(8)	2.194(8)	Fe(2)-N(13)	2.186(8)
Fe(1)-N(2)	2.228(8)	Fe(2)-N(7)#2	2.236(7)	Fe(2)-N(14)	2.117(8)
N(1)#1-Fe(1)-N(2)	94.0(3)	N(8)#1-Fe(1)-N(2)	86.6(3)	N(13)#4-Fe(2)-N(13)	94.9(4)
N(1)-Fe(1)-N(2)	85.6(3)	N(8)#1-Fe(1)-N(8)	91.2(4)	N(14)#4-Fe(2)-N(7)#2	85.0(3)
N(1)#1-Fe(1)-N(8)	94.4(3)	N(7)#3-Fe(2)-N(7)#2	99.9(4)	N(14)-Fe(2)-N(7)#2	92.7(3)
N(1)-Fe(1)-N(8)	86.1(3)	N(13)-Fe(2)-N(7)#2	83.1(3)	N(14)#4-Fe(2)-N(13)	94.9(3)
N(2)#1-Fe(1)-N(2)	96.8(4)	N(1)-C(1)-S(1)	178.3(10)	N(14)-Fe(2)-N(13)	87.6(3)
C(14)-N(14)-Fe(2)	156.4(8)	N(14)-C(14)-S(2)	177.1(10)	C(1)-N(1)-Fe(1)	168.1(8)
Compound 12					
Fe(1)-N(1)	2.131(3)	Fe(1)-N(5)#5	2.109(3)	Fe(1)-N(9)	2.410(3)
Fe(1)-N(3)	2.264(3)	Fe(1)-N(7)	2.158(3)	Fe(1)-N(11)#6	2.153(3)
N(1)-Fe(1)-N(3)	74.51(10)	N(5)#5-Fe(1)-N(1)	94.99(11)	N(7)-Fe(1)-N(3)	94.83(11)
N(1)-Fe(1)-N(9)	93.57(11)	N(5)#5-Fe(1)-N(7)	92.78(12)	N(7)-Fe(1)-N(9)	72.21(11)
N(1)-Fe(1)-N(11)#6	100.76(12)	N(5)#5-Fe(1)-N(9)	89.03(10)	N(11)#6-Fe(1)-N(3)	89.94(10)
N(3)-Fe(1)-N(9)	80.63(10)	N(5)#5-Fe(1)-N(11)#6	103.22(11)	N(11)#6-Fe(1)-N(7)	91.37(12)

Symmetry transformations used to generate equivalent atoms: #1 = -x, y, -z - 1/2; #2 = x, y - 1, z; #3 = -x - 1, y - 1, -z - 3/2; #4 = -x - 1, y, -z - 3/2; #5 = -x + 1/2, y - 1/2, -z + 1; #6 = x, -y + 1, z - 1/2.

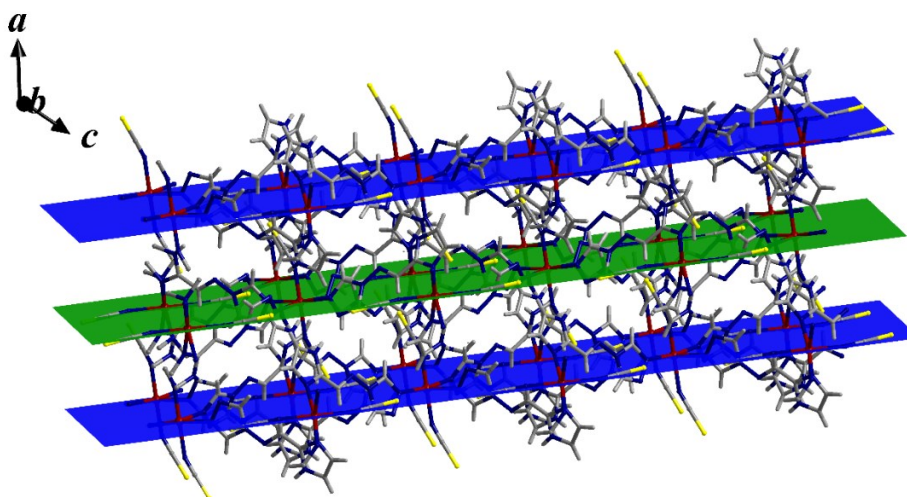


Figure 5.4.: Illustration of the layered packing in compound **10**. The colored plane represent the 2D sheets shared by the Fe(II) atoms along *bc* axis. Supramolecular interactions were found between the layers.

In compound **10**, the adjacent 2D sheets are interconnected through different groups of supramolecular interactions. (Figure 5.4) The thiocyanate anions that lie in the axial positions around Fe2 is now linked to the adjacent layer via a group of S \cdots π N13a-ring interaction ($a = x, -y - 2, z - \frac{1}{2}$; S \cdots centroid distance of 3.739(8) Å). Another two groups of H-bonding interaction are also found to link the adjacent layers: N3-H3 \cdots N12b (H3 \cdots N12b distance of 2.030(5) Å, N3 \cdots N12b distance of 2.8670(7) Å, $b = -x - 1, -y - 1, -z - 1$); N9-H9 \cdots N6c (H9 \cdots N6c distance of 1.991(3) Å, N9 \cdots N6c distance of 2.824(4) Å, $c = -x, -y - 1, -z$). The sheets alternate so that the iron atoms in one sheet lie vertically above and below the centers of the squares formed by the iron atoms of adjacent sheets, leading to a nonporous 3D supramolecular framework, with the shortest Fe \cdots Fe distance between the layers being 8.740(9) Å. (Figure 5.4, Figure 5.5)

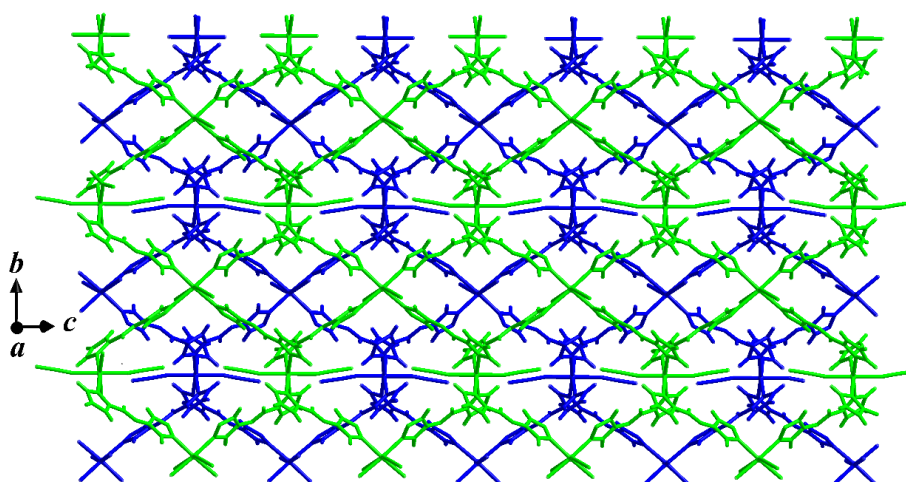


Figure 5.5.: The 2D alternated sheets arrangement in compound **10**.

Crystal structure of [Fe^{II}(5-imztrz)₂](ClO₄)₂ (**C12**)

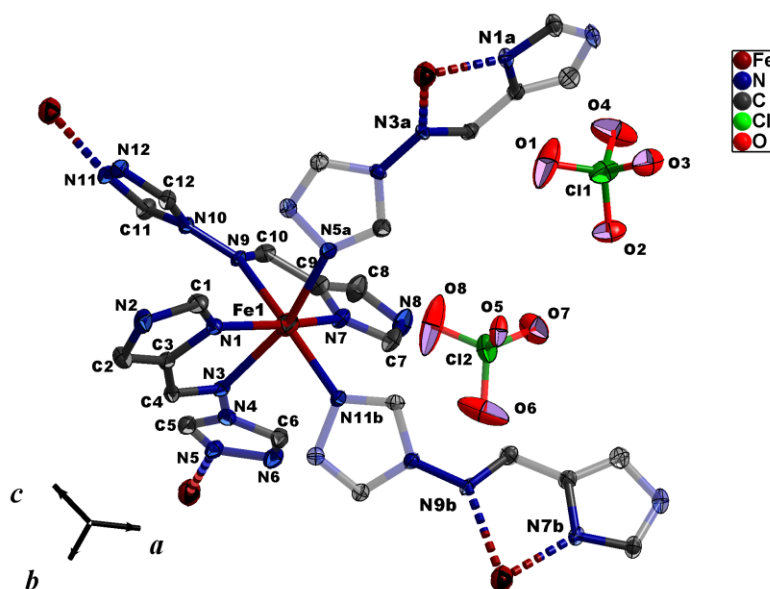


Figure 5.6.: View of the asymmetric units in **C12** at 173 K, showing the coordination mode of the ligand 5-imztrz and the pseudo-octahedral configuration around the Fe(II) center. Only selected atoms are labelled for clarity. $a = -x + 0.5, y - 0.5, -z + 0.5$; $b = x, -y + 1, z - 0.5$.

The atomic numbering scheme and coordinate environment for **C12** are shown in figure 5.6. The structure was refined in the monoclinic $C12/c1$ space group and crystallographic detailed data are listed in Table 5.1. Within the structure, each Fe(II) ion is located on an inversion center exhibiting a distorted octahedral [FeN₆] geometry. The ligand 5-imztrz adopts a tridentate coordinate mode to complete the pseudo-octahedral configuration. Firstly, four positions of the coordination sphere are occupied by two chelating 5-imztrz ligands. Each of these ligands is bound to the Fe(II) ion through one of the imidazolyl nitrogen atoms (N1, N7) and the Schiff base nitrogen atoms in *cis* position (N3, N9), giving rise to a stable five-membered chelate ring. Then another two triazole nitrogen atoms (N5a, N11b) from the two neighbouring [Fe(5-imztrz)₂] units complete the slightly compressed geometry, with the in-plane equatorial positions defined by the four nitrogen atoms from the triazole and Schiff base groups (Figure 5.7). The Fe–N bond distances are in the range 2.109(3)–2.410(3) Å, whereas *cis* N–Fe–N angles are in the range 72.21(11)–103.22(11)°. Unlike in compound **10**, the dihedral angles between the triazole ring and the imidazole ring within the independent 5-imztrz molecules here are 36.25 (N1 containing) and 31.77° (N7 containing), respectively, indicating a large distortion between the imine linkage to favor the compressed octahedral geometry.

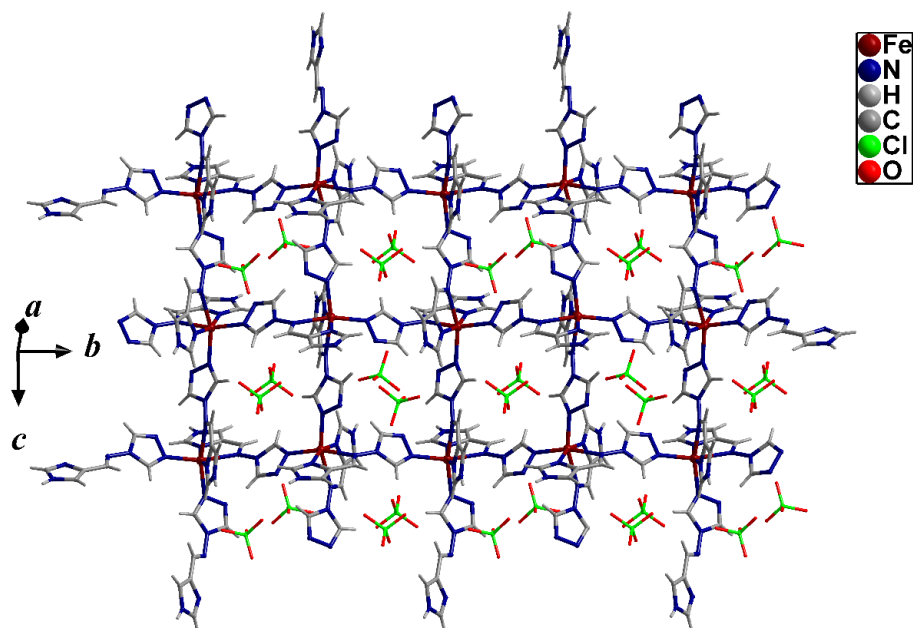


Figure 5.7.: The layered structure along bc plane in compound **12**, with perchlorate anions embedded in the grid among the plane.

Two Fe(II) ions are bound together via a tridentate bridging 5-imztrz ligand, and the linked Fe(II) ion is further connected to three other Fe(II) ions by another three 5-imztrz ligands, thus generating near-square grid-like sheets parallel to the bc plane (Figure 5.7). Within the $\{\text{Fe}_4\}$ units, the intralayer Fe...Fe separations through the triazolate rings are 7.390(8) Å and 7.740(9) Å, forming a porous grid with perchlorate anions embedded inside.

Table 5.3. Hydrogen-bonding interactions in compound **12**.

D-H	A	H...A (Å)	D...A (Å)	$\angle\text{D-H}\cdots\text{A}$ (°)	Symmetry codes of A
N2-H2	N12	2.355	2.987(3)	130.63	$-x, y, -z + \frac{1}{2}$
N2-H2	O6	2.499	3.224(3)	142.52	$-x + \frac{1}{2}, -y - \frac{1}{2}, -z + \frac{1}{2}$
N8-H8	O5	1.958	2.792(2)	163.14	x, y, z
C5-H5	O2	2.472	3.399(3)	175.46	$x - \frac{1}{2}, y + \frac{1}{2}, z$
C7-H7	O5	2.489	3.053(3)	119.78	$-x + 1, y, -z + \frac{1}{2}$
C10-H10	O2	2.516	3.370(3)	153.49	$-x + 1, -y + 1, -z + 1$
C11-H11	O2	2.544	3.372(3)	147.85	$-x + 1, -y + 1, -z + 1$
C12-H12	O6	2.518	3.127(3)	123.37	$x - \frac{1}{2}, y - \frac{1}{2}, z$
C12-H12	N6	2.447	3.175(3)	135.27	$-x + \frac{1}{2}, y - \frac{1}{2}, -z + \frac{1}{2}$

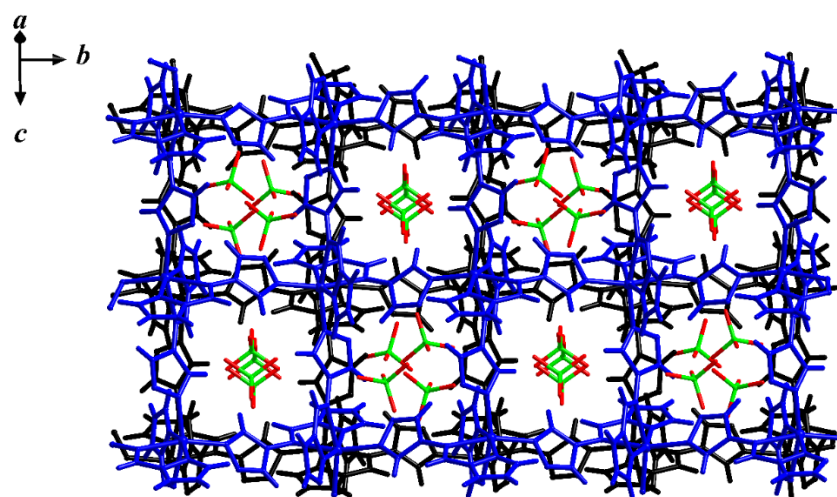


Figure 5.8.: The 2D network stacked perpendicularly along *a* axis in compound **12**.

Unlike the case for compound **10**, where the adjacent sheets are alternatively arranged between the layers, a close packing framework is formed. Herein, for compound **2**, the 2D sheets are stacked to each other in a perpendicular direction so that the formed framework indeed has a minor porous character, with perchlorate anions embedded inside the channel. (Figure 5.8) The ClO_4^- is bound to the adjacent 5-imztrz ligands from different layers via multiple groups of H-bonding interactions. (Table 5.3) Additionally, a group of face-to-face $\pi_{\text{imidazole}} \cdots \pi_{\text{imidazole}}$ stacking was found to strengthen the packing between the adjacent layers (centroid \cdots centroid distance of 3.587(6) Å). (Figure 5.9) The rather intense $\pi \cdots \pi$ stacking from the imidazole rings and H-bonding with ClO_4^- involved lead to a shortest Fe \cdots Fe distance between the layers of 8.051(5) Å, obviously shorter than that value in compound **10** (8.740(9) Å).

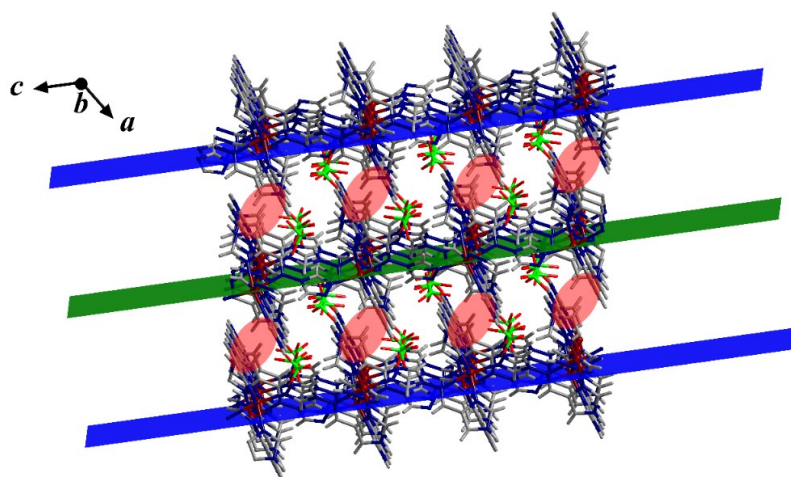


Figure 5.9.: Illustration of the layered packing in compound **12**. The colored plane represent the 2D sheets shared by the Fe(II) atoms along *bc* axis. Supramolecular interactions were found between the layers, and the red circles represent the $\pi \cdots \pi$ stacking between the layers.

5.4.2 FT-IR spectroscopy

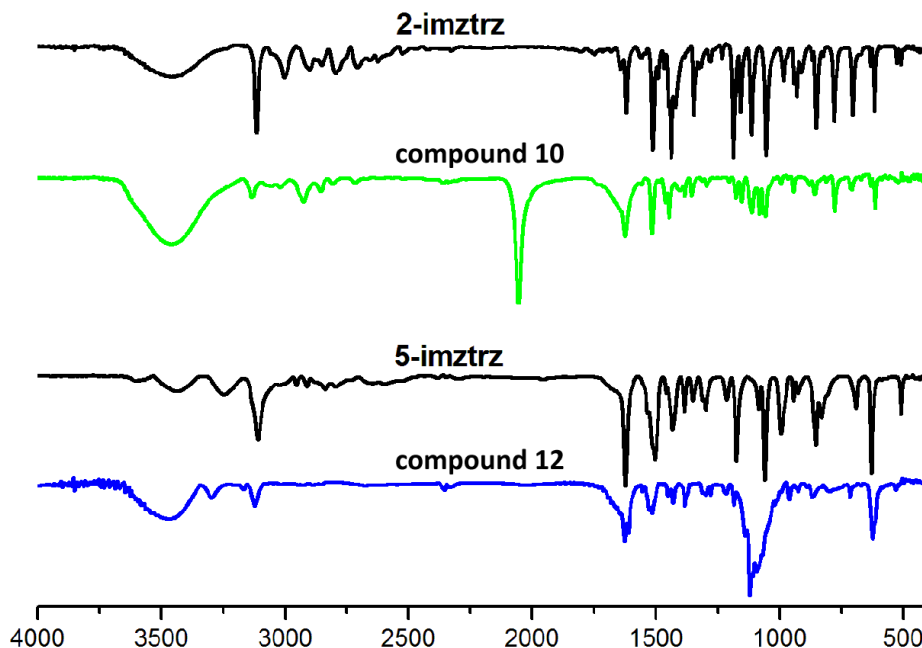


Figure 5.10.: The FT-IR spectra of ligand 5-imztrz, 2-imztrz and compounds **10**, **12**.

The FT-IR spectra of the two compounds indicate that the ligand imztrz almost exhibit the same vibration to that of the free ligand. As shown in Figure 5.10, the spectra of compound **10** and compound **12** are very similar compared to the corresponding ligand 2-imztrz and 5-imztrz. However, some significant changes could be identified due to the coordination of the compound. The bands 3115 (2-imztrz), 3109 (5-imztrz), 3134 (**C10**), 3122 (**C12**) cm^{-1} and 1626-1297 cm^{-1} (1626, 1517, 1447 and 1385 for **C10**; 1612, 1516, 1431 and 1384 for **C12**) are attributable to the C-H, C_{ar}-C_{ar}, and C_{ar}=N stretching vibration frequencies of the aromatic group. The peaks at 1515 (**2-imztrz**) cm^{-1} and 1518 (**C12**) cm^{-1} can be ascribed to the characteristic band for the triazole ω -ring vibration. The corresponding peaks show up at 1503 cm^{-1} for ligand 5-imztrz and 1515 cm^{-1} for compound **12**. The relative hypsochromic shift in the compounds compared to the free ligand indicates the N-donor coordination to the Fe metal centers. ^[24] In addition, the peaks at 1177 (m), 1057 (s), and 778 (s) for **C10**; 1185 (s), 1095 (vs), and 715 (s) cm^{-1} can be assigned to the C-H in-plane or out-of-plane bend ring breathing, and ring deformation absorptions among the organic ligands. The spectrum of **C10** showed strong C=N stretching at 2057 cm^{-1} suggesting the present of the thiocyanate in the compounds. ^[25] Moreover, the peaks at 1141 (s), 1121 (vs) and 624 (vs) in the spectrum of **C12** can be assigned to the signature bands for the perchlorate counteranion.

5.4.3 Magnetic properties and Mössbauer Spectroscopy

As shown in figure 5.11, the variable-temperature magnetic susceptibility data of compound **10** has been recorded in the temperature range 300–2 K. At the temperature of 300 K, the $\chi_{\text{M}}T$ value of $6.05 \text{ cm}^3 \cdot \text{K} \cdot \text{mol}^{-1}$ can be ascribed to the corresponding two high spin Fe(II) ions in the crystallographic smallest unit. This value remains almost constant around $6.05 - 5.98 \text{ cm}^3 \cdot \text{K} \cdot \text{mol}^{-1}$ from 300 K down to 90 K. The $\chi_{\text{M}}T$ value starts to decrease more and more abruptly below 90 K, until it reaches a value of $2.28 \text{ cm}^3 \cdot \text{K} \cdot \text{mol}^{-1}$ at 2 K. This temperature dependent behavior reveals typical antiferromagnetic magnetic coupling between two adjacent Fe(II) ions.

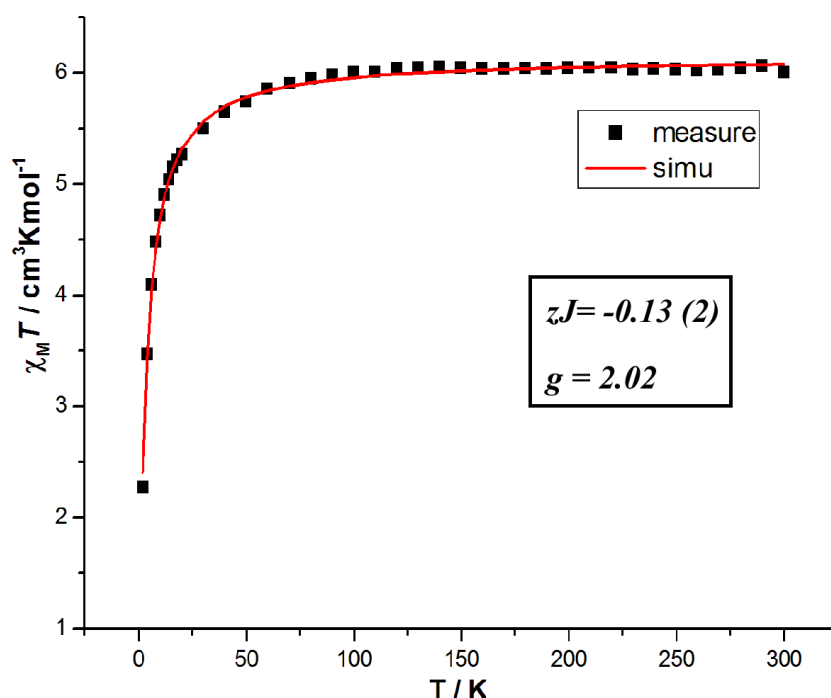


Figure 5.11.: The temperature-dependent magnetic susceptibility for compound **10** (the solid line represents the best fit curve).

From the analysis of crystal structure, we assume that there is no effective magnetic exchange through the bridged ligand, as the shortest covalently linked Fe...Fe distance of $9.617(8) \text{ \AA}$. While the layered structure was found to have a shortest Fe...Fe distance of $8.740(9) \text{ \AA}$, linked through different supramolecular interactions. Such the decrease of $\chi_{\text{M}}T$ value at low temperatures can be explained as weak dipolar antiferromagnetic interaction. The magnetic behavior of compound **10** such can be treated as isolated Fe(II) ions showing magnetic coupling throughout the supramolecular interactions in the crystal lattice. To evaluate this antiferromagnetic interaction for the two the crystallographic independent

Chapter 5 Two 2D Fe^{II} Networks Built Up from Imztrz: Antiferromagnetic v.s. Ferromagnetic Interaction

Fe(II) ions, the magnetic data of the entire temperature range are simulated using the PHI [26] program with value $g = 2.02(1)$ and only a mean-field parameter $zJ = -0.13(2) \text{ cm}^{-1}$. (Figure 5.11) This rather small coupling constant suggests that the antiferromagnetic coupling through the supramolecular interactions between the Fe^{II} centers in the crystal lattice is weak.

Temperature dependent magnetic susceptibility measurements on a bulk crystalline sample of compound **12** was also made from 300 K to 4 K range. The value of $\chi_M T$ at room temperature is ca. $3.91 \text{ cm}^3 \cdot \text{K} \cdot \text{mol}^{-1}$, which is larger than the expected spin only Fe(II) ion ($\chi_M T = 3.0 \text{ cm}^3 \cdot \text{K} \cdot \text{mol}^{-1}$ with $g = 2.0$), indicating that an important orbital contribution is involved. The value is comparable to those of other reported ferrous Fe(II) complex ($4.2, 4.1 \text{ emu K mol}^{-1}$). [27] Upon cooling, the $\chi_M T$ value increases rapidly to a maximum value of $4.51 \text{ cm}^3 \cdot \text{K} \cdot \text{mol}^{-1}$ at 30 K, confirming a typical ferromagnetic coupling between the Fe(II) centers. Upon further cooling to 4 K, the $\chi_M T$ value drops sharply, which may be attributed to zero-field splitting of Fe(II) ions and/or antiferromagnetic coupling.

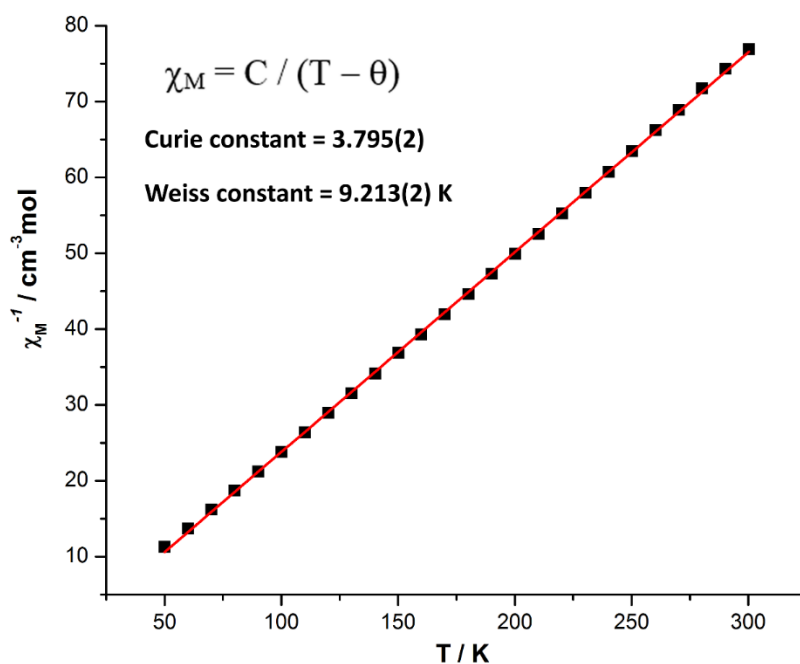


Figure 5.12.: Plots of χ_M^{-1} vs T for compound **12** with fitting to the Curie–Weiss Law, with the red solid line represents the best fit curve.

The magnetic susceptibility in the range 50–300 K obeys the Curie–Weiss law, as shown in figure 5.12, the application of least-squares method gave us an excellent fitting of the χ_M^{-1} vs. T plot, with a Curie constant $C = 3.795(2) \text{ cm}^3 \cdot \text{K} \cdot \text{mol}^{-1}$ and a Weiss temperature $\theta = 9.213(2) \text{ K}$. The C here sits in the usual range of octahedral high-spin Fe(II) ions. [28] The

rather large positive θ value here further proved the existence of ferromagnetic interactions among the adjacent Fe(II) ions in compound **12**. From the structural analysis, we get to know that within the basic square-like {Fe₄} units, there are two different Fe...Fe separations through the triazolate rings: 7.390(8) Å and 7.740(9) Å. This gives the adjacent Fe(II) centers two possible pathways for the effective magnetic coupling. Different approaches have been applied to evaluate the detailed ferro/anti-ferromagnetic interaction in compound **12**.

The first attempt was to analyze the magnetic data using a uniform chain model, assuming the 7.390(8) Å linkage has a dominating coupling effect compared to the 7.740(9) Å bridge. As Fe(II) is usually affected by a strong spin-orbit coupling and a large orbital contribution, reflecting by the relative large χ_{MT} value in compound **12**. To model the 1D chain data, the equation (equ 5.1) from Drillon et al. [29] was applied. The magnetic coupling through the longer linkage (7.740(9) Å bridge) can be included by using the mean field approximation (equ 5.2). [30]

$$\chi = \frac{2Ng^2\mu_B^2}{k_B T} \exp(4J_1 / k_B T) \text{ (Equation 5.1)}$$

$$\chi_M = \frac{\chi}{1 - (2J_2 / N\beta^2 g^2) \chi} \text{ (Equation 5.2)}$$

This model reproduces quite satisfactorily magnetic properties of compound **12** while still did not cover all the measured data points with $g = 2.27$, $J_1 = 4.43 \text{ cm}^{-1}$, $J_2 = -1.57 \text{ cm}^{-1}$ (figure 5.13, solid blue line). A note must be given that even if this fit is mathematically good, it must be taken with caution, because the main J_1 value is very close to the J_2 value. The molecular field model only is appropriate when the J_1/J_2 ratio is very small. [30] Maybe the only conclusion we can state from this simulation is that the magnetic coupling through the imidazole-imine moiety is confirmed, and it has two pathways through the two different distances of linkage.

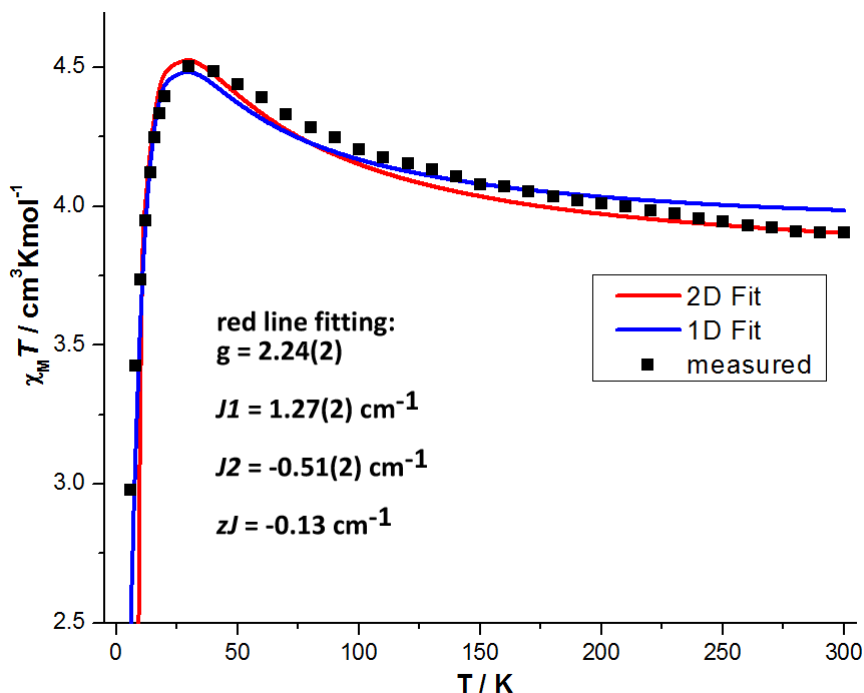


Figure 5.13.: The temperature-dependent magnetic susceptibility ($\chi_M T$ v.s. T) for compound **12** from 4K to 300K. The blue line represent the fitting result based on the chain model, and the red line stands for the best fitting with the 2D Heisenberg quasi-quadratic layer model.

Given the size of the local interacting spins ($S = 2$, Fe(II), HS), we can consider them as classical spins and, therefore, the second approximate method was made by means of the analytical expression derived by Curély^[31] for the isotropic Heisenberg 2D square system. Herein, we consider a two J coupling quasi-quadratic layer model, with the magnetic interaction between the adjacent 2D layers defined by the molecular field approximation.
[30]

$$\chi_{2D \text{ square}} = \frac{Ng^2\mu_B^2}{3k_B T} \frac{S(S+1)(W_1+W_2)}{(1-u_1^2)(1-u_2^2)} \quad (\text{Equation 5.3})$$

Where $W_1 = (1 + u_1^2)(1 + u_2^2) + 4u_1u_2$, $W_2 = 2u_1(1 + u_2^2) + 2u_2(1 + u_1^2)$,

and $u_i = \cos[J_i S(S + 1) / kT] - kT / J_i S(S + 1)$

$$\chi_M = \frac{\chi_{2D \text{ square}}}{1 - (2zJ / N\beta^2 g^2) \chi_{2D \text{ square}}} \quad (\text{Equation 5.4})$$

In the above equations, N is Avogadro's number, μ_B is the Bohr magneton, k is the Boltzmann constant, J_i is the exchange coupling and zJ stands for the supramolecular coupling parameter between the adjacent layers. The best-fit parameters through eq 4 for compound **12** are $g = 2.24(1)$, $J_1 = 1.27(2) \text{ cm}^{-1}$, $J_2 = -0.51(2) \text{ cm}^{-1}$ and $zJ = -0.13(2) \text{ cm}^{-1}$. Clearly, the parameters obtained with this approximation are more realistic and the model

reproduces quite well the magnetic data for the whole temperature region, although the middle region is not perfectly reproduced (Figure 5.13, red solid lines). As also mentioned in previous reports, the Fe(II) ion high-spin d^6 configuration is usually accompanied by sizeable zero field splitting and spin-orbital coupling contributions. [32] Unfortunately, a model including all these contributions is not available in the present and would include too many correlated parameters that would lead to an unreliable result.

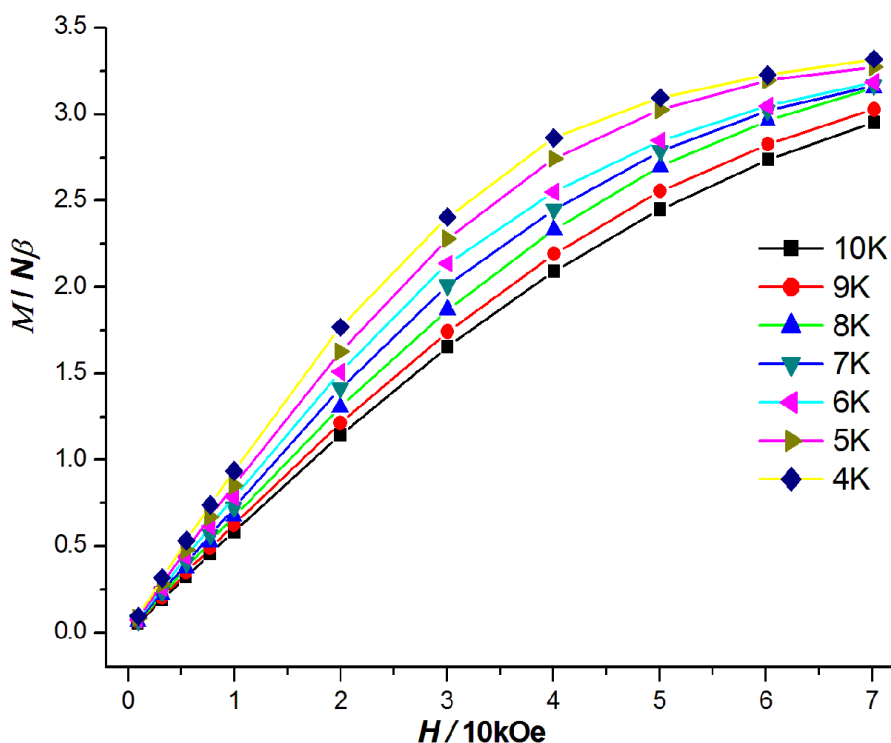


Figure 5.14: Plot of reduced magnetization ($M/N\beta$) v.s. H for compound **12** in the 4–10 K range. The lines are just for the guidance of the eye, dose not represent any simulated results.

A further confirmation of the overall ferromagnetic coupling found in compound **12** is provided by magnetization measurements. As shown in figure 5.14 as variable field isotherms, the magnetization measurements were performed in the range 4–10 K under external magnetic fields up to 70 kOe. The magnetization stays almost linear up to $1.78(1) N\beta$ at 20 kOe (4K), and then it shows a slight positive curvature (non-linear) with the field up to $3.31(1) N\beta$ at 70 kOe (4K). Compared to the theoretical saturation magnetization value of Fe(II) ion ($4.00 N\beta$), the maximum value of $3.31(1) N\beta$ at 70 kOe (4K) suggests that the ground state of the Fe(II) is not well-defined.

Chapter 5 Two 2D Fe^{II} Networks Built Up from Imztrz: Antiferromagnetic v.s. Ferromagnetic Interaction

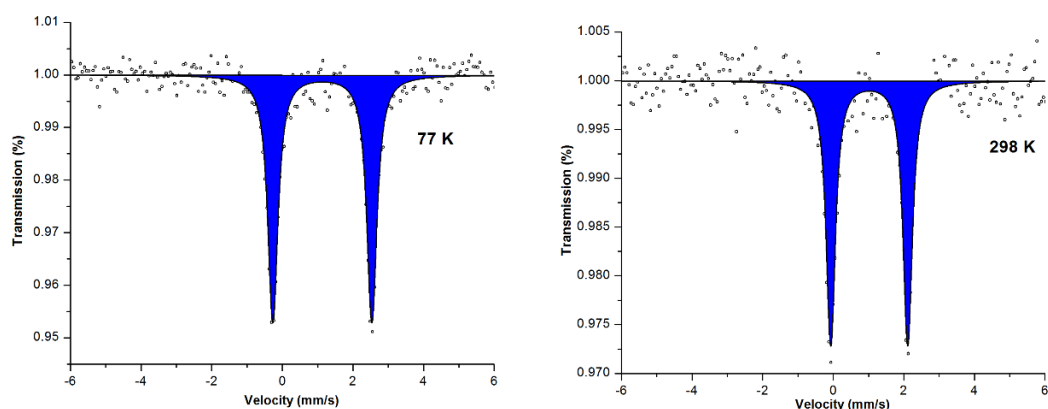


Figure 5.15.: Mössbauer spectrum of **C12** recorded at 77 and 298 K.

In addition, ⁵⁷Fe–Mössbauer measurement of compound **12** at two different temperatures (77K, 298K) was performed (Figure 5.15) to test for possible electronic isomerization for the distorted octahedral Fe(II) cores. As illustrated in figure 12, both spectra show only one doublet peaks. The isomer shifts δ (1.13 and 1.02 mm·s⁻¹), quadrupole splitting Δ_{EQ} (2.81 and 2.18 mm·s⁻¹) lie clearly in the range expected for Fe(II) ions in octahedral or quasi-octahedral environments (Table 5.4). [33a, 33b] On the other hand, the quadrupole splitting (Δ_{EQ}) values are also consistent with the high spin electronic configuration for the Fe(II) ions. [33c]

Table 5.4.: Mössbauer parameters for compound **12** at 77 K and 298 K with the isomer shift δ , quadrupole splitting Δ_{EQ} and lorentzian line width Γ and site population.

Temperature (K)	isomer shifts δ (mm·s ⁻¹)	quadrupole splitting	lorentzian line width
		Δ_{EQ} (mm·s ⁻¹)	Γ (mm·s ⁻¹)
77	1.13 ± 0.03	2.81 ± 0.04	0.33 ± 0.03
298	1.02 ± 0.03	2.18 ± 0.04	0.30 ± 0.03

Considering the structural features of compound **12**, the observed J values can be explained on the basis of the possible exchange pathways present in the compound. In compound **12**, each Fe(II) ion is surrounded by four triazole-imine bridges in the quasi-quadratic layer, with two different groups of linking distance owing to the slightly distorted coordination geometry. The dominating ferromagnetic interaction is assumed coupled through the longer linkage, while the mediated antiferromagnetic coupling is assigned to the shorter exchange pathway. This is the first example with an effective magnetic coupling found in the triazole-imine linkage. The magnetic exchange pathway for pyrazine-/imidazole-containing Fe(II) complexes have been well-established, suggesting that an effective d(metal)- π (pyz, imidazole) overlap is operative in many cases. [35] The obtained J value in the present work can be very well compared with the several published Fe(II) in the pyrazine-/imidazole system as they shared in the same range separation around the adjacent Fe(II) centers (6.5~7.5 Å). [27,28]

5.5 Conclusion

The work described herein represents two scarce examples of two-dimensional Fe(II) network compounds from 4-substituted 1,2,4-triazole. Based on the ligands 4-(1*H*-imidazol-5-ylmethylene-amino)-4*H*-1,2,4-triazole (5-imztrz) and 4-(1*H*-imidazol-2-ylmethylene-amino)-4*H*-1,2,4-triazole (2-imztrz), a group of two 2D Fe^{II} layered compounds, that is, [Fe^{II}₂(2-imztrz)₄(SCN)₄] (**C10**) and [Fe^{II}(5-imztrz)₂](ClO₄)₂ (**C12**) have been synthesized and magnetically characterized. Compound **12** represents the first example of structurally and magnetically characterized ferromagnetic coupled 2D network through the triazole-imine linkage. Compound **10** stayed at high spin state accompanied by a weak antiferromagnetic exchange coupling through the lattice supramolecular interactions. The two 2D networks obtained here were quite different from the previous reported bidentate triazole linked networks. The two newly isolated compounds showed the possibility of combining the triazole ligand with a second coordination site to construct high dimensional Fe(II) complex with a [FeN₆] core. Future work of these two compounds should be made in regards to tuning the ligand field strength for 2D SCO studies.

5.6 Acknowledgement

We acknowledge the *SPIN + X* Program with the support for Mössbauer measurement at *Technische Universität Kaiserslautern*. We kindly thank Dr. Dieter Schollmeyer and Regine Jung-Pothmann (*Johannes Gutenberg University, Mainz*) for collecting the crystal structural data. A.M.L. acknowledges the financial support from MAINZ graduate school and is a recipient of a DFG fellowship through the Excellence Initiative by the Graduate School Materials Science in Mainz (DFG/GSC 266).

5.7 Reference

- [1] a) C. Janiak, *Dalton Trans.*, **2003**, 2781–1804; b) S. Kitagawa, R. Kitaura and S.-I. Noro, *Angew. Chem. Int. Ed.*, **2004**, *43*, 2334–2375; c) *Magnetism: Molecules to Materials*, ed. J. S. Miller and M. Drillon, VCH, Weinheim, **2001**; d) S. I. Ohkoshi, H. Tokoro, T. Matsuda, H. Takahashi, H. Irie, K. Hashimoto, *Angewandte Chemie.*, **2007**, *119*, 3302–3305.; e) G.-C. Xu, X.-M. Ma, L. Zhang, Z.-M. Wang, S. Gao, *J. Am. Chem. Soc.*, **2010**, *132*, 9588–9590.
- [2] O. Kahn, M. C. Jay, *Science*, 1998, *279*, 44-48.
- [3] O. Kahn, *Molecular Magnetism*, VCH, Weinheim, **2001**.
- [4] a) D. Zhang, H. Wang, L. Tian, H. Z. Kou, J. Jiang, Z. H. Ni, *Cryst. Growth Des.*, **2009**, *9*, 3989-3996.; b) E. Colacio, M. Ghazi, H. Stoeckli-Evans, F. Lloret, J. M. Moreno, C. Pérez, *Inorg. Chem.*, **2001**, *40*, 4876-4883..
- [5] a) M. B. Hursthouse, M. E. Light, D. J. Price, *Angew. Chem., Int. Ed.*, **2004**, *43*, 472–475; b) H. Tamaki, Z. J. Zhong, N. Matsumoto, S. Kida, M. Koikawa, N. Achiwa, Y. Hashimoto, H. Okawa, *J. Am. Chem. Soc.*, **1992**, *114*, 6974–6979; c) W. Li, H. P. Jia, Z. F. Ju, J. Zhang, *Dalton Trans.*, **2008**, *39*, 5350–5307; d) Y.-Z. Zheng, W. Xue, M.-L. Tong, X.-M. Chen, F. Grandjean, G. J. Long, *Inorg. Chem.*, **2008**, *47*, 4077–4087.
- [6] a) S. Konar, E. Zangrando, M. G. B. Drew, T. Mallah, J. Ribas, N. R. Chaudhuri, *Inorg. Chem.*, **2003**, *42*, 5966–5973; b) Z.-G. Gu, Y.-F. Xu, X.-J. Yin, X.-H. Zhou, J.-L. Zuo, X.-Z. You, *Dalton Trans.*, **2008**, *41*, 5593–5602; c) L.-F. Tang, L. Zhang, P. Cheng, Z.-H. Wang, J.-T. Wang, *Inorg. Chem.*, **1999**, *38*, 6326–6328; d) H.-R. Wen, C.-F. Wang, Y. Song, J.-L. Zuo, X.-Z. You, *Inorg. Chem.*, **2005**, *44*, 9039–9045.
- [7] a) M. Wriedt, I. Jess, C. Naether, *Eur. J. Inorg. Chem.*, **2009**, *10*, 1406–1413; b) H. N. Bordallo, L. Chapon, J. L. Manson, C. D. Ling, J. S. Qualls, D. Hall, D. N. Argyriou, *Polyhedron*, **2003**, *22*, 2045–2049.
- [8] a) N. Moliner, M. C. Muñoz, S. Létard, L. Salmon, J. P. Tuchagues, A. Bousseksou, J. A. Real, *Inorg. Chem.*, **2002**, *41*, 6997–7005; b) C. Genre, G. S. Matouzenko, E. Jeanneau, D. Luneau, *New J. Chem.*, **2006**, *30*, 1669–1674.
- [9] a) Y. Wang, F.-H. Zhao, A.-H. Shi, Y.-X. Che and J.-M. Zheng, *Inorg. Chem. Commun.*, **2012**, *20*, 23–26; b) J. Yao, Z.-D. Lu, Y.-Z. Li, J.-G. Lin, X.-Y. Duan, S. Gao, Q.-J. Meng and C.-S. Lu, *CrystEngComm*, **2008**, *10*, 1379–1383; c) Z. Su, M. Chen, T. A. Okamura, M.-S. Chen, S.-S. Chen and W.-Y. Sun, *Inorg. Chem.*, **2011**, *50*, 985–991; d) E. Coronado, M. Gimenez-Marques, G. Minguez Espallargas and L. Brammer, *Nat. Commun.*, **2012**, *3*, 828.
- [10] a) S. A. Diener, A. Santoro, C. A. Kilner, J. J. Loughrey, M. A. Halcrow, *Dalton Trans.*, **2012**, *41*, 3731-3739; b) J. Olguín, G. N. Jameson, S. Brooker, *RSC Adv.*, **2011**, *1*, 52-57; c) J. Ramírez, A. M. Stadler, G. Rogez, M. Drillon, J. M. Lehn, *Inorg. Chem.*, **2009**, *48*, 2456-2463; d) A. R. Craze, N. F. Sciortino, M. M. Badbhade, C. J. Kepert, C. E. Marjo, F. Li, *Inorganics*, **2017**, *5*, 62; e) F. Tuna, M. R. Lees, G. J. Clarkson, M. J. Hannon, *Chem. Eur. J.*, **2004**, *10*, 5737-5750; f) M. Mimura, T. Matsuo, T. Nakashima, N. Matsumoto, *Inorg. Chem.*, **1998**, *37*, 3553-3560; f) L. Li, N. Saigo, Y. Zhang, D. J. Fanna, N. D. Shepherd, J. K. Clegg, R. Zheng, S. Hayami, L. F. Lindoy, J. R. Aldrich-Wright, C. G. Li, *J. Mater. Chem.*, **2015**, *3*, 7878-7882.
- [11] P. Baxter, J.-P. Lehn, A. DeCian, J. Fisher, *Angew. Chem., Int. Ed. Engl.*, **1993**, *32*, 703–706.

Chapter 5 Two 2D Fe^{II} Networks Built Up from Imztrz: Antiferromagnetic v.s. Ferromagnetic Interaction

- [12] L. R. MacGillivray, J. L. Atwood, *Nature*, **1997**, *389*, 469–472; b) D.-H. Ren, D. Qiu, C.-Y. Pang, Z. Li and Z.-G. Gu, *Chem. Commun.*, **2015**, *51*, 788–791; c) R. A. Bilbeisi, S. Zarra, H. L. C. Feltham, G. N. L. Jameson, J. K. Clegg, S. Brooker and J. R. Nitschke, *Chem.–Eur. J.*, **2013**, *19*, 8058–8062; d) A. Ferguson, M. A. Squire, D. Siretanu, D. Mitcov, C. Mathoniere, R. Clerac and P. E. Kruger, *Chem. Commun.*, **2013**, *49*, 1597–1599; f) N. Struch, C. Bannwarth, T. K. Ronson, Y. Lorenz, B. Mienert, N. Wagner, M. Engeser, E. Bill, R. Puttreddy, K. Rissanen, J. Beck, *Angew. Chem. Int. Ed.*, **2017**, *56*, 4930–4935.
- [13] R. F. Carina, G. Bernardinelli, A. F. Williams, *Angew. Chem., Int. Ed. Engl.*, **1993**, *32*, 1463–1465.
- [14] a) A. Grosjean, N. Daro, B. Kauffmann, A. Kaiba, J.F. Létard, P. Guionneau, *Chem. Commun.*, **2011**, *47*, 12382–12384; b) N. Pittala, F. Thétiot, S. Triki, K. Boukheddaden, G. Chastanet, M. Marchivie, *Chem. Mater.*, **2016**, *29*, 490–494.
- [15] Nangia, A. *Acc. Chem. Res.* **2008**, *5*, 595–604. (b) G. R. Desiraju, *Acc. Chem. Res.* **2002**, *35*, 565–573.
- [16] G.A. Bain, J.F. Berry, *J. Chem. Edu.* **2008**, *85*, p. 532.
- [17] *SMART 5.0 and SAINT 4.0 for Windows NT, Area Detector Control and Integration Software*, Bruker Analytical X-Ray Systems Inc., Madison, WI, 1998.
- [18] G. M. Sheldrick, *SADABS: Program for Empirical Absorption Correction of Area Detector Data*, University of Göttingen, Göttingen, Germany, 1996.
- [19] a) G. M. Sheldrick, *Acta Crystallogr.* **2015**, *C71*, 3–8; b) G. M. Sheldrick, *SHELXTL 5.1 for Windows NT: Structure Determination Software Programs*, Bruker Analytical X-ray Systems, Inc., Madison, WI, 1997.
- [20] O. V. Dolomanov, L. J. Bourhis, R. J. Gildea, J. A. K. Howard, H. J. Puschmann, *Appl. Crystallogr.* **2009**, *42*, 339–341.
- [21] *Diamond - Crystal and Molecular Structure Visualization Crystal Impact* - Dr. H. Putz & Dr. K. Brandenburg GbR, Kreuzherrenstr. 102, 53227 Bonn, Germany.
- [22] a) T. Khan, R. Yadav, *Heterocycl. Lett.* **2016**, *6*, 757–766; b) A. Kwiecień, M. Barys, Z. Ciunik, *Molecules* **2014**, *19*, 11160–11177.
- [23] P. Chakraborty, A. Tissot, L. Peterhans, L. Guenee, C. Besnard, P. Pattison, A. Hauser, *Phys. Rev. B* **2013**, *87*, 2143.
- [24] E. Borello, A. Zecchina, *Spectrochimica Acta*, **1963**, *19*, 1703–1715.
- [25] A. A. Salaudeen, C. A. Kilner, M. A. Halcrow, *Polyhedron*, **2008**, *12*, 2569–2576; K. Nakamoto, *Infrared and Raman Spectra of Inorganic and Coordination Compounds Part B (5th ed.)* Wiley Interscience, New York, **1997**, 116.
- [26] N. F. Chilton, R. P. Anderson, L. D. Turner, A. Soncini, K. S. Murray, *J. Comput. Chem.* **2013**, *34*, 1164.
- [27] a) G. De Munno, T. Poerio, G. Viau, M. Julve, F. Lloret, Y. Journaux and E. Riviere, *Chem. Commun.*, **1996**, *22*, 2587–2588; b) X. Hao, Y. Wei, S. Zhang, *Chem. Commun.*, **2000**, *22*, 2271–2272.
- [28] a) J. López-Cabrelles, M. Giménez-Marqués, G.M. Espallargas, E. Coronado, *Inorg. Chem.*, **2015**, *54*, 10490–10496; b) S. J. Rettig, A. Storr, D. A. Summers, R. C. Thompson, J. Trotter, *J. Am. Chem. Soc.*, **1997**,

Chapter 5 Two 2D Fe^{II} Networks Built Up from Imztrz: Antiferromagnetic v.s. Ferromagnetic Interaction

- 119, 8675- 8680; c) J. Ramirez, A.-M. Stadler, G. Rogez, M. Drillon, J.-M. Lehn, *Inorg. Chem.*, **2009**, *48*, 2456–2463.
- [29] a) T. D. Keene, I. Zimmermann, A. Neels, O. Sereda, J. Hauser, M. Bonin, M. B. Hursthouse, D. J. Price, S. Decurtins, *Dalton Trans.*, **2010**, *39*, 4937–4950; b) A. Maignan, V. Hardy, S. Hébert, M. Drillon, M. R. Lees, O. Petrenko, D. Mc,K. Paul and D. Khomskii, *J. Mater. Chem.*, **2004**, *14*, 1231–1234.
- [30] O'Connor, C. J. *Prog. Inorg. Chem.* **1982**, *29*, 203-283.
- [31] a) J. Curély *Europhys. Lett.*, **1995**, *32*, 529; b) Curély, *J. Phys. B*, **1998**, *245*, 263–276. (c) Delgado, F. S, Kerbellec, N, Ruiz-Pérez, C, Cano, J, Lloret, F, Julve, M. *Inorg. Chem.*, **2006**, *45*, 1012–1020.
- [32] a) J. S. Sun, H. H. Zhao, O. Y. Xiang, R. Clerac, J. A. Smith, J. M. Clemente-Juan, C. Gomez-Garcia, E. Coronado, K. R. Dunbar, *Inorg. Chem.*, **1999**, *38*, 5841-5855; b) G. DeMunno, M. Julve, J. A. Real, F. Lloret, R. Scopelliti, *Inorg. Chim. Acta*, **1996**, *250*, 81-85; c) P. Albores, E. Rentschler, *Inorg. Chem.*, **2010**, *49*, 8953-8961; d) S. Konar, E. Zangrando, M. G. B. Drew, T. Mallah, J. Ribas, N. R. Chaudhuri, *Inorg. Chem.*, **2003**, *42*, 5966-5973.
- [33] a) F. Menil, *J. Phys. Chem. Solids*, **1985**, *46*, 763-789; b) R. C. Mercader, E. J. Baran, M. Weil, *J. Phys. Chem. Solids*, **2006**, *67*, 1781-1785.
- [34] R. S. Drago, *Physical Methods in Inorganic Chemistry*, Reinhold Publ.: New York, 1965.
- [35] a) J. Darriet, M. S. Haddad, E. N. Duester, D. N. Hendrickson, *Inorg. Chem.*, **1979**, *18*, 2679-2682; b) R. C. E. Belford, I.E. E. Fenton, M. R. Truter, *J. Chem. Soc., Dalton Trans.*, **1974**, *1*, 17-24; c) M. A. Martínez Lorente, F. Dahan, V. Petrouleas, A. Bousseksou, J. P. Tuchagues, *Inorg. Chem.*, **1995**, *34*, 5346-5357.

Chapter 6 Crystal Structure of “*Fleeting Fe complexes*” and Ligands: Crystallization Consideration

Based on the results and discussion in last four chapters, we get to know that it is very important to isolate single crystal and determine the crystal structure for all compounds prepared to study SCO behavior. Actually, it was also addressed out by Olivier Kahn that the crystal structures is of vital importance in the field of molecular magnetism around 30 years ago when he wrote the famous book *Molecular Magnetism*.^[1] As it is not only the covalent bonds linking the spin active center that matters for the over all SCO process, but also the non-covalent bonds like H-bonding, as well as $\pi \dots \pi$ stacking make a huge difference. Additionally, the different or different amounts of solvents involved in the compounds may also have a tremendous effect on the final magnetic properties. These factors can completely change the physical properties of targeted compounds, even for compound with the same empirical formula. Unluckily, despite of the innumerable advances in many fields of crystallization science, the successful isolation of a crystal compound suitable for SC-XRD is sometimes considered more as a mixture of science and art with a pinch of creativity and luck.^[2-5] During the preparation of potential SCO compounds, there are also some unexpected crystals coming out of the arduous attempts. We will show here several of such resolved structures, with the intention of a better understanding of the crystallization process and detailed insight of the related organic ligands. The crystallographic data and refinement parameters of all the crystal data discussed in this chapter are listed in Table 9.3–9.7.

6.1 Mononuclear $[Fe^{II}(2-imztrz)_2(CH_3OH)_2(SCN)_2]$ (C11)

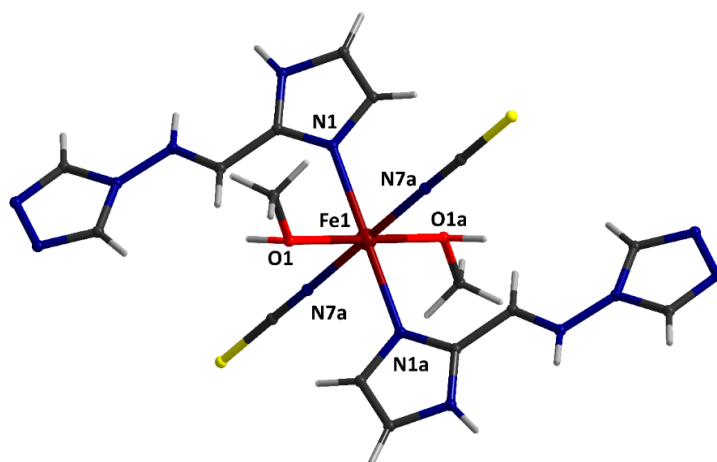


Figure 6.1.: Molecular structure of $[Fe^{II}(2-imztrz)_2(CH_3OH)_2(SCN)_2]$. Symmetry code: $a = -x + 1, -y + 1, -z$.

Chapter 6 Crystal Structure of “Fleeting Fe complexes” and Ligands: Crystallization Consideration

The centrosymmetric compound $[\text{Fe}^{\text{II}}(2\text{-imztrz})_2(\text{CH}_3\text{OH})_2(\text{SCN})_2]$ (**C11**) crystallizes in the monoclinic system with the space group P_{21}/c . The molecular structure of the neutral mononuclear complex is shown in Figure 6.1. The iron(II) atom lies in the centre of symmetry, and is octahedrally coordinated: two nitrogen atoms from two thiocyanate anions and two nitrogen atoms of imidazole rings forms the equatorial plane, the axial positions are occupied by two oxygen atoms from methanol molecules. Surprisingly, quite different from the other two reported mononuclear Fe complexes with triazole ligand, ^[6] the 2-imztrz here is coordinated to the Fe center via nitrogen atoms from the imidazole rings rather than triazole rings, and the additional coordinated two oxygen atoms makes this mononuclear complex stay in HS state. Crystal data indicates that all Fe–N and Fe–O distances are in the range of 2.107(2)–2.271(2) Å, typical for HS iron(II) compounds. (Table 6.1) In addition, the Fe–N_{2-imztrz} distances are longer than the Fe–N_{NCS} and Fe–O(MeOH) ones, where Fe–N_{NCS} = 2.141(2) Å and Fe–O_{MeOH} = 2.100(1) Å; Fe–N_{2-imztrz} = 2.228(2) Å. These bond distances are comparable with those in **C1** and **C5** discussed in chapter 2 and chapter 3. The angles around the iron ion vary from 88.1 (5)° to 180.0 (7)° (Table 6.1), pretty close to the ideal values of 90° and 180°, indicating the octahedral coordination being only slightly distorted.

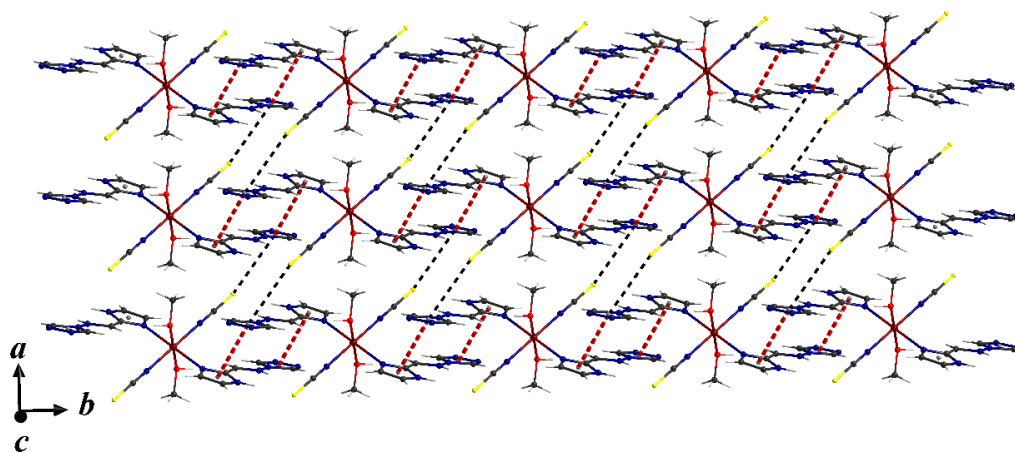


Figure 6.2.: Schematic representation of π - π stacking interactions linked 2D supramolecular network in **C11**. The red dashed lines represent the face-to-face aromatic $\pi \cdots \pi$ stackings and the black dashed lines stand for the $\text{S} \cdots \pi_{\text{triazole}}$ interactions.

In the title compound, the uncoordinated triazole rings are found to be involved in face-to-face aromatic $\pi \cdots \pi$ stacking interactions with the imidazole rings with the centroid to centroid distance of 3.719(1) Å (Fig. 6.2). The formed chain structure along the b axis is further connected to a two dimensional network via a group of non-classical $\text{S} \cdots \pi_{\text{triazole}}$

(S...centroid distance of 4.049(5) Å) interactions. The rather weak supramolecular interactions here partially explain the instability of this mononuclear complex.

Table 6.1 Selected bond lengths [Å] and angles [°] for **C11**.

Compound 11					
Fe(1)-O(1)	2.100(11)	Fe(1)-N(7)	2.141(2)	Fe(1)-N(1)	2.228(2)
O(1)-Fe(1)-O(1)#1	180.0	N(7)-Fe(1)-N(7)#1	180.0(7)	O(1)-Fe(1)-N(1)	90.1(5)
O(1)-Fe(1)-N(7)	91.9(5)	O(1)-Fe(1)-N(1)#1	89.9(5)	O(1)#1-Fe(1)-N(1)	89.9(5)
O(1)#1-Fe(1)-N(7)	88.1(5)	O(1)#1-Fe(1)-N(1)#1	90.1(5)	N(7)-Fe(1)-N(1)	90.8(5)
O(1)-Fe(1)-N(7)#1	88.1(5)	N(7)-Fe(1)-N(1)#1	89.2(5)	N(7)#1-Fe(1)-N(1)	89.2(5)
O(1)#1-Fe(1)-N(7)#1	91.9(5)	N(7)#1-Fe(1)-N(1)#1	90.8(5)	N(1)#1-Fe(1)-N(1)	180.0

Symmetry code: #1 = -x + 1, -y + 1, -z.

6.2 Dinuclear $[Fe^{II}_2(L4)_6(C_2O_4)(H_2O)_2](SeCN)_2(L4)_2(H_2O)_4$ (**C3**)

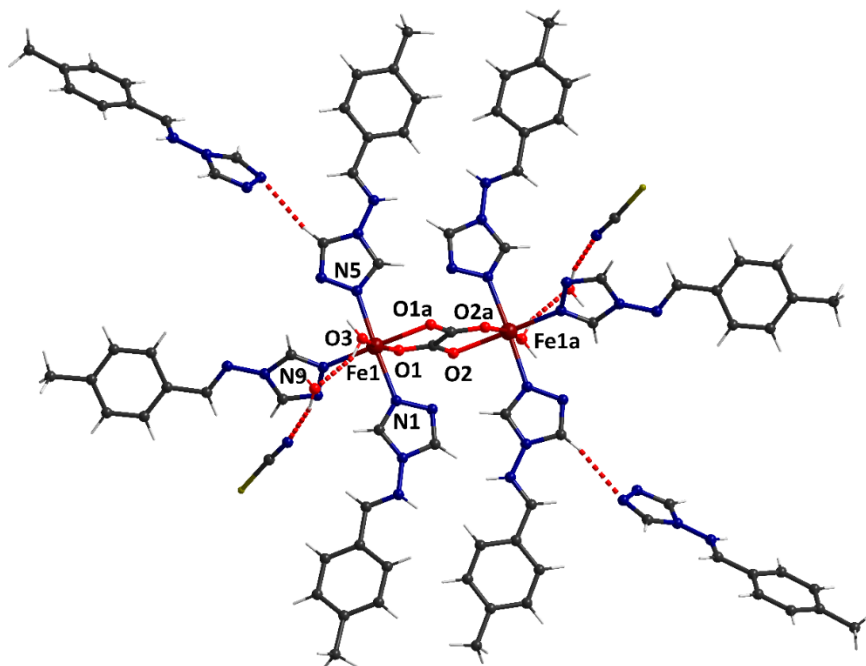


Figure 6.3.: Molecular structure of $[Fe^{II}_2(toltrz)_6(C_2O_4)(H_2O)_2](SeCN)_2(toltrz)_2(H_2O)_4$. Symmetry code: a = -x + 1, -y + 1, -z + 2.

Compound $[Fe^{II}_2(toltrz)_6(C_2O_4)(H_2O)_2](SeCN)_2(toltrz)_2(H_2O)_4$ (**C3**) crystallizes in the triclinic system with the space group *P*-1. **C3** is a dinuclear complex formed by two crystallographically related iron(II) centres. Each metal ion is coordinated to three N-donor atoms of triazole rings from the toltrz ligands. As shown in figure 6.3, the coordination sphere of the iron centre is completed by one aqua molecule and two O atoms of a bridging oxalato dianion, resulting in a distorted octahedral coordination geometry. There are two more aqua molecules embedded in the crystal lattice. The charge is balanced by a non-

Chapter 6 Crystal Structure of “Fleeting Fe complexes” and Ligands: Crystallization Consideration

coordinated selenocyanate, which is linked to the Fe molecule via H-bonding interactions through one water molecule. The Fe–N and Fe–O distances (Table 6.2) are within the expected ranges for a HS iron(II) species with this type of coordination environment. [7] The angles around the iron ion vary from 76.6 (2)° to 177.2 (3)° (Table 6.2), significantly different from the ideal values of 90° and 180°. This distortion of the octahedron is mainly due to the rigid bridging oxalato ligand imposing an O1–Fe1–O2^a (a = – x + 1, – y + 1, – z + 2) angle of 76.6 (2)°.

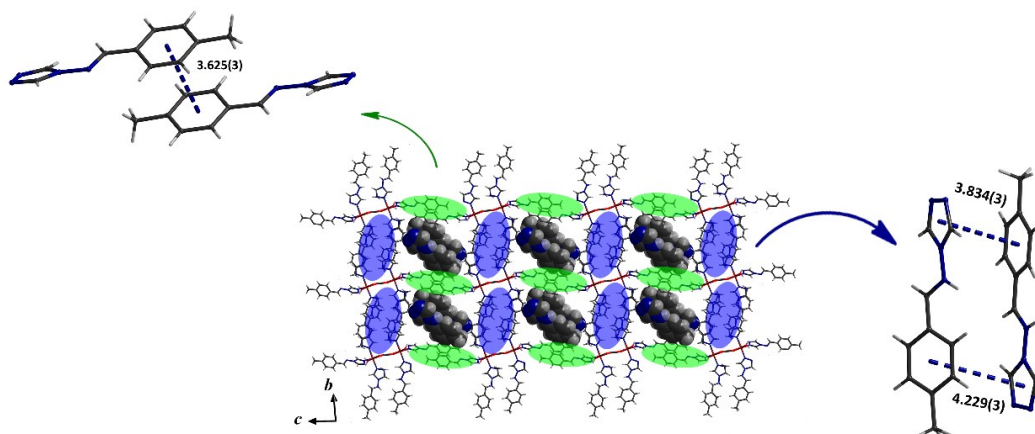


Figure 6.4.: Illustration of the 2D network in dinuclear complex **C3**, showing the different $\pi\cdots\pi$ stackings.

The crystal packing of **C3** shows the formation of a 2D supramolecular network by two sets of $\pi\cdots\pi$ stackings involving the phenyl and triazole rings (Fig. 6.4). Along the *b* axis, the tolrz molecules adapt a head_{phenyl}-to-tail_{triazole} mode of stacking, leading to a chain structure with the character of double iron chain parallel to each other. The chain structure is further connected into a 2D network via a head_{phenyl}-to-head_{phenyl} stacking along the *c* axis. The solvate tolrz molecules are embedded in the channel formed between the 2D networks via a group of C–H $\cdots\pi$ contacts. (distance of C \cdots C π is 3.534(3) Å).

Table 6.2 Selected bond lengths [Å] and angles [°] for **C3**.

Compound 3					
Fe(1)–O(3)	2.088(5)	Fe(1)–N(9)	2.124(7)	Fe(1)–N(1)	2.191(6)
Fe(1)–O(1)	2.106(5)	Fe(1)–N(5)	2.180(6)	Fe(1)–O(2)#1	2.213(5)
O(3)–Fe(1)–O(1)	168.3(2)	N(9)–Fe(1)–N(5)	91.1(2)	O(3)–Fe(1)–O(2)#1	91.7(2)
O(3)–Fe(1)–N(9)	93.8(2)	O(3)–Fe(1)–N(1)	92.2(2)	O(1)–Fe(1)–O(2)#1	76.7(2)
O(1)–Fe(1)–N(9)	97.9(2)	O(1)–Fe(1)–N(1)	86.6(2)	N(9)–Fe(1)–O(2)#1	174.5(2)
O(3)–Fe(1)–N(5)	88.6(2)	N(9)–Fe(1)–N(1)	91.3(2)	N(5)–Fe(1)–O(2)#1	88.6(2)
O(1)–Fe(1)–N(5)	92.1(2)	N(5)–Fe(1)–N(1)	177.4(3)	N(1)–Fe(1)–O(2)#1	88.9(2)

Symmetry code: #1 = – x + 1, – y + 1, – z + 2.

6.3 Three Polynuclear Fe^{II} Complex from Hcpt (L9)

6.3.1 1D Chain Structure of [Fe^{II}(cpt)(OH)(H₂O)₂]_n (C13)

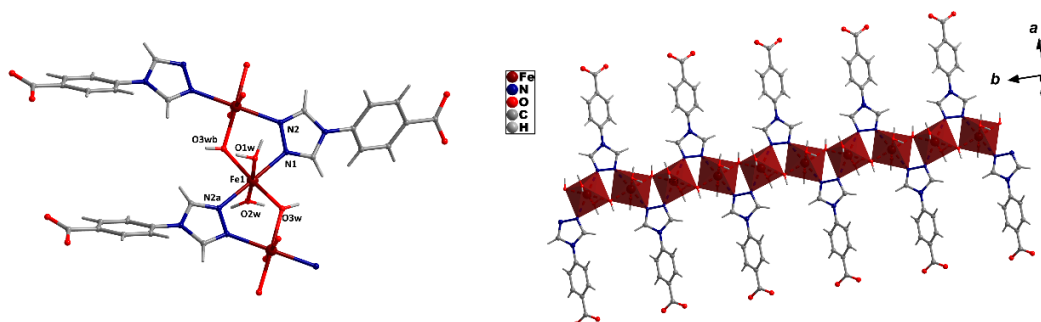


Figure 6.5.: Coordination environment of **C13**, and the view of the infinite polymeric [Fe(μ -cpt)(μ -OH)] chain. Symmetry code: a = -x + 1, y + 0.5, -z + 1.5; b = -x + 1, y - 0.5, -z + 1.5

Compound [Fe^{II}(cpt)(OH)(H₂O)₂]_n (**C13**) crystallizes in the monoclinic system with the space group *P*₂₁/*c*. As shown in figure 6.5, the asymmetric unit of **C13** contains one Fe(II) ion, one μ_2 -cpt anion, one OH⁻ ion and two coordinated aqua molecules. Each iron atom adopts a slightly distorted octahedral arrangement, where the basal plane is occupied by two nitrogen atoms (N1, N2a, a = -x + 1, y + 0.5, -z + 1.5) from two symmetry equivalent cpt⁻ ligands and two oxygen atoms (O3w and O3wb, b = -x + 1, y - 0.5, -z + 1.5) from two symmetry equivalent OH⁻ anions. The axial positions are occupied by two oxygen atoms from aqueous molecules (O1w, O2w). The Fe–N and Fe–O distances are within the expected ranges for a high-spin iron(II) species, which are listed in table 6.3. The octahedral arrangement around Fe(II) is distorted, as the angles around the iron ion vary from 85.07 (7)^o to 170.70 (2)^o (Table 6.3). The iron atoms are joined into an infinite polymeric chain by the μ_2 -hydroxo groups together with μ_2 -cpt⁻ along the *b* axis (Figure 6.5).

Table 6.3 Selected bond lengths [Å] and angles [°] for **C13**.

Compound 13					
Fe(1)-O(3w)	2.031(1)	Fe(1)-O(2W)	2.154(2)	Fe(1)-O(1w)	2.170(2)
Fe(1)-O(3w) ^a	2.040(1)	Fe(1)-N(1)	2.170(2)	Fe(1)-N(2) ^b	2.178(2)
O(3w)-Fe(1)-O(3w) ^a	170.70(2)	O(2W)-Fe(1)-N(1)	89.59(7)	O(3w)-Fe(1)-N(2) ^b	87.00(7)
O(3w) ^a -Fe(1)-O(2w)	90.71(7)	O(3W) ^a -Fe(1)-O(1W)	85.66(7)	O(2w)-Fe(1)-N(2) ^b	92.25(8)
O(3w)-Fe(1)-N(1)	93.45(7)	O(3W)-Fe(1)-O(2W)	98.56(7)	N(1)-Fe(1)-N(2) ^b	178.02(8)
O(3w) ^a -Fe(1)-N(1)	85.87(7)	N(1)-Fe(1)-O(1W)	90.80(7)	O(1w)-Fe(1)-N(2) ^b	87.31(7)

Symmetry code: a = -x + 1, y - 1/2, -z + 3/2; b = -x + 1, y + 1/2, -z + 3/2.

6.3.2 Hexanuclear structure of $[Fe^{II}_6(\mu_3-O)_2(OH)_2(cpt)_6(H_2O)_2]_n$ (C14)

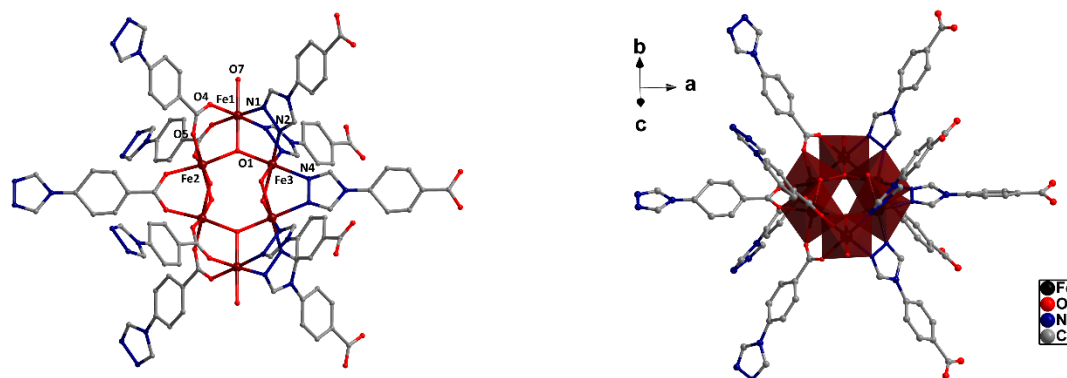


Figure 6.6.: Molecular structural unit of the μ_3 -O-bridged hexagonal $\{Fe_6\}$ cluster. Along a direction, the carboxylate groups are bound from the left side, while the triazolyl groups are bound to the opposite side.

Compound $[Fe^{II}_6(\mu_3-O)(OH)_2(cpt)_6(H_2O)_2]_n$ (C14) crystallizes in the orthorhombic system with the space group $Imm2$. It owns a hexanuclear iron core, with unit cell constants of $a = 16.150(5)$ Å, $b = 19.655(5)$ Å and $c = 19.670(5)$ Å. The final crystal data has a high R_I value of 0.1295, all the other crystallographic information is listed in table 9.4. The chemical formula was assigned based on the single crystal data and charge considerations. As shown in figure 6.6, the the molecular unit is composed of two symmetrical Fe(II) trinuclear oxo-centred (O1) equilateral triangles. For the crystallographic independent triangle, there are three different coordination environment for the iron centers. Fe1 is surrounded by two nitrogen atoms (N1, N1a, $a = -x - \frac{1}{2}, y - \frac{1}{2}, -z + \frac{1}{2}$) from two cpt^- ligands, two oxygen atoms (O4, O4b, $b = x - \frac{1}{2}, -y + \frac{1}{2}; -z + \frac{1}{2}$) from the carboxylate group of other cpt^- ligands, a μ_3 -O (O1) atom and an aqua molecule (O7). Fe2 is bridged to Fe1 via a μ_2 -bridged mode of the triazole ring (N2, N2a), which is further coordinated with two hydroxide anions (O2, O2c, $c = x, -y, z$), the μ_3 -O (O1) atom and another N atom from a third cpt^- ligand to finish the octahedral geometry. Unlike the linking mode between Fe1 and Fe2, Fe3 is connected to Fe1 via a μ_2 -bridged mode of the carboxylate group (O5, O5d, $d = x, -y, -z$), which is further coordinated with two hydroxide anions (O3, O3c, $c = x, -y, z$), the μ_3 -O (O1) atom and another O atom from another cpt^- ligand to complete the octahedral geometry. The adjacent triangles are symmetry related, and connected by the bridging group of hydroxide, triazole and carboxylate to end up with the hexanuclear $\{Fe_6\}$ cluster unit. The Fe–N and Fe–O distances are within the expected ranges for high-spin iron(II) species, which are listed in table 6.4. The angles around the iron ion vary from $86.1(6)^\circ$ to $177.9(5)^\circ$ (Fe1), $86.6(6)^\circ$ to $175.5(6)^\circ$ (Fe2), $86.7(6)^\circ$ to $104.1(9)^\circ$ (Fe3), (Table 6.4), slightly different from the ideal values of 90° and 180° , showing distortion around the iron centers.

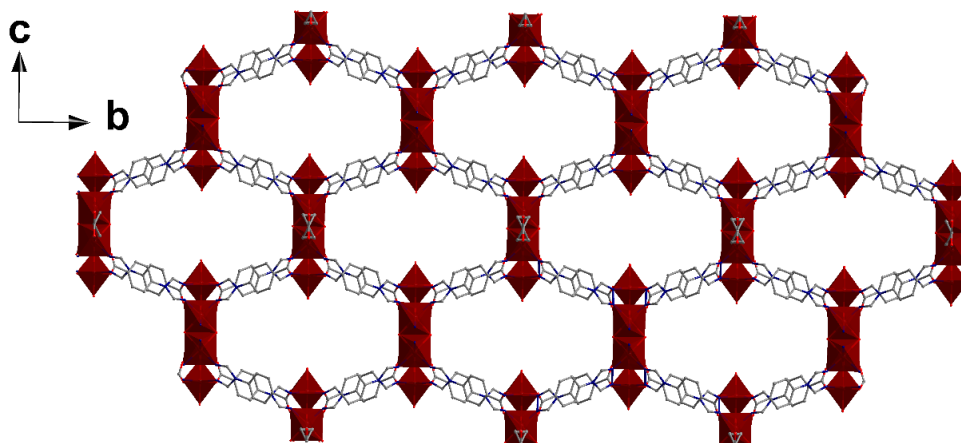


Figure 6.7.: The packing arrangement of **C14**, showing hexagonal honeycomb channels along the *a* axis.

Within the $\{\text{Fe}_6\}$ cluster, all Fe atoms are in a perfect plane, with all bridging ligands asymmetrically coordinated; all carboxylate moieties bind from one side (left) of the Fe_6^{II} hexagonal core and triazole groups binding from the other side (right) (Fig. 6.6). Hexagonal honeycomb channels are constructed along *a* axis (Fig. 6.7). Calculations using PLATON,^[8] showed that the effective volume for inclusion of these channels is about $6244.0 \text{ \AA}^3/\text{cell}$, comprising $\sim 65.7\%$ of the crystal volume.

Table 6.4 Selected bond lengths [\AA] and angles [$^\circ$] for **C14**.

Compound 14					
Fe(1)-O(1)	2.090(8)	Fe(2)-O(1)	2.069(19)	Fe(3)-O(5) ^b	2.038(17)
Fe(1)-O(4) ^a	2.106(18)	Fe(2)-N(2)	2.086(15)	Fe(3)-O(3)	2.046(12)
Fe(1)-O(7)	2.129(19)	Fe(2)-N(4)	2.21(3)	Fe(3)-O(1)	2.100(19)
Fe(1)-N(1)	2.13(2)	Fe(2)-O(2)	2.220(13)	O(2)-Fe(2) ^d	2.220(13)
O(1)-Fe(1)-O(4) ^a	91.8(6)	O(1)-Fe(2)-N(2)	86.8(5)	O(5) ^b -Fe(3)-O(3)	163.3(6)
O(1)-Fe(1)-O(7)	179.3(11)	N(2) ^c -Fe(2)-N(2)	90.9(9)	O(5) ^a -Fe(3)-O(3)	92.3(6)
O(4) ^a -Fe(1)-O(7)	88.6(8)	O(1)-Fe(2)-N(4)	179.7(7)	O(3)-Fe(3)-O(3) ^d	71.3(9)
O(7)-Fe(1)-N(1) ^c	93.4(8)	N(2)-Fe(2)-N(4)	93.4(6)	O(5) ^b -Fe(3)-O(6)	86.7(6)
O(1)-Fe(1)-N(1)	86.1(6)	O(1)-Fe(2)-O(2)	93.2(5)	O(3)-Fe(3)-O(6)	91.3(6)
O(4) ^a -Fe(1)-N(1)	177.9(5)	N(2) ^c -Fe(2)-O(2)	93.6(6)	O(5) ^b -Fe(3)-O(1)	88.7(5)
O(4) ^b -Fe(1)-N(1)	88.2(5)	N(2)-Fe(2)-O(2)	175.5(6)	O(3)-Fe(3)-O(1)	94.8(5)
O(7)-Fe(1)-N(1)	93.4(8)	N(4)-Fe(2)-O(2)	86.6(6)	O(3) ^d -Fe(3)-O(1)	94.8(5)
N(1) ^c -Fe(1)-N(1)	91.4(10)	O(2)-Fe(2)-O(2) ^d	81.9(7)	O(6)-Fe(3)-O(1)	172.5(6)

Symmetry code: $a = -x - \frac{1}{2}, y - \frac{1}{2}, -z + \frac{1}{2}$; $b = x - \frac{1}{2}, -y + \frac{1}{2}, -z + \frac{1}{2}$; $c = x, -y, z$; $d = x, -y, -z$.

6.3.3 3D structure of $[Fe^{II}_3(\mu_3-O)(OH)(cpt)_3(H_2O)_2]_n$ (C15)

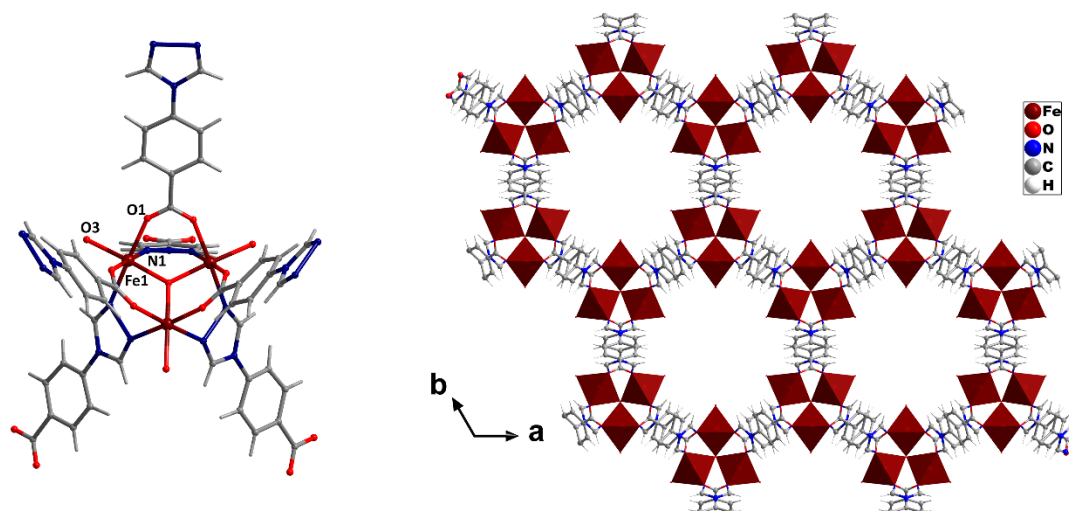


Figure 6.8: a) Molecular structural unit of the μ_3 -O-bridged equilateral triangle $\{Fe_3\}$ cluster. The carboxylate groups are bound from the up side, while the triazolyl groups are bound to the opposite side; b) The packing arrangement of C15, showing hexagonal honeycomb channels along the c axis.

Compound $[Fe^{II}_3(\mu_3-O)(OH)(cpt)_3]_n$ (C15) has a trinuclear iron core that resembles the MIL88 (MIL stands for a special type of MOF first developed at Institut Lavoisier) Cr(III) complex series,^[9] and a very similar structure has been reported with a cobalt core.^[10] This C15 iron complex can be treated as an isomorphous structure with the reported cobalt complex $[Co^{II}_3(\mu_3-O)(OH)(cpt)_3(H_2O)_2]_n \cdot xH_2O \cdot yDMF$. C15 crystallizes in the hexagonal space group, $P6_3/mc$, with unit cell constants of $a = b = 15.1907(3) \text{ \AA}$, $c = 20.1364(8) \text{ \AA}$ and $\gamma = 120^\circ$. All other crystallographic informations are listed in table 9.4. The chemical formula was assigned based on the single crystal data and charge considerations. As shown in figure 6.8, the molecular unit is composed of a Fe(II) trinuclear oxo-centred (O2) equilateral triangle. Each Fe(II) ion exhibits octahedral coordination with two O atoms (O1) from the carboxylate group of a cpt^- ligand, two N atoms (N1) from the triazole rings of other cpt^- ligands, a μ_3 -O (O2) atom and a hydroxide anion (O3). The hydroxide anion, which is presumably generated during the reaction, completes the charge balance of the entire framework. This hydroxide group was considered to be highly disordered; therefore the average atomic position of Fe(II) ions appears to be identical. In the reported cobalt isostructure, they assume that the hydroxide groups are occupied by the terminal positions rather than possible lattice position.^[10] The Fe–N and Fe–O distances are within the expected ranges for HS iron(II) species, which are listed in table 6.5.

Within the cluster, all bridging ligands are coordinating asymmetrically; all carboxylate moieties bind from one side (top) of the Fe₃^{II} triangular core and triazole groups binding from the other side (bottom) (Fig. 6.8). The topology of the trinuclear {Fe₃} cluster is similar to that of MIL88, [9] where three Cr^{III} ions are bridged via μ₃-O and terephthalic acid. Similarly to MIL88, hexagonal honeycomb channels are formed along *c* axis (Fig. 6.8 b). Calculations using PLATON, [8] showed that the effective volume for inclusion of these channels is about 4024.1 Å³/cell, comprising ~66.1% of the crystal volume.

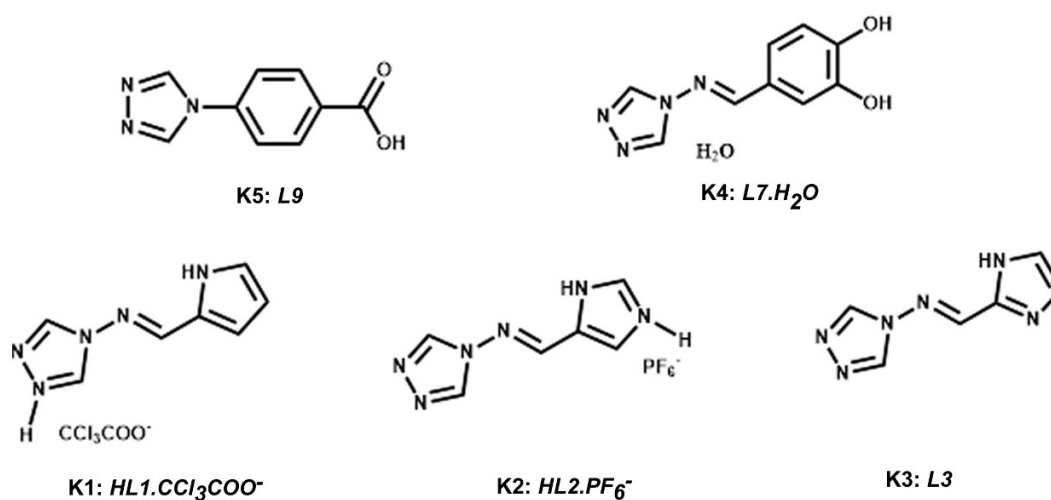
Table 6.5 Selected bond lengths [Å] and angles [°] for **C15**.

Compound 15					
Fe(1)-O(2)	1.950(2)	Fe(1)-O(1)#1	2.028(16)	O(2)-Fe(1)-O(3)	174.2(18)
Fe(1)-O(3)	2.006(16)	Fe(1)-N(1)	2.10(2)	O(2)-Fe(1)-O(1)#1	89.7(11)
O(3)-Fe(1)-O(1)#1	94.5(9)	O(2)-Fe(1)-N(1)	88.1(11)	O(1)#2-Fe(1)-N(1)	90.3(4)
O(1)#1-Fe(1)-O(1)#2	88.5(11)	O(3)-Fe(1)-N(1)	87.9(9)	N(1)#3-Fe(1)-N(1)	90.9(10)
O(1)#2-Fe(1)-N(1)#3	177.5(6)	O(1)#1-Fe(1)-N(1)	177.5(6)	O(3)-Fe(1)-O(1)#2	94.5(9)

Symmetry code: #1 = *y* + 1, *x*, *z* + ½; #2 = -*x* + 1, -*y*, *z* + ½; #3 = -*y* + 1, -*x* + 1, *z*.

6.4 Layered Structure of Half-Rigid Ligand

Despite the fact that the molecular features of the ligands show no exceptional specialities, the crystal structures, however, reveal interesting details due to the corresponding lattice packing in solid state. Herein we summarize five of the rigid or half-rigid ligand crystal structures **K1–K5** (scheme 6.1), with the intention of a better understanding of the solid state packing, and insight of the ligand potential.



Scheme 6.1.: Scheme of organic compounds for crystal structure 1 (**K1**) to crystal structure 5 (**K5**).

Chapter 6 Crystal Structure of “Fleeting Fe complexes” and Ligands: Crystallization Consideration

In general, the ligand molecules are hydrogen-bonded via the pyrrolyl (**K1**), imidazolyl (**K2**, **K3**), hydroxylic (**K4**), carboxylic (**K5**) functions and triazole rings, in case of **K1** and **K2** additional counteranions are also involved. Whereas carboxylic and hydroxylic groups typically form multiple and stronger H-bondings, the non-classical N-acceptors of pyrrolyl, imidazolyl and triazole ring are widely found responsible for the solid state packing among these ligands.

Even though the ligands are substituted with different functional groups, structures **K1** to **K5** were found sharing very similar arrangements: firstly, the ligands form a two dimensional plane linked by varieties of H-bonding interactions; then groups of $\pi\cdots\pi$ stacking facilitated the formation of the layered supramolecular networks with different distances between the adjacent layers. The detailed crystallographic information is listed in table 9.5–9.7. Figure 6.9–6.13 illustrate the 2D layered structure formed by H-bonding interactions for **K1** to **K5**, detailed values of these short interactions can be found in table 9.8.

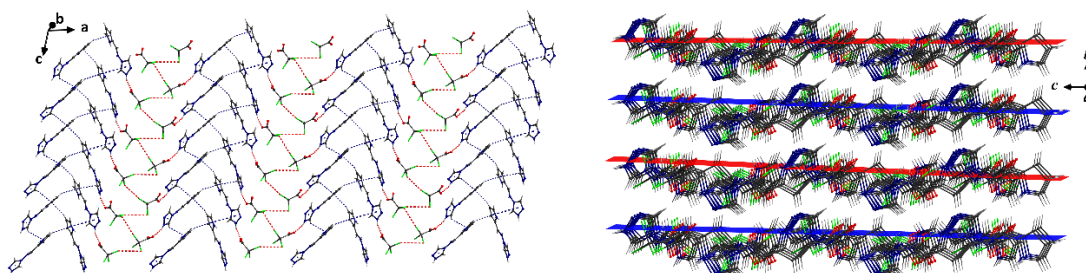


Figure 6.9.: The 2D network formed via multiple supramolecular interactions in *ac* plane, and the view of the layered structure in **K1**. The dashed lines represent the short supramolecular interactions involved.

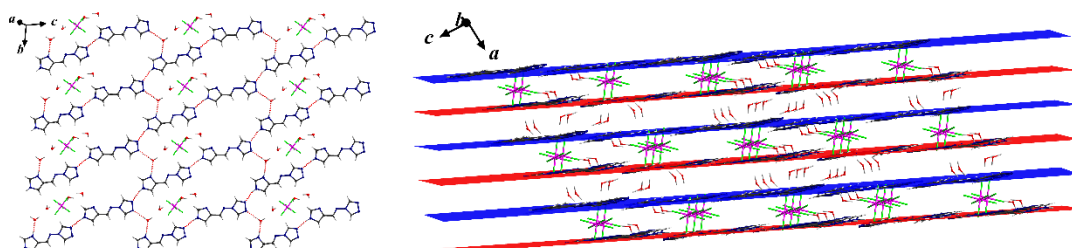


Figure 6.10.: The 2D network formed via multiple supramolecular interactions in *ac* plane, and the view of the layered structure in **K2**. The dashed lines represent the short supramolecular interactions involved.

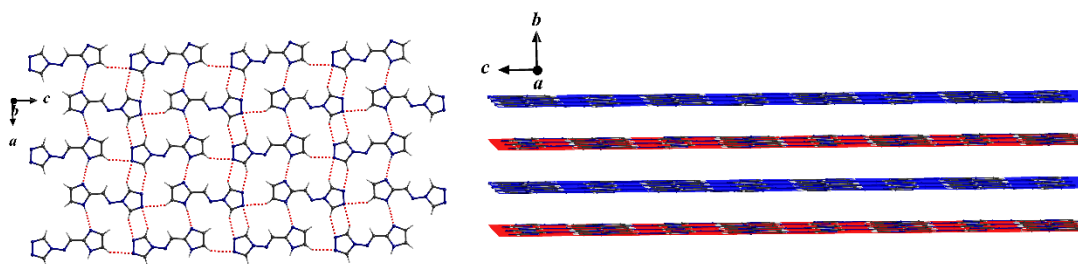


Figure 6.11.: The 2D network formed via multiple supramolecular interactions in ac plane, and the view of the layered structure in **K3**. The dashed lines represent the short supramolecular interactions involved.

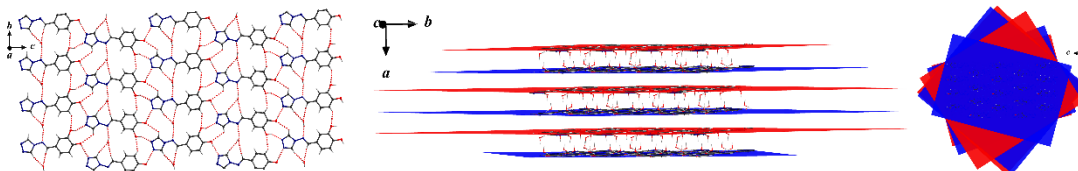


Figure 6.12.: The 2D network formed via multiple supramolecular interactions in ac plane, and the view of the layered structure in **K4**. The dashed lines represent the short supramolecular interactions involved.

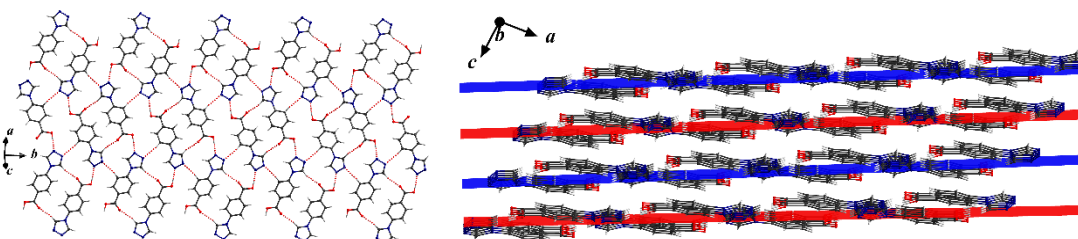
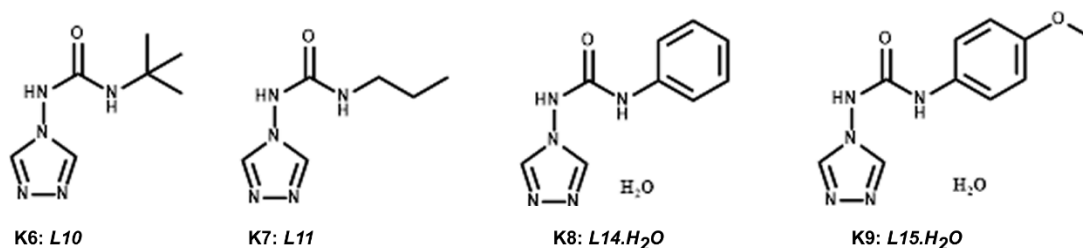


Figure 6.13.: The 2D network formed via multiple supramolecular interactions in ac plane, and the view of the layered structure in **K5**. The dashed lines represent the short supramolecular interactions involved.

The crystal structures allow us to make general assumptions on the competition between ligand crystallization and complex formation taking into account the strength of the overall supramolecular interactions. Detailed exploration of the relationship between potential H-bonding sites and supramolecular interaction strength of the formed compounds are made with the Hirshfeld surfaces analysis in section 6.6.

6.5 Layered Structure of Flexible Ligand

The urea-triazole ligand system has been found highly potential for the SCO construction, forming high $T_{1/2}$ SCO compounds, sometimes even with hysteresis loop. [11] After quite a lot of efforts were put into the crystallization of SCO compounds based on this type of ligand, the results turned out to be quite challenging to isolate the crystalline metal complex with the urea-triazole ligand. On the other hand, the urea group is widely used in polymer synthesis and supramolecular chemistry studies such as anion recognition, where the urea group as the dominant potential binding site is recognized as H-bonding receptors and donors. [12] The small molecular ligand herein, surprisingly, also confirms the fact that the urea group can indeed be involved with plenty of H-bonding interactions, which partially explains the difficulty of isolating crystalline metal complex with this type of ligand. Herein we summarize four of the flexible urea-triazole ligand crystal structures **K6–K9** (scheme 6.2), with the intention of a better understanding of the solid state packing, and the insight of this flexible ligand potential.



Scheme 6.2.: Scheme of organic compounds for crystal structure 6 (**K6**) to crystal structure 9 (**K9**).

The slight difference from the urea linking group indeed leads to quite different supramolecular connection comparing to the rigid ligand discussed in the last section. As shown in figure 9.14–9.17, **K6–K9** share the very similar structural packing as with **K1–K5**: starting from a 2D network to a stacked layered structure linked via different groups of supramolecular interactions. Quite different from the rigid ligand series, these four structures are connected by a rather stronger H-bonding through the urea group. As highlighted in figure 9.14–9.17, the urea groups herein adapt the typical bidentate urea linkage mode [12] in **K6**, **K7** and **K9**, while a solvent (water) involved binding mode was found in **K8**. The average 2.956 Å distance of donor...acceptor herein is obviously shorter comparing to that value in the rigid ligand system, (table 9.8, 9.9) indicating a stronger H-bonding interaction formed in these flexible ligand series. The detailed values of the involved short interactions are listed in table 9.9.

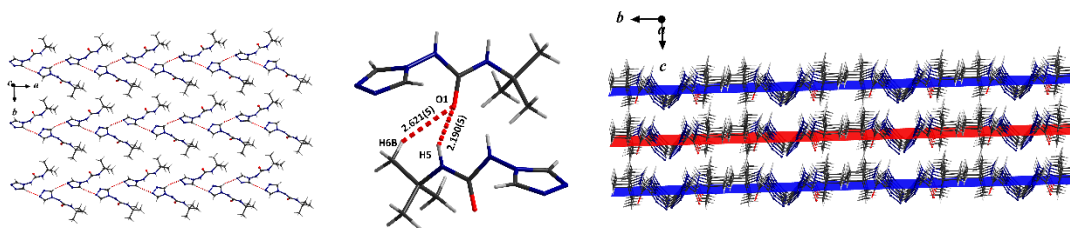


Figure 6.14.: The 2D network formed via multiple supramolecular interactions in ab plane, and the view of the layered structure in **K6**. The dashed lines represent the short supramolecular interactions involved. The urea involved H-bonding interaction is highlighted for clarity.

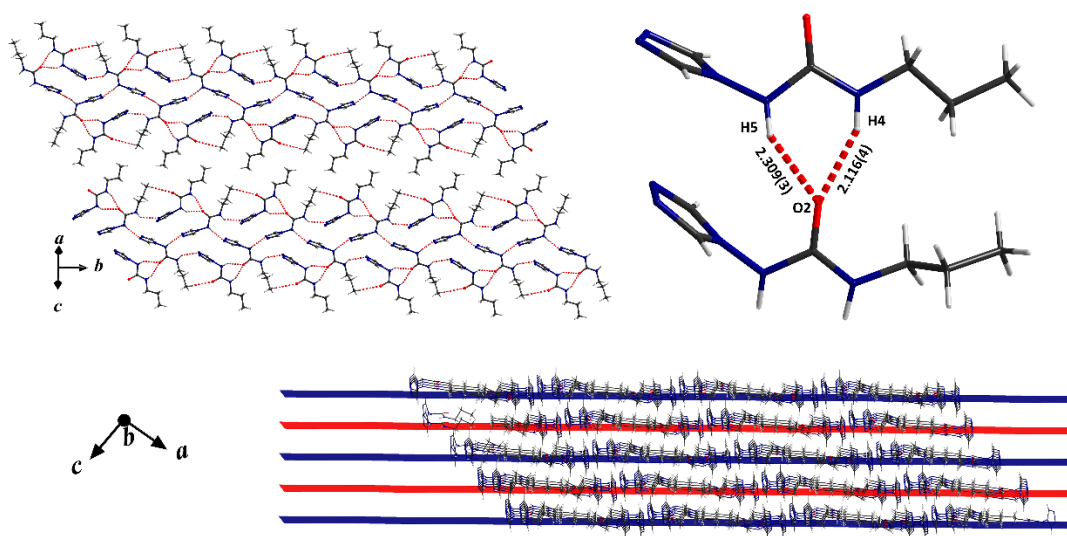


Figure 6.15.: The 2D network formed via multiple supramolecular interactions in $[1\ 0\ 1]$ plane, and the view of the layered structure in **K7**. The dashed lines represent the short supramolecular interactions involved. The urea involved H-bonding interaction is highlighted for clarity.

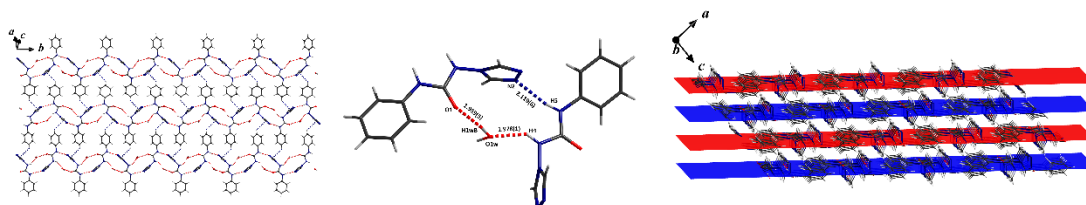


Figure 6.16.: The 2D network formed via multiple supramolecular interactions in bc plane, and the view of the layered structure in **K8**. The dashed lines represent the short supramolecular interactions involved. The urea involved H-bonding interaction is highlighted for clarity.

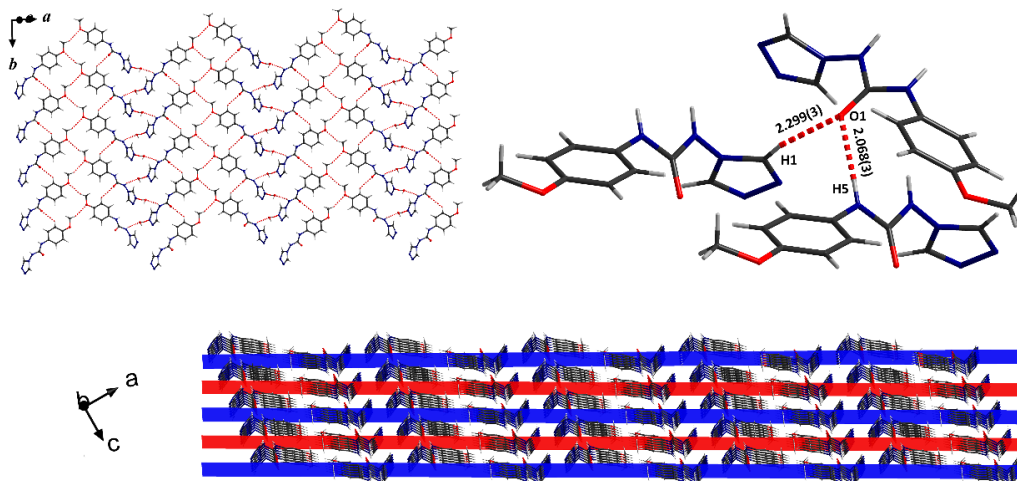


Figure 6.17.: The 2D network formed via multiple supramolecular interactions in *ab* plane, and the view of the layered structure in **K9**. The dashed lines represent the short supramolecular interactions involved. The urea involved H-bonding interaction is highlighted for clarity.

6.6 Rationalization of the Crystallization

The occasionally obtained Fe complexes (**C3**, **C11**, **C13–C15**), represent the competition between the expected μ_2 -*N1,N2*-triazole bridged stable form of Fe complex and the unstable “*fleeting*” structures obtained during the crystallization process. Compound $[\text{Fe}^{\text{II}}_2(\text{toltrz})_6(\text{C}_2\text{O}_4)(\text{H}_2\text{O})_2](\text{SeCN})_2(\text{toltrz})_2(\text{H}_2\text{O})_4$ (**C3**) stands for the difficulty of keeping the Fe(II) salts at rather low oxidation state (+2), the by-product of **C3**, together with the other three compounds summarized in chapter 4 proved that the addition of ascorbic acid to the reaction system indeed can prevent the Fe(II) salts from oxidating to Fe(III) state. While the resulting oxalate anion sometimes overcomes the formation of the triazole-bridged product, as the oxalate-bridged chain or 2D network is more likely to crystallize. Compound $[\text{Fe}^{\text{II}}(2\text{-imztrz})_2(\text{CH}_3\text{OH})_2(\text{SCN})_2]$ (**C11**) is truly a metastable form of compound as the crystal re-dissolves in the mother-liquid after one day. This can be a competition with compound $[\text{Fe}^{\text{II}}_2(2\text{-imztrz})_4(\text{SCN})_4]$ (**C10**), even though we successfully isolated and repeated **C10**, the stable form. Despite the completely different coordination environment and structural packing (1D, hexanuclear 3D and trinuclear 3D), compounds **C13–C15** came from the same reaction conditions with parallel batches. Further synthetic procedure proved that **C15** is the most stable form among the three polynuclear complexes. These three results demonstrated that the flexibility of the self-assembly process of crystallization, even though in most of the times success has been achieved with the most thermally-stable form of all the possible combinations.

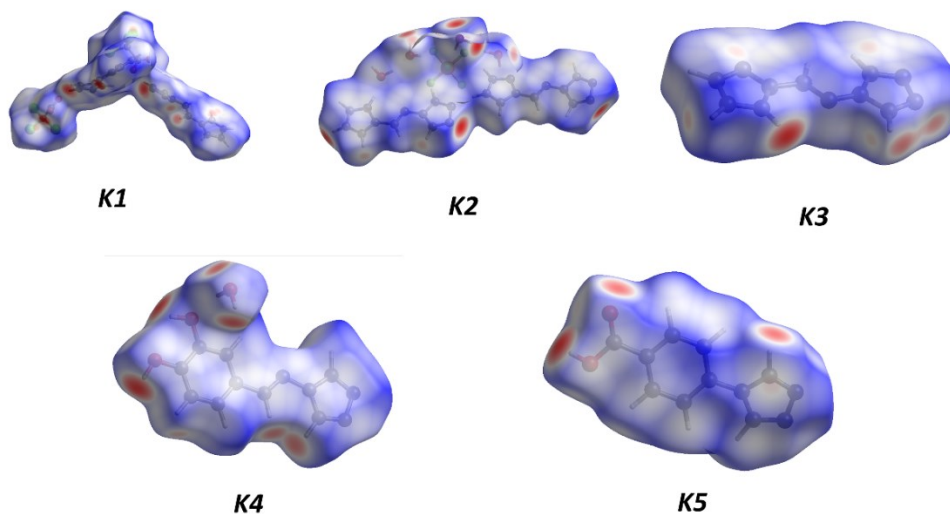


Figure 6.18.: Hirshfeld surface analysis mapped over d_{norm} showing intermolecular H-bonding interactions and $\pi \cdots \pi$ stackings for crystals **K1–K5**.

The organic ligand (salts) crystal structures (**K1 – K9**) were mainly isolated by occasion during the preparation of the corresponding Fe(II) complexes. From the ligand point of view, they share one distinguish character that might explain the overall formation of organic solid state compounds other than the desired Fe(II) complex: the multiple supramolecular interactions in the solid state packing among these structures. Apart from the structure description, the major H-bonding, $\pi \cdots \pi$ stackings discussed in the last two sections, the Hirshfeld surfaces were calculated to analyze the intermolecular interactions that stabilize the molecules in 3D space packing. Hirshfeld surfaces analysis of **K1–K5** are illustrated, showing the surfaces mapped over d_{norm} (Figure 6.18) and two-dimensional fingerprint plots showing intermolecular interactions with percentages contribution of intermolecular contact highlighted. (Figure 6.19). Hirshfeld surfaces showing red circles stand for C–H \cdots N and C–H \cdots O intermolecular interactions and the remaining faint red color spots represent for C–H \cdots π stacking interactions. In addition, the intermolecular H-bonding for C–H \cdots N and C–H \cdots O interactions are also reflected in the 2D finger plot by the two long spikes. The d_{norm} surface showing the visible red spots indicate C–H \cdots π , C–H \cdots N and C–H \cdots O intermolecular interactions, whereas the blue parts indicate H \cdots H and C \cdots C contacts.

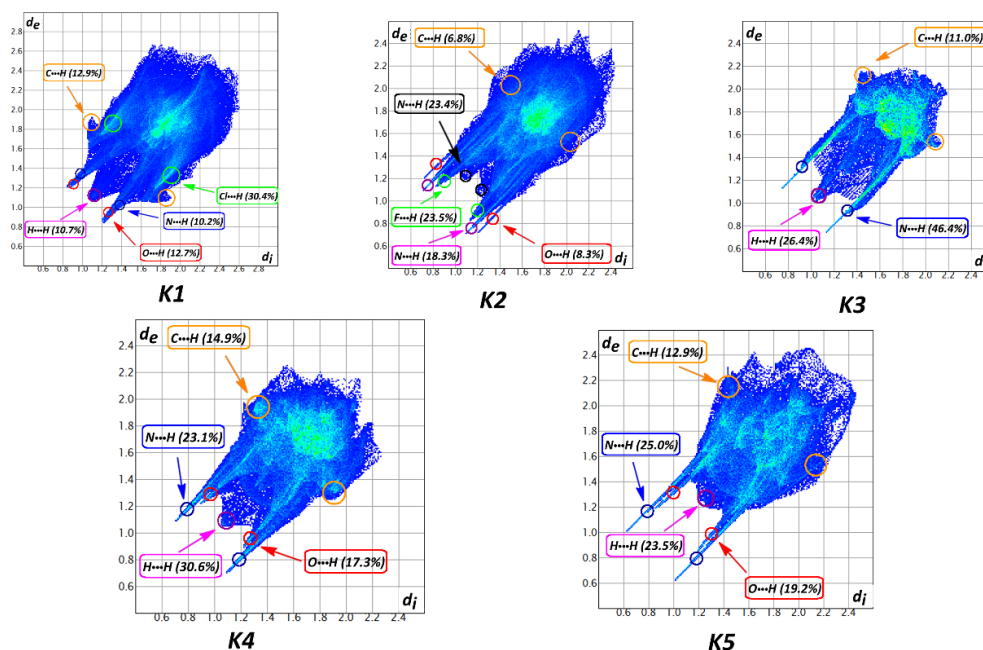


Figure 6.19.: The 2D fingerprint plots derived from Hirshfeld surface analysis for **K1–K5**.

Within the 2D fingerprint plots, analysis of the relative contributions due to the different interaction types for this group of crystal structures gives us valuable information about how the structure is packed and which contact dominates the 3D packing. For **K1–K5**, they share some same characters as they all have the very similar structure packing. The sharp spike-like green regions in the plots correspond to the H-Bondings (C–H...N and C–H...O), while the C...H/H...C contacts (defined as the C–H... π interactions) are appear as “wing” in the upper left and right of the 2-D fingerprint plot. The C...C contacts hold less than 1.2% to 2.5% contributions among all five compounds confirmed the fact that there are not so many fac-to-face π ... π stacking in these structures. For **K1** and **K2**, the additional counteranions (CCl_3COO^- and PF_6^-) dominates the major packing with Cl...H/H...Cl (**K1**) and F...H/H...F (**K2**) comprises 30.4% and 23.5% of the total Hirshfeld surfaces, respectively. The 46.4% high ratio of N...H/H...N contacts in **K3** tells us that it is mainly the H-bonding involved with N atoms from the ligand stabilizing the solid packing, rather than π ... π stacking. Additionally, H...H contacts were found to play major roles in the construction of the 3D architectures for **K3** to **K5**.

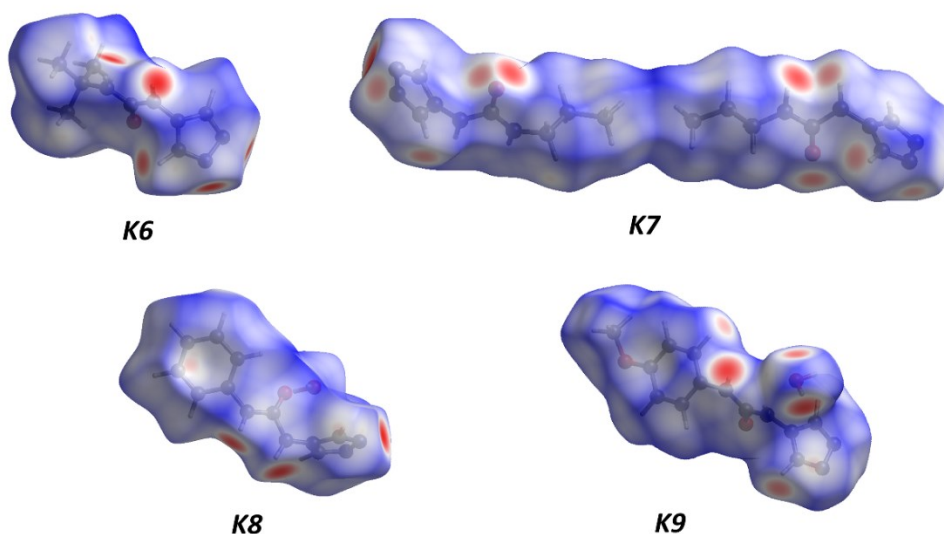


Figure 6.20.: Hirshfeld surface analysis mapped over d_{norm} showing intermolecular H-bonding interactions and $\pi\cdots\pi$ stackings for crystals **K6–K9**.

Figure 6.20 illustrates the Hirshfeld surfaces analysis of **K6–K9** and the corresponding 2D fingerprint plots are shown in figure 6.21. Evidently, the Hirshfeld surfaces give us the information of strong H-Bonding involving the urea group (NH–CO–NH) and the nitrogen atoms from the triazole ring, indicating as the red circle spots on the surface. The blue parts represent the H...H and C...H contacts. Additionally, the rather faint red spot around the benzyl ring on **K8** reflects the weak C–H... π stacking involved.

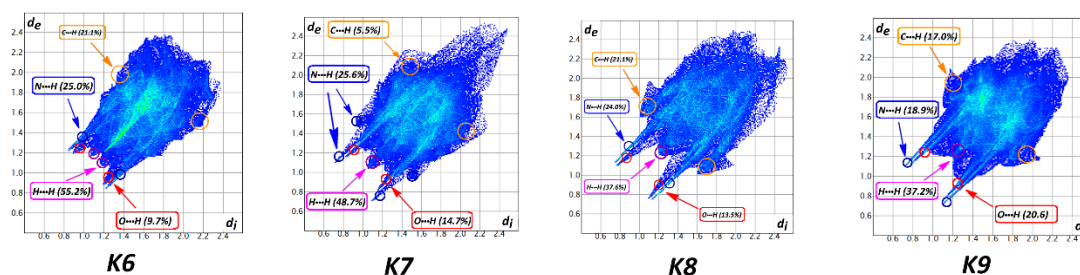


Figure 6.21.: The 2D fingerprint plots derived from Hirshfeld surface analysis for **K6–K9**.

The 2D fingerprint plots give us information about the C–H...N, C–H...O H-bonding interactions and the C–H... π stacking involved for the 3D solid packing. The C...C contacts are only found in **K8** and **K9** with the occupation of 1.5% and 1.2%, indicating the negligible face-to-face stacking in the structure. Apart from the fingerprint of H-bonding that appears as upper and lower spikes in the 2D plots, the H...H contacts make a large contribution to the total Hirshfeld surfaces and are reflected in the middle of the scattered points. Very interestingly, **K6–K8** share similar O...H/ H...O contribution due to the oxygen atoms from

Chapter 6 Crystal Structure of “Fleeting Fe complexes” and Ligands: Crystallization Consideration

the urea group, which comprises 9.7%, 12.8 %, and 14.7% of the total Hirshfeld surfaces for **K6**, **K7** and **K8** respectively. Introducing of another oxygen atom on **K9**, however, leads to an augment of that ratio to 20.6%, indicating a 5% of surface increasing with H-Bonding with a solely oxygen addition. That information provides us solid experience for a further ligand design purpose.

In summary, the Hirshfeld surface analysis and 2D fingerprint plots allow us a visual insight into the differences in the packing modes and the intermolecular contacts present in the crystal lattices among these crystal structures. The multiple supramolecular interactions involved supply an explanation of the competition between the Fe complex isolation and ligand crystallization. These information can guide us through further crystallization process.

6.7 Reference

- [1] O. Kahn, *Molecular Magnetism*, VCH Publishers Inc., New York, **1993**.
- [2] D. K. Bučar, R. W. Lancaster, J. Bernstein, *Angew. Chem., Int. Ed.* **2015**, *54*, 6972–6993.
- [3] J. D. Dunitz, J. Bernstein, *Acc. Chem. Res.* **1995**, *28*, 193–200.
- [4] B. R. Pamplin, *Crystal Growth: International Series on the Science of the Solid State*; Elsevier: Amsterdam, **2013**.
- [5] B. Spingler, S. Schnidrig, T. Todorova, F. Wild, *CrystEngComm*, **2012**, *14*, 751–757.
- [6] a) X. X. Wu, Y. Y. Wang, P. Yang, Y. Y. Xu, J. Z. Huo, B. Ding, Y. Wang, X. Wang, *Cryst. Growth Des.*, **2013**, *14*, 477–490; b) B. Zhai, Z. Y. Li, X. F. Zhang, X. X. Wu, J. H. Guo, J. Z. Huo, B. Ding, *Z. Anorg. Allg. Chem.*, **2016**, *642*, pp.260–267.
- [7] a) L.L. Li, K.J. Lin, C.J. Ho, C.P. Sun, H.D. Yang, *Chem. Commun.*, **2006**, 1286–1288; b) T.K. Paine, J. England, L. Que, *Chem. Eur. J.*, **2007**, *13*, 6073–6081; c) G. De Ruiter, J. S. Costa, K. Lappalainen, O. Roubeau, P. Gamez, J. Reedijk, *Inorg. Chem. Commun.*, **2008**, *11*, 787–790.
- [8] A. Spek, *PLATON, A Multipurpose Crystallographic Tool*, Utrecht University, Holland, **1998**.
- [9] a) C. Serre, C. Mellot-Draznieks, S. Surble, N. Audebrand, Y. Filinchuk and G. Férey, *Science*, **2007**, *315*, 1828; b) C. Serre, F. Millange, S. Surble and G. Férey, *Angew. Chem., Int. Ed.*, **2004**, *43*, 6286.
- [10] T. Aharen, F. Habib, I. Korobkov, T. J. Burchell, R. Guillet-Nicolas, F. Kleiz, M. Murugesu, *Dalton Trans.*, **2013**, *42*, 7795–7802.
- [11] E. Rentschler, M. Christian, *Inorganica Chim. Acta.*, **2008**, *361*, 3646–3653.
- [12] a) B. Isare, S. Pensec, M. Raynal, L. Bouteiller, *Comptes Rendus Chimie*, **2016**, *19*, 148–156; b) N. Iqbal, M. Tripathi, S. Parthasarathy, D. Kumar, P. K. Roy, *RSC Adv.*, **2016**, *6*, 109706–109717; c) V. Amendola, L. Fabbri, L. Mosca, *Chem. Soc. Rev.*, **2010**, *39*, pp.3889–3915; d) R. Custelcean, *Chem. Commun.*, **2008**, *3*, 295–307.

Chapter 7 General Discussion and Perspective

The primary aim of the present study in this thesis was to synthesize new Fe(II) complexes with the potential to exhibit SCO transition, extending from molecular clusters to higher dimensional (1D, 2D, 3D) materials. To achieve this goal, a number of multi-dentate triazole-based ligand systems with different substituents as well as their Fe(II) complexes were synthesized. These compounds were analyzed using a variety of techniques including crystallography, SQUID magnetization and Mössbauer spectroscopy. Different magnetic properties have been found among the isolated compounds, like SCO transitions, antiferromagnetic coupling and ferromagnetic coupling.

After a general introduction in Chapter 1, Chapter 2 and Chapter 3 discuss a series of three dinuclear and two trinuclear *N1,N2*-triazole bridged Fe(II) complexes which differed only in the terminal ligand groups and counteranions. All five of these discrete multi-nuclear species shared similar geometric properties. Quite interestingly, the two trinuclear complexes (**C4**, **C6**) exhibit SCO behavior with different patterns (gradual vs. abrupt transition). The considerable effects of supramolecular interactions on these two SCO compounds were explored. For both trinuclear complexes the central SCO-Fe(II) centers are surrounded by triazole nitrogens, while the terminal Fe(II) centers are coordinated by water molecules and thus do not undergo spin transition. This intrigues us the idea of design-synthesizing similar triazole mediated SCO compounds by changing of suitable terminal ligand other than the bridging triazole ligand is also possible and plausible.

The study was then moved to three polynuclear Fe compounds, discussed in Chapter 4. The coordination sphere of the iron ions in these three compounds were all linked by a second carboxyl-based ligand (oxalate, citrate). The structures differed from a Fe(III) dimer to a Fe(II) one dimensional chain to a Fe(II) three dimensional framework. Remarkably, the two Fe(II) complexes owned the porous features of the metal-organic-frameworks (MOFs). Detailed magnetic studies showed that all three compounds exhibit different degree of antiferromagnetic coupling between the adjacent active Fe centers. This work here gave us good experience that the ascorbic acid adding to the synthetic system aiming at prevention of Fe(II) oxidation could lead to quite different unexpected results, as the decomposed oxalate seemed to have a better coordination ability comparing to the nitrogen donors from the ligand. If one has to use ascorbic acid for this purpose during the synthesis of Fe(II) complex, one should maintain the synthetic condition under a rather mild condition.

Additionally, the results here have shown the potential of triazole ligand acting as bidentate linkers, like 4,4'-bipyridine, to construct high dimensional framework.

High dimensional networks built up from a [FeN₆] core were obtained and are summarized in Chapter 5. Two examples of 2D Fe(II) networks sharing similar structural characters but revealing different magnetic behavior are reported. Surprisingly, these two 2D networks do not show SCO upon cooling to 2K. The reason might be that the mediated coordinated nitrogen atoms from the imidazole ring leading to a rather small ligand field around the Fe centers. Pleasantly, [Fe^{II}(5-imztrz)₂](ClO₄)₂ (**C12**) was found to behave as a ferromagnetic model, while [Fe^{II}₂(2-imztrz)₄(SCN)₄] (**C10**) stays at high spin state accompanied by a weak antiferromagnetic exchange coupling through the lattice supramolecular interactions.

The two 2D networks obtained here were quite different from a reported bidentate triazole linked network. This showed the possibility of combining the triazole ligand with a second coordination site to construct high dimensional Fe(II) complex. For a future extension work of this idea, one should take the ligand field strength into consideration as well as the second coordination site. The imidazole and imine groups here contributed too small ligand field strength and the compound do not show SCO. Moreover, compound **12** represents the first example of structurally and magnetically characterized ferromagnetic coupled 2D network through the triazole-imine linkage.

Chapter 6 summarizes several crystal structures that formed as *unexpected* result when trying to synthesize Fe(II) complexes. The structures here mainly resulted from the competition between the crystallization of the targeted compounds and the isolated *by-product*, either Fe complex or pure ligand form. Detailed discussion has been made in regard to explore the relationship between the supramolecular interactions and the unexpected crystals formation. During the preparation of compounds **13–15**, we have found that the solvothermal synthesis of SCO Fe complex is problematic. Firstly, both mixed and metastable products can be obtained, and the harsh synthesis method can even give decomposition of solvents and chemicals, which in most circumstances is undesirable. Secondly, even though sometimes we successfully get the desired crystals, they tend to embedded into a pile of dark powder resulting from the decomposition of other solvents and chemicals, which makes it very difficult to separate the clean crystals. Consequently, when designing SCO Fe complex by solvothermal synthesis, one has to take good care of these facts. The analysis of Hirshfeld surfaces and fingerprint plots of the organic crystal structures provides insight into the intermolecular interactions in the molecular structures.

Relationship has been explored that the multi-supramolecular interactions found in these structures not only stabilize the solid packing in the crystal lattice, but also partially explain the reason why it more likely tend to crystallize as ligand rather than in an Fe-complex. Especially for the urea-triazole ligand system, the urea group indeed can bring lots of H-bonding when forming the solid structure, while this also brings the problem of crystallization with this highly H-bonded system. Hence, it is reasonable to introduce more supramolecular interactions in a SCO system to increase the cooperativity between the active metal centers, while one should also keep in mind that too much of the uncontrollable intermolecular interactions might lead to difficulty of isolating the corresponding crystalline compounds, which is also of vital importance for the SCO studies.

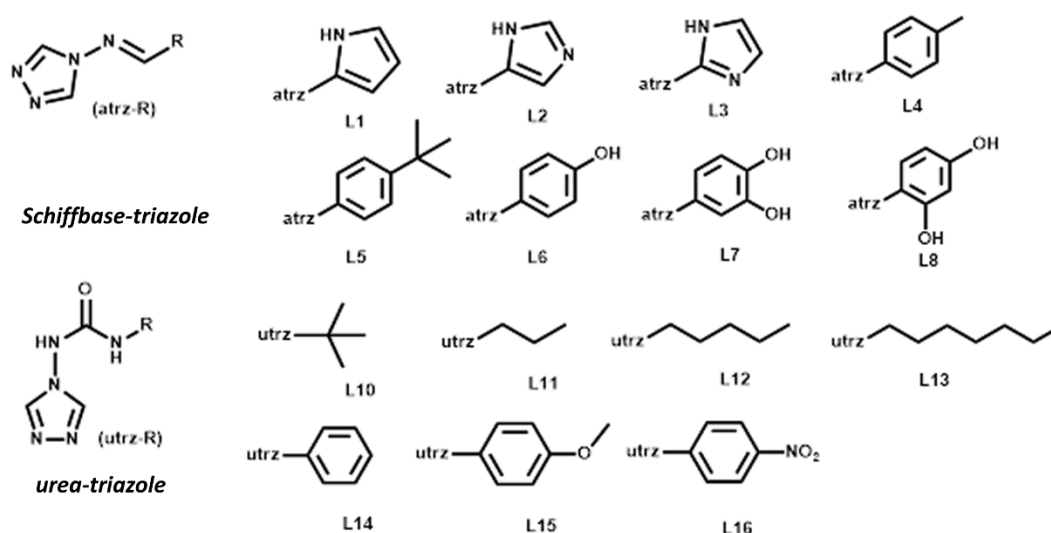


Figure 7.1.: The two typically ligand systems applied in the present study: Schiff base triazole and urea-triazole ligand.

Based on the above results and the discussion, an assumption of the two major ligand systems can be made. As shown in figure 7.1, the obtained Fe(II) complex centered on L1 to L4, representing ligands with rather less potential supramolecular interactions. Ligand 6 to L8 bear too much potential H-bonding sites that makes it difficult to crystallize the corresponding Fe complex. In addition, the hydroxyl group can be a coordination competition with the triazole nitrogen donors. The urea-triazole system did not give any crystalline compounds, even though most of the powder obtained was light-colored (light-reddish, pink, even white) at room temperature, indicating the highly possible low spin state iron complex. As our aims were to explore the relationship between the supramolecular interactions, covalently linked bonds and the SCO behavior, the obtained non-crystalline powder was not our study subject herein. Further continuation of this work could focus more

on ligands with less supramolecular interaction potential, like ligand 1 to ligand 4, which have been proved showing flexible coordination mode and effective to form SCO Fe centers. Attempt could also be made to change the terminal ligand site of the obtained dinuclear and trinuclear complex. Additionally, the ease in modification of the Schiff base triazole system through different combinations of aldehydes, makes this ligand system ideal for further research.

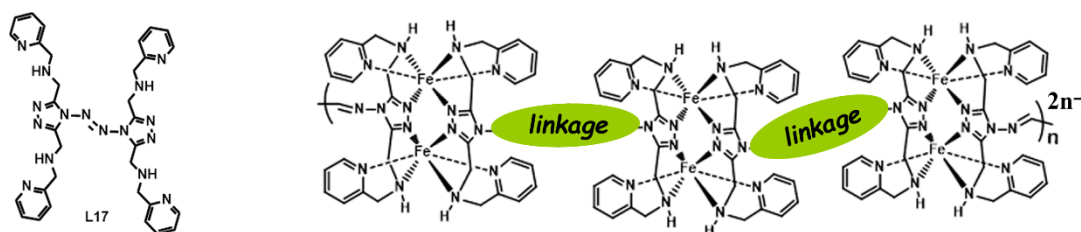


Figure 7.2.: The newly synthesized ligand 17 and the ideal D chain model for further SCO compounds synthesis.

Finally, the newly synthesized ligand 17 represent the idea of linking the well-studied dinuclear system into one dimensional chain structure. As illustrated in figure 7.2, the application of this ligand could lead to a 1D chain with a dimeric Fe core. As the triazole-based dinuclear system is already a well-studied system, the formed compound should have the right ligand field strength to switch the spin state. The linkage between the dimeric core could be phenyl, vinyl or other rigid or half-rigid functions. Future efforts should focus on the crystallization of compounds with this type of ligand. The targeted 1D chain structure could then be compared to the famous triazole-based 1D chain, which would be very helpful to explore the relationship between the covalent linked active Fe centers and SCO properties.

Chapter 8 Methodology and Technique

8.1 Materials and Characterization

8.1.1 Materials

All commercially purchased chemicals and solvents were used without further purification (unless specified). Chemicals were purchased mainly from *Alfa Aesar*, *Acros Organics*, *Fisher Chemicals*, *Sigma-Aldrich* and *TCI Chemicals*. The solvents used for the complex syntheses were degassed with argon, even though in some cases, with ascorbic acid added. All complex syntheses were performed in an argon or nitrogen atmosphere to prevent the oxidation of Fe(II) to Fe(III).

8.1.2 NMR-Spectroscopy

The NMR spectra were recorded at room temperature using a Bruker DRX 400 spectrometer ($\nu(^1\text{H}) = 400.13$ MHz, $\nu(^{13}\text{C}) = 100.61$ MHz). The data was processed and analyzed with the programs Bruker *TopSpin 1.3* and *MestReNova*.^[1]

8.1.2 Single X-ray Crystallography

Single-crystal X-ray diffraction data were collected on a Bruker Smart APEX II CCD diffractometer, operating at 45 kV and 35 mA using Mo K α radiation ($\lambda = 0.71073$ Å), the diffractometer was equipped with a nitrogen cold stream operating at 173(2) K. The low temperature (120K) data was collected on a STOE IPDS 2T diffractometer at the Johannes Gutenberg-University Mainz. Each data reduction was performed using the SMART and SAINT software^[2] and an empirical absorption correction was applied using the SADABS program.^[3] All structures were solved by direct methods and refined by full-matrix least-squares on F^2 using the SHELXTL program package,^[4] and the Olex2 program.^[5] The ordered non-hydrogen atoms in each structure were refined with anisotropic displacement parameters, while the hydrogen atoms were placed in idealized positions and allowed to ride on their parent atoms. The disordered fraction in all crystal data is specified separately on each case, with different restrains and constrains parameters applied to get a better model. All structure figures are generated with DIAMOND-3.^[6]

8.1.3 SQUID Measurements

Magnetic susceptibility data were collected with a Quantum Design SQUID magnetometer MPMS XL-7 (at the Johannes Gutenberg-University Mainz) in a temperature range of 2-300 K with an applied field of 1 kOe. The molar susceptibility was calculated with the program julX 1.4.1 of Eckhard Bill (MPI Mülheim/Ruhr).

The simulation of the magnetic data has been performed with PHI. [7] The used Hamiltonian in the program PHI

$$\hat{H} = \hat{H}_{SO} + \hat{H}_{EX} + \hat{H}_{CF} + \hat{H}_{ZEE} \text{ (Equation 8.1, taken from ref [7])}$$

contains the spin-orbit coupling Hamiltonian (\hat{H}_{SO}), exchange interaction Hamiltonian (\hat{H}_{EX}), Crystal Field Hamiltonian (\hat{H}_{CF}) and Zeeman Hamiltonian (\hat{H}_{ZEE}). It was possible to solely consider the exchange interaction Hamiltonian (\hat{H}_{EX}) and Crystal Field Hamiltonian (\hat{H}_{CF}) for the treated systems.

$$\hat{H}_{EX} = \sum_{i < j}^{i, j \in N} J_{ij} \mathcal{S}_i \cdot \mathcal{S}_j \text{ (Equation 8.2, taken from ref [7])}$$

$$\hat{H}_{CF} = \sum_{i=1}^N \sum_{k=2,4,6} \sum_{q=-k}^k B_{ki}^q \theta_k \mathcal{O}_{ki}^q \text{ (Equation 8.3, taken from ref [7])}$$

In some cases a temperature independent paramagnetism (TIP) and diamagnetic impurity fraction (ρ) had to be included in the simulation.

8.1.5 Mössbauer Measurements

^{57}Fe Mössbauer spectra were recorded at different temperature on a self-made Mössbauer spectrometer with a CryoVac He-Bath-Cryostat. The data was recorded and analyzed by fitting to Lorentzian lines in the group of Prof. Dr. Volker Schünemann at *Technische Universität Kaiserslautern* by Dr. Juliusz A. Wolny and Tim Hochdörffer.

8.1.6 Infrared Spectroscopy

Infrared spectra (FT-IR) were recorded as potassium bromide pellets in the range from 4000 cm^{-1} to 400 cm^{-1} with a JASCO FT/IR-4200. The data processing was performed with JASCO Spectra Manager.

8.1.7 Elemental Analysis

Elemental analyses (C, H, N and S) were measured at the micro-analytical laboratory of the Johannes Gutenberg University Mainz with a Foss Heraeus Vario EL elemental analyzer.

8.2 Synthetic Method

8.2.1 Preparation of Ligands

The Schiff base ligands (L1 to L8) were prepared in a similar manner via a modified procedure from the reported article. [8] To avoid the possible by-product, ethanol was chosen as the reaction solvent. Unless stated differently, the ligand synthesis procedure was the following:

4-amino-1,2,4-triazole (1.68 g, 0.02 mol, 1.0 eq.) and the corresponding aldehyde (*x* g, 0.022 mol, 1.1 eq.) were dissolved in ethanol with the addition of few drops of H₂SO₄, acting as acidic catalyst. The reaction mixture was slowly heated up to 80 °C until it started to boil, then refluxed at this temperature for 10 h. When it cooled down to r.t., the excess of the solvent was removed by rotary evaporator at 35 °C. The products such obtained was washed with small amount of cold ethanol, diethyl ether and then dried in the desiccator with phosphorus pentoxide as dry agent. The isolated powder products were used for the complex synthesis without further purification.

8.2.1.1 4-((1H-pyrrol-2-yl)methylene-amino)-4H-1,2,4-triazole (L1)



From 4-amino-1,2,4-triazole (1.68 g, 0.02 mol, 1.0 eq.) and pyrrole-2-carboxaldehyde (2.09 g, 0.022 mol, 1.1 eq.), dark purple powder was obtained.

Yield: 3.14 g (19.49 mmol, 97.52%)

M.P.: 207.5–210.7 °C

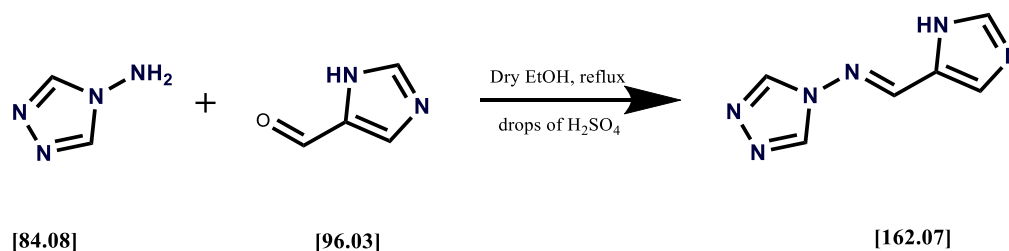
¹H-NMR: (400 MHz, *d*⁶-DMSO, 25 °C): (Figure 9.1)

δ (ppm): 7.91 (s, 1H, Ar-H), 7.99 (s, 1H, Ar-H), 8.92 (s, 1H, H-C=N), 9.07 (s, 2H, triazole).

Selected IR (KBr): (Figure 9.20)

ν (cm⁻¹): 3127(s), 2956 (m), 2853 (m), 1609 (vs), 1508 (s), 1420 (s), 1361 (s), 1169 (s), 1062 (vs), 858(s), 762 (vs), 623 (s), 498 (m).

8.2.1.2 4-(1H-imidazol-5-ylmethylene-amino)-4H-1,2,4-triazole (L2)



From 4-amino-1,2,4-triazole (1.68 g, 0.02 mol, 1.0 eq.) and 1H-imidazole-4-carbaldehyde (2.11 g, 0.022 mol, 1.1 eq.), light-yellow powder was obtained.

Yield: 2.98 g (18.39 mmol, 91.89%)

M.P.: 253.5–265.7 °C

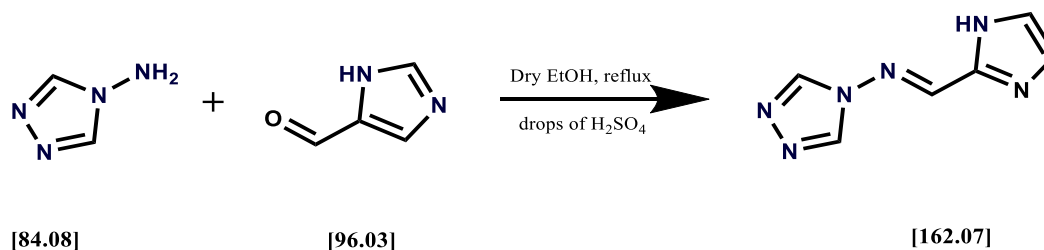
¹H-NMR: (400 MHz, *d*⁶-DMSO, 25 °C): (Figure 9.2)

δ (ppm): 9.07 (s, 2H, triazole), 8.92 (s, 1H, H-C=N), 7.91 (s, 1H, imidazole ring), 7.79 (s, 1H, imidazole ring).

Selected IR (KBr): (Figure 9.21)

ν (cm⁻¹): 3109(s), 2838 (w), 1625 (vs), 1504 (vs), 1434 (s), 1386 (s), 1299 (s), 1214 (w), 1175 (vs), 1060 (vs), 995 (s), 945 (w), 853 (s), 691 (m), 630 (vs), 510 (m).

8.2.1.3 4-(1H-imidazol-2-ylmethylene-amino)-4H-1,2,4-triazole (L3)



From 4-amino-1,2,4-triazole (1.68 g, 0.02 mol, 1.0 eq.) and 2-imidazolecarboxaldehyde (2.11 g, 0.022 mol, 1.1 eq.), light-yellow powder was obtained.

Yield: 2.56 g (15.80 mmol, 78.98 %)

M.P.: 217.6–233.5 °C

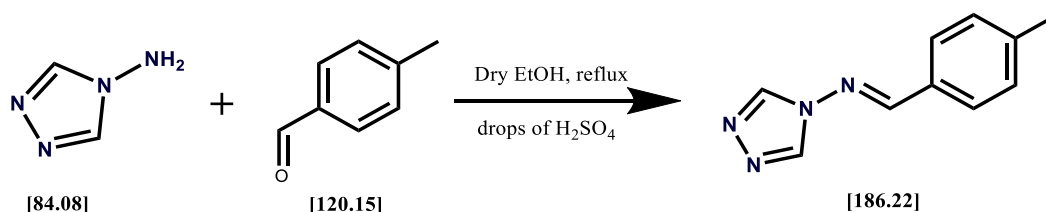
¹H-NMR: (400 MHz, *d*⁶-DMSO, 25 °C): (Figure 9.3)

δ (ppm): 13.33 (s, H-N_{imidazole}), 9.16 (s, 2H, triazole), 8.96 (s, 1H, H-C=N), 7.45 (s, 1H, imidazole ring), 7.27 (s, 1H, imidazole ring).

Selected IR (KBr): (Figure 9.22)

ν (cm⁻¹): 3115(vs), 3005 (m), 2795 (m), 2711 (m), 1622 (s), 1515 (vs), 1440 (vs), 1348 (s), 1233 (w), 1189 (vs), 1159 (s), 1120 (vs), 1056 (vs), 985 (s), 931 (w), 853 (vs), 781 (vs), 705 (vs), 618 (s), 509 (w).

8.2.1.4 4-(*p*-tolylidene-amino)-4*H*-1,2,4-triazole (L4)



From 4-Amino-1,2,4-triazole (1.68 g, 0.02 mol, 1.0 eq.) and 4-methylbenzaldehyde (2.65 g, 0.022 mol, 1.1 eq.), white powder with intense smelling was obtained.

Yield: 3.53 g (18.96 mmol, 94.85%)

M.P.: 137–163 °C

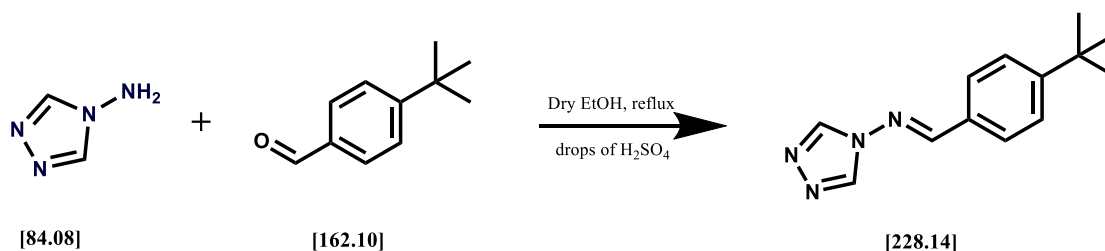
¹H-NMR: (400 MHz, *d*⁶-DMSO, 25 °C): (Figure 9.4)

δ (ppm): 9.13 (s, 2H, triazole), 9.04 (s, H-C=N), 7.76–7.74 (d, 2H, Ar-H), 7.38–7.36 (d, 2H, Ar-H), 2.39 (s, 3H, *p*-CH₃).

Selected IR (KBr): (Figure 9.23)

ν (cm⁻¹): 3086 (vs), 2921 (w), 1606 (vs), 1502 (vs), 1459 (m), 1328 (m), 1290 (m), 1217 (s), 1162 (vs), 1065 (vs), 973 (s), 938 (s), 866 (m), 816 (vs), 724 (m), 623 (vs), 515 (s).

8.2.1.5 4-[(4-(*tert*-butyl)benzylidene)-amino]-4*H*-1,2,4-triazole (L5)



From 4-Amino-1,2,4-triazole (1.68 g, 0.02 mol, 1.0 eq.) and 4-*tert*-butylbenzaldehyde (3.57 g, 0.022 mol, 1.1 eq.), white powder with intense smelling was obtained.

Yield: 3.90 g (17.10 mmol, 85.47%)

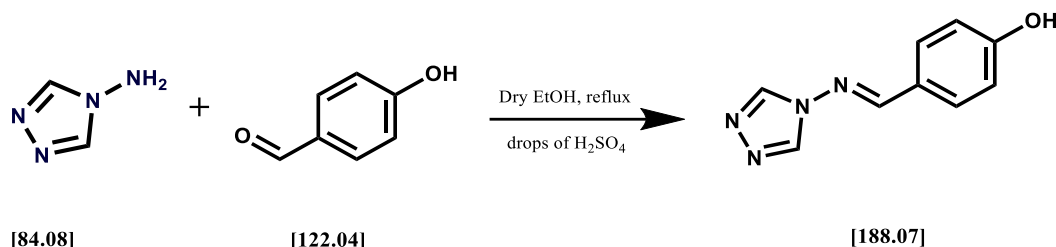
¹H-NMR: (400 MHz, CD₃OD, 25 °C): (Figure 9.5)

δ (ppm): 9.05 (s, 2H, triazole), 8.95 (s, 1H, H-C=N), 7.86–7.84 (d, 2H, Ar-H), 7.59–7.57 (d, 2H, Ar-H), 1.36 (s, 9H, -C(CH₃)₃).

Selected IR (KBr): (Figure 9.24)

ν (cm⁻¹): 3100 (vs), 2966 (vs), 1606 (s), 1494 (vs), 1391 (m), 1287 (m), 1185 (m), 1162 (s), 1107 (w), 1048 (vs), 989 (m), 938 (m), 861 (m), 836 (s), 670 (m), 625 (vs), 560 (m), 504 (m).

8.2.1.6 4-[(4*H*-1,2,4-Triazol-4-ylimino)methyl]phenol (L6)



From 4-Amino-1,2,4-triazole (1.68 g, 0.02 mol, 1.0 eq.) and *p*-hydroxybenzaldehyde (2.69 g, 0.022 mol, 1.1 eq.), white powder with intense smelling was obtained.

Yield: 3.43 g (18.23 mmol, 91.15%)

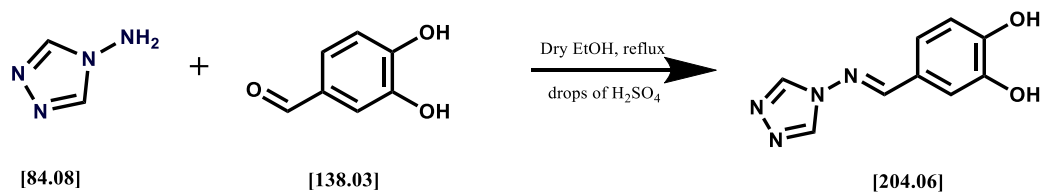
¹H-NMR: (400 MHz, *d*⁶-DMSO, 25 °C): (Figure 9.6)

δ (ppm): 9.07 (s, 2H, triazole), 8.92 (s, 1H, H-C=N), 7.71–7.69 (d, 2H, Ar-H), 6.92–6.90 (d, 2H, Ar-H).

Selected IR (KBr): (Figure 9.25)

ν (cm⁻¹): 3116 (vs), 3000 (w), 2948 (w), 2813 (m), 2693 (m), 2611 (s), 1597 (vs), 1512 (vs), 1473 (s), 1449 (s), 1395 (m), 1335 (m), 1287 (vs), 1240 (s), 1171 (vs), 1112 (w), 1055 (vs), 1010 (m), 963 (m), 876 (m), 828 (s), 723 (w), 674 (w), 627 (s), 536 (s), 510 (m), 446 (m).

8.2.1.7 4-[(4*H*-1,2,4-Triazol-4-ylimino)methyl]-1,2-benzenediol (L7)



From 4-Amino-1,2,4-triazole (1.68 g, 0.02 mol, 1.0 eq.) and 3,4-dihydroxybenzaldehyde (3.04 g, 0.022 mol, 1.1 eq.), white powder with intense smelling was obtained.

Yield: 3.52 g (17.23 mmol, 86.15%)

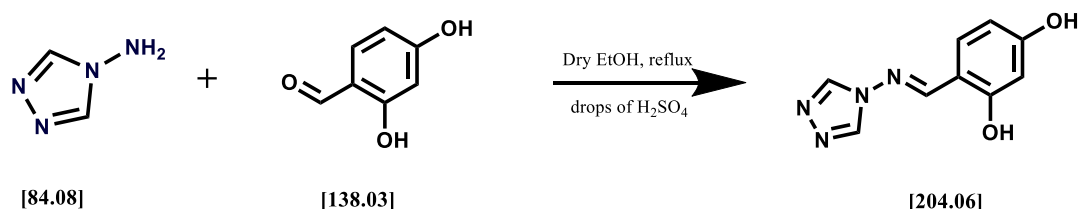
¹H-NMR: (400 MHz, *d*⁶-DMSO, 25 °C): (Figure 9.7)

δ (ppm): 9.06 (s, 2H, triazole), 8.83 (s, 1H, H-C=N), 7.30 (s, 1H, Ar-H), 7.14–7.12 (d, 1H, Ar-H), 6.88–6.86 (d, 1H, Ar-H).

Selected IR (KBr): (Figure 9.26)

ν (cm⁻¹): 3145 (s), 3112 (s), 2958 (w), 2872 (w), 2776 (m), 2587 (m), 1597 (vs), 1511 (vs), 1420 (s), 1348 (s), 1319 (s), 1295 (vs), 1253 (m), 1202 (m), 1180 (s), 1156 (w), 1120 (s), 1063 (vs), 1010 (m), 961 (m), 926 (w), 856 (m), 832 (m), 809 (m), 778 (m), 732 (w), 633 (vs), 568 (s), 508 (m).

8.2.1.8 4-[(4*H*-1,2,4-Triazol-4-ylimino)methyl]-1,3-benzenediol (L8)



From 4-Amino-1,2,4-triazole (1.68 g, 0.02 mol, 1.0 eq.) and 2,4-dihydroxybenzaldehyde (3.04 g, 0.022 mol, 1.1 eq.), greenish powder was obtained.

Yield: 4.00 g (19.63 mmol, 98.15%)

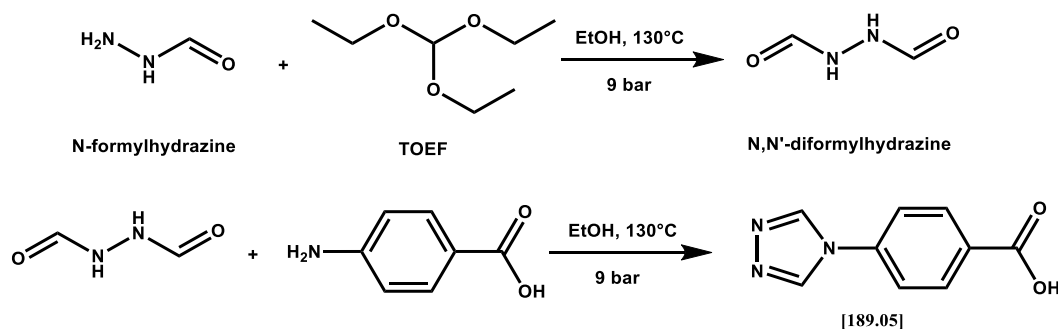
¹H-NMR: (400 MHz, *d*⁶-DMSO, 25 °C): (Figure 9.8)

δ (ppm): 10.33 (2H, broad, -OH), 9.09 (s, 2H, triazole), 8.98 (s, 1H, H-C=N), 7.62–7.60 (d, 1H, Ar-H), 6.41–6.39 (dd, 2H, Ar-H).

Selected IR (KBr): (Figure 9.27)

ν (cm⁻¹): 3148 (m), 3114 (s), 2913 (w), 2601 (m), 1613 (vs), 1579 (vs), 1523 (s), 1476 (m), 1455 (m), 1405 (m), 1303 (m), 1265 (vs), 1206 (m), 1192 (s), 1173 (m), 1111 (s), 1064 (vs), 1005 (w), 978 (m), 878 (m), 833 (s), 788 (m), 741 (w), 713 (m), 630 (s), 530 (s), 481 (s).

8.2.1.9 4-(*p*-Carboxyphenyl)-1,2,4-triazole (L9)



The Hcpt ligand was prepared according to a modified known procedure. [9] Formylhydrazide (0.225 g, 3.25 mmol) and triethylorthoformate (TEOF, 0.935 mL, 5.65 mmol) was placed in a 20 mL microwave tube containing 10 mL ethanol. The sealed tube was then mounted in a CEM laboratory microwave apparatus. After 10 min at 130 °C and 9 bars of pressure with stirring, a clear solution was obtained. To this clear solution (diformylhydrazide formed after the first reaction), 4-aminobenzoic acid (PABA, 0.5 g, 3.25

mmol) was added immediately and the reaction tube was placed back in the microwave. Keep the reaction conditions for the the same as the previous step, continue for another 10 minutes. A white powder formed with slightly pink solution, the white powder was collected by centrifuged the reaction solution under 3000 round per minute (rpm) for 15 minutes. The raw product was purified by recrystallisation in minimum (5 ~ 10 mL) dimethylformamide (DMF) with diethyether. After recrystallisation, the final product was collected as a fine white powder.

Yield: 0.32 g (1.69 mmol, 52.01%).

¹H-NMR: (400 MHz, *d*⁶-DMSO, 25 °C): (Figure 9.9)

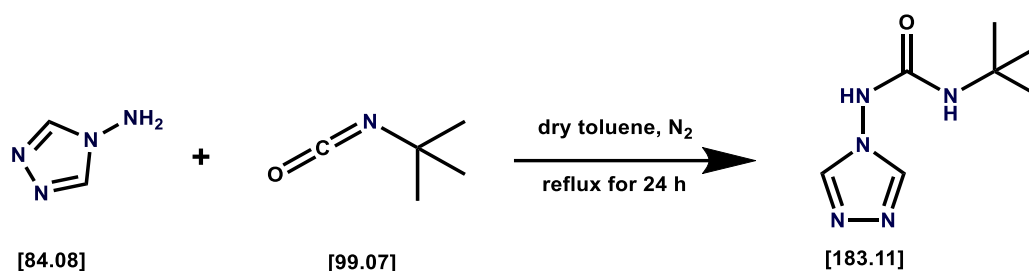
δ (ppm): 9.24 (s, 2H, triazole), 8.10–8.08 (d, 2H, 2H, Ar-H), 7.87–7.85 (d, 2H, Ar-H).

Selected IR (KBr): (Figure 9.28)

ν (cm⁻¹): 3114 (s), 3060 (w), 2807 (w), 2509 (m), 1909 (s), 1691 (vs), 1609 (vs), 1534 (vs), 1506 (s), 1455 (vs), 1373 (s), 1337 (vs), 1309 (vs), 1266 (s), 1247 (s), 1208 (m), 1086 (s), 1015 (s), 964 (m), 863 (vs), 805 (s), 771 (vs), 695 (s), 623 (s), 525 (s), 433 (m).

The urea triazole ligands (L10 to L16) was prepared in a similar manner via a procedure reported by our group. ^[10] The solvent toluene used here was dried in an auto-solvent drying machine. The general ligand synthesis procedure was the following:

First put 4-amino-1,2,4-triazole (1.85 g, 0.022 mol, 1.1 eq.) into a 250 mL two-neck flash filled with dry toluene. One neck of the flask was protected with N₂, while the other neck was connected with a drooping funnel filled with the corresponding isocyanate (*x* g, 0.02 mol, 1.0 eq.) dissolved in dry toluene (20 mL). Slowly heated the reaction up until 110 °C until the 4-amino-1,2,4-triazole melts, forming a two phase mixture with the toluene. Then added the tert-butyl isocyanate dropwise through the dropping funnel in about one hour. Two hours later, the reaction system became cloudy, then kept the reaction at 110 °C for 3 days. After cooling the reaction to 80 °C, 15 mL methanol and 5 mL H₂O were added to quence the unreacted isocyanate. Keep the reaction at 80 °C for another two hours before cool the system to room temperature. Then remove the solvent by rotary evaporator at 35 °C. The products such obtained was washed with small amount of diethyl ether and then dried in the desiccator with phosphorus pentoxide as dry agent. The isolated powder or crystalline products were used for the complex synthesis without further purification.

8.2.1.10 4-(3-*tert*-Butyl ureido)-4*H*-1,2,4-triazole (L10)

From 4-amino-1,2,4-triazole (1.85 g, 0.022 mol, 1.1 eq.) and tert-butyl isocyanate (1.98 g, 0.02 mol, 1.0 eq.), fine white powder was obtained.

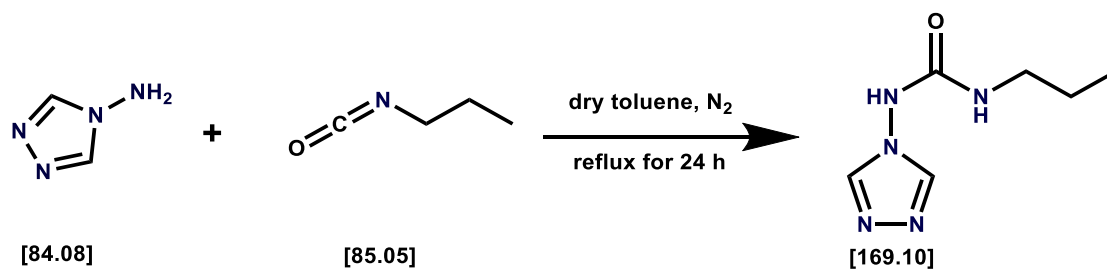
Yield: 2.64 g (14.42 mmol, 72.10%)

¹H-NMR: (400 MHz, *d*⁶-DMSO, 25 °C): (Figure 9.10)

δ (ppm): 9.14 (1H, s, N-NH-C=O), 8.52 (2H, s, triazole), 6.75 (1H, t, O=C-NH), 1.26 (9H, t, -C(CH₃)₃).

Selected IR (KBr): (Figure 9.29)

ν (cm⁻¹): 3288 (vs), 3110 (m), 2960 (s), 1710 (s), 1677 (vs), 1555 (vs), 1491 (s), 1461 (s), 1399 (s), 1364 (s), 1323 (m), 1289 (vs), 1232 (s), 1214 (s), 1074 (vs), 1022 (m), 969 (s), 830 (s), 709 (w), 685 (w), 624 (s).

8.2.1.11 4-(3-*n*-propyl ureido)-4*H*-1,2,4-triazole (L11)

From 1.85 g (0.022 mol, 1.1 eq.) 4-amino-4*H*-1,2,4-triazole and 1.70 g (0.02 mol, 1.0 eq.) *n*-propyl-isocyanate, pure colourless crystalline needles were obtained.

Yield: 1.78 g (10.53 mmol, 52.65%)

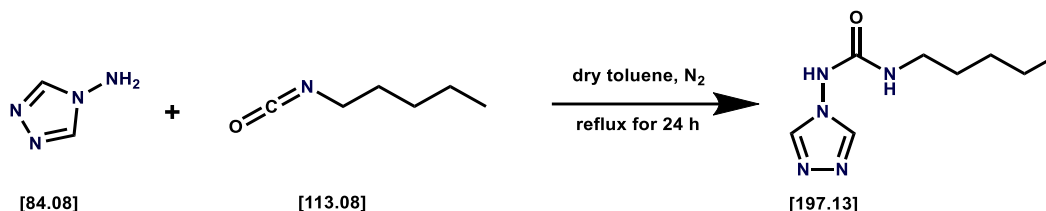
¹H-NMR: (400 MHz, *d*⁶-DMSO, 25 °C): (Figure 9.11)

δ (ppm): 9.52 (1H, s, -N-NH-C=O), 8.55 (2H, s, triazole), 7.00 (1H, t, -NH-CH₂-), 3.01 (2H, m, -NH-CH₂-CH₂-), 1.43 (2H, m, -CH₂-CH₂-CH₃), 0.85 (3H, t, -CH₃).

Selected IR (KBr): (Figure 9.30)

ν (cm⁻¹): 3368 (vs), 3299 (s), 3105 (s), 2968 (s), 2876 (s), 1725 (vs), 1669 (vs), 1561 (vs), 1468 (s), 1435 (s), 1405 (s), 1375 (s), 1325 (s), 1274 (s), 1232 (s), 1155 (s), 1096 (s), 1070 (vs), 996 (s), 947 (s), 884 (s), 832 (s), 758 (s), 621 (vs), 514 (s).

8.2.1.12 4-(3-*n*-pentyl ureido)-4*H*-1,2,4-triazole (L12)



From 1.85 g (0.022 mol, 1.1 eq.) 4-amino-4*H*-1,2,4-triazole and 2.26 g (0.02 mol, 1.0 eq.) *n*-pentyl-isocyanate, white powder was isolated.

Yield: 1.65 g (8.37 mmol, 41.85%)

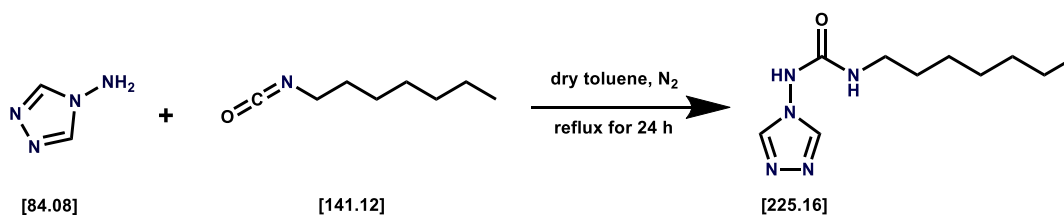
¹H-NMR: (400 MHz, *d*⁶-DMSO, 25 °C): (Figure 9.12)

9.53 (1H, s, -N-NH-C=O), 8.55 (2H, s, triazole), 6.98 (1H, t, -NH-CH₂-), 3.03 (2H, m, -NH-CH₂-CH₂-), 1.42 (2H, m, -NH-CH₂-CH₂-), 1.26 (4H, m, -CH₂-CH₂-CH₃), 0.87 (3H, t, -CH₃).

Selected IR (KBr): (Figure 9.31)

ν (cm⁻¹): 3366 (vs), 3287 (vs), 3122 (vs), 2955 (vs), 2930 (vs), 2872 (vs), 1723 (vs), 1667 (vs), 1561 (vs), 1467 (s), 1398 (s), 1326 (s), 1266 (vs), 1209 (vs), 1157 (s), 1100 (s), 1071 (vs), 1033 (s), 978 (s), 949 (s), 879 (s), 729 (s), 699 (s), 621 (vs), 574 (m).

8.2.1.13 4-(3-*n*-heptyl ureido)-4*H*-1,2,4-triazole (L13)



From 1.85 g (0.022 mol, 1.1 eq.) 4-amino-4*H*-1,2,4-triazole and 2.82 g (0.02 mol, 1.0 eq.) *n*-heptyl-isocyanate, light-yellow product was obtained as fine powder by recrystallization of the raw product from hot DMF/iced water system.

Yield: 2.43 g (10.79 mmol, 53.95%)

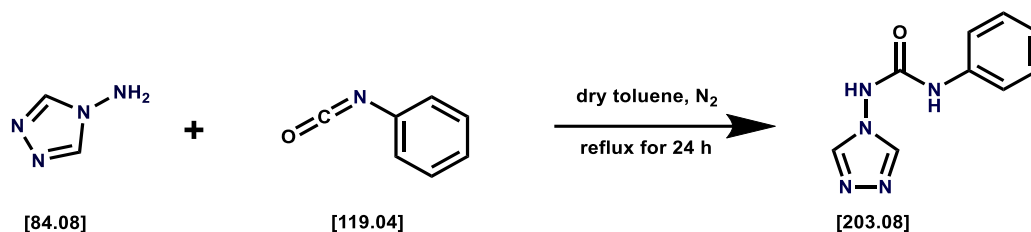
¹H-NMR: (400 MHz, *d*⁶-DMSO, 25 °C): (Figure 9.13)

9.50 (1H, s, -N-NH-C=O), 8.55 (2H, s, triazole), 6.98 (1H, t, -NH-CH₂-), 3.03 (2H, m, -NH-CH₂-CH₂-), 1.41 (2H, m, -NH-CH₂-CH₂-), 1.26 (8H, m, -CH₂-CH₂-CH₂-CH₂-CH₃), 0.87 (3H, t, -CH₃).

Selected IR (KBr): (Figure 9.32)

ν (cm⁻¹): 3363 (vs), 3107 (vs), 2929 (vs), 2855 (vs), 1722 (vs), 1667 (vs), 1618 (s), 1560 (vs), 1467 (s), 1379 (s), 1325 (s), 1277 (s), 1238 (s), 1213 (s), 1158 (s), 1099 (s), 1070 (vs), 991 (m), 947 (s), 883 (s), 834 (m), 769 (m), 724 (s), 621 (vs), 526 (w).

8.2.1.14 4-(3-phenyl ureido)-4H-1,2,4-triazole (L14)



From 1.85 g (0.022 mol, 1.1 eq.) 4-amino-4H-1,2,4-triazole and 2.38 g (0.02 mol, 1.0 eq.) phenyl-isocyanate, The pure white powder product was isolated by recrystallization from DMF/diethylether.

Yield: 2.34 g (11.52 mmol, 57.60%).

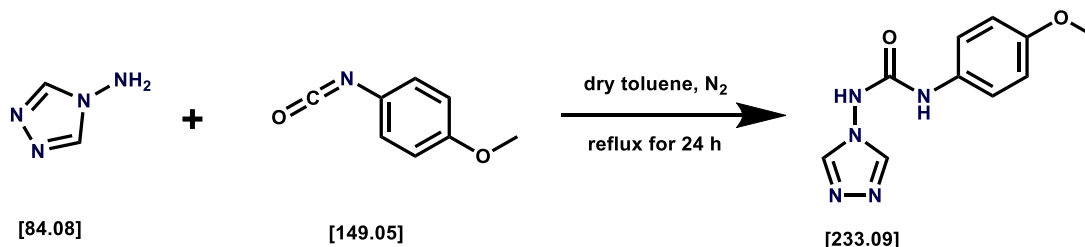
¹H-NMR: (400 MHz, *d*⁶-DMSO, 25 °C): (Figure 9.14)

δ (ppm): 9.82 (1H, s, -N-NH-C=O), 9.53 (1H, s, -O=C-NH-C=), 8.66 (2H, s, triazole), 7.48–7.46 (2H, dd, Ar-H), 7.31–7.27 (2H, tt, Ar-H), 7.02 (1H, t, Ar-H).

Selected IR (KBr): (Figure 9.33)

ν (cm⁻¹): 3251 (vs), 3201 (s), 3132 (s), 3087 (vs), 2914 (vs), 2801 (w), 2732 (w), 1711 (s), 1685 (vs), 1602 (vs), 1552 (vs), 1502 (vs), 1446 (vs), 1396 (s), 1322 (vs), 1255 (vs), 1210 (s), 1070 (vs), 1043 (s), 976 (s), 943 (s), 886 (s), 835 (s), 760 (vs), 742 (s), 696 (s), 624 (vs), 565 (s), 507 (s), 408 (m).

8.2.1.15 4-(3-4-methoxyphenyl ureido)-4H-1,2,4-triazole (L15)



From 1.85 g (0.022 mol, 1.1 eq.) 4-amino-4H-1,2,4-triazole and 2.98 g (0.02 mol, 1.0 eq.) 4-methoxyphenyl-isocyanate, the pure product was obtained as light-pink powder by recrystallization from DMF/H₂O system.

Yield: 1.94 g (8.32 mmol, 41.60%)

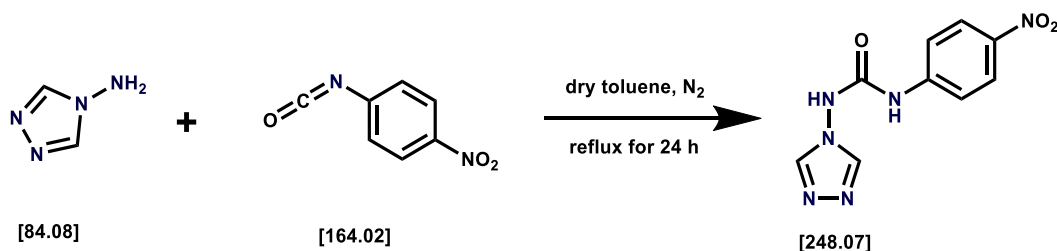
¹H-NMR: (400 MHz, *d*⁶-DMSO, 25 °C): (Figure 9.15)

δ (ppm): 9.75 (1H, s, $-N-NH-C=O$), 9.33 (1H, s, $-O=C-NH-C=$), 8.64 (2H, s, triazole), 7.37–7.35 (2H, dd, Ar–H), 6.88–6.86 (2H, tt, Ar–H), 3.71 (3H, t, $-CH_3$).

Selected IR (KBr): (Figure 9.34)

ν (cm^{-1}): 3251 (vs), 3142 (s), 3117 (vs), 3052 (m), 2916 (m), 2836 (w), 1684 (s), 1667 (vs), 1634 (m), 1607 (s), 1594 (vs), 1549 (vs), 1511 (vs), 1471 (s), 1414 (s), 1303 (vs), 1239 (vs), 1178 (s), 1164 (s), 1108 (m), 1070 (vs), 1025 (vs), 978 (s), 950 (s), 892 (s), 869 (s), 825 (s), 786 (w), 626 (vs), 523 (s), 417 (m).

8.2.1.16 4-(3-4-nitrophenyl ureido)-4H-1,2,4-triazole (L16)



From 1.85 g (0.022 mol, 1.1 eq.) 4-amino-4H-1,2,4-triazole and 3.28 g (0.02 mol, 1.0 eq.) 4-nitrophenyl-isocyanate, yellow powder was isolated by recrystallization from DMF/diethylether.

Yield: 3.39 g (13.67 mmol, 68.35%).

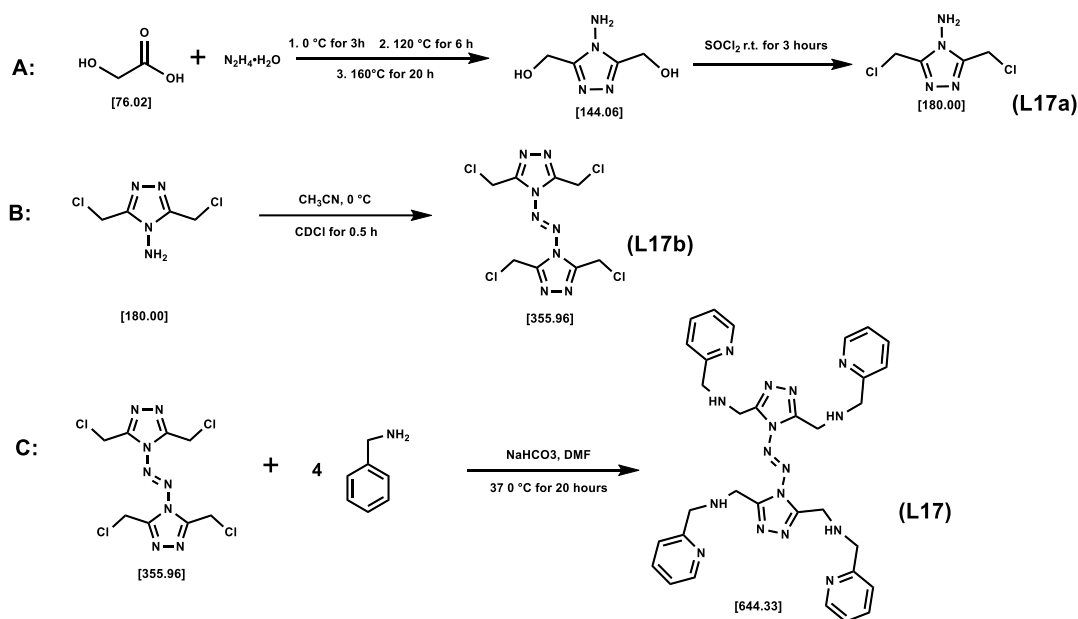
1H -NMR: (400 MHz, d^6 -DMSO, 25 °C): (Figure 9.16)

δ (ppm): 10.29 (1H, s, $-N-NH-C=O$), 10.18 (1H, s, $-O=C-NH-C=$), 8.71 (2H, s, triazole), 8.22–8.20 (2H, dd, Ar–H), 7.74–7.72 (2H, tt, Ar–H).

Selected IR (KBr): (Figure 9.35)

ν (cm^{-1}): 3273 (w), 3222 (s), 3165 (s), 3124 (s), 3073 (m), 3020 (s), 2977 (m), 1731 (vs), 1630 (s), 1588 (vs), 1502 (vs), 1417 (s), 1339 (vs), 1272 (s), 1232 (s), 1199 (s), 1115 (s), 1068 (vs), 1031 (s), 978 (s), 951 (s), 849 (vs), 751 (s), 689 (s), 615 (s), 532 (m), 491 (s), 426 (s).

8.2.1.17 3,3',5,5'-tetra[(2-pyridylmethyl)amino-methyl]-4,4'-azo-1,2,4-triazole (L17)



Ligand 17 was prepared in three steps:

Step A was prepared according to a reported procedure ^[11]: At 0°C , hydrazine monohydrate (10.61 g, 0.21 mol) was added dropwise into an aqueous glycolic acid solution (10.58 g, 0.14 mol). The resulting mixture was heated under refluxing condition at 120°C for 6 h. Afterwards, the reflux condenser was replaced with a downward condenser and the reaction temperature was raised to 160°C for another 24 h to remove excess hydrazine and water. After cooling, the resulting yellowish crystalline solid was washed with minimum cold water, dried in the air. To the dry intermediate product 4-amino-4H-1,2,4-triazole-3,5-dimethanol, thionyl chloride was added (25 mL). The reaction was stirred for 4 hours at room temperature, during which time a vigorous exothermic reaction took place. After removing the excess thionyl chloride by extraction with diethylether, the obtained yellow oil was dissolved in a mixed solvent of ethyl acetate and H_2O (1:1 by volum ratio). Then sodium hydrogen carbonate (23.52 g, 0.28 mol) was added in portions into the heterogeneous mixture with vigorously stirring. After complete addition, the layers were separated and the aqueous layer was extracted with ethyl acetate (5×25 mL). The combined organic layers were dried over anhydrous sodium sulfate. Evaporation of the solvent by rotary evaporator at 35°C gave analytically pure **L17a** as a colourless (slightly yellowish) crystalline solid.

Yield: 6.78 g (37.67 mmol, 53.81% based on glycolic acid).

$^1\text{H-NMR}$: (400 MHz, d^6 -DMSO, 25°C): (Figure 9.17)

δ (ppm): 6.13 (s, 2H, $-\text{NH}_2$), 4.87 (s, 4H, $2 \times -\text{CH}_2\text{Cl}$).

Step B was prepared via a reported procedure [12]: Compound 17a (3.6 g, 20 mmol) in acetonitrile (50 mL) was cooled in an ice-salt bath. To this solution, a mixture of sodium dichloro-isocyanurate (SDCI, 4.54 g, 20 mmol) and AcOH (5 mL) in water (5 mL) was added dropwise at 0 °C. After the addition, the reaction mixture was stirred for 30 min at 0 °C and neutralized to pH 7–8 with Na₂CO₃. The precipitate was collected by filtration, washed thoroughly with cold water and dried under vacuum to give **L17b** as a white powder.

Yield: 3.27 g (9.18 mmol, 91.86%)

¹H-NMR: (400 MHz, *d*⁶-DMSO, 25 °C): (Figure 9.18)

δ (ppm): 5.23 (s, 8H, 4 × -CH₂Cl).

Step C: A suspension of 2-picoylamine (2.6 g, 24.03 mol) and sodium hydrogen carbonate (10.09 g, 120.17 mol) in DMF (100 mL) was heated to 35 °C. A solution of L17b (2.07 g, 5.82 mmol) in DMF (10 mL) was added and the reaction mixture was heated for 18 hours. The potassium carbonate was filtered and the filtrate was poured into 300 mL iced water. Then the mixture was extracted with chloroform 7 times. Evaporation of the collected chloroform by rotary evaporator at 35 °C gave a raw product as a dark reddish oil. The dark reddish oil was purified by column chromatography (silica, absolute methonal as elute) to give the pure ligand as an orange oil.

Yield: 0.76 g (1.18 mmol, 20.27%)

¹H-NMR: (400 MHz, *d*⁶-DMSO, 25 °C): (Figure 9.19)

δ (ppm): 3.81 (s, 8H, 4 × PyCH₂), 4.12 (s, 8H; 4 × TrzNH₂), 7.17~7.20 (t, 4H, 4 × 5-PyH), 7.34~7.36 (d, 4H, 4 × 2-PyH), 7.66~7.69 (t, 4H, 4 × 4-PyH), 8.43~8.46 (d, 4H, 4 × 6-PyH).

IR (KBr): (Figure 9.36)

ν (cm⁻¹): 3423 (s), 3058 (w), 3009 (w), 2924 (m), 2831 (m), 1662 (m), 1592 (vs), 1570 (s), 1529 (w), 1474 (s), 1435 (vs), 1397 (m), 1329 (w), 1273 (m), 1222 (w), 1148 (s), 1121 (s), 1050 (s), 996 (s), 848 (m), 763 (vs), 630 (m), 404 (m).

8.2.2 Preparation of Fe Complex

The general methods for the complex synthesis is as following: Firstly, mix the ligand and FeX₂ (X= ClO₄⁻, BF₄⁻, CF₃SO₃⁻, *p*-toluenesulfonate) salts (ligand to Fe salts molar ration as 3:1, 2:1, 1:1) in a small glass beaker with common solvents, like CH₃CN, MeOH, EtOH, H₂O or a mixture of these solvents. Then stire the reaction mixture for several hours. Afterwards, filtrate the obtained solution with rapid filter paper. The finally step is applied

with different approaches with the intention of better crystallization condition. The details are shown in the following section.

As we mentioned in chapter 6, crystal structure is of vital importance for the SCO studies. Herein, we are only focused on the compounds with successful isolation of the crystal structure. For many compounds during the crystallization growth process, we only obtained as a powder, in these cases, no other measurements were made.

In addition, depend on different ligand systems, the crystals of the organic part were formed other than the expected Fe complex in several cases. No attempt was made to grow the organic crystal individually, such no conclusion can be made regarding to solvent-dependent crystallization or concentration factors for the crystallization. Most probably the Fe salts also played some role in the process of these organic assembling. As we discussed in Chapter 6, the assembling process of the organic ligand or salt can be a competition with the crystallization process of the Fe complex.

8.2.2.1 $[Fe^{II}_2(toltrz)_5(SCN)_4] \cdot 3H_2O$ (C1)

To a stirring solution of toltrz (150 mg, 0.8 mmol) in methanol (5 mL) was added an aqua solution of $FeSO_4 \cdot 7H_2O$ (90 mg, ~ 0.3 mmol) and NH_4SCN (50 mg, ~ 0.6 mmol). The solution turned from colorless to light yellow immediately. One spatula-amount (~ 35 mg) of ascorbic acid were added to prevent possible oxidation process. The reaction mixture was then stirred for around 3~ hours before filtrated with rapid filter paper. The obtained clear light reddish solution was kept in a small vial and left stand still to evaporate the solvent slowly. After one week, light yellow plate-like crystals of complex 1 were deposited at the bottom of the vial. After removing the mother liquid, the single crystals were quickly dried in an argon stream, and stored under argon. Yield: 62.3 mg (47.15% based on Fe). Anal. Calcd (Found) for $C_{54}H_{49}N_{24}O_3S_4Fe_2$: C, 49.06 (49.17); H, 3.74 (4.03); N, 25.43 (25.38). IR (KBr) n/cm^{-1} : 3104 (w), 2976 (m), 2920 (w), 2072 (s), 1607 (vs), 1121 (vs), 1062 (m), 817 (m), 620 (vs), 505 (m), 396 (w).

8.2.2.2 $[Fe^{II}_2(toltrz)_5(SeCN)_4] \cdot 3H_2O$ (C2)

Caution! The over acidity condition might lead to possible $HSeCN$, which is pretty dangerous human's skin and respiratory system. To avoid the possible decomposition of seleno- compounds with the exposure of light, this experiment is preceeded under dark atmosphere.

To a stirring solution of toltrz (150 mg, 0.8 mmol) in methanol (3 mL) was added an aqua solution of 5 mL $\text{Fe}(\text{ClO}_4)_4 \cdot 6\text{H}_2\text{O}$ (80 mg, ~ 0.3 mmol) and KSeCN (87 mg, ~ 0.6 mmol). The solution turned from colorless to light yellow immediately. Then two spatula-amount (~70 mg) of ascorbic acid (round about 60 mg, ~ 0.3 mmol) were added to prevent possible oxidation process. The reaction mixture was then stirred at 60 °C for 3~4 hours before filtrated with rapid filter paper. The obtained clear yellow solution was kept in a small vial and left stand still under dark enviroment to evaporate the solvent slowly. After three weeks, light yellow stick-like crystals of **C1** were deposited at the bottom of the vial. Yield: 63.4 mg (41.97% based on Fe). Anal. Calcd (Found) for $\text{C}_{54}\text{H}_{50}\text{N}_{24}\text{O}_3\text{Se}_4\text{Fe}_2$: C, 42.93 (42.48); H, 3.34 (3.48); N, 22.25 (21.46). IR (KBr) cm^{-1} : 3217 (w), 3108 (m), 2975 (w), 2854 (m), 2070 (s), 1607 (vs), 1524 (s), 1369 (m), 1179 (m), 1115 (vs), 1063 (m), 881 (m), 817 (m), 755 (m), 622 (vs), 509 (m), 443 (w).

8.2.2.3 $[\text{Fe}^{\text{II}}_2(\text{toltrz})_6(\text{C}_2\text{O}_4)(\text{H}_2\text{O})_2](\text{SeCN})_2(\text{toltrz})_2(\text{H}_2\text{O})_4(\text{C3})$

One batch of the reaction during the preparation of **C2** showed several light yellow block crystals at the bottom of the reaction vial, which was confirmed by SXRD as **C3**. A dinuclear complex linked by oxalate anion, the oxalate here must come from the decomposing compounds of ascorbic acid. As a by-product, we only isolated several crystals of this complex.

8.2.2.4 $[\text{Fe}^{\text{II}}_3(\text{toltrz})_6(\text{H}_2\text{O})_6](\text{BF}_4)_6 \cdot 2\text{H}_2\text{O} \cdot 2\text{CH}_3\text{CH}_2\text{CO}_2\text{CH}_3(\text{C4})$

First dissolved $\text{Fe}(\text{BF}_4)_2 \cdot 6\text{H}_2\text{O}$ (135 mg, 0.4 mmol) in 10 mL ethyl acetate, with one spatula-amount (~35 mg) of ascorbic acid added to prevent possible oxidation process. After the completeness of dissolving the iron salt, a solution of toltrz (150 mg, 0.8 mmol) dissolved in ethyl acetate (5~10 mL) was slowly added into the above solution. This reaction solution was then stirred for around 3~4 hours before filtrated with rapid filter paper. The obtained almost colorless solution was kept in a small vial and left stand still to evaporate the solvent slowly. After five days, light-green block crystals of **C4** were deposited at the bottom of the vial. After removing the mother liquid, the single crystals were quickly dried in an argon stream, and stored under argon. Yield: 61.26 mg (58.18% based on Fe). Anal. Calcd (Found) for $\text{C}_{34}\text{H}_{36}\text{N}_{12}\text{O}_6\text{B}_3\text{F}_{12}\text{Fe}_{1.5}$: C, 38.79 (34.14); H, 3.45 (3.84); N, 15.96 (16.51). IR (KBr) cm^{-1} : 3132 (m), 3032 (m), 2975 (w), 2921 (w), 2859 (m), 1606 (vs), 1567 (s), 1532 (s), 1307 (m), 1181 (m), 1084 (vs), 1073 (vs), 1037 (vs), 993 (m), 889 (w), 817 (m), 726 (m), 627 (s), 533 (m), 522 (m), 397 (w).

8.2.2.5 $[\text{Fe}^{\text{II}}_2(\text{pyrtrz})_5(\text{SCN})_4] \cdot 4\text{H}_2\text{O}(\text{C5})$

To a stirring solution of pyrtrz (129 mg, 0.8 mmol) in methanol (5 mL) was added an aqua solution of $\text{FeSO}_4 \cdot 7\text{H}_2\text{O}$ (90 mg, ~ 0.3 mmol) and NH_4SCN (50 mg, ~ 0.6 mmol). The solution turned from light yellow to dark red immediately. One spatula-amount (~ 35 mg) of ascorbic acid was added to prevent possible oxidation process. The reaction mixture was then stirred for around 3~4 hours before filtrated with rapid filter paper. The obtained clear light reddish solution was kept in a small vial and left stand still to evaporate the solvent slowly. After one week, light brown block-like crystals of **C5** were deposited at the bottom of the vial. After removing the mother liquid, the single crystals were quickly dried in an argon stream, and stored under argon. Yield: 127.1 mg (34.90% based on Fe). Anal. Calcd (Found) for $\text{C}_{39}\text{H}_{35}\text{Fe}_2\text{N}_2\text{O}_4\text{S}_4$: C, 38.59 (36.38); H, 2.91 (3.63); N, 33.46 (32.62). IR (KBr) n/cm^{-1} : 3125 (w), 2927 (m), 2856 (w), 2078 (s), 1609 (vs), 1523 (m), 1422 (w), 1385 (vs), 1311 (m), 1246(vs), 1127 (s), 1063 (m), 1037 (m), 985 (m), 881(w), 759(m), 621 (s), 593 (m), 506 (w).

8.2.2.6 [$\text{Fe}^{\text{II}}_3(\text{pyrtrz})_6(\text{TsO})_6$]. $6.5\text{H}_2\text{O} \cdot \text{CH}_3\text{OH}$ (C6)

Freshly prepared $\text{Fe}(\text{TsO})_2$ (120 mg, ~ 0.3 mmol) in 3 mL H_2O was added into a stirring solution of pyrtrz (97 mg, 0.6 mmol) dissolved in MeOH (2~3 mL). One spatula-amount (~ 35 mg) of ascorbic acid was added to prevent possible oxidation process. This solution was then stirred for around 3~4 hours before filtrated with rapid filter paper. The obtained clear light yellow solution was then kept in a small vial and left stand still to evaporate the solvent slowly. After two weeks, light pink needle-like crystals of **C6** were deposited at the bottom of the vial. After removing the mother liquid, the single crystals were quickly dried in an argon stream, and stored under argon. Yield: 257.3 mg (35.83% based on Fe). Anal. Calcd (Found) for $\text{C}_{85}\text{H}_{88}\text{Fe}_3\text{N}_3\text{O}_{31.5}\text{S}_6$: C, 42.65 (42.26); H, 3.71 (4.22); N, 17.55 (17.62). IR (KBr) n/cm^{-1} : 3097 (w), 2988(w), 2922(w), 2857 (w), 1605 (vs), 1530 (s), 1446(m), 1423(m), 1368 (s), 1189(vs), 1125 (s), 1072 (s), 1035 (vs), 1010(s), 883 (m), 844(m), 815 (m), 752 (m), 682(s), 624 (m), 606(w), 566 (s), 513 (w).

8.2.2.7 [$\text{Fe}^{\text{II}}(\text{toltrz})_2(\text{C}_2\text{O}_4)$]. $5\text{H}_2\text{O}$ (C7)

This complex was first obtained as an unexpected product from the following procedure: To a stirring solution of toltrz (150 mg, 0.8 mmol) in methanol (3 mL) was added an 5 mL aqua solution of $\text{Fe}(\text{ClO}_4)_4 \cdot 6\text{H}_2\text{O}$ (80 mg, ~ 0.3 mmol). The solution turned from colorless to a slightly dark reddish color solution. Then two spatula-amount of ascorbic acid (round about 70 mg) were added to prevent possible oxidation process. The reaction mixture was then stirred at 60 °C for 3~4 hours before filtrated with rapid filter paper. The obtained clear

reddish solution was kept in a small vial and left stand still to evaporate the solvent slowly. After three weeks, light yellow needle-like crystals of **C7** were deposited at the bottom of the vial. After removing the mother liquid, the single crystals were quickly dried in an argon stream, and stored under argon. Yield: 35.7 mg (34.80% based on Fe). While the oxalate anion from the X-ray diffraction result violates the basic start materials we put into the reaction in the first place, the only explanation would be that it came from the decomposing compounds from the ascorbic acid when it was working against the oxidation of Fe^{II} ions, there are several reports regarding this way to achieve the oxalate as starting material [13]. Then we tried the standard way of preparing the oxalate compound by using (NH₄)₂(C₂O₄) (38 mg, ~ 0.3 mmol, with the ratio of 1:1 compared to Fe) instead of ascorbic acid in a rather mild reaction conditions (stirred at r.t.). Same light-yellow crystals formed after one week with a higher yield of 66.96% (68.7 mg, based on Fe). Anal. Calcd (Found) for C₂₂H₂₀FeN₈O₁₁: C, 42.06 (41.44); H, 3.21 (3.59); N, 17.83 (17.57). IR (KBr) cm^{-1} : 3115 (m), 2921 (w), 1643 (vs), 1605 (s), 1523 (m), 1421 (w), 1122 (m), 829 (m), 619 (m), 489 (w).

8.2.2.8 [Fe^{II}(5-imztrz)(C₂O₄)]·2H₂O (**C8**)

This complex was also first obtained as an unexpected product with the same procedure for complex **7**, except for changing of toltrz (150 mg, 0.8 mmol) to 5-imztrz (130 mg, 0.8 mmol). Yield: 38.7 mg (20.54% based on Fe). And the preparation with ammonium oxalate give us the same crystalline compound with a yield of 72.98% (137.5 mg, based on Fe) Anal. Calcd (Found) for C₈H₁₀FeN₆O₆: C, 28.09 (27.75); H, 2.95 (3.28); N, 24.57 (23.70). IR (KBr) cm^{-1} : 3121 (m), 2923 (w), 1683 (vs), 1634 (vs), 1616 (vs), 1520 (m), 1433 (w), 1353 (m), 1311 (m), 1167 (m), 1113 (vs), 1062 (vs), 1006 (m), 956 (m), 799 (s), 693 (m), 647 (m), 620 (s), 513 (m), 485 (w).

8.2.2.9 [Fe^{III}(cit)(H₂O)](5-imztrzH)·3H₂O (**C9**)

To a stirring 3 mL methanolic solution of 5-imztrz (130 mg, 0.8 mmol), Fe(ClO₄)₄·6H₂O (80 mg, ~ 0.3 mmol) in 5 mL H₂O was added. The solution color changed from light yellow to a bit darker. Then citric acid (60 mg, ~ 0.3 mmol) was added as a powder into the reaction solution, the reaction was then kept stirring at 60 °C for 5 hours before filtrated with rapid filter paper. The obtained light-yellow solution was kept in a small vial and left stand still to evaporate the solvent slowly. After five days, light-yellow (looks like white too) block crystals of **C9** were deposited at the bottom of the vial. After removing the mother liquid, the single crystals were picked up and blew with an argon stream to dryness before stored

in a small vial. Yield: 81.7 mg (56.85% based on Fe). Anal. Calcd (Found) for C₁₂H₁₉FeN₆O₁₁: C, 30.08 (30.78); H, 4.00 (3.75); N, 17.54 (18.37). IR (KBr) ν /cm⁻¹: 3136 (m), 2959 (w), 2853 (w), 2620 (w), 1683 (vs), 1634 (vs), 1617 (vs), 1570 (m), 1523 (m), 1506 (w), 1343 (w), 1384 (w), 1351 (m), 1313 (m), 1257 (w), 1164 (m), 1112 (s), 1063 (s), 1007 (m), 958 (m), 863 (m), 801 (s), 690 (w), 620 (m), 512 (m), 486 (m).

8.2.2.10 [Fe^{II}(2-imztrz)₄(SCN)₄] (C10)

To a stirring solution of 2-imztrz (129 mg, 0.8 mmol) in methanol (5 mL) was added an aqueous solution of FeSO₄ · 7H₂O (112 mg, 0.4 mmol), together with NH₄SCN (61 mg, ~ 0.8 mmol). The solution turned from colorless to light reddish immediately. One spatula-amount (~35 mg) of ascorbic acid were added to prevent possible oxidation process. The reaction mixture was then stirred for 3~4 hours at room temperature before filtrated with rapid filter paper. The obtained clear dark reddish solution was kept in a small vial and left stand still to evaporate the solvent slowly. After two weeks, red block crystals of **10** were deposited at the bottom of the vial. After removing the mother liquid, the single crystals were picked up and blew with an argon stream to dryness before stored in a small vial. Yield: 107.3 mg (54.05% based on Fe). Anal. Calcd (Found) for C₁₄H₁₂FeN₁₄S₂: C, 33.88 (29.38); H, 2.44 (2.37); N, 39.51 (37.99). IR (KBr) ν /cm⁻¹: 3134 (m), 3020 (w), 2925 (m), 2854 (w), 2809 (w), 2718 (w), 2057 (vs), 1626 (s), 1517 (s), 1463 (s), 1447 (s), 1385 (m), 1357 (m), 1297 (w), 1205 (w), 1177 (m), 1155 (s), 1113 (s), 1084 (s), 1057 (s), 996 (m), 945 (m), 858 (m), 778 (s), 708 (m), 633 (m), 616 (s).

8.2.2.11 [Fe^{II}(2-imztrz)₂(CH₃OH)₂(SCN)₂] (C11)

During one batch of the above preparation (**C10**), light yellow crystals of **C11** were isolated. We managed to pick up one of the several needle crystals for SXRD. The collected crystal data looks good, indicating relative stable of the mononuclear complex. While very surprisely, one week after, all the crystals were re-dissolved in the mother liquid. The following several batched ended up with the two dimensional **C10** as the only complex obtained from this reaction procedure.

8.2.2.12 [Fe^{II}(5-imztrz)₂](ClO₄)₂ (C12)

To a stirring solution of 5-imztrz (129 mg, 0.8 mmol) in methanol (5 mL) was added a methonolic solution of Fe(ClO₄)₂ · 7H₂O (112 mg, 0.4 mmol). The solution turned from light yellow to light green immediately. After stiring for half hour, one spatula-amount (~35 mg) of ascorbic acid was added. The reaction mixture was then stirred for another 3 hours at room temperature before filtrated with rapid filter paper. The obtained clear greenish to

reddish solution was kept in a small vial and left stand still to evaporate the solvent slowly. After three weeks, light yellow block crystals of **12** were deposited at the bottom of the vial. After removing the mother liquid, the single crystals were quickly dried in an argon stream, and stored under argon. Yield: 117.46 mg (50.71% based on Fe). Anal. Calcd (Found) for C₃₉H₃₅Fe₂N₂₉O₄S₄: C, 24.89 (24.32); H, 2.09 (2.04); N, 29.03 (28.47). IR (KBr) $\tilde{\nu}$ /cm⁻¹: 3296 (s), 3122 (s), 1627 (vs), 1612 (vs), 1516 (s), 1454 (w), 1431 (s), 1384 (s), 1300 (m), 1280 (m), 1217 (m), 1185 (s), 1141 (s), 1121 (vs), 1095 (vs), 961 (s), 927 (m), 869 (s), 799 (w), 715 (s), 624 (vs), 531 (w).

8.2.2.13 Complex 13, 14 and 15

Complex $[Fe^{II}(cpt)(OH)(H_2O)_2]_n$ (**C13**), $[Fe^{II}_6(\mu_3-O)(OH)_2(cpt)_6(H_2O)_2]_n$ (**C14**) and $[Fe^{II}_3(\mu_3-O)(OH)(cpt)_3]_n$ (**C15**) were obtained via the same procedure under the same condition, while the most stable form is found to be **C14**.

A mixture of Hcpt (114 mg, ~ 0.6 mmol) and FeSO₄·7H₂O (90 mg, ~ 0.3 mmol) was placed in a thin glass tube (10 mL), with a mixed solvent of CH₃CN/CH₃OH (3:1 by molar ratio). Then one spatula-amount (~35 mg) of ascorbic acid was added into the reaction vial. The tube was put under ultrasonic condition for around 10 minutes before moved to a Teflon vial (35 mL). The well-sealed Teflon vial was kept at 180 °C for 72 hours and upon slow cooling (-5°C/h) crystals of different shapes were obtained. From individual batches with the same synthetic condition, three complexes were isolated independently from individual vial:

$[Fe^{II}(cpt)(OH)(H_2O)_2]_n$ (**C13**) was obtained as light-yellow irregular block crystals; $[Fe^{II}_6(\mu_3-O)(OH)_2(cpt)_6(H_2O)_2]_n$ (**C14**) was collected as yellow rhombus crystals and $[Fe^{II}_3(\mu_3-O)(OH)(cpt)_3]_n$ (**C15**) was isolated as yellow square block.

Later on we tried to change different solvents: MeOH, DMF, H₂O, EtOH or a mixture of the above solvent; and different ration of ligand to Fe salts: 1:1, 3:1, 6:1. Surprisingly, the outcome was the same, that is, in all cases, we collected **C14** as the only product. **C13** and **C15** have not been reproduced again with this synthetic procedure. It seems that the three dimensional form (**C14**) is the most stable form of this three complexes under the solvent thermal reaction conditions. Even though **C14** can be reproduced, the crystals obtained were covered with dark powder from the decomposing of ascorbic acid, which is very difficult to remove completely, such no other measurement was made on this complex.

8.3 References

- [1] J. C. Cobas, F. J. Sardina, *Concepts Magn. Reson.* **2003**, *19A*, 80–96.
- [2] *SMART 5.0 and SAINT 4.0 for Windows NT, Area Detector Control and Integration Software*, Bruker Analytical X-Ray Systems Inc., Madison, WI, **1998**.
- [3] G. M. Sheldrick, *SADABS: Program for Empirical Absorption Correction of Area Detector Data*, University of Göttingen, Göttingen, Germany, **1996**.
- [4] a) G. M. Sheldrick, *Acta Crystallogr.* **2015**, *C71*, 3–8; b) G. M. Sheldrick, *SHELXTL 5.1 for Windows NT: Structure Determination Software Programs*, Bruker Analytical X-ray Systems, Inc., Madison, WI, 1997.
- [5] O. V. Dolomanov, L. J. Bourhis, R. J. Gildea, J. A. K. Howard, H. J. Puschmann, *Appl. Crystallogr.* **2009**, *42*, 339–341.
- [6] *Diamond - Crystal and Molecular Structure Visualization Crystal Impact* - Dr. H. Putz & Dr. K. Brandenburg GbR, Kreuzherrenstr. 102, 53227 Bonn, Germany.
- [7] N. F. Chilton, R. P. Anderson, L. D. Turner, A. Soncini, K. S. Murray, *J. Comput. Chem.* **2013**, *34*, 1164–1175.
- [8] a) T. Khan, R. Yadav, *Heterocycl. lett.*, **2016**, *6*, 757–766; (b) A. Kwiecien, M. Barys, Z. Ciunik, *Molecules*, **2014**, *19*, 11160–11177; (c) W. S. Zhao, H. L. Zhou, J. L. Mao, Q. L. Hu, *Huaxue Shijie*, **2008**, *49*, 738–740.
- [9] a) J. M. Lehn, *Supramolecular Chemistry: Concepts and Perspectives*; VCH: Weinheim, Germany, **1995**; b) . D. Savard, P. H. Lin, T. J. Burchell, I. Korobkov, W. Wernsdorfer, R. Clérac and M. Murugesu, *Inorg. Chem.*, **2009**, *48*, 11748–11754.
- [10] a) E. Rentschler, M. Christian, *Inorganica Chim. Acta.*, **2008**, *361*, 3646–3653; b) C. Bülow, F. Weber, *Ber. Dtsch. Chem. Ges.*, **1909**, *42*, 2715–2721.
- [11] M. H. Klingele, B. Moubaraki, K. S. Murray, S. Brooker, *Chem. Eur. J.*, **2005**, *11*, 6962–6973.
- [12] Y. Tang, J. M. Shreeve, *Chem.-Eur. J.*, **2015**, *21*, 7285–7291.
- [13] a) G. De Ruiter, J. S. Costa, K. Lappalainen, O. Roubeau, P. Gamez, J. Reedijk, *Inorg. Chem. Commun.* **2008**, *11*, 787–790; b) W. T. Liu, J. Y. Li, Z. P. Ni, X. Bao, Y. C. Ou, J. D. Leng, J. L. Liu, M. L. Tong, *Cryst. Growth Des.* **2012**, *12*, 1482–1488; c) A. S. Dinca, S. Shova, A. E. Ion, C. Maxim, F. Lloret, M. Julve, M. Andruh, *Dalton Trans.* **2015**, *44*, 7148–7151.

Chapter 9 Appendix

9.1 Crystallographic Parameters and Tables

Table 9.1 Dinuclear Fe(II) Complexes Based on Functionalized 4-R-1,2,4-Triazole Ligands.

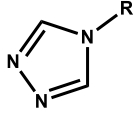
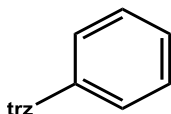
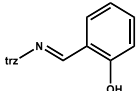
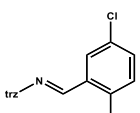
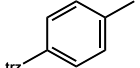
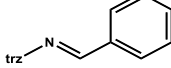
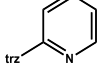
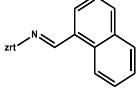
	dinuclear complex	SCO behavior / $T_{1/2}$	Ref
	$[\text{Fe}_2(\mu_2\text{-L})_3(\text{L})_2(\text{NCS})_4] \cdot \text{CH}_3\text{OH} \cdot \text{CH}_3\text{CH}_2\text{OH}$	incomplete / $T_{1/2} = 116$ K	1
	$[\text{Fe}_2(\mu_2\text{-L})_3(\text{L})_2(\text{NCS})_4] \cdot 2\text{CH}_3\text{CH}_2\text{OH}$	incomplete / $T_{1/2} = 122$ K	1
	$[\text{Fe}_2(\mu_2\text{-L})_3(\text{L})_2(\text{NCS})_4] \cdot 2\text{CH}_3\text{CH}_2\text{OH} \cdot 1.5\text{H}_2\text{O}$	HS	1
	$[\text{Fe}_2(\mu_2\text{-L})_3(\text{L})_2(\text{NCS})_4] \cdot 4\text{MeOH}$	abrupt / $T_{1/2} = 157$ K	2a
	$[\text{Fe}_2(\mu_2\text{-L})_3(\text{L})_2(\text{NCS})_4] \cdot 4\text{H}_2\text{O}$	HS	2b
	$[\text{Fe}_2(\mu_2\text{-L})_3(\text{L})_2(\text{NCS})_4] \cdot \text{H}_2\text{O}$	gradual / $T_{1/2} = 150$ K	3
	$[\text{Fe}_2(\mu_2\text{-L})_3(\text{L})_2(\text{NCS})_4] \cdot [\text{Fe}(\text{L})_2(\text{NCS})_2(\text{H}_2\text{O})_2]$	abrupt / $T_{1/2} = 111$ K	4
	$[\text{Fe}_2(\mu_2\text{-L})_3(\text{L})_2(\text{NCS})_4] \cdot 3.5\text{MeOH}$	gradual / $T_{1/2} = 115$ K	5
	$[\text{Fe}_2(\mu_2\text{-L})_3(\text{L})_2(\text{NCS})_4] \cdot 2\text{H}_2\text{O}$	HS	6
	$[\text{Fe}_2(\mu_2\text{-L})_3(\text{L})_2(\text{NCS})_4] \cdot \text{CH}_3\text{OH} \cdot \text{CH}_3\text{CH}_2\text{OH}$	incomplete / $T_{1/2} = 116$ K	6
	$[\text{Fe}_2(\mu_2\text{-L})_3(\text{L})_2(\text{NCSe})_4] \cdot 2\text{DMF} \cdot 2\text{H}_2\text{O}$	HS with LIESST effect	7

Table 9.2 Trinuclear Fe(II) Complexes Based on Functionalized 4-R-1,2,4-Triazole Ligands.

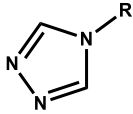
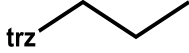
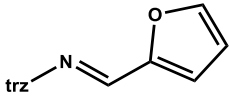
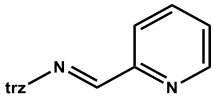
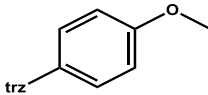
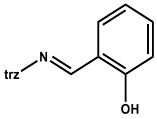
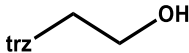
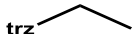
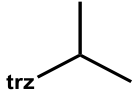
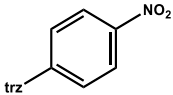
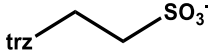
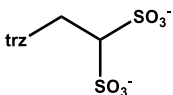
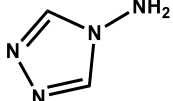
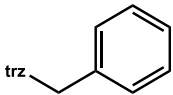
	Trinuclear complex	SCO behavior / T1/2	Ref
	$[\text{Fe}_3(\mu_2\text{-L})_6(\text{ReO}_4)_4(\text{H}_2\text{O})_2](\text{ReO}_4)_2 \cdot \text{H}_2\text{O}$	gradual / T1/2=185 K	8
	$[\text{Fe}_3(\mu_2\text{-L})_6(\text{Tos})_2](\text{Tos})_4 \cdot 4\text{MeOH}$	gradual / T1/2~170 K	9
	$[\text{Fe}_3(\mu_2\text{-L})_6(\text{L})_2(\text{H}_2\text{O})_4](\text{NO}_3)_6$	gradual / T1/2=208 K	10
	$[[\text{Fe}_3(\mu_2\text{-L})_6(\text{L})_2(\text{H}_2\text{O})_4](\text{ClO}_4)_6$	HS	10
	$[\text{Fe}_3(\mu_2\text{-L})_6(\text{L})_2(\text{H}_2\text{O})_4](\text{Br})_6$	HS	10
	$[\text{Fe}_3(\mu_2\text{-L})_6(\text{L})_2(\text{H}_2\text{O})_4](\text{BF}_4)_6 \cdot 2\text{H}_2\text{O}$	HS	11
	$[\text{Fe}_3(\mu_2\text{-L})_6(\text{H}_2\text{O})_6](\text{Tos})_6 \cdot 4\text{H}_2\text{O}$	gradual / T1/2 =245 K	11
	$[\text{Fe}_3(\mu_2\text{-L})_6(\text{H}_2\text{O})_6](\text{Tos})_6$	gradual / T1/2=330 K	11
	$[\text{Fe}_3(\mu_2\text{-L})_6(\text{H}_2\text{O})_2(\text{EtOH})_4](\text{ClO}_4)_6 \cdot 2\text{EtOH}$	HS	2b
	$[\text{Fe}_3(\mu_2\text{-L})_6(\text{H}_2\text{O})_6](\text{CF}_3\text{SO}_3)_6$	gradual / T1/2=290 K	12
	$[\text{Fe}_3(\mu_2\text{-L})_6(\text{H}_2\text{O})_6](\text{CF}_3\text{SO}_3)_6$	abrupt / T1/2=205 K	13
	$[\text{Fe}_3(\mu_2\text{-L})_6(\text{H}_2\text{O})_6](\text{Tos})_6 \cdot 2\text{H}_2\text{O}$	gradual / T1/2=242 K	14
	$[\text{Fe}_3(\mu_2\text{-L})_6(\text{H}_2\text{O})_6](\text{CF}_3\text{SO}_3)_6$	gradual / T1/2=185 K	14
	$[\text{Fe}_3(\mu_2\text{-L})_6(\text{H}_2\text{O})_2(\text{EtOH})_4](\text{Tos})_6 \cdot 4\text{EtOH}$	gradual / T1/2=148 K	15
	$[\text{Fe}_3(\mu_2\text{-L})_6(\text{H}_2\text{O})_6] \cdot 5\text{H}_2\text{O}$	Hysteresis with T1/2(↑)=357 K, T1/2(↓)=343K	16
	$(\text{Me}_2\text{NH}_2)_6[\text{Fe}_3(\mu_2\text{-L})_6(\text{H}_2\text{O})_6]$	Hysteresis with T1/2(↑)=400 K, T1/2(↓)=310K	17
	$[\text{Fe}_3(\mu_2\text{-L})_6(\text{SCN})_5(\text{H}_2\text{O})](\text{SCN}) \cdot 4\text{H}_2\text{O}$	Hysteresis with T1/2(↑)=222 K, T1/2(↓)=218K	18
	$[\text{Fe}_3(\mu_2\text{-L})_6(\text{tenset})_6]$ (tenset = 1,1,3,3-tetracyano-2-thioethylpropene)	abrupt / T1/2 = 318 K	19

Table 9.3 Crystallographic data of C3 and C11.

Compound	C3	C11
Empirical formula	C ₄₂ H ₄₇ FeN ₁₇ O ₅ Se	C _{15.5} H _{20.5} FeN ₁₄ O ₂ S ₂
Formula weight	1004.77	554.93
Crystal size	0.26×0.18×0.12	0.21×0.18×0.09
Crystal system	Triclinic	Monoclinic
Space group	<i>P</i> $\bar{1}$ (No. 2)	<i>P</i> 21/ <i>c</i> (No. 14)
<i>a</i> (Å)	7.513(4)	7.172(3)
<i>b</i> (Å)	14.017(8)	9.849(4)
<i>c</i> (Å)	22.117(11)	17.455(7)
α (°)	85.477(19)	90
β (°)	86.255(12)	101.285(13)
γ (°)	84.632(12)	90
<i>V</i> (Å ³)	2308(2)	1209.1(9)
<i>Z</i>	2	2
<i>D</i> _{calc} (g/cm ³)	1.446	1.524
μ (Mo-K α) (mm ⁻¹)	1.179	0.841
<i>F</i> (000)	1036	571
Reflections collected	16347	8460
Independent reflections	10854(0.1306)	2138(0.1193)
Parameters	603	170
Goodness-of-fit	0.796	2.046
<i>R</i> ₁ [<i>I</i> > 2 σ (<i>I</i>)] ^a	0.0725	0.1910
<i>wR</i> ₂ (all data) ^b	0.1824	0.5146

$${}^a R_1 = \frac{\sum ||F_o| - |F_c||}{\sum |F_o|}, {}^b wR_2 = \left\{ \frac{\sum [w(F_o^2 - F_c^2)]}{\sum [w(F_o^2)]} \right\}^{1/2}$$

Table 9.4 Crystallographic data of C13, C14 and C15.

Compound	C13	C14	C15
Empirical formula	C ₉ H ₁₁ FeN ₃ O ₅	C ₄₆ H ₃₀ Fe ₆ N ₁₅ O ₂₁	C ₅₄ H ₃₆ Fe ₆ N ₁₈ O ₂₄
Formula weight	297.06	1463.95	1656.11
Crystal size	0.13×0.11×0.03	0.19×0.18×0.17	0.14×0.04×0.02
Crystal system	Monoclinic	Orthorhombic	Hexagonal
Space group	<i>P21/c</i> (No. 14)	<i>Imm2</i> (No. 44)	<i>P6₃mc</i> (No. 186)
<i>a</i> (Å)	13.5118(18)	16.150(5)	15.1907(13)
<i>b</i> (Å)	7.1096(10)	19.655(5)	15.1907(13)
<i>c</i> (Å)	10.9425(15)	19.670(5)	20.1364(18)
α (°)	90	90	90
β (°)	94.241(3)	90	90
γ (°)	90	90	120
<i>V</i> (Å ³)	1048.3(2)	6244(3)	4024.1(8)
<i>Z</i>	4	2	1
<i>D</i> _{calc} (g/cm ³)	1.882	0.779	0.683
μ (Mo-K α) (mm ⁻¹)	1.458	0.720	0.565
<i>F</i> (000)	608	1470	834
Reflections collected	7234	24313	29879
Independent reflections	2536(0.0408)	6636(0.1051)	3477(0.3409)
Parameters	163	116	94
Goodness-of-fit	1.076	1.191	0.931
<i>R</i> ₁ [<i>I</i> > 2 σ (<i>I</i>)] ^a	0.0351	0.1295	0.1008
<i>wR</i> ₂ (all data) ^b	0.0981	0.3880	0.3517

$$^a R_1 = \frac{\sum ||F_o| - |F_c||}{\sum |F_o|}, \quad ^b wR_2 = \left\{ \frac{\sum [w(F_o^2 - F_c^2)]^2}{\sum [w(F_o^2)]^2} \right\}^{1/2}$$

Chapter 9 Appendix

Table 9.5 Crystallographic data of **K1**, **K2** and **K3**.

Compound	K1	K2	K3
Empirical formula	C ₁₈ H ₁₈ Cl ₆ N ₁₀ O ₄	C ₁₂ H ₂₀ F ₆ N ₁₂ O ₄ P	C ₆ H ₆ N ₆
Formula weight	651.12	541.37	162.17
Crystal size	0.28×0.12×0.02	0.55×0.40×0.32	0.25×0.10×0.05
Crystal system	Monoclinic	Triclinic	Orthorhombic
Space group	<i>Cc</i> (No.9)	<i>P</i> $\bar{1}$ (No. 2)	<i>Pnma</i> (No. 62)
<i>a</i> (Å)	22.190(2)	7.1573(5)	10.0363(9)
<i>b</i> (Å)	9.8066(8)	9.6891(6)	6.3457(6)
<i>c</i> (Å)	12.6381(11)	16.1378(9)	10.9958(10)
α (°)	90	97.0143(14)	90
β (°)	106.553(2)	93.9287(15)	90
γ (°)	90	93.3226(18)	90
<i>V</i> (Å ³)	2636.2(4)	1105.65(12)	700.29(11)
<i>Z</i>	4	2	4
<i>D</i> _{calc} (g/cm ³)	1.641	1.626	1.538
μ (Mo-K α) (mm ⁻¹)	0.700	0.223	0.109
<i>F</i> (000)	1320	554	336
Reflections collected	11521	14232	7077
Independent reflections	4756(0.0457)	5283(0.0254)	919(0.0613)
Parameters	397	341	74
Goodness-of-fit	1.089	1.063	1.001
<i>R</i> ₁ [<i>I</i> > 2 σ (<i>I</i>)] ^a	0.0887	0.0763	0.0347
<i>wR</i> ₂ (all data) ^b	0.2545	0.1949	0.0926

$$^a R_1 = \frac{\sum ||F_o| - |F_c||}{\sum |F_o|}, \quad ^b wR_2 = \left\{ \frac{\sum [w(F_o^2 - F_c^2)]^2}{\sum [w(F_o^2)]^2} \right\}^{1/2}$$

Table 9.6 Crystallographic data of **K4**, **K5** and **K6**.

Compound	K4	K5	K6
Empirical formula	C ₉ H ₁₀ N ₄ O ₃	C ₉ H ₇ N ₃ O ₂	C ₇ H ₁₃ N ₅ O
Formula weight	222.21	189.18	183.22
Crystal size	0.25×0.17×0.04	0.45×0.25×0.07	0.66×0.21×0.02
Crystal system	Monoclinic	Monoclinic	Orthorhombic
Space group	<i>C2/c</i> (No.15)	<i>P2₁/c</i> (No.14)	<i>Pca2₁</i> (No. 29)
<i>a</i> (Å)	8.8011(16)	7.1573(5)	9.712(9)
<i>b</i> (Å)	11.6932(19)	9.6891(6)	10.660(11)
<i>c</i> (Å)	8.0651(14)	16.1378(9)	9.167(10)
α (°)	90	97.0143(14)	90
β (°)	96.762(4)	93.9287(15)	90
γ (°)	90	93.3226(18)	90
<i>V</i> (Å ³)	824.2(2)	1105.65(12)	949.0(16)
<i>Z</i>	4	2	4
<i>D</i> _{calc} (g/cm ³)	1.524	1.626	1.282
μ (Mo-K α) (mm ⁻¹)	0.112	0.223	0.092
<i>F</i> (000)	392	554	392
Reflections collected	7095	14232	4416
Independent reflections	1990(0.0690)	5283(0.0254)	2281(0.1237)
Parameters	131	341	118
Goodness-of-fit	0.978	1.063	0.793
<i>R</i> ₁ [<i>I</i> > 2 σ (<i>I</i>)] ^a	0.0461	0.0763	0.0597
<i>wR</i> ₂ (all data) ^b	0.1146	0.1949	0.1526

$${}^a R_1 = \frac{\sum ||F_o| - |F_c||}{\sum |F_o|}, {}^b wR_2 = \left\{ \frac{\sum [w(F_o^2 - F_c^2)]^2}{\sum [w(F_o^2)]^2} \right\}^{1/2}$$

Table 9.7 Crystallographic data of **K7**, **K8** and **K9**.

Compound	K7	K8	K9
Empirical formula	C ₁₂ H _{21.5} N ₁₀ O ₂	C ₉ H ₁₁ N ₅ O ₂	C ₁₀ H ₁₃ N ₅ O ₃
Formula weight	337.93	221.23	251.25
Crystal size	1.00×0.3×0.12	0.48×0.19×0.17	0.32×0.32×0.05
Crystal system	Monoclinic	Monoclinic	Monoclinic
Space group	<i>P2₁/c</i> (No.14)	<i>P2₁/c</i> (No.14)	<i>P2₁/c</i> (No.14)
<i>a</i> (Å)	5.4818(5)	5.9653(6)	19.844(7)
<i>b</i> (Å)	11.1074(10)	11.9429(12)	7.214(3)
<i>c</i> (Å)	27.929(2)	14.9920(15)	7.969(3)
α (°)	90	90	90
β (°)	95.468(3)	94.674(2)	90.253(11)
γ (°)	90	90	90
<i>V</i> (Å ³)	1692.8(3)	1064.52(19)	1140.8(8)
<i>Z</i>	4	4	4
<i>D</i> _{calc} (g/cm ³)	1.326	1.380	1.463
μ (Mo-K α) (mm ⁻¹)	0.097	0.103	0.112
<i>F</i> (000)	718	464	528
Reflections collected	13208	7880	7694
Independent reflections	3982(0.0216)	2520(0.0298)	1998(0.0842)
Parameters	236	145	171
Goodness-of-fit	1.031	1.043	1.034
<i>R</i> ₁ [<i>I</i> > 2 σ (<i>I</i>)] ^a	0.0581	0.0380	0.0594
<i>wR</i> ₂ (all data) ^b	0.1586	0.0936	0.1376

$$^a R_1 = \frac{\sum ||F_o| - |F_c||}{\sum |F_o|}, \quad ^b wR_2 = \left\{ \frac{\sum [w(F_o^2 - F_c^2)]^2}{\sum [w(F_o^2)]^2} \right\}^{1/2}$$

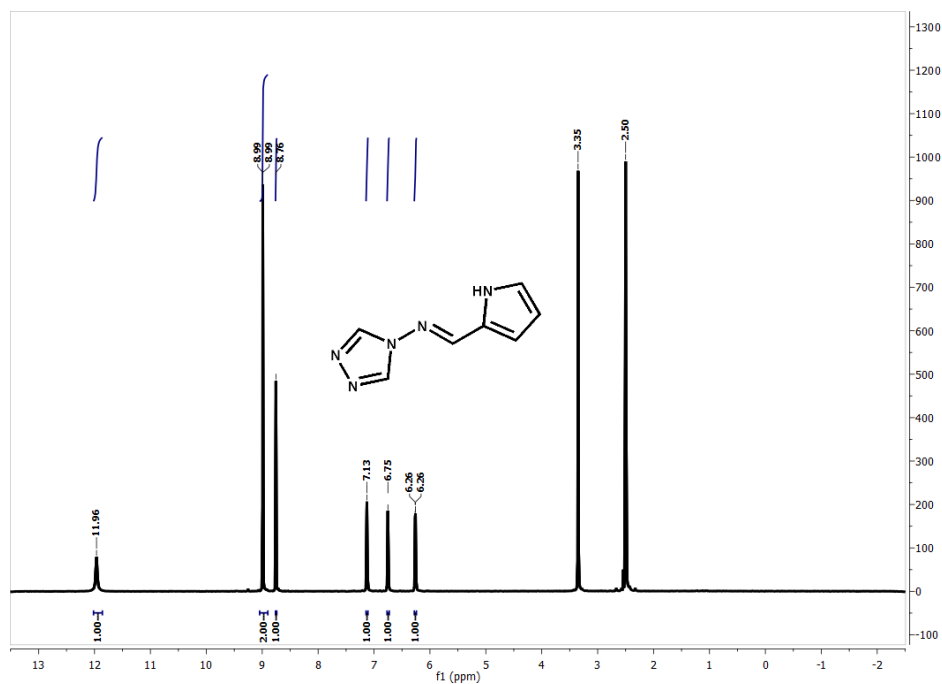
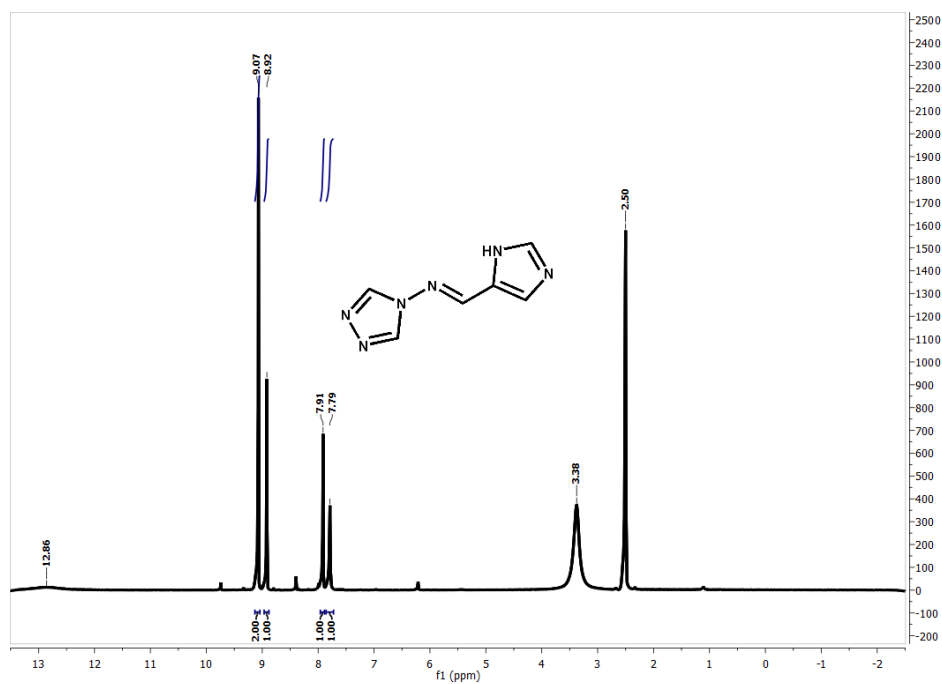
Table 9.8 Hydrogen-bonding interactions in **K1–K5**.

D–H	A	H···A (Å)	D···A (Å)	<D–H···A (°)	Symmetry codes of A
K1					
N1–H1	O1	1.742	2.581(3)	159.32	$\frac{1}{2} + x, \frac{1}{2} + y, l + z$
N5–H5	O4	2.203	2.998(2)	149.71	$x, l - y, -\frac{1}{2} + z$
N6–H6a	O3	1.742	2.589(4)	161.19	$-\frac{1}{2} + x, \frac{1}{2} - y, -\frac{1}{2} + z$
N10–H10	O2	2.205	2.995(4)	149.67	x, y, z
C1–H1a	N7	2.172	2.930(3)	136.37	$l/2+x, 3/2-y, l/2+z$
C3–H3	O3	2.433	3.318(3)	156.52	$x, -y, -l/2+z$
C8–H8	N2	2.217	2.943(2)	133.67	$-l/2+x, l/2-y, -l/2+z$
C9–H9a	O1	2.481	3.293(3)	144.61	$x, y + l, z$
K2					
O1w–H1wa	O2w	1.923	2.755(2)	165.32	x, y, z
O1w–H1wb	N7	2.025	2.873(2)	177.35	$2-x, l-y, -z$
O2w–H2wa	F6	2.173	2.952(3)	153.21	$l+x, y, z$
O2w–H2wb	F3	2.283	2.993(2)	141.37	x, y, z
N5–H5	O1w	1.832	2.674(2)	165.69	x, y, z
N6–H6	N8	2.032	2.861(3)	163.73	$2-x, 2-y, -z$
O3w–H3wb	N1	1.964	2.807(3)	175.89	$l-x, l-y, l-z$
N12–H12	N2	1.973	2.844(3)	168.89	$l-x, l-y, l-z$
C7–H7	F2	2.213	3.045(2)	148.67	$l+x, y, z$
C8–H8	F6	2.126	3.005(3)	157.78	$l+x, l+y, z$
K3					
N6–H6	N5	2.043	2.897(3)	172.38	$-l/2+x, 3/2-y, l/2-z$
C1–H1	N2	2.475	3.288(3)	146.73	$l/2+x, 3/2-y, -l/2-z$
C2–H2	N1	2.389	3.227(3)	151.37	$-l/2+x, 3/2-y, -l/2-z$
C6–H6a	N2	2.597	3.398(3)	145.68	$x, y, l+z$
K4					
O1–H1	N2	1.965	2.782(3)	165.69	$x, l-y, l/2+z$
O2w–H1wa	O2	2.107	2.935(3)	161.37	$-x, -l+y, l/2-z$
O2–H2	O1	2.356	2.783(3)	113.42	x, y, z
O2–H2	N1	2.036	2.777(3)	147.86	$x, 2-y, l/2+z$
O1w–H1wb	N4	2.128	2.943(3)	157.21	$x, -l+y, z$
C2–H2a	O1w	2.263	3.161(3)	157.82	x, y, z
C3–H3	O1w	2.326	3.243(3)	163.46	x, y, z
C6–H6	O2	2.495	3.251(3)	139.64	$x, -l+y, z$
K5					
O2–H2	N2	1.586	2.638(2)	173.49	$l+x, l/2-y, -l/2+z$
C1–H1	O1	2.193	3.123(2)	165.87	$l-x, -y, -z$
C9–H9	N1	2.435	3.347(3)	161.48	$-x, l/2+y, l/2-z$

Table 9.9 Hydrogen-bonding interactions in **K6–K9**.

D–H	A	H···A (Å)	D···A (Å)	<D–H···A (°)	Symmetry codes of A
K6					
N4–H4	N1	2.207	2.859(2)	145.38	<i>l-x, l-y, -1/2+z</i>
N5–H5	O1	2.195	2.786(2)	125.67	<i>3/2-x, y, -1/2+z</i>
C1–H1	N2	2.348	3.169(2)	146.32	<i>1/2+x, l-y, z</i>
C5–H5b	O1	2.395	3.007(2)	121.87	<i>x, y, z</i>
K7					
N4–H4	O2	2.304	2.966(2)	132.56	<i>-1+x, y, z</i>
N5–H5	O2	2.117	2.904(2)	149.38	<i>-1+x, y, z</i>
N9–H9	N7	1.958	2.826(2)	171.47	<i>l-x, -1/2+y, 1/2-z</i>
N10–H10	N2	2.546	3.125(3)	124.83	<i>l+x, -1+y, z</i>
C2–H2	O1	2.308	3.229(3)	164.78	<i>-1+x, y, z</i>
C7–H7	O2	2.375	3.275(3)	159.83	<i>-1+x, y, z</i>
K8					
O1w–H1wa	N1	1.997	2.873(2)	168.57	<i>3/2-x, -1/2+y, 1/2-z</i>
O1w–H1wb	O1	1.963	2.803(2)	157.89	<i>1/2-x, -1/2+y, 1/2-z</i>
N4–H4	O1w	1.982	2.710(2)	139.68	<i>l+x, y, z</i>
N5–H5	N2	2.124	2.976(2)	163.93	<i>3/2-x, -1/2+y, 1/2-z</i>
C5–H5a	O1	2.413	2.887(2)	111.38	<i>x, y, z</i>
K9					
O1w–H1wa	N1	2.013	2.839(2)	161.48	<i>x, -1+y, z</i>
O1w–H1wb	N2	1.942	2.827(2)	166.57	<i>l-x, 2-y, -z</i>
N4–H4	O1w	2.124	2.726(2)	126.36	<i>x, 3/2-y, 1/2+z</i>
N5–H5	O1	2.073	2.933(2)	167.39	<i>x, 3/2-y, 1/2+z</i>
C1–H1	O1	2.278	3.186(2)	154.65	<i>x, 5/2-y, 1/2+z</i>
C2–H2	O1w	2.276	3.085(2)	141.86	<i>x, y, z</i>

9.2 NMR Spectra

Figure 9.1: ¹H-NMR spectrum of L1.Figure 9.2: ¹H-NMR spectrum of L2.

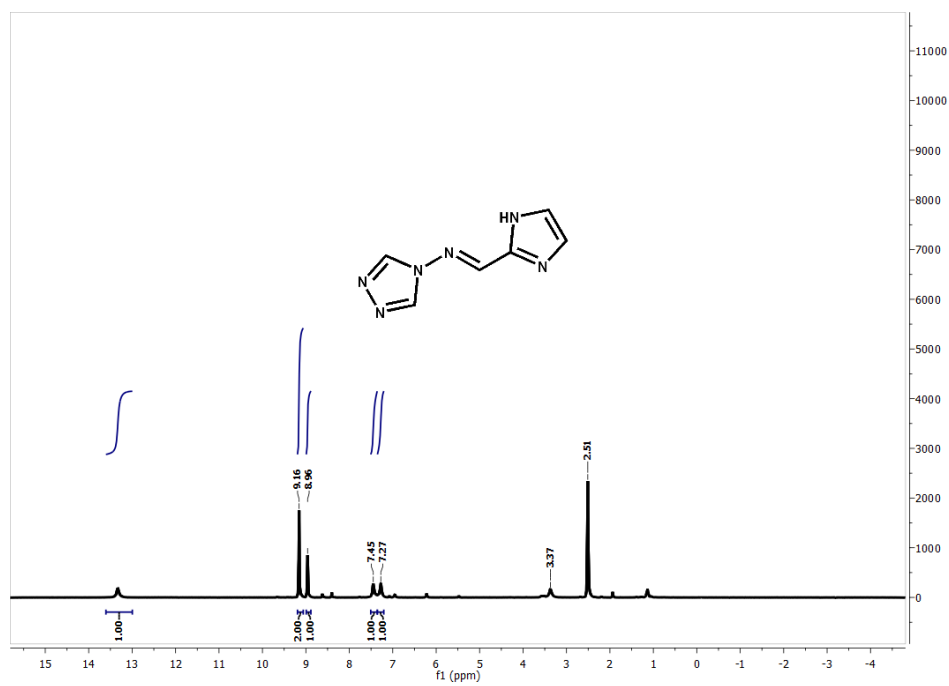


Figure. 9.3: ¹H-NMR spectrum of L3.

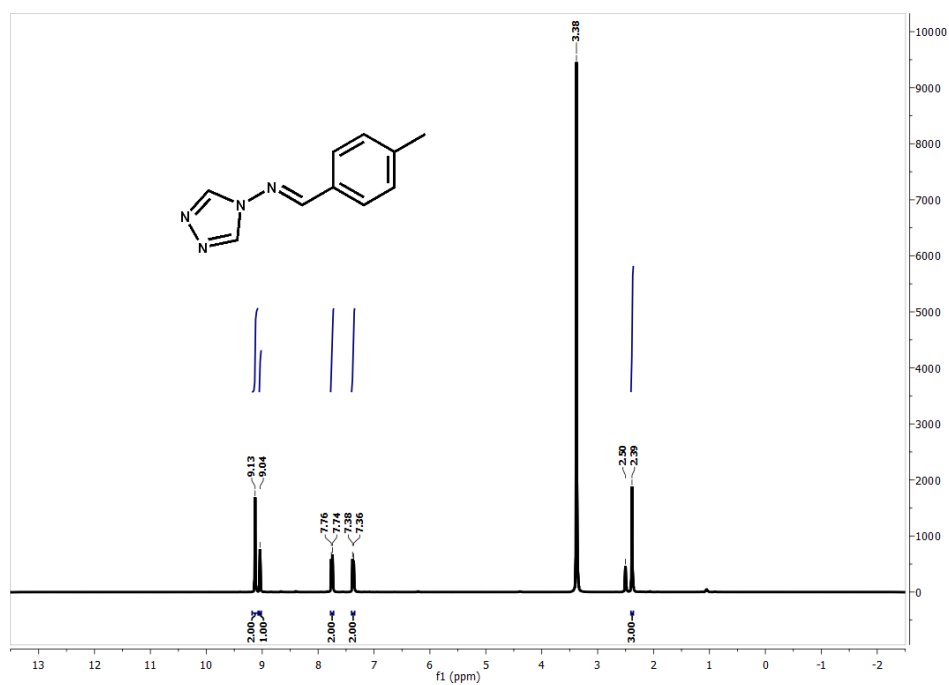
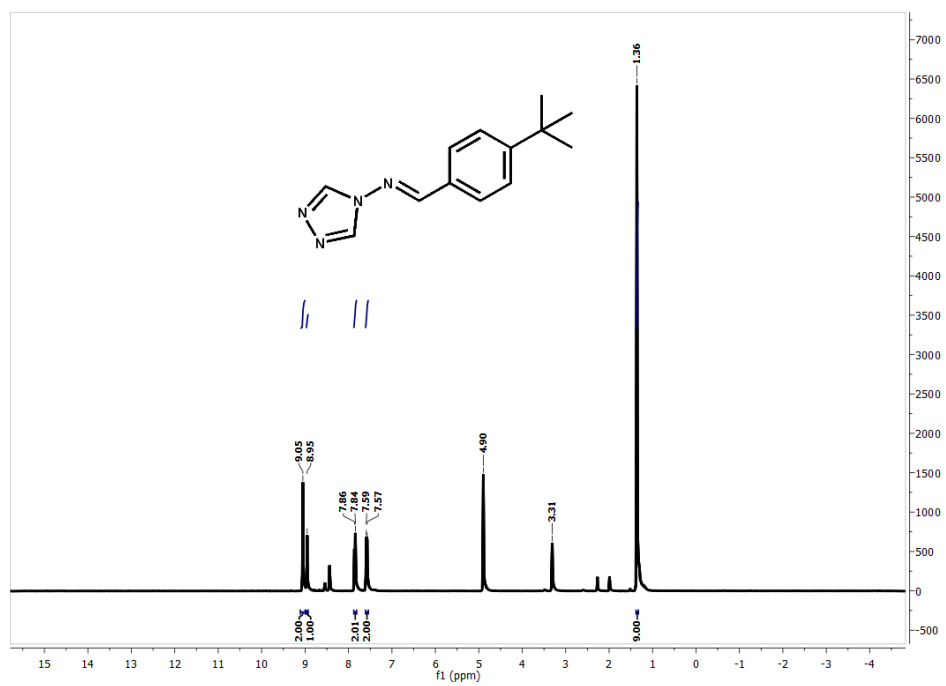
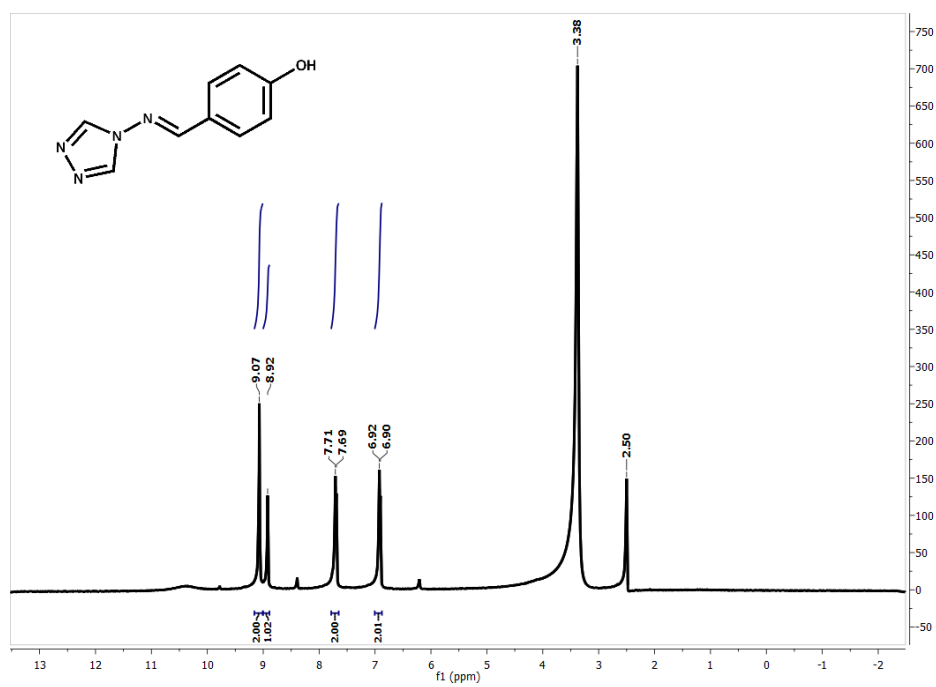


Figure. 9.4: ¹H-NMR spectrum of L4.

Figure. 9.5: ¹H-NMR spectrum of L5.Figure. 9.6: ¹H-NMR spectrum of L6.

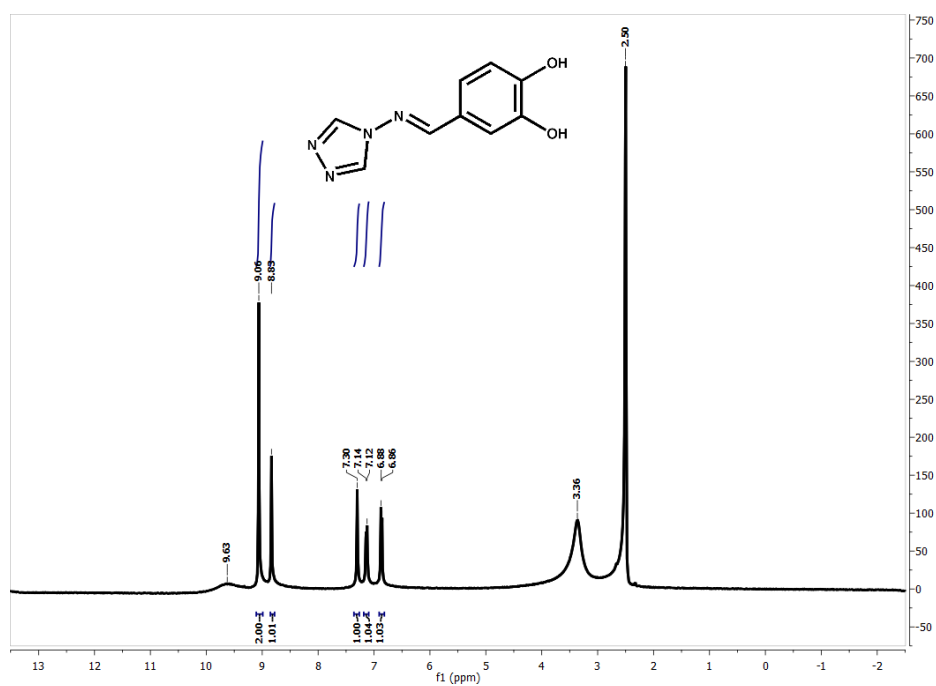


Figure. 9.7: $^1\text{H-NMR}$ spectrum of L7.

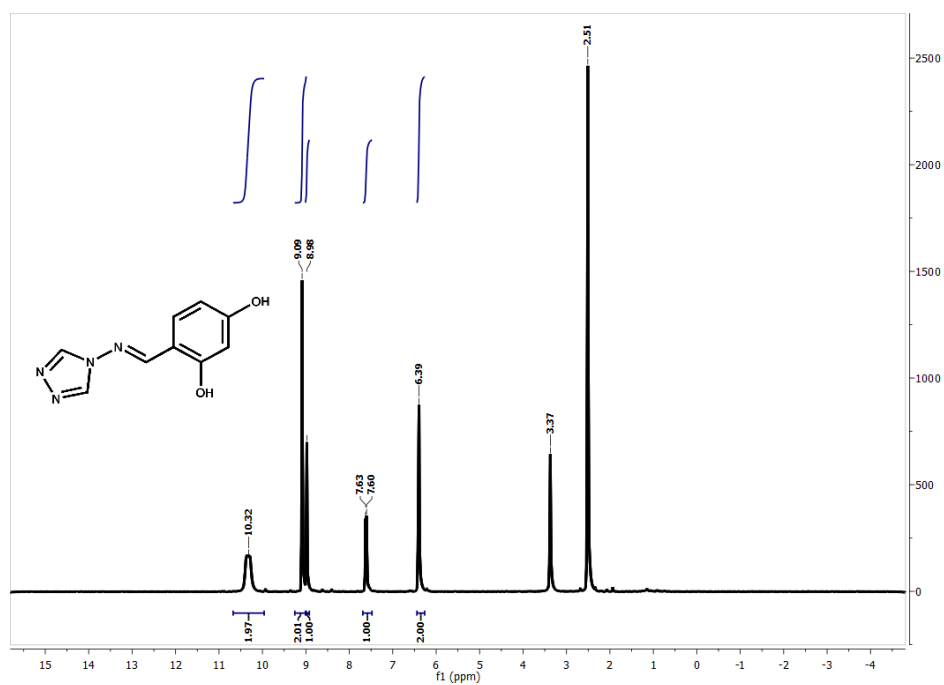
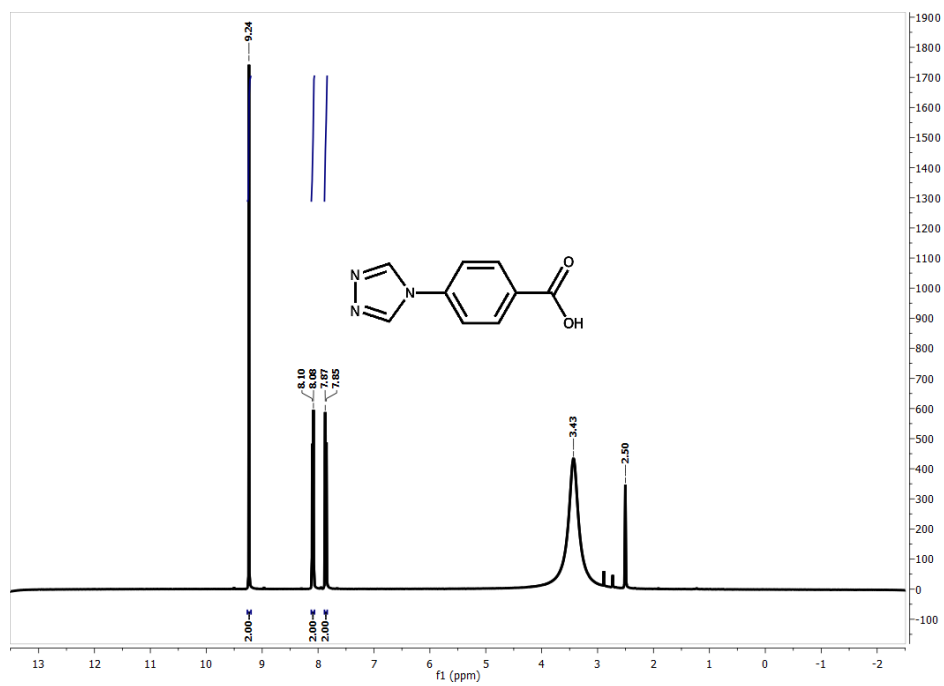
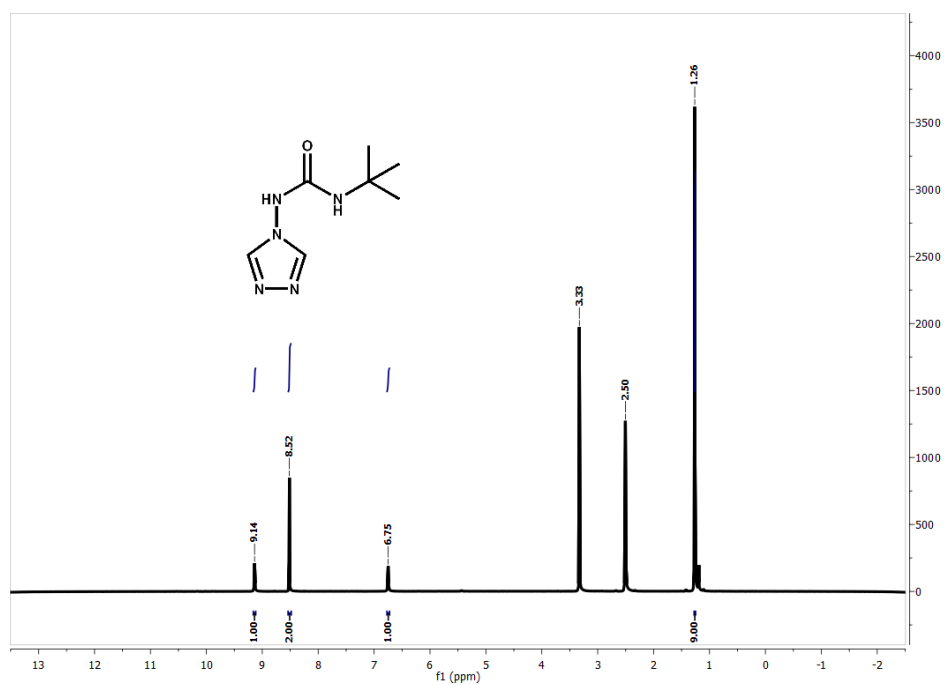


Figure. 9.8: $^1\text{H-NMR}$ spectrum of L8.

Figure 9.9: ¹H-NMR spectrum of L9.Figure 9.10: ¹H-NMR spectrum of L10.

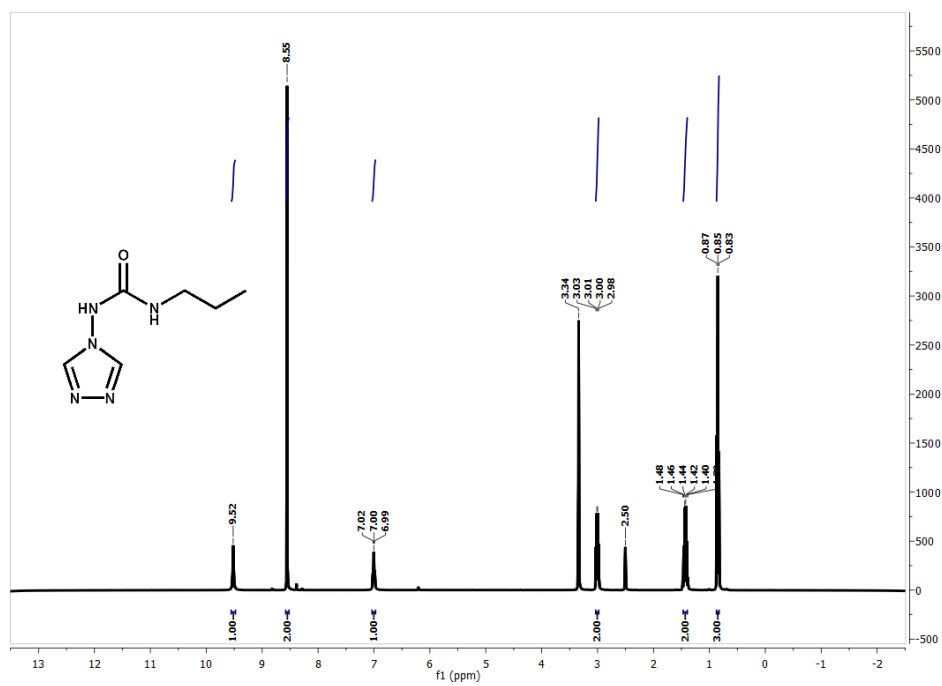


Figure. 9.11: $^1\text{H-NMR}$ spectrum of **L11**.

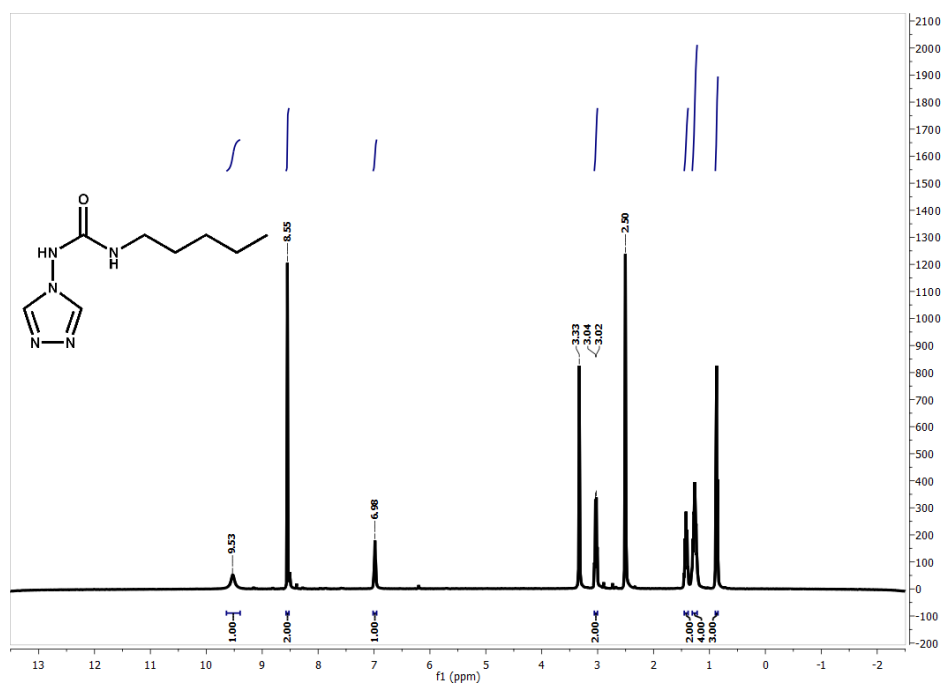
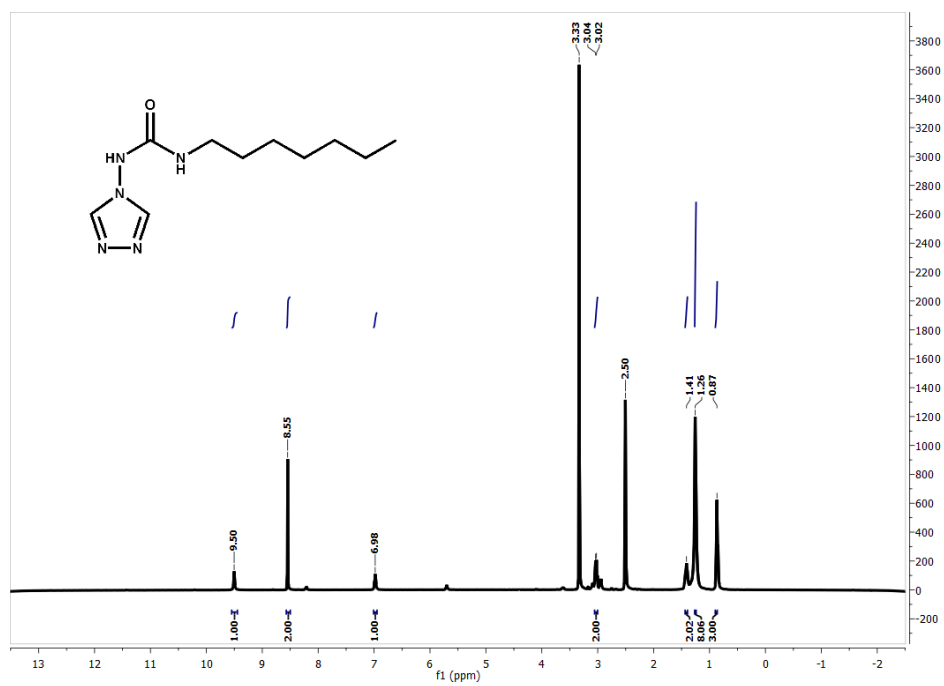
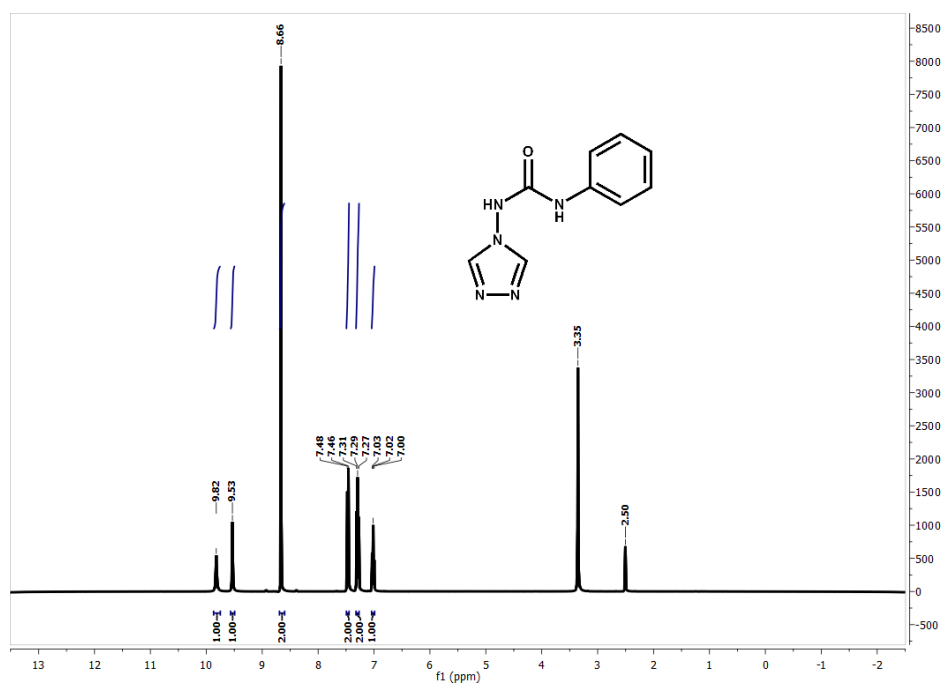


Figure. 9.12: $^1\text{H-NMR}$ spectrum of **L12**.

Figure 9.13: ¹H-NMR spectrum of L13.Figure 9.14: ¹H-NMR spectrum of L14.

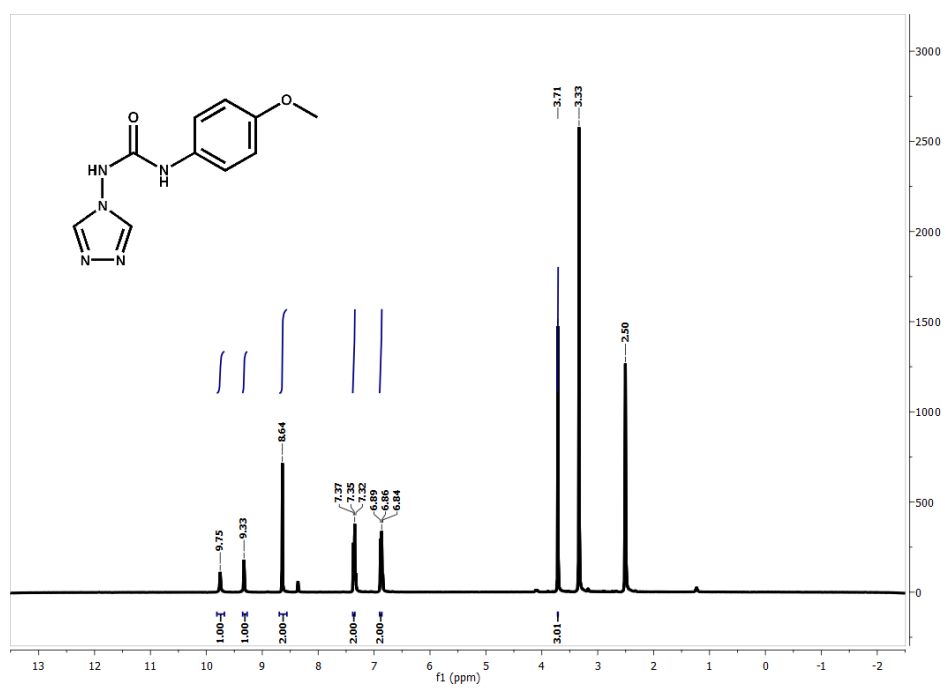


Figure. 9.15: $^1\text{H-NMR}$ spectrum of **L15**.

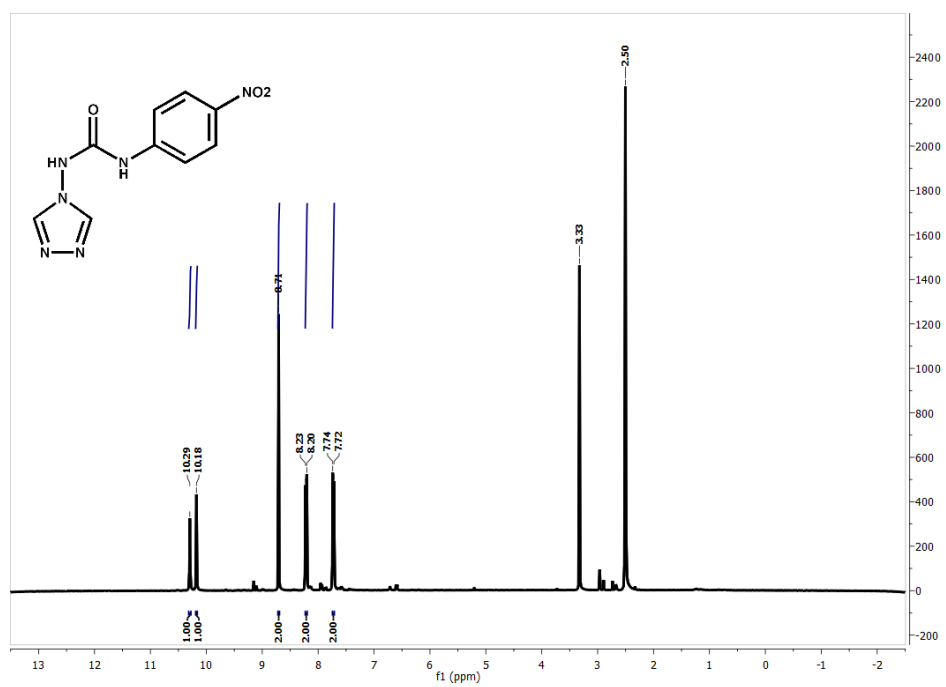
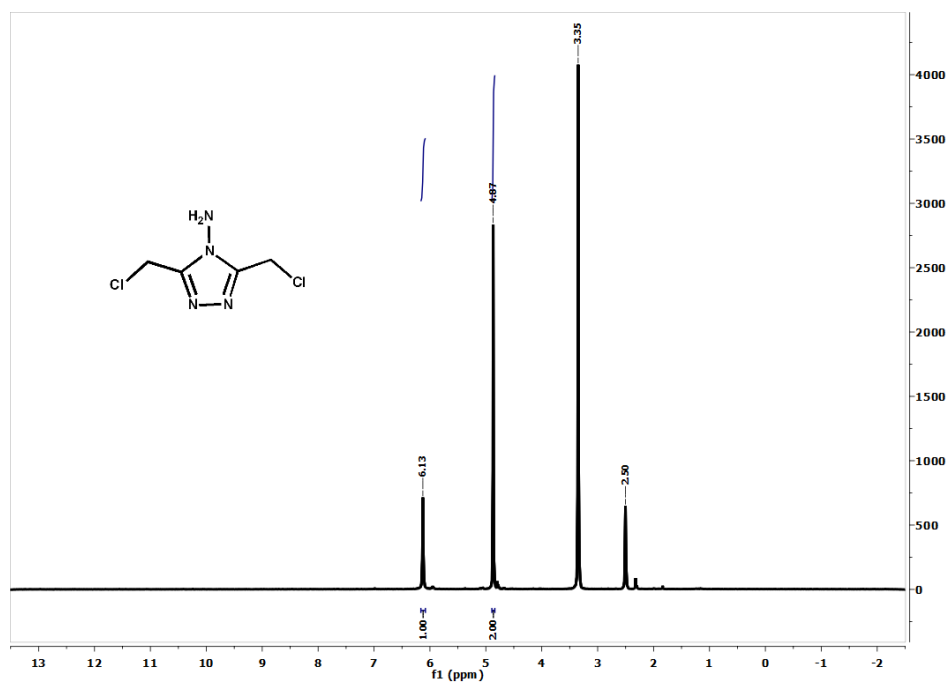
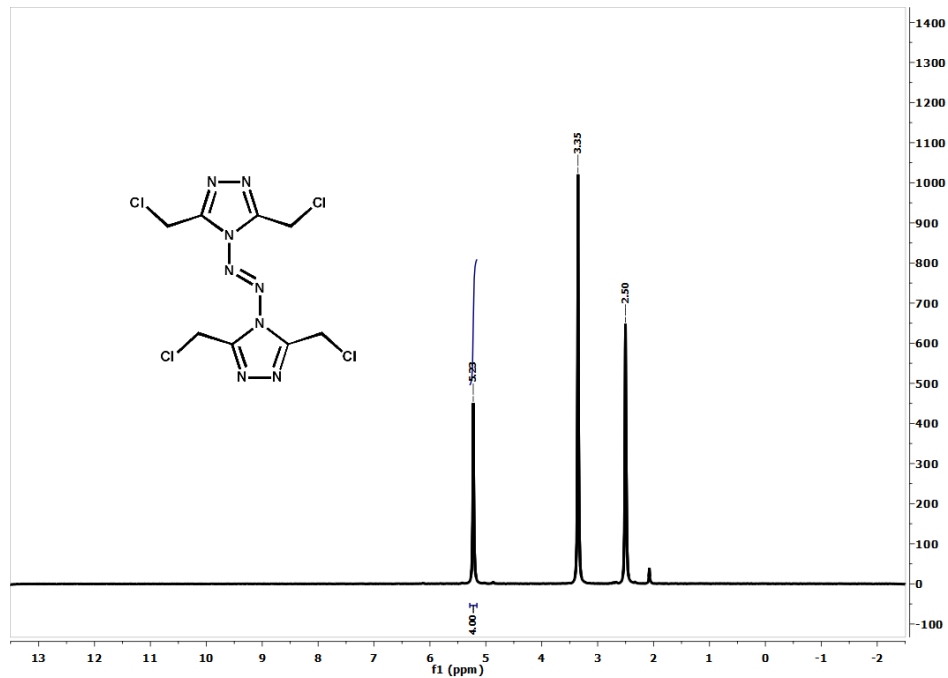


Figure. 9.16: $^1\text{H-NMR}$ spectrum of **L16**.

Figure 9.17: ¹H-NMR spectrum of L17a.Figure 9.18: ¹H-NMR spectrum of L17b.

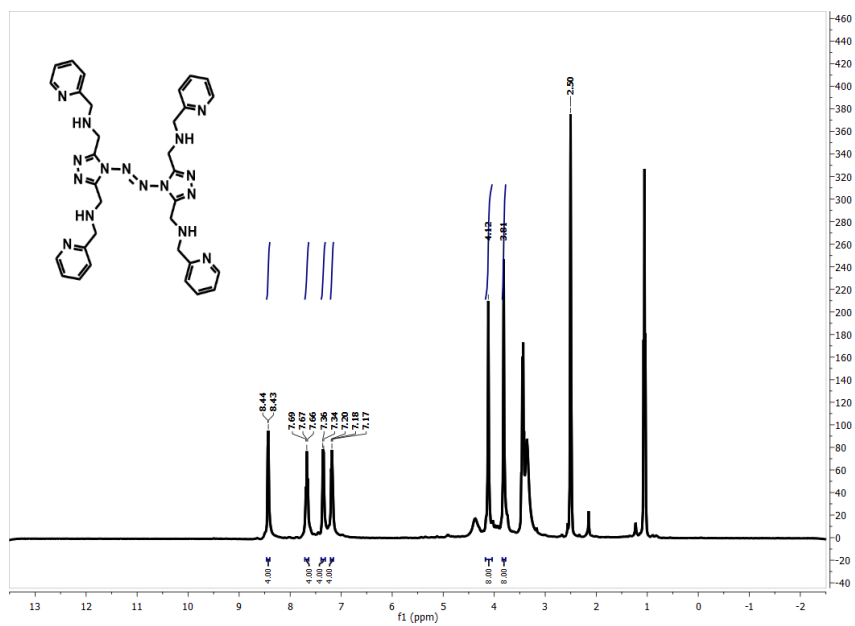


Figure. 9.19: ¹H-NMR spectrum of **L17**.

9.3 Infrared Spectra

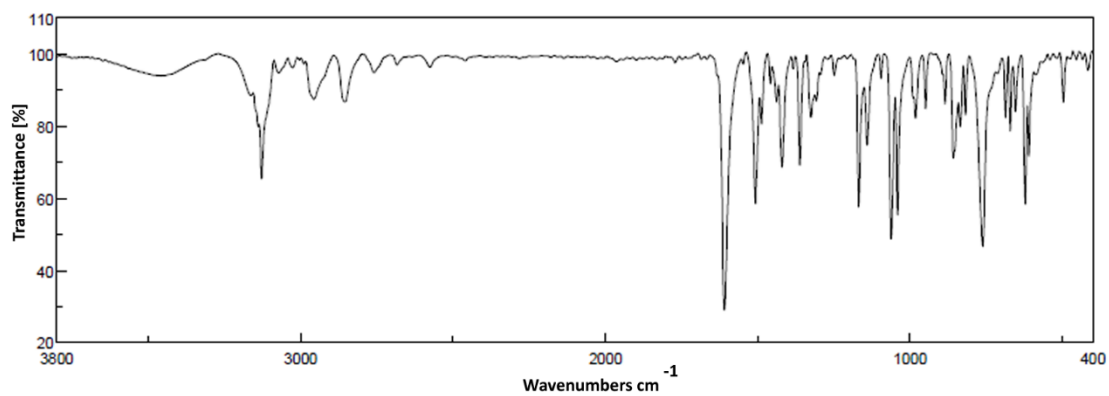


Figure. 9.20: Infrared spectrum of **L1**.

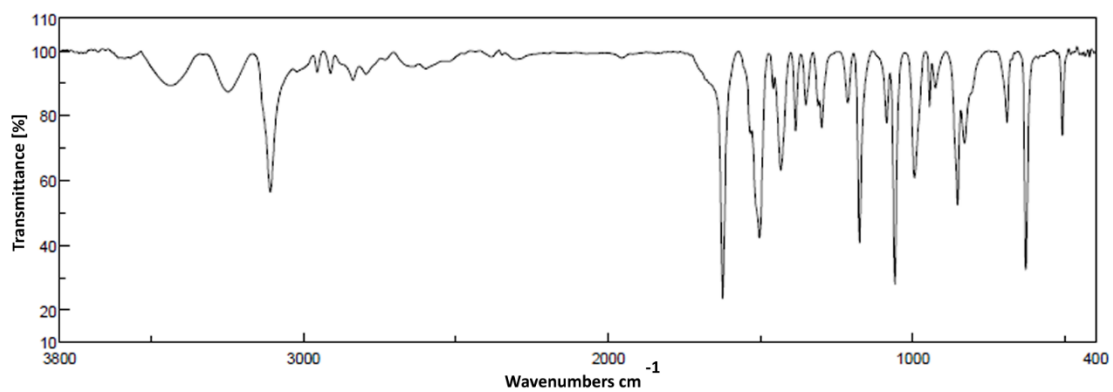


Figure 9.21: Infrared spectrum of L2.

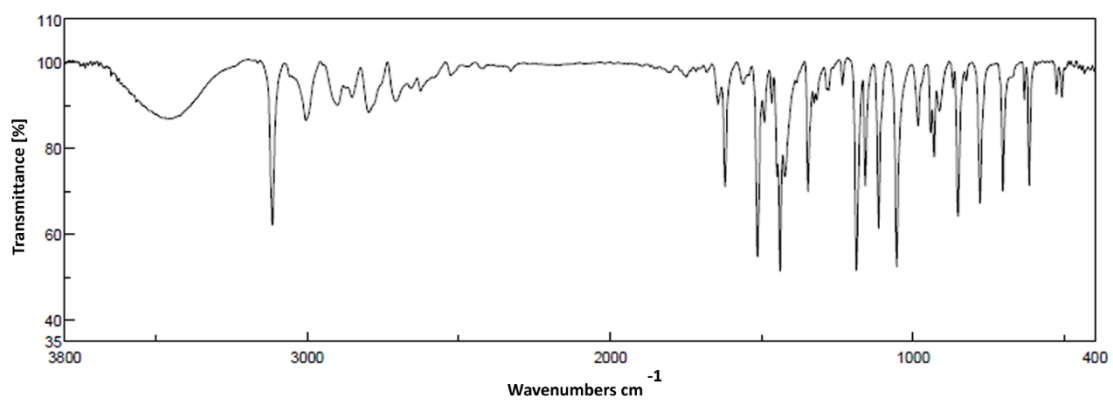


Figure 9.22: Infrared spectrum of L3.

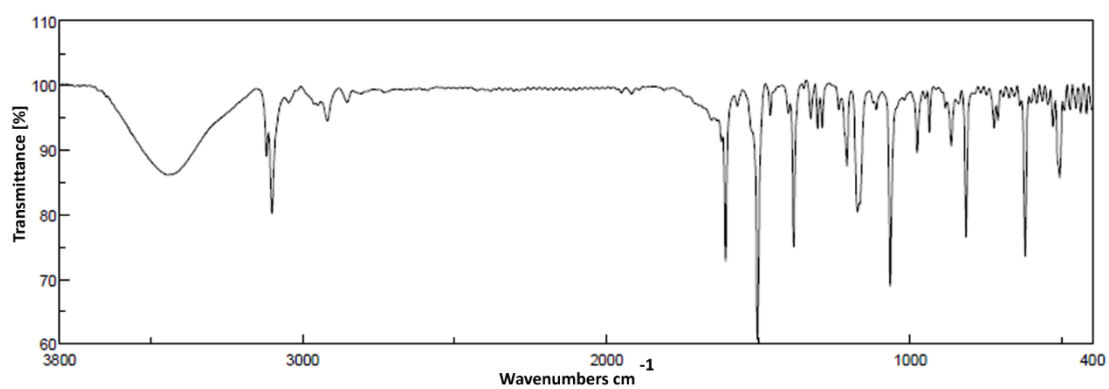


Figure 9.23: Infrared spectrum of L4.

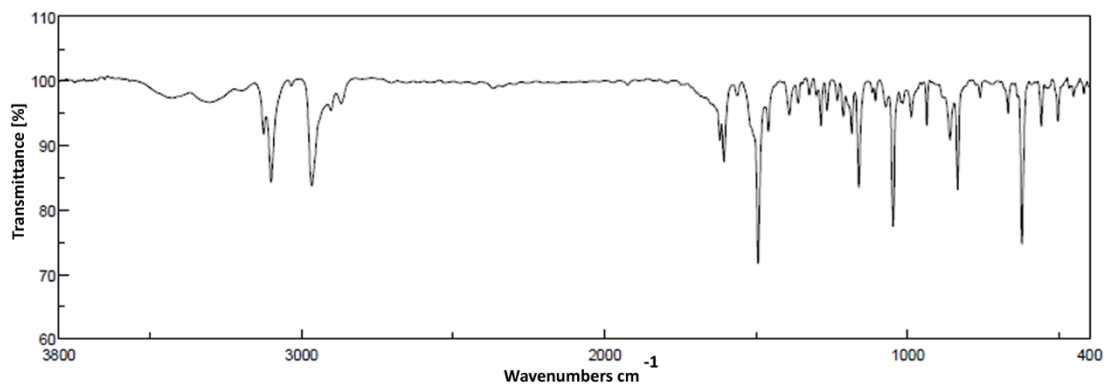


Figure 9.24: Infrared spectrum of L5.

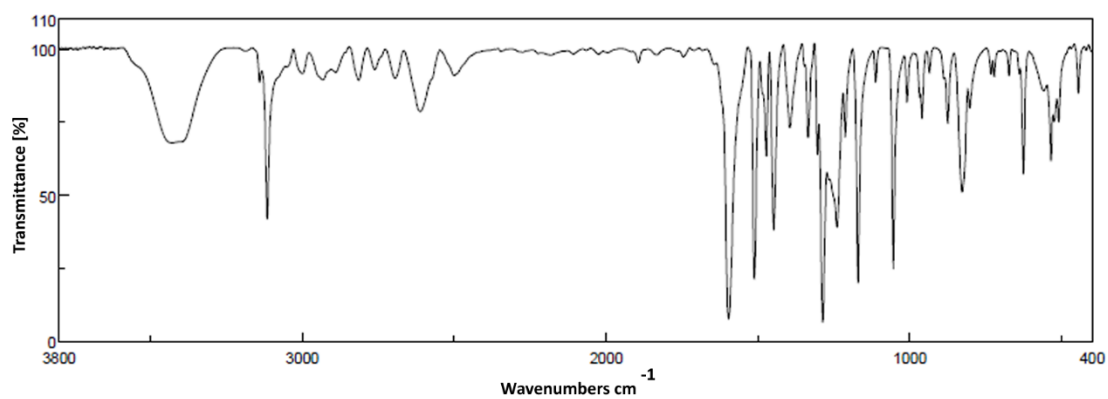


Figure 9.25: Infrared spectrum of L6.

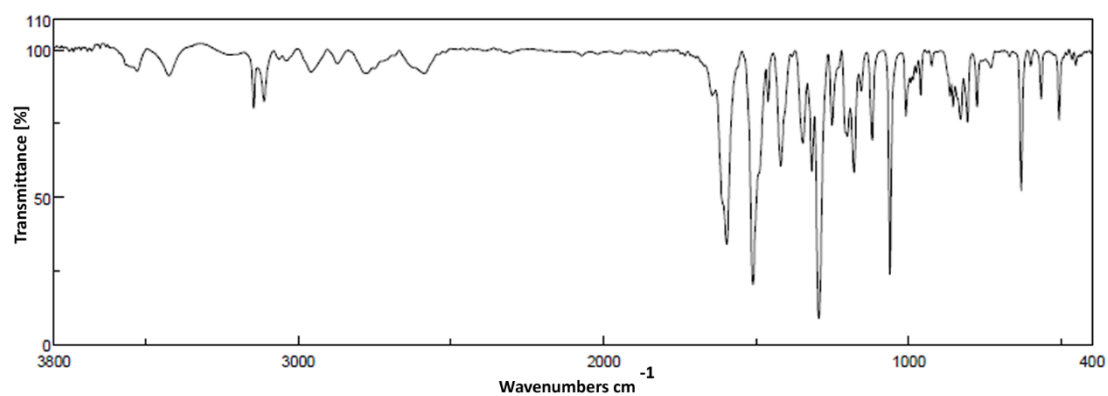
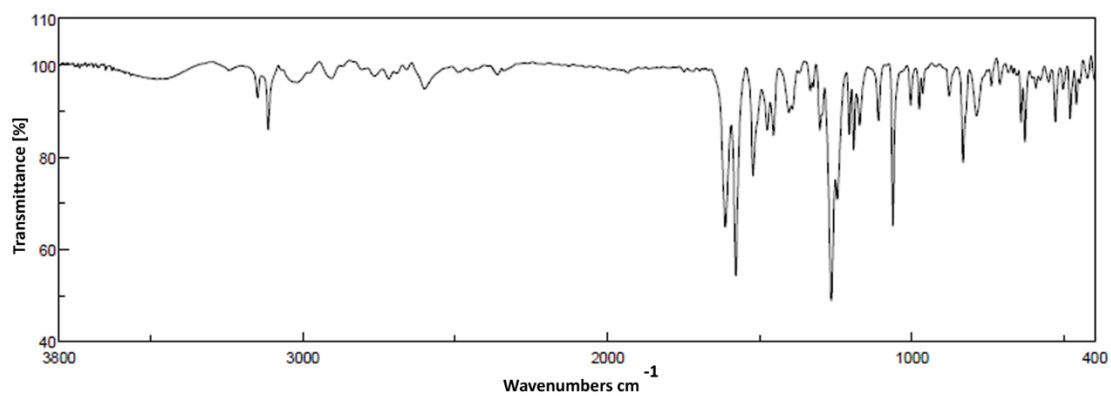
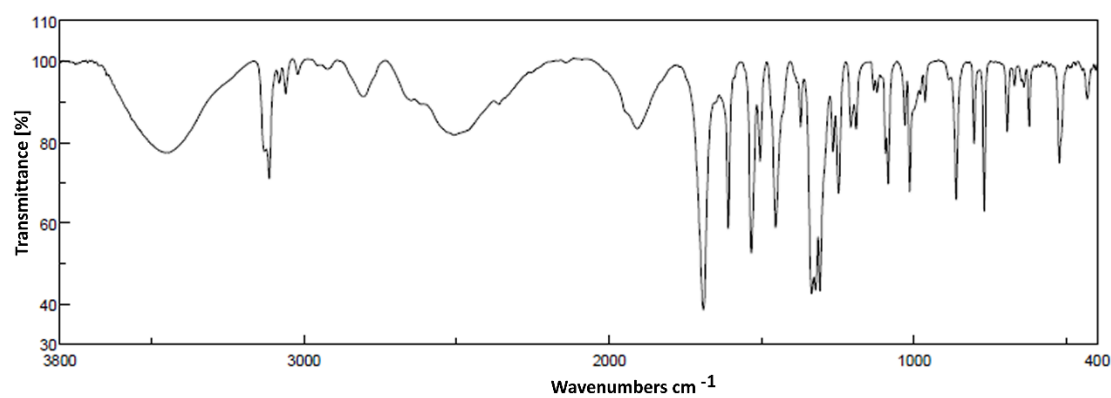
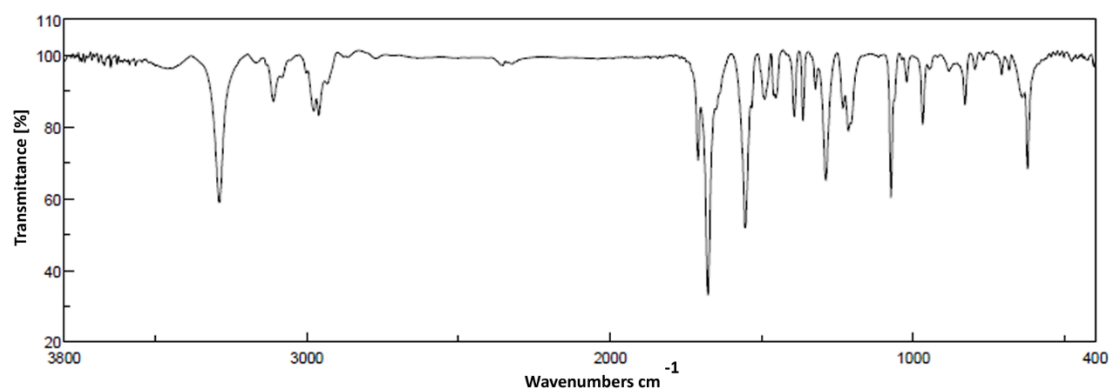


Figure 9.26: Infrared spectrum of L7.

Figure 9.27: Infrared spectrum of **L8**.Figure 9.28: Infrared spectrum of **L9**.Figure 9.29: Infrared spectrum of **L10**.

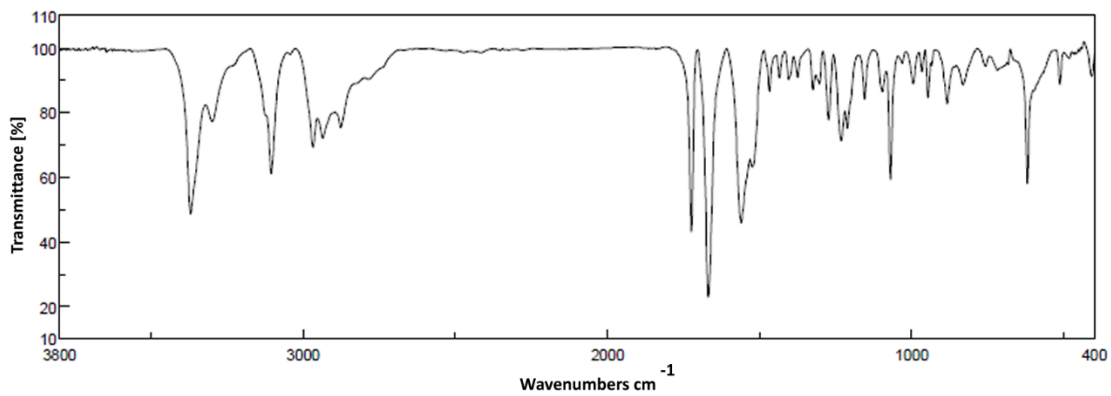


Figure 9.30: Infrared spectrum of L11.

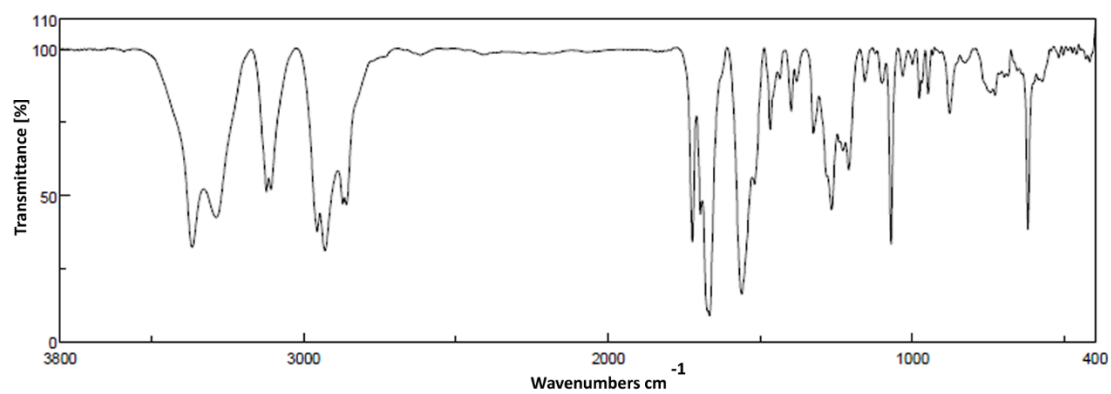


Figure 9.31: Infrared spectrum of L12.

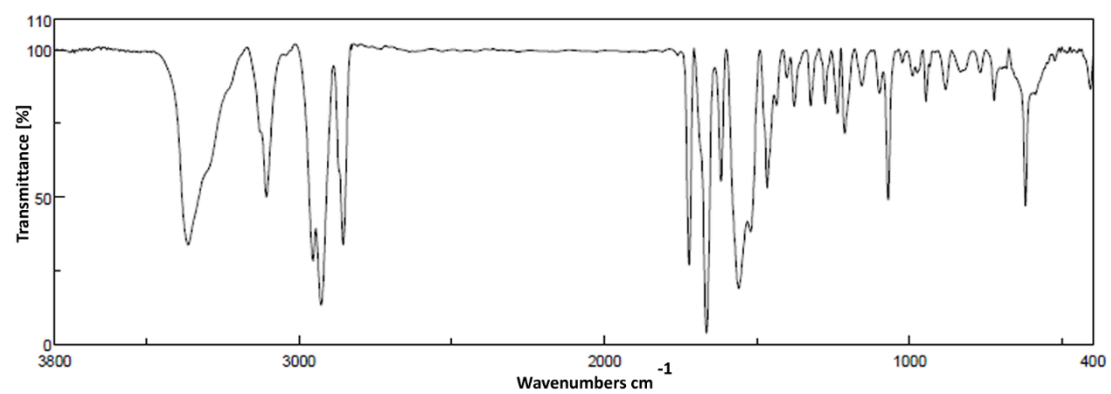


Figure 9.32: Infrared spectrum of L13.

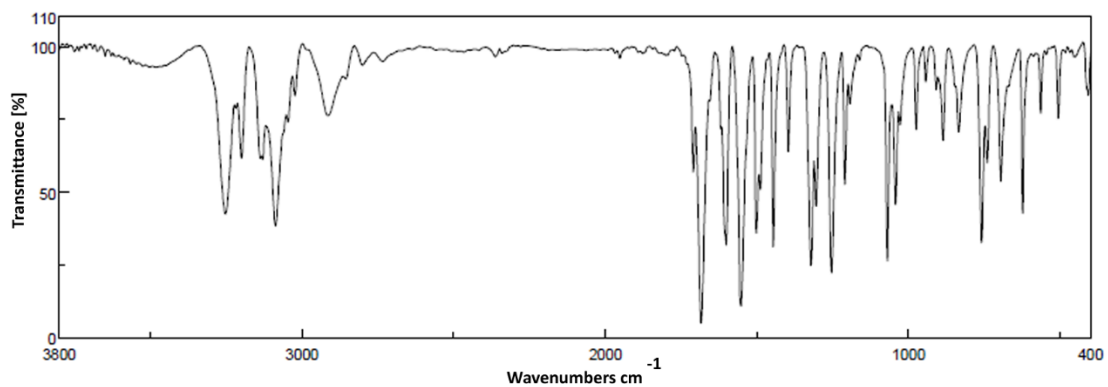


Figure 9.33: Infrared spectrum of L14.

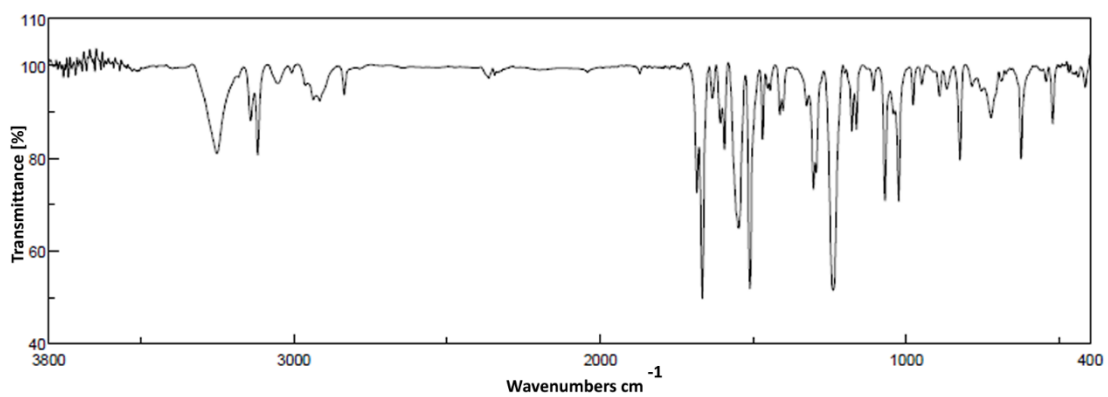


Figure 9.34: Infrared spectrum of L15.

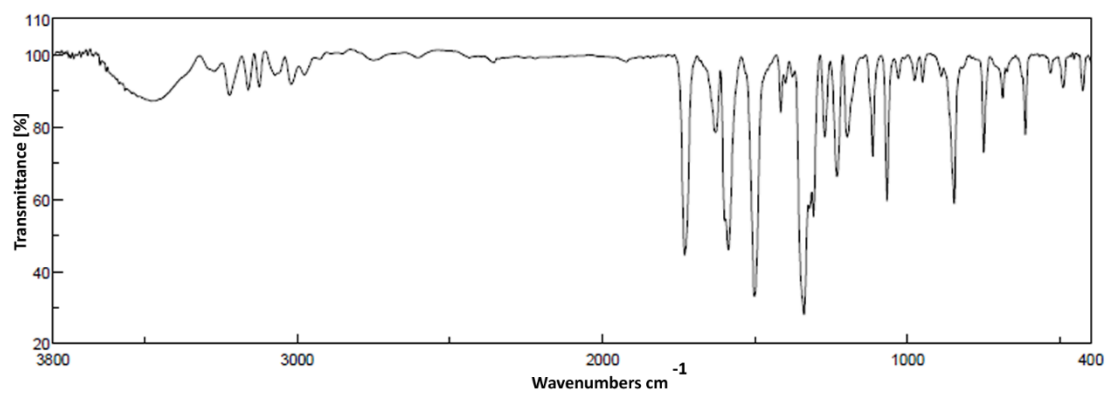


Figure 9.35: Infrared spectrum of L16.

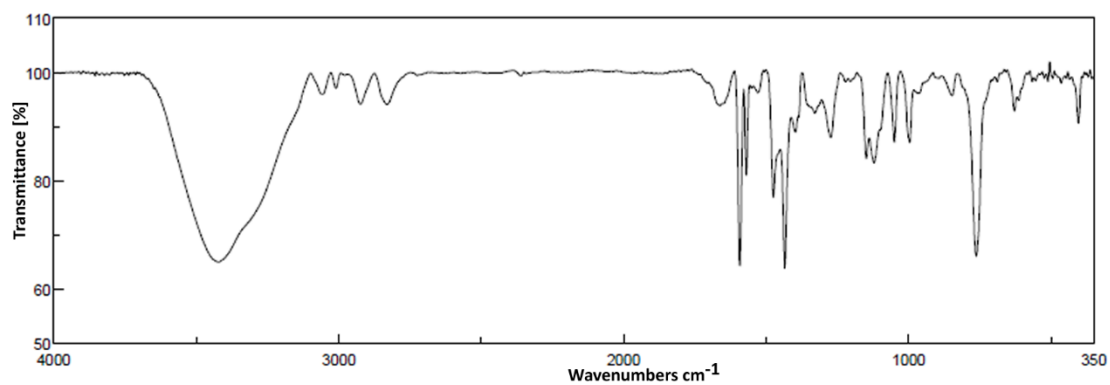


Figure. 9.36: Infrared spectrum of L17.

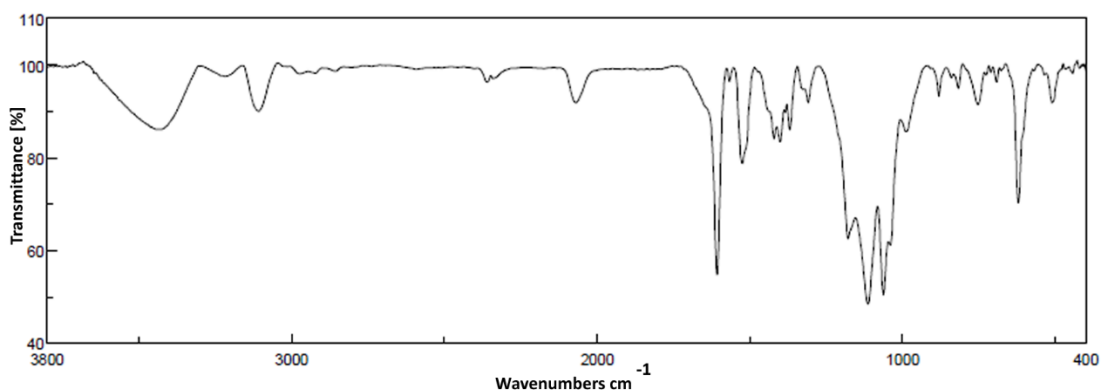


Figure. 9.37: Infrared spectrum of C1.

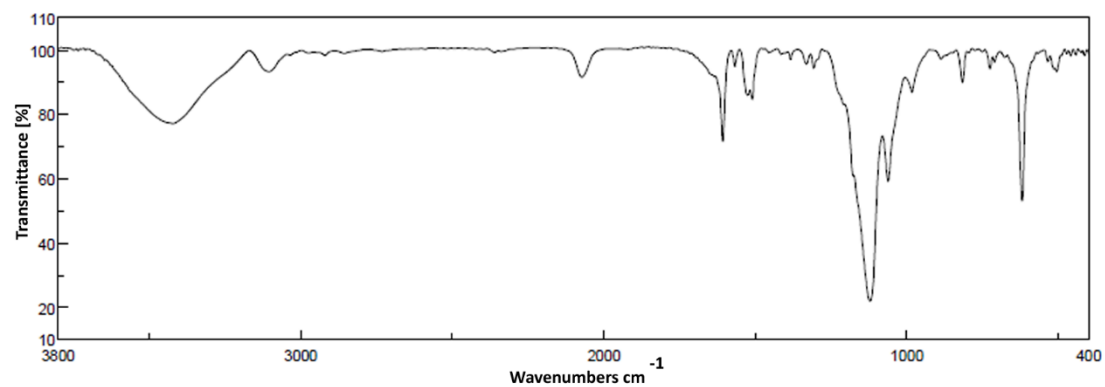


Figure. 9.38: Infrared spectrum of C2.

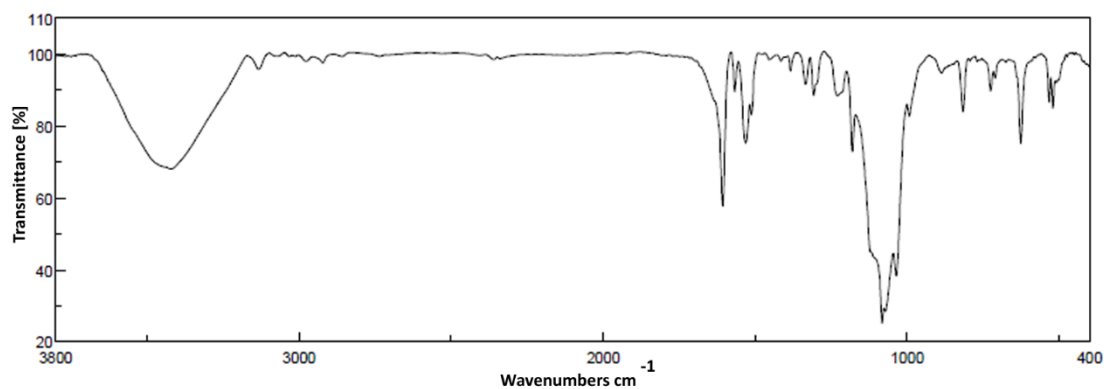


Figure 9.39: Infrared spectrum of C4.

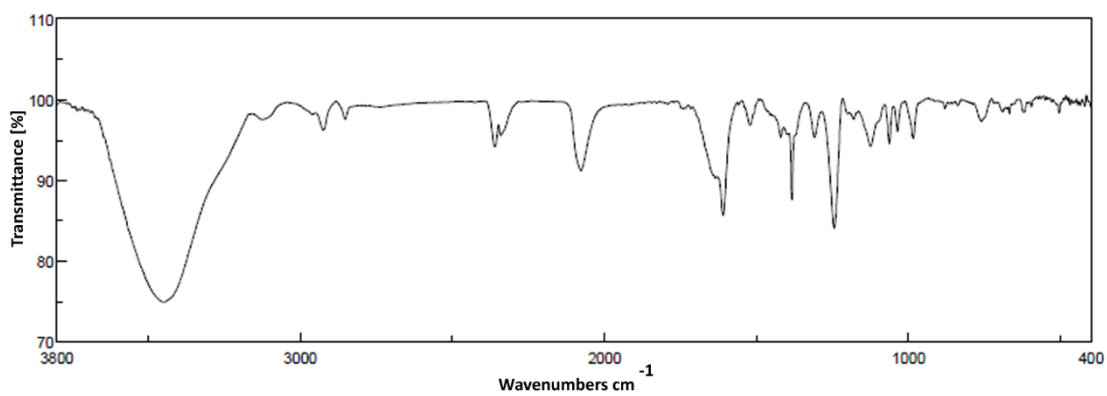


Figure 9.40: Infrared spectrum of C5.

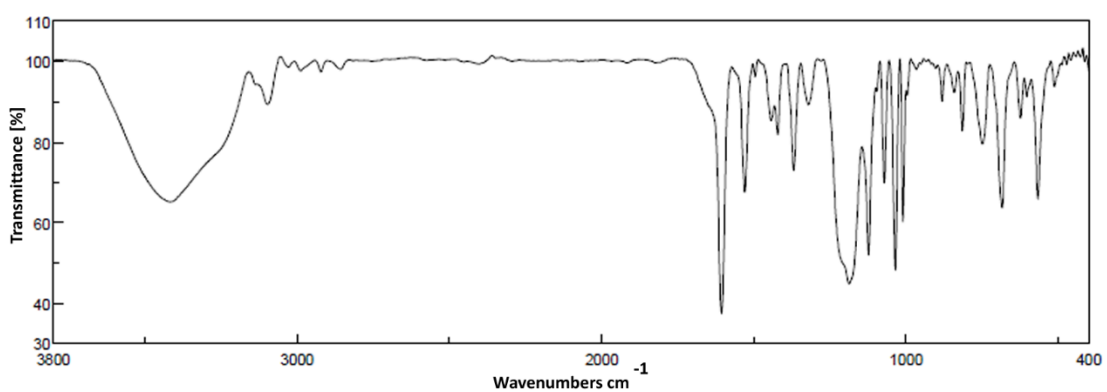


Figure 9.41: Infrared spectrum of C6.

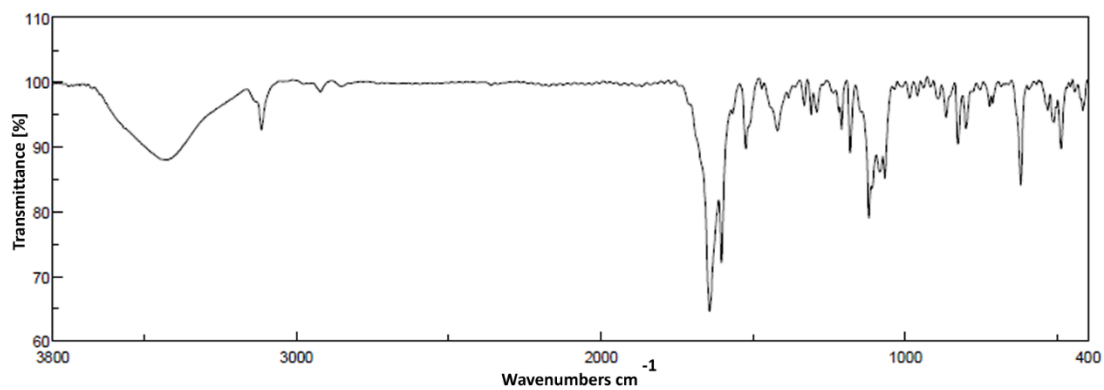


Figure. 9.42: Infrared spectrum of C7.

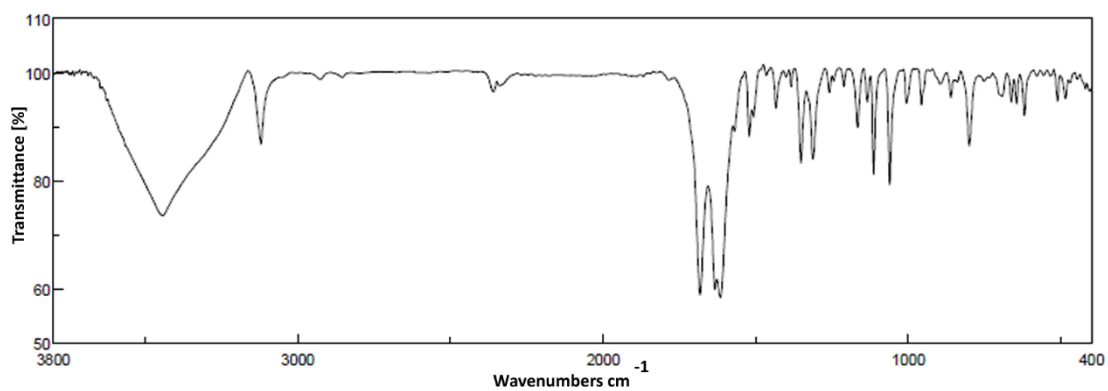


Figure. 9.43: Infrared spectrum of C8.

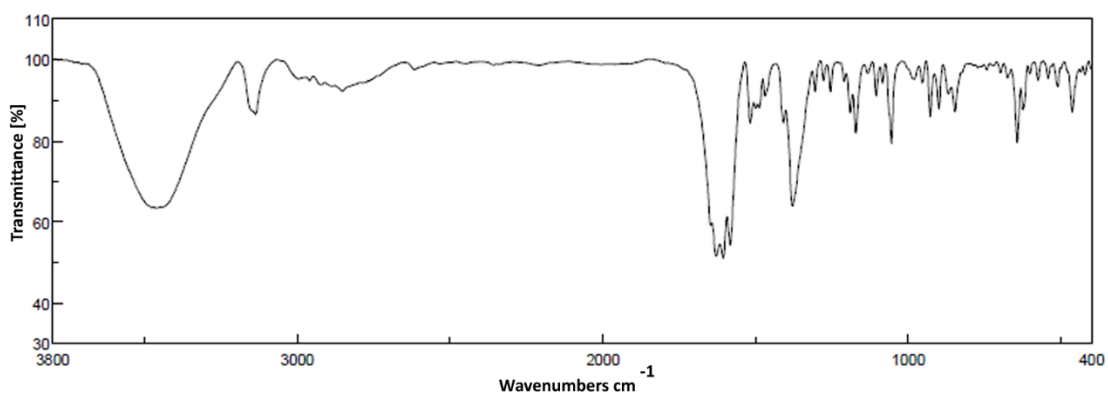


Figure. 9.44: Infrared spectrum of C9.

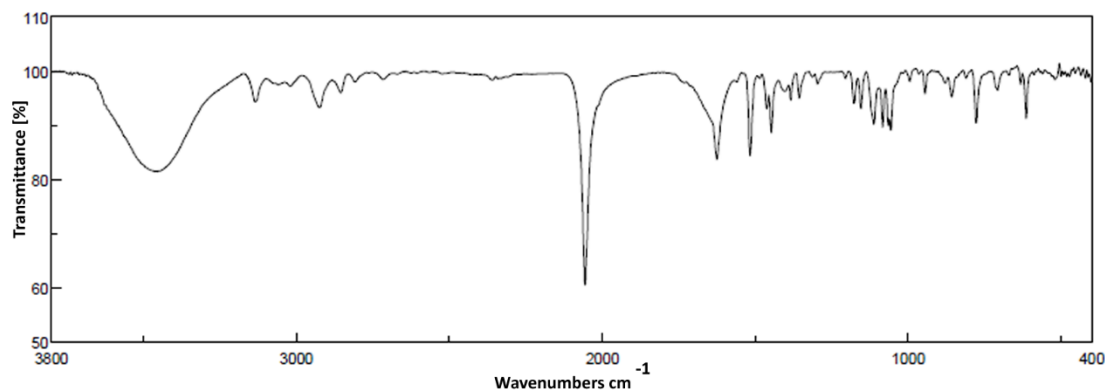


Figure 9.45: Infrared spectrum of C10.

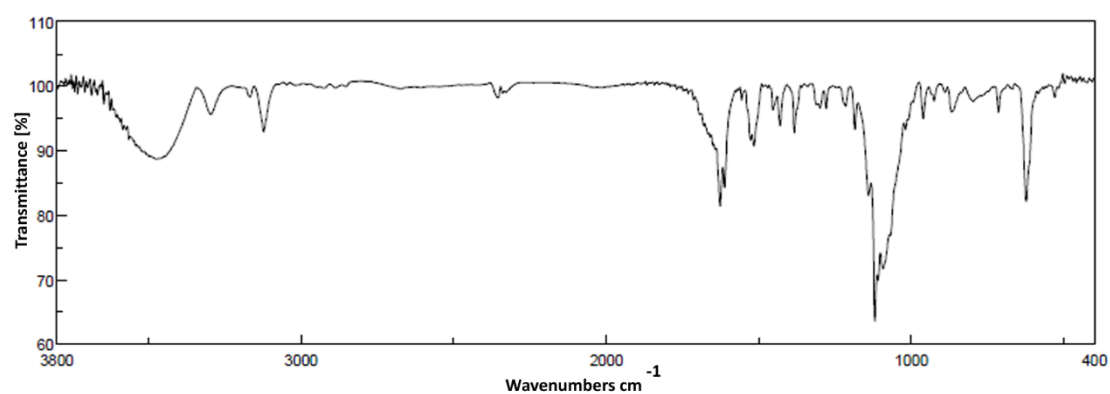


Figure 9.46: Infrared spectrum of C12.

9.4 References

- [1] X. X. Wu, Y. Y. Wang, P. Yang, Y. Y. Xu, J. Z. Huo, B. Ding, Y. Wang, X. Wang, *Cryst. Growth Des.*, **2013**, *14*, 477-490.
- [2] a) Y. Garcia, F. Robert, A. D. Naik, G. Y. Zhou, B. Tinant, K. Robeyns, S. Michotte, L. Piraux, *J. Am. Chem. Soc.*, **2011**, *133*, 15850–15853; b) H. Z. Scott, T. M. Ross, B. Moubaraki, K. S. Murray, S. M. Neville, *Eur. J. Inorg. Chem.*, **2013**, 803-812.
- [3] X. Cheng, Q. Yang, C. Gao, B. W. Wang, T. Shiga, H. Oshio, Z. M. Wang, S. Gao, *Dalton Trans.*, **2015**, *44*, 11282–11285.
- [4] A. Kolnaar, J. Jeroen, M. I. de Heer, H. Kooijman, A. L. Spek, G. Schmitt, V. Ksenofontov, P. Gülich, J. G. Haasnoot and J. Reedijk, *Eur. J. Inorg. Chem.*, **1999**, 881–886.
- [5] O. Roubeau, P. Gamez, S. J. Teat, *Eur. J. Inorg. Chem.*, **2013**, 934–942.
- [6] B. Ding, Y. Y. Liu, Y. Wang, J. G. Ma, Z. Niu, W. Shi, P. Cheng, *Inorg. Chem. Commun.*, **2013**, *31*, 44–48.
- [7] J. L. Wang, Q. Liu, Y. S. Meng, H. Zheng, H. L. Zhu, Q. Shi, T. Liu, *Inorg. Chem.*, **2017**, *56*, 10674-10680.

- [8] M. B. Bushuev, L. G. Lavrenova, Yu. G. Shvedenkov, A. V. Virovets, L. A. Sheludyakova and S. V. Larionov, *Russ. J. Inorg. Chem.*, **2007**, *52*, 46-51
- [9] Y. M. Klein, N. F. Sciortino, C. E. Housecroft, C. J. Kepert, and S. M. Neville, *Magnetochemistry*, **2016**, 2-8.
- [10] O. G. Shakirova, L. G. Lavrenova, Y. G. Shvedenkov, G. A. Berezovskii, D. Y. Naumanov, L. A. Sheludyakova, G. V. Dolgushin and S. V. Larionov, *Russ. J. Coord. Chem.*, **2004**, *30*, 473-479.
- [11] M. Thomann, O. Kahn, J. Guilhem and F. Varret, *Inorg. Chem.*, **1994**, *33*, 6029-6037.
- [12] Y. Garcia, P. Guionneau, G. Bravic, D. Chasseau, J. A. K. Howard, O. Kahn, V. Ksenofontov, S. Reiman and P. Gülich, *Eur. J. Inorg. Chem.*, **2000**, 1531-1538.
- [13] G. Vos, R. A. Le Febre, R. A. G. de Graaff, J. G. Haasnoot and J. Reedijk, *J. Am. Chem. Soc.*, **1983**, *105*, 1682-1683; b) G. Vos, R. A. De Graaff, J. G. Haasnoot, A. M. Van der Kraan, P. De Vaal, J. Reedijk, *Inorg. Chem.*, **1984**, *23*, 2905-2910.
- [14] J. J. A. Kolnaar, G. van Dijk, H. Koojiman, A. L. Spek, V. Ksenofontov, P. Gülich, J. G. Haasnoot and J. Reedijk, *Inorg. Chem.*, **1997**, *36*, 2433-2440.
- [15] D. Savard, C. Cook, G. D. Enright, I. Korobkov, T. J. Burchell and M. Murugesu, *CrystEngComm.*, **2011**, *13*, 5190-5197.
- [16] V. Gómez, J. Benet-Buchholz, E. Martin and J. R. Galan-Máscaros, *Chem. Eur. J.*, **2014**, *20*, 5369-5379.
- [17] V. Gómez, C. S. de Pipaón, P. Maldonado-Illescas, J. C. Waerenborgh, E. Martin, J. Benet-Buchholz and J. R. Galan-Máscaros, *J. Am. Chem. Soc.*, **2015**, *137*, 11924-11927.
- [18] W. B. Chen, J. D. Leng, Z. Z. Wang, Y. C. Chen, Y. Miao, M. L. Tong, W. Dong, *Chem. Commun.*, **2017**, *53*, 7820-7823.
- [19] N. Pittala, F. Thétiot, C. Charles, S. Triki, K. Boukheddaden, G. Chastanet, M. Marchivie, *Chem. Commun.*, **2017**, *53*, 8356-8359.

List of Abbreviations

CFT	crystal field theory
LFT	ligand field theory (LFT)
O_h	octahedral coordination geometry
LFS ($\Delta_o/10Dq$)	ligand field splitting parameter
P	spin pairing energy
LS	low spin
HS	high spin
SCO	Spin Crossover
E_p	potential energy
Δ_r	bond length difference
ΔE^0_{HL}	zero-point energy-difference of the LS and HS state
$k_B T$	thermal energy
ΔH	enthalpy difference
ΔS	entropy difference
ΔG	<i>Gibbs</i> free energy change
LIESST	Light-Induced Excited Spin-State Trapping
ST	spin transition
MOFs	Metal Organic Frameworks
Htrz	1,2,4-triazole
Atrz	4-amino-1,2,4-triazole
EXAFS	X-ray absorption experiments
PXRD	powder diffraction
bpy	4,4'-bipyridine
SCSC	single-crystal-to-single-crystal
IR	Infra-Red
UV/Vis	UV-Visible
EPR	Electron Paramagnetic Resonance spectroscopy
DSC	differential scanning calorimetry
SC-XRD	Single Crystal X-Ray Diffraction
Σ_{ODP}	octahedral distortion parameter
SQUID	Superconducting QUantum Interference Device

List of Abbreviations

δ	isomer shift (relative to α -iron)
Δ_{EQ}	quadrupole splitting
QTAIM	quantum theory of atoms in molecules
WS	Wigner–Seitz Cell
r^{vdW}	van der Waals radius
TIP	temperature independent paramagnetism
1D	one dimensional
2D	two dimensional
3D	three dimensional
4-R-trz	4-substituted-1,2,4-triazole
NMR	Nuclear Magnetic Resonance
R	substituent
$T_{1/2}$	spin transition temperature
vs.	versus
χ_M	molar susceptibility

List of Compounds

Ln stands for ligand with number n;

Cn stands for compound with number n;

Kn stands for organic crystalline compound with number n.

- L1** 4-((1H-pyrrol-2-yl)methylene-amino)-4*H*-1,2,4-triazole (pytrtz)
- L2** 4-(1*H*-imidazol-5-ylmethylene-amino)-4*H*-1,2,4-triazole (5-imztrz)
- L3** 4-(1*H*-imidazol-2-ylmethylene-amino)-4*H*-1,2,4-triazole (2-imztrz)
- L4** 4-(*p*-tolylidene-amino)-4*H*-1,2,4-triazole (toltrz)
- L5** 4-[(4-(*tert*-butyl)benzylidene)-amino]-4*H*-1,2,4-triazole
- L6** 4-[(4*H*-1,2,4-Triazol-4-ylimino)methyl]phenol
- L7** 4-[(4*H*-1,2,4-Triazol-4-ylimino)methyl]-1,2-benzenediol
- L8** 4-[(4*H*-1,2,4-Triazol-4-ylimino)methyl]-1,3-benzenediol
- L9** 4-(*p*-Carboxyphenyl)-1,2,4-triazole (Hcpt)
- L10** 4-(3-*tert*-Butyl ureido)-4*H*-1,2,4-triazole
- L11** 4-(3-*n*-propyl ureido)-4*H*-1,2,4-triazole
- L12** 4-(3-*n*-pentyl ureido)-4*H*-1,2,4-triazole
- L13** 4-(3-*n*-heptyl ureido)-4*H*-1,2,4-triazole
- L14** 4-(3-phenyl ureido)-4*H*-1,2,4-triazole
- L15** 4-(3-4-methoxyphenyl ureido)-4*H*-1,2,4-triazole
- L16** 4-(3-4-nitrophenyl ureido)-4*H*-1,2,4-triazole
- L17** 3,3',5,5'-tetra[(2-pyridylmethyl)amino-methyl]-4,4'-azo-1,2,4-triazole
-
- C1** $[Fe^{II}_2(L4)_5(SCN)_4] \cdot 3H_2O$
- C2** $[Fe^{II}_2(L4)_5(SeCN)_4] \cdot 3H_2O$
- C3** $[Fe^{II}_2(L4)_6(C_2O_4)(H_2O)_2](SeCN)_2(L4)_2(H_2O)_4$
- C4** $[Fe^{II}_3(LA)_6(H_2O)_6] \cdot 6(BF_4) \cdot H_2O \cdot CH_3CH_2CO_2CH_3$
- C5** $[Fe^{II}_2(L1)_5(SCN)_4] \cdot 6H_2O$
- C6** $[Fe^{II}_3(L1)_6(TsO)_6] \cdot 7H_2O \cdot 0.2CH_3OH$

List of Compounds

C7	$[Fe^{II}(L4)_2(C_2O_4)] \cdot 5H_2O$
C8	$[Fe^{II}(L2)(C_2O_4)] \cdot 2H_2O$
C9	$[Fe^{III}(cit)(H_2O)](HL2) \cdot 3H_2O$
C10	$[Fe^{II}_2(L3)_4(SCN)_4]$
C11	$[Fe^{II}(L3)_2(CH_3OH)_2(SCN)_2]$
C12	$[Fe^{II}(L2)_2](ClO_4)_2$
C13	$Fe^{II}(L9)(OH)(H_2O)_2]_n$
C14	$[Fe^{II}_6(\mu_3-O)(OH)_2(L9)_6(H_2O)_2]_n$
C15	$[Fe^{II}_3(\mu_3-O)(OH)(L9)_3]_n$
K1	$(HL1 \cdot CCl_3COO)$
K2	$(HL2 \cdot PF_6)$
K3	$L3$
K4	$(L7 \cdot H_2O)$
K5	$L9$
K6	$L0$
K7	$L11$
K8	$(L14 \cdot H_2O)$
K9	$(L15 \cdot H_2O)$

Curriculum Vitae